2016

Microbial Modification of Soil for Ground Improvement

Hai Lin
Lehigh University

Microbial Modification of Soil for Ground Improvement

By

Hai Lin

A Dissertation

Presented to the Graduate and Research Committee

Of Lehigh University

In Candidacy for the Degree of

Doctor of Philosophy

In

Civil Engineering

Lehigh University

May, 2016

Hai Lin

Microbial Modification of Soil for Ground Improvement

Approved and recommended for acceptance as a dissertation in partial fulfillment of the requirements for the degree of Doctor of Philosophy in Civil Engineering on this date of _____.

_____ _____

Muhannad T. Suleiman, Ph.D
Dissertation Supervisor and Advisor
Department of Civil and Environmental Engineering
Lehigh University

Sibel Pamukcu, Ph.D.
Committee Chairperson
Department of Civil and Environmental Engineering
Lehigh University

_____ _____

Derick G. Brown, Ph.D.
Co-Dissertation Advisor
Department of Civil and Environmental Engineering
Lehigh University

Clay J. Naito, Ph.D.
Internal Committee Member
Department of Civil and Environmental Engineering
Lehigh University

_____ _____

Amy H. Camp, Ph.D.
External Committee Member
Department of Biological Sciences
Mount Holyoke College

Jeffery Helm, Ph.D.
External Committee Member
Department of Mechanical Engineering
Lafayette College

Date Accepted: _____

To my family for all their support…

Thank you, I couldn't have done it without you…

This is for you…

ACKNOWLEDGEMENT

I would first like to thank and express my extreme gratitude to my advisor Professor Muhannad Suleiman. He has been an inspiring role model not only in his profound knowledge, admirable work ethic and integrity but also in the way that he works with his students and his peers. Special thanks to my co-advisor Professor Derick Brown for the opportunity to work with him and his students in his lab.

I would also like to thank all other members of my committee for their insightful and valuable advices and encouragement: Dr. Sibel Pamukcu, Dr. Clay Naito, Dr. Amy Camp, and Dr. Jeffery Helm.

I want to thank my family for their unconditional love and encouragement, which are always my inspiration and courage during my study.

I feel grateful to my friends at Lehigh University for their continuous support throughout the time in grad school, including but not limited to: Yi Dong, Lusu Ni, Ryan Smith, Suguang Xiao, Michael German, Jialan Zhu, Hang Dong, Hanna Moussa Jabbour, Hankai Zhu, Rehab Elzeiny, Mathu Davis, and also the undergraduate students: Pierre Bick, Alexa Hendricks, Yassira Alaziz, Xi Qi, and Devon Gallagher.

Last but by not least, thanks the Lehigh University and National Science Foundation for supporting this research.

TABEL OF CONTENTS

LIST OF TABLES

LIST OF FIGURES

ABSTRACT

Biomediated geochemical processes in soil offer innovative and sustainable potential solutions to some geotechnical challenges. Microbial Induced Carbonate Precipitation (MICP) has been the most researched process for geotechnical problems. Most of the research that have been performed on MICP focused on investigating its effects on soil behavior at small lab-scale. Limited particle-scale (micro-scale) and field-or large laboratory-scale tests were conducted. Furthermore, challenges of upscaling MICP to real applications still exist, including heterogeneous $CaCO_3$ distribution due to bio-clogging, soil properties (e.g. modulus and permeability) monitoring, and byproducts management, etc. The goal of the research presented in this dissertation focuses on investigating the MICP-treated soil behavior ranging from particle-scale to macro-scale, addressing some upscaling challenges, and advancing MICP towards practically-feasible field applications.

The major effort of this research focuses on investigating physical properties of MICP-treated sand and MICP bio-grouted permeable pile system ranging from particle- to large laboratory-scale (e.g. micrometer to meter scale). The results from tests at different scales demonstrate that MICP improved soil mechanical behavior and enhanced the capacity of permeable pile foundation system. The research demonstrate a promising potential for field-scale foundation enhancement using MICP, which is

envisioned to be the main focus of future research. In addition, a preliminary study on the effects of biofilm modification on the physical sand properties is conducted.

1. INTRODUCTION

1.1 OVERVIEW

Although microbes are abundant in soils, they have not been widely considered in classical geotechnical engineering. The first explicit discussion of applications of biological processes in geotechnical engineering was reported by Mitchell and Santamarina (2005). Instead of considering soil as an inert engineering material, soil, which is a living ecosystem, can offer innovative and sustainable solutions to geotechnical problems (DeJong et al. 2013). With more recent studies, the potential of applying microbiology in geotechnical engineering has been considered as a new sub-discipline called bio-geotechnical engineering. The current research of bio-geotechnical engineering includes mineral precipitation, gas generation, and biofilm formation. However, the emerging bio-geotechnical engineering still faces several challenges (or knowledge gaps) including upscaling the process from laboratory to field scale, in-situ monitoring of reaction processes, bio-geo-chemical-mechanical interactions and modeling, and byproducts management (DeJong et al. 2013).

The research summarized in this dissertation addresses some of these knowledge gaps focusing on investigating the physical behavior of sand matrix and permeable pile system treated by Microbial Induced Carbonate Precipitation (MICP). In addition, a preliminary study on biofilm formation and its effects on the physical properties of sand matrix was performed.

1.2 MOTIVATION AND IMPORTANCE

Pasten and Santamarina (2012) reported that the world population is expected to increase by ~30% by the year of 2040. To support this significant increase of human population, the American Society of Civil Engineers estimated that a $1.6 trillion investment in civil infrastructure is necessary in the United States (ASCE 2006). Such large expected rehabilitation and expansion of civil infrastructure raises the concerns regarding the sustainability of civil engineering practices that rely on energy-intensive materials and techniques (DeJong et al. 2010 and 2013).

Ground improvement techniques are utilized to enhance the stability of soil, allow for water drainage (consolidation), reduce settlement and improve the resistance to seismic loading, which are necessary for the rehabilitation and expansion of civil infrastructure. However, traditional ground improvement construction techniques requires heavy machinery, disturbs urban infrastructure, and involves cement and other chemicals that have significant environmental impacts (Ivanov and Chu 2008, van Paassen 2009, and Al Qabany 2011). Therefore, new ground improvement alternatives that are environmental-friendly and have similar construction efficiency are greatly needed.

Bio-geotechnical engineering, a new branch of geotechnical engineering, is one of the environmental-friendly and efficiency potential options. In 2006, the US National Research Council (NRC 2006) identified bio-geotechnical engineering as one of the significant research areas for the 21st century. Bio-geotechnical engineering rely on

bio-mediated geochemical processes that offer an environmental-friendly development, utilize low viscosity fluids which can penetrate into deep stratum, require low cost and minimum extra energy, and sequestrates carbon underground to mitigate greenhouse gases (DeJong et al. 2006; Ivanov and Chu 2008; van Paassen 2009, Phillips et al. 2013).

Exploring bio-mediated geochemical processes adds new concepts to traditional soil mechanics and geotechnical engineering (Mitchell and Santamarina 2005; Rebata-Landa 2007; Ivanov and Chu 2008; DeJong et al. 2013). Mineral precipitation induced by microbes can cement particles increasing soil strength and stiffness. In addition, the generation of gas bubbles from microbial metabolic activity affects the bulk modulus of the pore fluid and thus reduces the generation of excess pore water pressure during shearing. Furthermore, microorganisms can form biofilm and secret biopolymer, which may clog the pore space, reducing the permeability of the soil matrix.

The most commonly researched bio-mediated process for bio-geotechnical applications is Microbial induced carbonate precipitation (MICP). Several research groups have been investigating its effects on soil behavior mainly at small lab-scale (Rebata-Landa 2007; Ivanov and Chu 2008; van Paassen 2009; DeJong et al. 2010; Al Qabany 2011; and Cheng et al. 2013a). However, limited particle-scale (micro-scale) and field or large laboratory-scale tests have been conducted. Applications of the MICP technique in both laboratory column tests and limited field tests have encountered practical difficulties, including bioplugging (permeability reduction accompanying the induced mineral precipitation). Bioplugging limits the distribution of precipitation

agents within the soil. Due to this limitation, mass stabilization of soil using MICP remains problematic. The research presented in this dissertation addresses some of the knowledge gaps and limitations faced by bio-geotechnical engineering. The goal of the research presented in this dissertation focus on investigating the MICP-treated soil behavior ranging from particle-scale to macro-scale, addressing some upscaling challenges, and advancing MICP towards practically-feasible field applications.

1.3 SCOPE AND ORGANIZATION

The goal of the research presented in this dissertation is to investigate the MICP-treated soil behavior ranging from particle-scale to macro-scale, address upscaling challenges, and advancing MICP towards practically-feasible field applications. The outline of this dissertation research activities that focused on achieving this research goal is listed below.

- Chapter Two: This chapter presents a general literature review of three biogeochemical processes that have the potential for practical applications of geotechnical engineering. Their effects on physical behavior of soils and application potentials are also reviewed.
- Chapter Three: This chapter focuses on investigating the $CaCO_3$ spatial distributions and $CaCO_3$ bond strength at particle-scale and their effects on the mechanical and permeability properties of the MICP-treated sand. The measured shear wave (S-wave) and compression wave (P-wave) velocities, Poisson's ratio,

and permeability versus $CaCO_3$ contents were compared with their calculated values using the cemented-sand, uncemented-sand, Kozeny-Carman, and Panda-Lake models. The characteristics of the $CaCO_3$ bond, bond force and strength were measured.

- Chapter Four: The mechanical behavior of sands treated by MICP has been investigated. Triaxial and confined compression tests with embedded shear and compression wave (S-wave and P-wave) sensors were conducted on two MICP-treated sands, Ottawa 50/70 and 20/30 silica sands.
- Chapter Five: This chapter focuses on evaluating the feasibility of enhancing the response of permeable piles using MICP bio-grouting under axial pull-out loading. Two instrumented pervious concrete piles with and without MICP bio-grouting were tested under axial pull-out load at the soil-structure interaction (SSI) facility at Lehigh University. The mechanical responses of the pile and surrounding soil were analyzed, along with shear wave (S-wave) velocities, moisture and $CaCO_3$ contents of the surrounding soil.
- Chapter Six: This chapter evaluates the feasibility of enhancing the permeable piles using MICP bio-grouting under axial compression loading. Two instrumented pervious concrete piles with and without MICP bio-grouting were tested under axial compression loading at the soil-structure interaction (SSI) facility at Lehigh University. The mechanical responses of the pile and surrounding soil were

analyzed, along with shear wave (S-wave) velocity, moisture content, $CaCO_3$ and ammonium contents of the surrounding soil.

- Chapter Seven: The goal of this chapter is to investigate the mechanical behavior of biofilm-cemented sand. Three types of tests at variable conditions were conducted including anaerobic tests, syringe tests, and triaxial tests. The bacteria density (OD_{600}), pH, and nitrate concentration during biofilm treatment was monitored. S-and P-wave velocities were also monitored during biofilm treatment and loading of the triaxial test. After the tests, biomass content and Scanning Electron Microscope (SEM) images of sand samples were analyzed for biofilm distribution and morphology in the sand matrix.
- Chapter Eight: This chapter provides general conclusions and offers recommendations for future studies.

2. LITERATURE REVIEW

2.1 POTENTIAL BIOGEOCHEMICAL PROCESSES

Harnessing the biogeochemical processes in soil is a transformative practice in geotechnical engineering (DeJong et al. 2013). Several biogeochemical processes have been investigated mainly at the lab-scale, including mineral precipitation (mainly Microbially Induced Carbonate Precipitation, MICP), biogas generation, and biofilm formation. This section provides a review of these biogeochemical processes and discuss the literature related to MICP in details.

2.1.1 Mineral Precipitation

Microbial Induced Carbonate Precipitation (MICP)

Realizing Microbial Induced Carbonate Precipitation (MICP) using urea hydrolysis bacteria *Sporosarcina pasteurii* (*S. Pasteurii*, ATCC 11859) is the most widely researched process. The process of MICP is shown schematically in Figure 2.1. *S. Pasteurii* (ATCC 11859), an alkalophilic soil bacterium with a highly active urease enzyme (Ferris et al. 1996), decomposes urea into ammonium (NH_4^+), bicarbonate (HCO_3^-), and hydroxide ions (OH^-) and creates an alkaline environment (pH>7). This alkaline environment shifts the chemical equilibrium of carbon dioxide to supersaturated carbonate, which is required for the precipitation of calcium carbonate ($CaCO_3$). Calcium carbonate is nucleated on bacteria cell surface containing

immobilized calcium (Ca^{2+}) ion and form calcite or vaterite (determined by urease activity, Van Paassen 2009). Simultaneously, the negatively charged bacterial cell may attach to the soil particle surface due to the interaction between attractive London-van der Waals force and the repulsive electrostatic force between sand and bacteria surfaces (Logan et al. 1995; Hermansson 1999). During this process, the growth of $CaCO_3$ will bridge between soil particles and create a bond, enhancing the strength and stiffness of soil matrix are enhanced (DeJong et al. 2006; Whiffin et al. 2007).

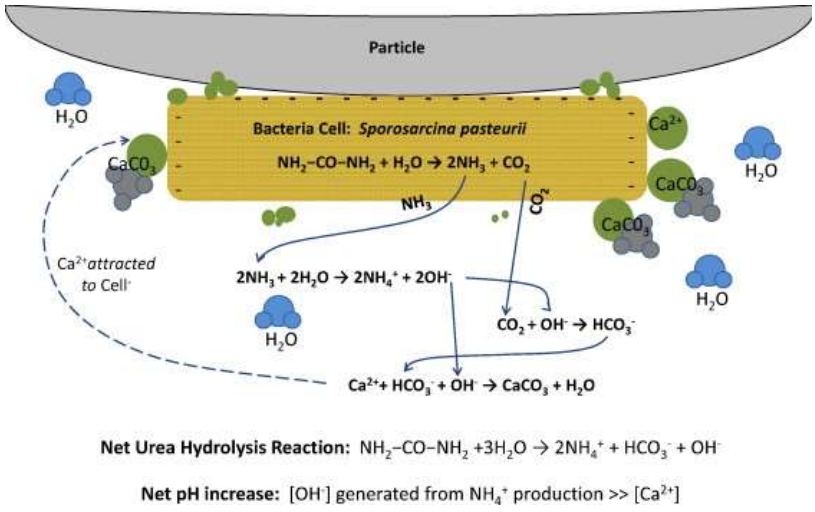

Figure 2.1. The process of Microbial Induced Carbonate Precipitation (MICP) (DeJong et al. 2010).

Other Types of Bio-Mediated Mineral Precipitation

MICP involves a microbially-regulated process of $CaCO_3$ precipitation, which can be induced by different metabolic activities including microbial-catalyzed hydrolysis of urea and microbial-denitrification of calcium nitrate (Stocks-Fischer et al. 1999; DeJong et al. 2006; Ivanov and Chu 2008; van Paassen et al. 2010a; Hamdan et al. 2011). During denitrification, acetate is oxidized to produce alkalinity and carbonate ions, and simultaneously nitrate is reduced to nitrogen gas. By adding calcium ion (Ca^{2+}), $CaCO_3$ precipitates. The overall equation is shown below (Equation 2-1).

$$1/2.6Ca(C_2H_3O_2)_2 + 1.6/2.6Ca(NO_3)_2 \rightarrow CaCO_3 + 1.6/2.6N_2 + 1.4/2.6CO_2 \quad \text{Equation 2-1}$$

The advantage of utilizing denitrification induced carbonate precipitation includes not producing harmful by-products (such as ammonium from MICP), good functionality under oxygen deficient subsurface environment since facultative anaerobes are used.

In addition to carbonate precipitation, the precipitation of ferric hydroxide was also utilized to improve soil behavior. Ivanov et al. (2010) reported that the iron-reducing bacteria is used to produce a ferrous/ferric-containing solution from iron ore and organic waste (Equation 2-2). Simultaneously, ureolysis, denitrification, or sulfate-reducing bacteria could be used to increase the pH of the system. This process can have a low-cost potential since it utilizes iron ore and organic waste.

$$(HCOO)_3Fe + 3OH^- + 3NH_4^+ \rightarrow Fe(OH)_3 \downarrow + 3HCOONH_4 \quad \text{Equation 2-2}$$

Instead of bio-mediated mineral precipitation, urease enzyme was also utilized to catalyze urea hydrolysis, producing ammonium and carbonate with pH=~9 condition (Equation 2-3). By adding calcium ion (Ca^{2+}), $CaCO_3$ precipitates (Equation 2-4). This process is termed as enzyme induced carbonate precipitation (EICP) (Hamdan 2014).

$$CO(NH_2)_2+2H_2O \rightarrow 2NH_4^{+}+CO_3^{2-} \quad \text{Equation 2-3}$$

$$CO_3^{2-}+Ca^{2+} \rightarrow CaCO_3 \quad \text{Equation 2-4}$$

As compared with MICP, EICP does not require the need of microbes which require the cultivation and the organic substrate (urea) for their own growth (Neupane et al. 2013; Hamdan 2014). In addition, the small size of the urease (~12 nm) of EICP can remediate the bio-clogging issue encountered with MICP treatment and allow EICP to penetrate into the silt-sized particle range.

Upon comparing the different processes of mineral precipitation, the MICP using ureolysis bacteria is the most widely researched because of its highest reaction rate (DeJong et al. 2010). Thus, following sections on mineral precipitation will focus mainly on MICP.

2.1.2 Gas Generation

Biogeochemical processes can lead to the production of gases in porous media (Mitchell and Santamarina 2005; DeJong et al. 2013). Rebata-Landa and Santamarina (2012) summarized the involved processes and species that can lead to biogenic gas generation from literature as shown in Table 2.1. The gas production rate can be

controlled by limiting bacterial metabolic activity based on nutrient availability and environment factors such as temperature, pH, etc. As shown in Table 2.1, several gases can be generated, such as CO_2, H_2, CH_4, and N_2. Nitrogen gas (N_2) is neither explosive nor a greenhouse gas, which presents a good application potential for geotechnical applications (Rebata-Landa and Santamarina 2012).

To date, most studies focused on investigating the biogenic process of N_2 based on respiratory denitrification for geotechnical applications (Rebata-Landa and Santamarina 2012; He et al. 2013; He and Chu 2014). Nitrate is reduced to nitrogen gas through the process of denitrification. Electron donors are provided from organic compounds such as methanol, ethanol, or sodium acetate as shown in Equation 2-5, Equation 2-6, and Equation 2-7 (He et al. 2013). Several types of bacteria were used to realize denitrification to generate N_2 in the soil matrix, including *Paracoccus denitrificans* (ATCC 13543, Rebata-Landa and Santamarina 2012), *Acidovorax sp.* (He et al. 2013; He and Chu 2014). During the denitrification, N_2 and CO_2 are generated and desaturate the soil matrix, reducing the generation of excess pore water pressure and increasing liquefaction resistance.

$$5CH_3OH + 6NO_3^- \rightarrow 3N_2 + 5CO_2 + 7H_2O + 6OH^- \quad \text{Equation 2-5}$$

$$5C_2H_5OH + 12NO_3^- \rightarrow 6N_2 + 10CO_2 + 9H_2O + 12OH^- \quad \text{Equation 2-6}$$

$$5CH_3COO^- + 8NO_3^- \rightarrow 4N_2 + 10CO_2 + H_2O + 13OH^- \quad \text{Equation 2-7}$$

Table 2.1. Previous studies on biogenic gas generation (Rebata-Landa and Santamarina 2012).

Species	Remarks	Gases	Reference
Indigenous bacteria from two mine soils in east Texas	NO_3^- added; no NO_3^- added; $NO_3^- + H_2O \downarrow$ added	N_2O, N_2	Johns et al. 2004
Indigenous bacteria from interstitial waters of sulfate-depleted marine sediments	After sulfate depletion Rate of ~13 μmole/liter/day	CH_4	Martens and Berner 1974
Indigenous bacteria from a Brookston loam	NO_3^- added	N_2O, N_2	Firestone et al. 1980
Methanobacterium thermoautotrophicum	Methane production started after 1 h lag and ceased after 5 h	CH_4, H_2	Daniels et al. 1980
Indigenous bacteria from soils used for tomato plants	After a lag phase of ~ 20 h, gas was produced for 75 h	H_2	Logan et al. 2002
Mixed anaerobic bacteria	Gas production inversely proportional to SRT. Total gas production ranged from 4 to 10 L/day	CH_4, H_2	Nakamura et al. 1993
Clostridium acetobutylicum	Vigorous gas production	CO_2, H_2	Behlulgil and Mehmetoglu 2002
Indigenous bacteria from soil at an experimental site	Maximum gas production started after 71 h	N_2O, N_2	Cardenas et al. 2003
Mixed denitrifying bacteria	Nitrogen gas (N_2) was present almost entirely in the gas phase	N_2O, N_2, CO_2	Chung and Chung 2000
Indigenous bacteria from an estuarine clayey silt	Gas produced after 21 days and held in the sediment bed for the next 17 days	CH_4, CO_2	Sills and Gonzalez 2001
Indigenous bacteria from a wood compost bed medium	NO_x removal (and presumed N_2 production) was rapidly performed in batch studies	N_2, N_2O	Barnes et al. 1995
Indigenous bacteria from a fluvic hypercalcaric cambisol	Ratio $N_2O/(N_2O+N_2)$ was around 0.54 in all cases	N_2O, N_2, CO_2	Cannavo et al. 2004

2.1.3 Biofilm Formation

Biofilms are a combination of microbial cells and associated exopolysacharide (EPS). It could be beneficially utilized for engineering purposes such as drinking water and waste water treatment, ethanol production, etc. However, it also causes several problems including friction losses in water distribution pipelines, biofouling in the food

industry and persistent infections of medical implant devices (Aggarwal, et al. 2010). The classic view of the biofilm formation process is listed below (Bryers and Characklis 1981; Alavi and Belas 2001; Dunne 2002; Liu and Tay 2002; Gilbert et al. 2013).

i. Physical movement of bacteria to solid surface. The forces involved include, hydrodynamic force, diffusion force, gravity force, thermodynamic forces, (e.g. Brownian movement), and cell mobility by means of flagella, cilia or pseudopods.

ii. Initial attractive forces to move bacteria to contact solid surfaces. Those attractive forces include,

- Physical forces: Van der Waals forces, opposite charge attraction, thermodynamic forces including free energy of surface, surface tension, hydrophobicity, and filamentous bacteria that can link or bridge individual cells together.
- Chemical forces: hydrogen liaison, formation of ionic pairs, formation of ionic triplet, inter-particulate bridge and so on.
- Biochemical forces: cellular surface dehydration and cellular membrane fusion.

iii. Microbial activities that make attached bacteria or aggregated bacteria mature. The activities include, production of extracellular polymer, such as exopolysaccharides (EPS), etc., growth of cellular cluster, metabolic change and genetic competence induced by environment, which facilitate and further strengthen the cell–cell interaction, and result in the high density of adhering cells.

iv. *Steady state three-dimensional structure of microbial aggregate shaped by hydrodynamic shear forces.*

These biofilms can be single bacterial species or complex microbial communities of many species undergoing symbiotic relationships.

Biofilms can also detach, which could be attributed to the increase of the fluid shear, and nutrient and oxygen limitations (Poppele and Hozalski 2003; Aggarwal, et al. 2009). Several researches have measured the biofilm strength utilizing different kinds of equipment at different scales (Table 2.2, Aggarwal et al. 2009). As shown in Table 2.2, the strength of biofilm manifested a range of 2 orders of magnitude variation, showing that biofilms are heterogeneous and anisotropic with respect to their mechanical properties.

Table 2.2. Summary of biofilm strength (Aggarwal et al. 2009)

Bacterial species	Method/technique employed	Parameter measured	Range of strength values	References
Denitrifiers	Centrifugation	Adhesive strength	0–50 Pa	Ohashi and Harada (1994)
Denitrifiers	Centrifugation and plate drop method	Tensile strength; Shear strength	0-8 Pa; 100-800 Pa	Ohashi and Harada (1996)
P. fluorescens	Micromanipulation technique	Adhesive strength	0.05-0.2 J/m^2	Chen et al. (1998)
Denitrifiers and aerobes	Tensile test device	Tensile strength	500-1,000 Pa	Ohashi et al. (1999)
Mixed culture and *P. aeruginosa*	In situ fluid shear variation	Shear modulus; Elastic modulus	27 Pa; 17–240 Pa	Stoodley et al. (1999)
P. aeruginosa	Uniaxial compressive stress	Yield stress; Elastic modulus	900-2,000 Pa; 6,000-50,000 Pa	Korstgens et al. (2001)
Mixed culture	Rotating disk rheometer	Shear modulus	0.2-24 Pa	Towler et al. (2003)
P. aeruginosa	Microcantilever method	Tensile strength	395-15,640 Pa	Poppele and Hozalski (2003)
P. fluorescens	Micromanipulation technique	Adhesive shear strength	0.12–0.65 J/m^2	Chen et al. (2005)
Aerobic and anaerobic biofilms	Couette–Taylor reactor	Cohesive shear strength	2-13 Pa	Coufort et al. (2007)
Mixed species biofilm	Fluid dynamic gauging	Cohesive shear strength	6–7 Pa	Mohle et al. (2007)
Undefined mixed culture	Atomic force microscopy	Cohesive energy	0.1–2.05 nJ/mm^3	Ahimou et al. (2007b)
S. epidermidis; *P. aeruginosa*	Microcantilever method for intact biofilms	Tensile strength	61–5,842 Pa; 59–18,898 Pa	Aggarwal, et al. 2009

2.2 PROCESS CONTROL AND OPTIMIZATION OF MICP

The biogeochemical process needs to be optimized to achieve a practically-feasible time frame and optimal reaction efficiency for real applications. To date, most studies of the biogeochemical process focus on MICP. Thus, this section discusses factors that affect the MICP process and addresses possible optimization methods.

2.2.1 Bacterial Attachment

Most studies focusing on the optimization of MICP process are shown in Table 2.3. The first stage to conduct MICP treatment is to inject bacteria and enhance fixation of bacteria cells in the soil matrix. In most studies, the bacteria is injected and waited for 4 hrs to 4 days. However, Whiffin et al. (2007), Harkes et al. (2010), and Cheng and Cord-Ruwisch (2012) utilized a different procedure by utilizing a fixing solution [0.05M $CaCl_2$ in deionized water in Whiffin et al. (2007) and Harkes et al. (2010), 1 M urea and 1 M $CaCl_2$ in Cheng and Cord-Ruwisch (2012)] to enhance fixation of bacteria cells. As compared with the test flushed with deionized water, test flushed with fixing solution showed almost none of the bacteria were washed out.

2.2.2 Precipitation Efficiency and Uniformity of $CaCO_3$ in the Soil Matrix

Once bacteria are attached to the soil surface, $CaCl_2$ combined with urea can be injected every few hours to days (retention time) or continuously to let $CaCO_3$ precipitate as shown in Table 2.3. During the MICP treatment, the reported flow rates were all smaller than 10 ml/min. Martinez et al. (2013) also reported that the uniformity of $CaCO_3$ can be optimized using stopped-flow injection instead of continuous flow injection. Al Qabany (2012) proposed that if the urea and $CaCl_2$ input rate (input concentration over retention time) was below 0.042 mol/L/h, a high efficiency of $CaCO_3$ precipitation can be achieved as shown in Figure 2.2 and Table 2.3 under the condition of OD_{600} (bacteria concentration) between 0.8 to 1.2 and input concentration

of urea and $CaCl_2$ up to 1M. In Table 2.3, the varying concentrations of calcium and urea (between 0.05M and 1.1M) produced the efficiency of $CaCO_3$ precipitation ranged from 45% to 100%. Al Qabany (2012) also concluded that better uniformity of $CaCO_3$ in the soil matrix at pore-scale could be achieved utilizing a lower chemical concentration of urea and $CaCl_2$. Martinez et al. (2013) experimentally confirmed that the distribution of microbes is the most important factor for achieving uniform $CaCO_3$ precipitation at lab-scale (0.5 meter sand column).

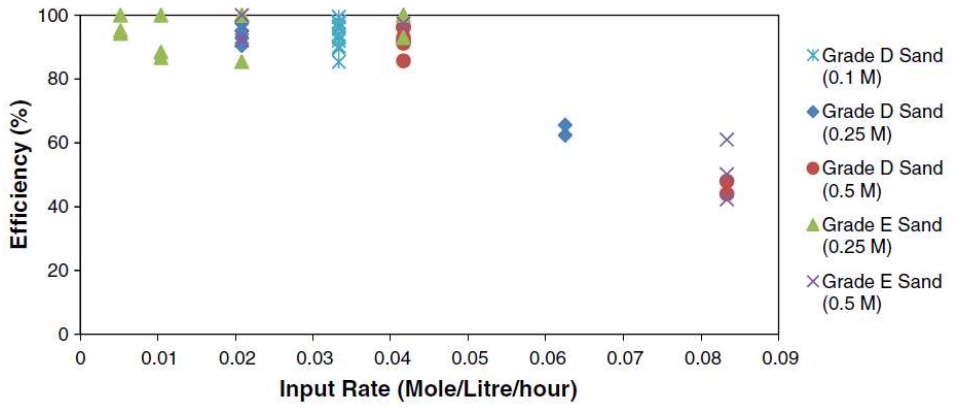

Figure 2.2. Efficiency of $CaCO_3$ precipitation under different input rates (Al Qabany et al. 2012).

Table 2.3. Summary of Treatment Methods of MICP.

Reference	Sand	Flow rate (ml/min)	Treatment Procedure	Calcium (M)	Urea (M)	Input Rate (mol/L/h)	Calcium Efficiency	Reduction in Permeability
Phillips et al., 2012; Cunningham et al., 2011; Ebigbo et al., 2012	40-mesh quartz	10	1. Inoculate G.M. with *S.P.;* 2. Wait 6 hrs. for cell attachment; 3. Inject G.M. for 18 hrs.; 4. Flush calcium free and urea free D. M. (2 pore volume); 5. Flush calcium G.M. (2 pore volume) and wait 4-8 hrs. 6.Between bio-mineralization stages, flush D.M. without calcium to recover bacteria population.	0.33	0.33	0.05	71%	61%
Qabany et al., 2012	Silica Grade D and E sand	Percolation	1. Pack sand in syringe with *S.P.*; 2. Inoculated urea and calcium G. M. from the top of the syringe; 3. Wait for specific retention time; 4. Replaced old liquid with new urea calcium G. M.	0.1, 0.25, 0.5	0.1, 0.25, 0.5	0.002~0.167	45%~100%	NA
DeJong et al., 2006	Ottawa 50-70	4	1. Pump 400ml of *S.P.* with urea and calcium G. M.; 2. Wait 4 hrs. for cell attachment; 3. Flush urea and calcium G. M. every 4 hrs.	0.1	0.33	0.025	92%	NA
Whiffin et al., 2007	Itterbeck	5.8	1. Inject *S.P.* solution; 2. Inject Calcium (0.05M) fixing solution (1 pore volume); 3. Inject reaction urea and calcium G.M.;	1.1	1.1	0.009	88%	53%
Rebata-Landa et al., 2007	Ottawa F110	percolation	1. Mix *S.P.* with sand, urea and calcium G.M. and pack them in syringe; 2. Introduce new urea and calcium G.M. and drain the old solution in syringe; 3. Wait for 4 days and introduce another new solution.	0.25	0.25	0.042	95%	NA
Mortensen et al., 2011b	Ottawa 50-70	10	1. Pump S.P. with G.M. (2 pore volume); 2. Wait for 4-6 hrs. for cell attachment; 3. Flush G.M. with urea and calcium (2 pore volume) every 3 hrs.	0.05	0.33	0.01	80.70%	NA
Burbank et al., 2012	Snake River Sand	4.1~6.6	1. Pump enrichment solution; 2. Wait 4 days for bacteria enrichment; 3. Flush bio-mineralization solution 10 times every day	0.25	0.33	0.01	NA	NA
Cheng and Cord-Ruwisch, 2012	Pure silica sand	percolation	1. Percolate bacteria suspension and fixation solution for multi-layers alternately; 2. Incubation for 12 hrs.; 3. Percolate cementation solution; 4.Incubate for 12 hrs.	1	1	0.08	72%	NA

Note: G.M.: growth medium, D.M.: displacement medium, S.P.: *S. pasteurrii*

2.2.3 Pumping Injection versus Percolation

The discussions of previous two sections mainly focus on media injection using a pump. Another injection technique, surface percolation, was mainly investigated by Cheng and Cord-Ruwisch (2012) and (2013b). All solutions were percolated at the top of the sand columns. The bacterial suspension was applied first and then followed by percolating the cementation solution, which was repeated for 6 or 12 layers of alternating bacterial suspension and cementation solution. The sand column was incubated 24 hours and then percolated with cementation solution (Figure 2.3). Two types of dry sands, fine sand (diameter <0.5 mm) and coarse sand (diameter >0.5 mm), and 1M of urea and $CaCl_2$ were utilized in this study. It was ovserved that $CaCO_3$ bioclogging happened in the fine sand treatment, resulting a limited cementation depth of less than 1 m. However, this clogging was not observed in the MICP treatment of coarse sand showing $CaCO_3$ cementation up to soil depth of 2 m (size of the sand box). The cementation depth was determined by the percolation infiltration rate of the cementation solution and the in-situ urease activity.

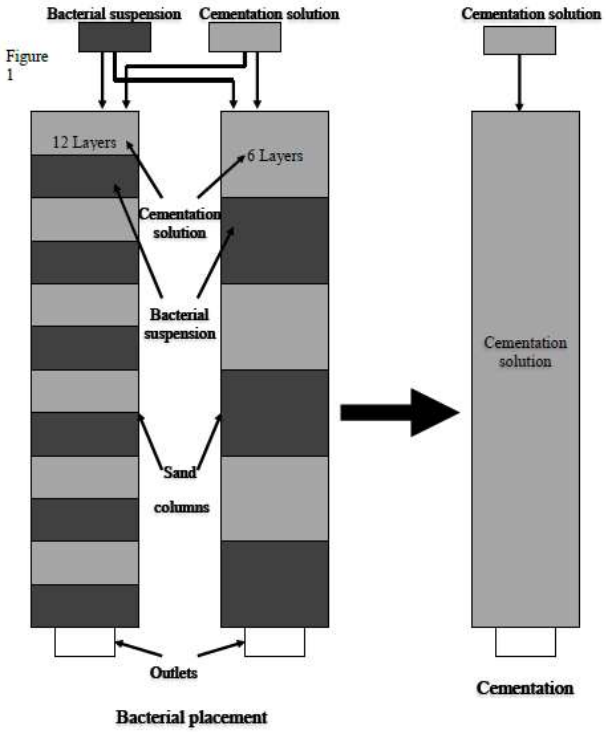

Figure 2.3. Schematic diagram of surface percolation by alternating bacterial suspension and cementation solution for 6 or 12 times (Cheng and Cord-Ruwisch 2013b).

2.2.4 Mineral Type and Particle-Size Distribution

Different types of soil treated with MICP have been investigated by Rebata-Landa (2007) (Figure 2.4). Maximum $CaCO_3$ content was observed at soil grain size of 100 μm. Very coarse and very fine soils did not show a high $CaCO_3$ content as compared with that of 100μm soil grain size. It could be attributed to small permeability in fine soils and limited number of particle contacts in the very coarse soils (Mortensen et al. 2011). It was also concluded that MICP can be realized in the presence of most soil minerals (Rebata-Landa 2007; and Mortensen et al. 2011).

Soon et al. (2014) investigated the viability of MICP to improve behavior of a tropical residual soil. It was concluded that the improvement of the engineering properties of the MICP-treated residual soils is similar to those of fine sands treated by MICP. Using MICP for residual soil was also researched by Lee et al. (2013), which showed that the stiffness and peak strength of residual soil were improved by MICP.

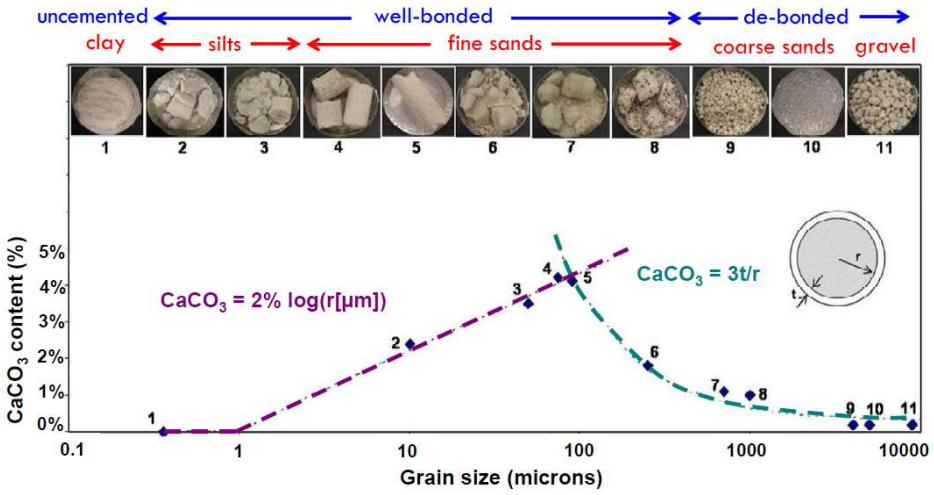

Figure 2.4. $CaCO_3$ content as a function of the soil grain size (Rebata-Landa, 2007).

2.2.5 Bio-Stimulation

The need for bacteria cultivation and injection has restricted the application of MICP from becoming a cost-effective and environmentally favorable alternative to traditional ground improvement methods (Gomez et al. 2014b). Burbank et al. (2011) and (2013) investigated MICP using natural indigenous bacteria. The test results demonstrated that indigenous bacteria can induce $CaCO_3$ precipitation, increasing soil strength and resistance to seismic-induced liquefaction.

2.2.6 Other Factors

Mortensen et al. (2011) experimentally confirmed that ureolytic bacteria are able to function and grow in different types of freshwater conditions including 100% seawater. The high salinity of the sea water enhances the rate of precipitation due to the increased alkalinity and additional cation availability. In addition, the urease activity is not affected by high ammonium concentration and anaerobic condition.

Martinez et al. (2013) conducted a series of half-meter one-dimensional flow sand column experiments to optimize MICP. They reached conclusion that the primary factors controlling bacteria distribution during bacteria injection are initial concentration of microbes and retention period. To control the effluent ammonium concentrations, reducing the urea to calcium ratio has been confirmed as an effective method. However, the ratio of urea to calcium should be kept at greater than 1 to sustain ureolysis and $CaCO_3$ precipitation rate. The most effective recipe for achieving a uniform distribution is the injection with microbe concentration of 7×10^5 cells/mL pulsed at 10 mL/min for 1.5 pore volumes followed by a 6-h retention period.

Chou et al. (2011) investigated the effects of growing, resting, and dead *S. Pasteurii* cells on the mechanical behavior of silica sand using direct shear and California Bearing Ratio (CBR) tests. It was concluded that growing bacteria cells improved the sand properties, whereas dead and resting cells caused negligible increase in strength.

2.3 EFFECTS OF BIOGEOCHEMICAL PROCESSES ON THE PHYSICAL PROPERTIES OF SOIL

Soil behavior under biological treatment has been overlooked in conventional geotechnical engineering (Mitchell and Santamarina, 2005). The main investigation on soil behavior under biological treatment was started approximately ten years ago (Mitchell and Santamarina, 2005; DeJong et al. 2006; Whiffin et al. 2007). This section addresses the variations of physical properties of soil under biogeochemical treatment including mineral precipitation (mainly MICP), biogas generation, and biofilm formation.

2.3.1 Effects of Bio-Mediated Mineral Precipitation on Soil Behavior

Bio-mediated mineral precipitation is a common diagenesis process for soils and rocks (Li et al. 2011). Cementation can increase contact area between particles and bond neighboring particles together (Yun and Santamarina 2005). It can also reduce permeability of the particle matrix (Davis et al. 2006). Previous researches concluded that the effect of cementation on soil behavior depends on: (1) the amount and type of cementing agent, (2) distribution of cementing agent at pore-scale, (3) the grain size distribution of the soil (e.g. higher specific surface, thinner the layer of cement around grains), (4) soil density (e.g. affects inter-particle coordination number), and (5) the degree of confinement at the time of cementation (Clough et al. 1981; Baig et al. 1997; Yun and Santamarina 2005). Since most studies of bio-mediated mineral precipitation

focuses on MICP, the following sections discuss the effect of MICP on the soil behavior under factors shown above.

Particle-Scale Observation

The physical behavior of soil treated by MICP is controlled by the physical properties and distribution of $CaCO_3$ at particle-scale. Several morphologies of $CaCO_3$ were observed in the MICP-treated sand matrix, including spherical vaterite and cubic calcite (Figure 2.5, DeJong et al. 2006; Burbank et al. 2013b; Armstrong and Ajo-Franklin 2011). Different morphologies are controlled mainly by the hydrolysis rate of urea and $CaCO_3$ precipitation rate (van Paassen, 2009; and Cuthbert et al. 2012). However, the effects of different morphologies on the soil behavior were not reported, which were assumed to have similar effects between different morphologies (Rebata-Landa 2007; van Paassen, 2009). Rebata-Landa (2007) summarized the effect of MICP on soil properties at particle-scale (Table 2.4). As $CaCO_3$ content increases, the stiffness, strength, and dilatancy of MICP-treated soil increase while the hydraulic conductivity decreases. In addition, different types of $CaCO_3$ distributions at pore-scale will affect the soil physical behavior differently. For example, Yun and Santamarina (2005) reported that cementing materials developed at particle contacts has maximum influence on granular mechanical response.

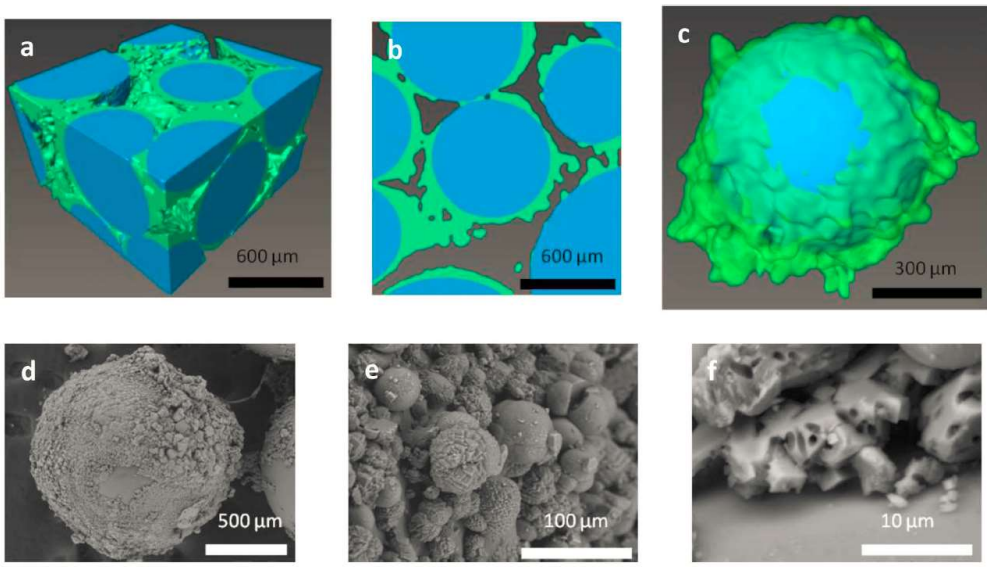

Figure 2.5. $CaCO_3$ morphologies and distribution around the glass bead, (a)-(c) x-ray computed microtomography images (blue=glass bead, green=$CaCO_3$), (d-f) SEM images (Armstrong and Ajo-Franklin, 2011).

Table 2.4. Effect of MICP on soil properties at particle-scale (Rebata-Landa 2007).

Mechanical Effects				
STIFFNESS	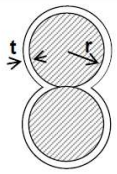 $\frac{E_{tan}}{G_g} = \frac{1}{(1-\nu_g)}\sqrt{(CC+1)^{2/3} - 1 + \left[\frac{3\cdot(1-\nu_g)}{2}\left(\frac{\sigma}{G_g}\right)\right]^{2/3}}$ *[Fernández & Santamarina, 2001]*			
STRENGTH				
	Surface roughness	**Contact tensile strength**	**Pore filling and rotational frustration**	**Dilation**
	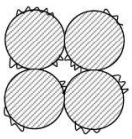	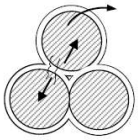	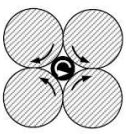	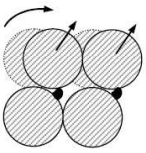
HYDRAULIC CONDUCTIVITY	**Uncemented**	**Reduced pore-throat**		
	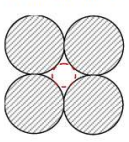	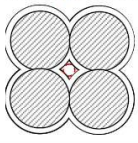	$\frac{k_{final}}{k_{initial}} = \frac{(d_{pore} - 2\cdot t)^2}{d_{pore}^{\ 2}} = \left(1 - \frac{2\cdot t}{d_{pore}}\right)^2$	

Shear Strength

Unconfined compression test has been used to investigate the soil shear strength treated by MICP. Al Qabany and Soga (2013) experimentally demonstrated that the unconfined compressive strength increases with the increase of $CaCO_3$ content, which is consistent with the results from literature as shown in Figure 2.6 (Ismail et al. 2002; Ivanov et al. 2010; and Al Qabany and Soga 2013). Similar results were also obtained and confirmed by Whiffin et al. (2007), van Paassen (2012), Cheng et al. (2013a), and Lee et al. (2013). Whiffin et al. (2007) also reported a threshold $CaCO_3$ content of approximately 3.6% before the unconfined compressive strength of MICP-treated sand started to increase. However, Soon et al. (2014) concluded a different threshold of $CaCO_3$ content of 1% after which the strength of MICP-treated sand and residual soil started increasing using unconfined compression and triaxial tests.

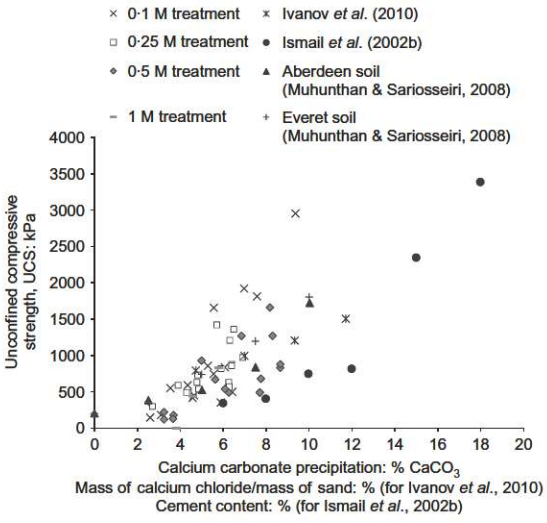

Figure 2.6. Unconfined compressive strength versus $CaCO_3$ content using MICP, cement mixing, and iron-based bio-grouting (Ismail et al. 2002; Ivanov et al. 2010; Al Qabany and Soga 2013).

The triaxial tests were used to investigate the mechanical behavior of sand under MICP treatment by varying the confining pressures, drainage conditions, and different levels of $CaCO_3$ cementation (Montoya and DeJong 2015; and Feng and Montoya 2015). In the triaxial tests, the peak shear strength increased with the increase of cementation level, which accompanied with a transition from strain hardening to strain softening and a corresponding transition from bulging failure to localized shear-band failure. MICP cementation also increased the dilatancy of the loose sand. At critical state, the shear strength was not significantly affected by the cementation levels and was similar to that of sand without treatment.

Feng and Montoya (2015) reported that by changing the confining pressures, larger peak and residual friction angles compared to untreated sand were obtained. The value of peak and residual friction angles increased with the increase of cement content and decrease of confining pressure (Figure 2.7). The effect of MICP on the increase of cohesion is limited. van Paassen (2009) concluded that as dry densities increases due to the increase of $CaCO_3$ content, both cohesion and friction angle increase as shown in Table 2.5. However, Cheng et al. (2013a) reported that peak friction angle is constant until 6% $CaCO_3$ content and then starts to increase. However, cohesion starts to increase initially with the increase of $CaCO_3$ content (Figure 2.8).

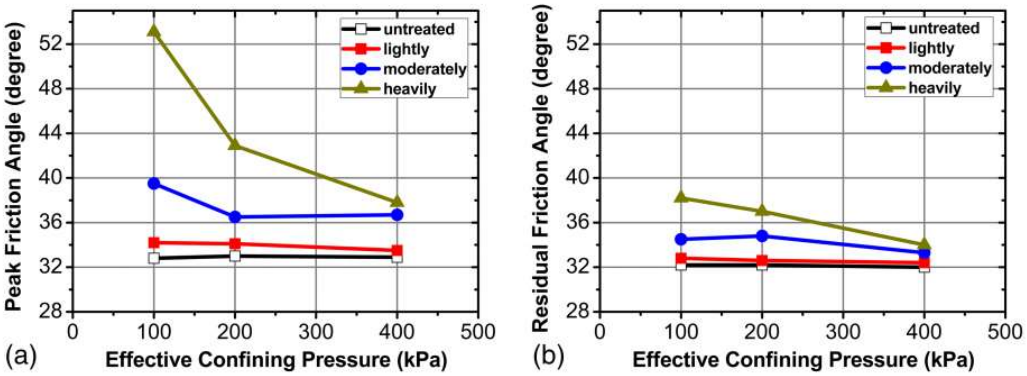

Figure 2.7. Friction angle as a function of effective confining pressure for (a) peak, and (b) residual friction angles.

Table 2.5. Summary of parameters on the Mohr-Coulomb failure criteria of MICP cemented sand at low confining stresses (<500 kPa) for different dry densities (modified after van Paassen 2009).

Dry density (kg/m^3)	1700	1800	1900
Cohesion,c (MPa)	0.27	0.39	0.54
Friction angle, ø (˚)	40	50	58

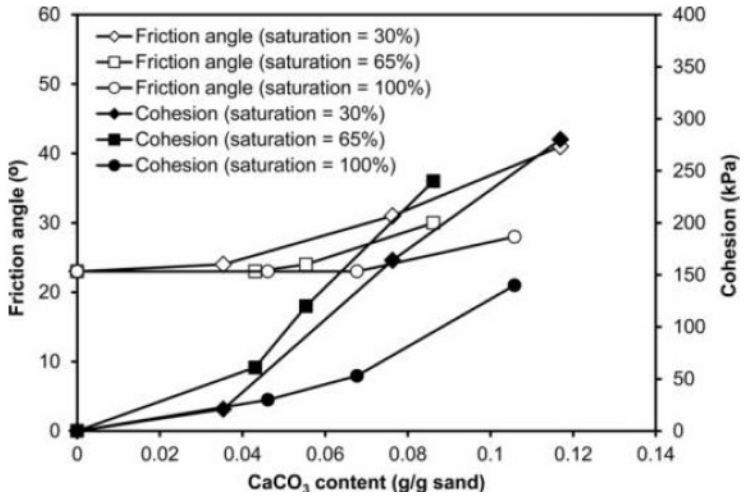

Figure 2.8. Friction angle versus $CaCO_3$ content at different degree of saturation levels.

Stiffness

Shear wave (S-wave) velocity has been used for process monitoring of MICP and measurement of soil stiffness (Lee and Santamarina 2005; Yun and Santamarina 2005; Weil et al. 2012; and Montoya and Dejong 2015). During the MICP treatment, S-wave velocity increased with time since $CaCO_3$ precipitated at soil particle contacts, bonding particles together (DeJong et al. 2006; and Montoya and DeJong 2015). The measured S-wave velocities versus $CaCO_3$ contents at the end of MICP treatment reported by several researchers are summarized in Figure 2.9. S-wave velocities increased with the increase of the $CaCO_3$ contents. Estimation of the S-wave velocity versus $CaCO_3$ content using linear fitting equation has been proposed by several authors (Al Qabany et al. 2011; Weil et al. 2012; and Martinez et al. 2013). However, as shown in Figure 2.9, the best-fit linear equation is difficult to simulate the wide variation of S-wave velocities versus $CaCO_3$ content. This wide variation of the S-wave velocities could be attributed to the varying porosities, coordination numbers, applied confining pressures, urea and $CaCl_3$ concentrations, and $CaCO_3$ spatial distributions in the sand matrix, which were discussed by Weil et al. (2011). In addition, S-wave velocity was also used to measure the degradation of soil stiffness during triaxial loading (Montoya and DeJong 2015). S-wave velocity measurement has been considered as valuable technique for process monitoring as MICP is upscaled towards field implementation (DeJong et al. 2006; Al Qabany et al. 2011; Weil et al. 2012; and Montoya and DeJong 2015).

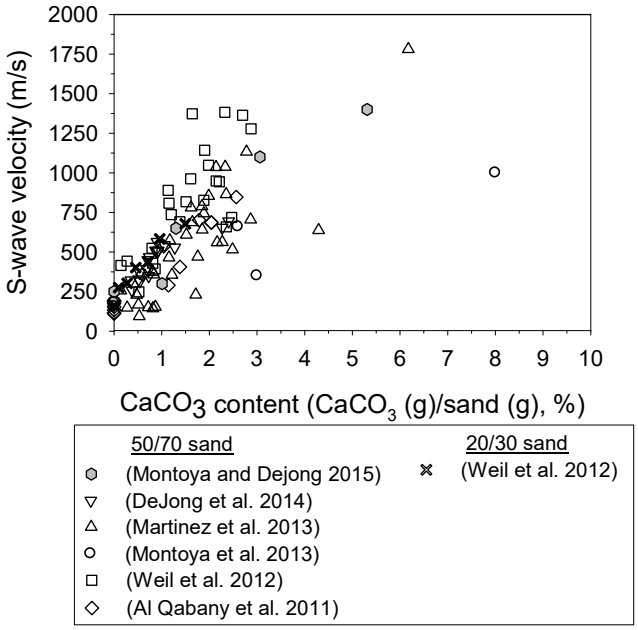

Figure 2.9. Measured S-wave velocities versus $CaCO_3$ contents from literature.

Stiffness was also characterized from stress-strain curves using triaxial and unconfined compression tests. The summarized elastic modulus versus $CaCO_3$ content at the end of the MICP treatment is shown in Figure 2.10. Most of the studies calculated the initial tangent modulus (E_i) except the presented E_{50} (secant modulus) reported by van Paassen et al. (2010). The modulus measured from triaxial tests showed that the elastic modulus increased in the range of $CaCO_3$ content between 2% and 3.5% and was then stabilized as $CaCO_3$ content continues increasing. The elastic modulus measured from unconfined compression tests increased continuously with the increase of $CaCO_3$ content. The modulus obtained from triaxial tests were higher than that of unconfined compression tests at the same $CaCO_3$ content due to the applied confining pressure of triaxial tests. Cheng et al. (2013) investigated mechanical behavior of

MICP-treated under different saturation levels. At the same $CaCO_3$ content, the modulus increases as the degree of saturation level decreases (Figure 2.10). This higher modulus at low degree of saturation level is attributed to the $CaCO_3$ cementation position preferably at particle contacts as the degree of saturation level is low, forming water-bridge between particles.

The variation of the modulus versus confinement of triaxial tests was also investigated by Feng and Montoya (2015). Both studies observed similar conclusions which the slope of the modulus decreases with increasing MICP cementation. The confining pressure has less influence on the variation of modulus as the cementation level increases (Figure 2.11).

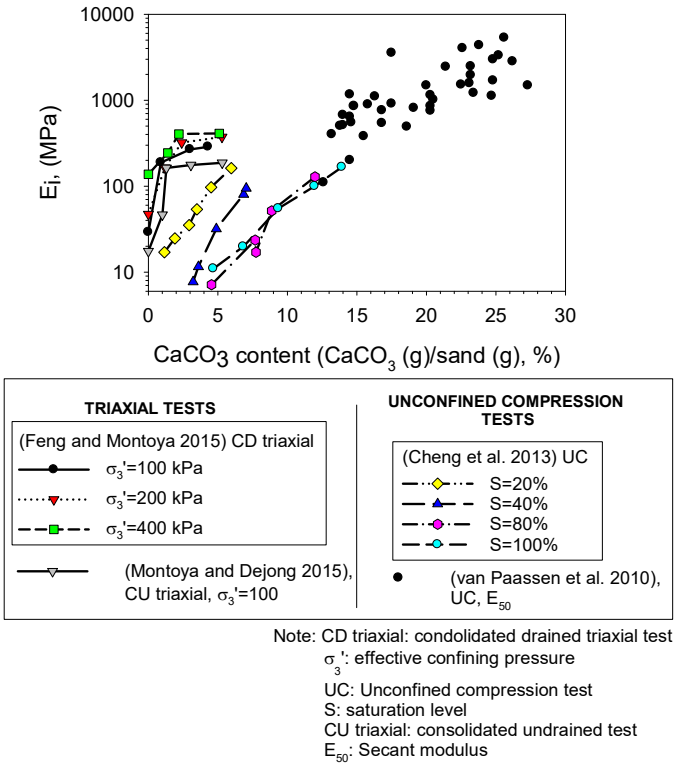

Figure 2.10. Summary of elastic modulus versus $CaCO_3$ content.

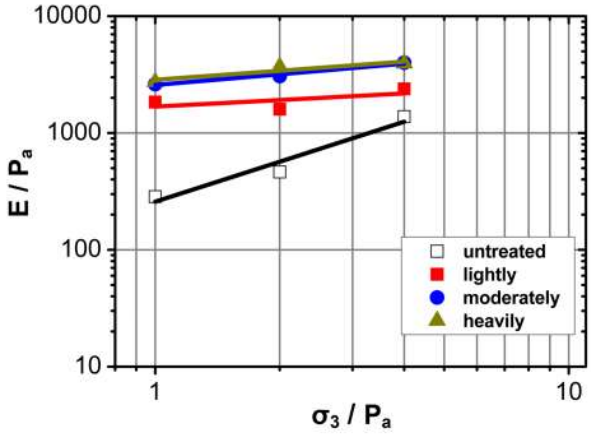

Figure 2.11. Modulus versus effective confining pressure under different level of cementations (Feng and Montoya 2015).

Settlement Characteristics

Unconfined compression tests on MICP-treated soil were conducted by Lee et al. (2013) and Feng and Montoya (2014). The MICP-treated specimens are less compressible compared to the untreated specimens and the specimens with higher $CaCO_3$ content are less compressible than the specimens of the same grain size with lower $CaCO_3$ content. Compression index decreases with the increase of the $CaCO_3$ content before the fracture of $CaCO_3$ bonds.

Permeability

The summary of normalized permeability from literature (permeability normalized by the initial permeability) versus $CaCO_3$ content is shown in Figure 2.12. During MICP treatment, the precipitated $CaCO_3$ which deposited around particles and occupied pore space reduces the permeability of the soil matrix. The highest reduction of the permeability was obtained in Yasuhara et al. (2011) and Al Qabany and Soga

(2013), showing a maximum reduction of approximate 99%. The permeability of fine and coarse sands of Cheng et al. (2013) showed a slower reduction with the maximum reduction of 80%. The reduction of permeability of Martinez et al. (2013) and Whiffin et al. (2007) was between those reported by Al Qabany and Soga (2013) and Cheng et al. (2013). This wide variation of permeability reduction versus $CaCO_3$ content could be attributed to the differences of sand types, relative densities, concentrations of urea and $CaCl_2$, and test conditions (Al Qabany and Soga 2013).

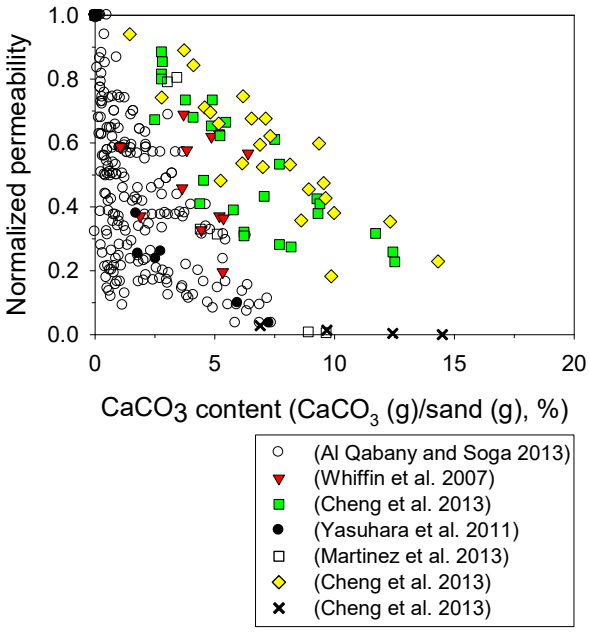

Figure 2.12. Summary of normalized permeability versus $CaCO_3$ content from literature.

Liquefaction Resistance

MICP was used to mitigate liquefiable soil. Montoya et al. (2013) investigated the effect of MICP on soil resistance to liquefaction using centrifuge testing and cyclic direct simple shear. The results showed that the MICP-treated soil manifested lower

excess pore pressure genration, reduced settlement, but greater peak surface accelerations as compared with the untreated loose saturated sand. When conducted the cyclic direct simple shear test with maximum cycles of 3000, the Cyclic Stress Ratio (CSR) of MICP-treated sand increased by 0.3 as compared with the sand without treatment.

2.3.2 Effect of Gas Generation on Soil Behavior

Most studies of using bio-mediated gas generation focused on denitrification, which N_2 and CO_2 is the end-product. The presence of generated gas in saturated soil showed a decrease of P-wave velocity from 1600 to 700 m/s (Figure 2.13a), which was attributed to the reduction of the saturation level and bulk stiffness of the soil matrix (Rebata-Landa and Santamarina 2012). The presence of generated gas and reduction of the saturation level reduced the generation potential of excess pore water pressure, increased the undrained shear strength, and liquefaction resistance as shown in Figure 2.13b (Rebata-Landa and Santamarina 2012; He et al. 2013; and He and Chu 2014). It is important to note that even a small reduction of saturation level can significantly reduce the susceptibility of soil to liquefaction.

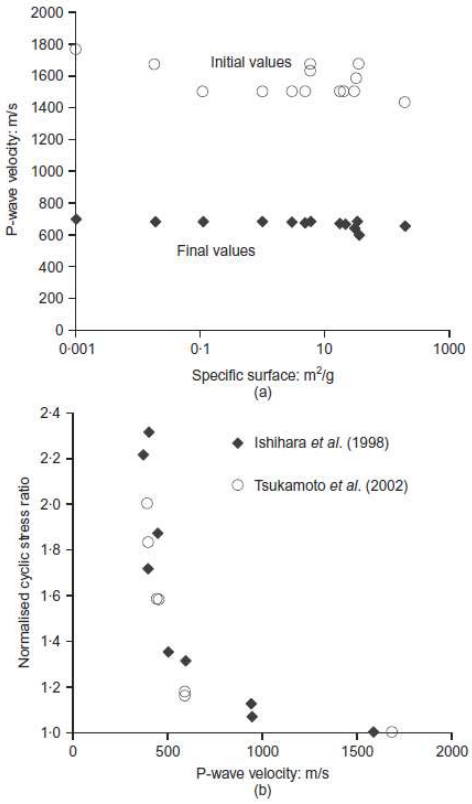

Figure 2.13. (a) P-wave velocity monitoring during biogas by denitrification, (b) P-wave velocity versus normalized cyclic stress ratio (Rebata-Landa and Santamarina, 2012).

2.3.3 Effect of Biofilm Formation on Soil Behavior

When biofilms form in porous media, they can form thick layers that can reduce the porosity and permeability of soil (e.g., Bryers and Characklis 1981; Taylor and Jaffe 1990; and Gilbert et al. 2013). Biofilm accumulation in soil will result in a reduction of permeability by decreasing the pore volume and modifying the shape of the pore space (Taylor and Jaffe 1990; Stewart and Fogler 2000; and Rockhold et al. 2002), which is usually referred to as bioclogging. For example, hydraulic conductivity of compacted silty sand was reduced by 2 to 3 orders of magnitude by adding exopolysacharide

(EPS)-producing bacteria, *Beijerinckia indica*, which can be used as a low cost soil stabilization additive for containment barriers and landfills (Dennis and Turner, 1998). Stewart and Fogler (2001) investigated the biofilm plugging process in porous media and concluded three phases of biofilm development scheme including the exopolymer-induction phase, the plugging phase, and the plug-propagation phase (Figure 2.14).

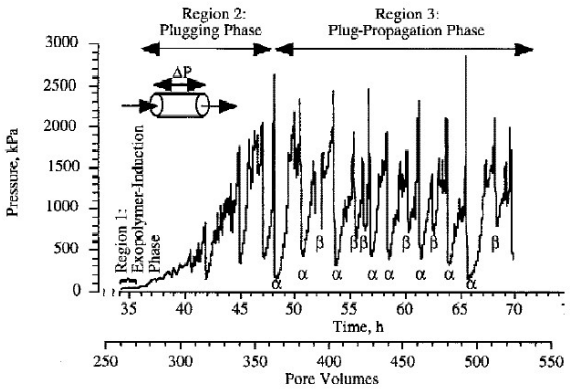

Figure 2.14. Measured injection pressure versus time during constant-rate injection of nutrients (Stewart and Fogler 2001).

Biofilm accumulation in porous media depends on microbial adsorption and metabolic activities on surfaces, which involve many short-range forces such as dipole-dipole interactions, dipole-induced dipole interactions, ion-dipole interactions, hydrogen bonding, hydrophobic interactions, or polymeric bridging, etc. (Robb 1984; O'Toole et al. 2000; Donlan 2002; and Palmer 2007). These forces may provide additional cohesion for shear resistance of the sand matrix. On the other hand, the lubricating properties of the biofilm resulting from its viscous property may lead to a decrease of the inter-particle friction leading to a reduction of soil shear resistance (Perkins et al. 2000). These short-range bonding forces along with the viscous nature

of the biofilm will affect the mechanical behavior of soil interactively. The research on mechanical behavior of biofilm-cemented soils is very limited and shows contradictory conclusions. For example, Perkins et al. (2000) showed that *Klebsiella oxytoca*-produced biofilm had negligible influence on the strength and stiffness of the sand but increased time-dependent creep deformation using triaxial and oedometer tests. Daniels et al. (2009) concluded that *Beijerinckia indica*-produced biofilm had a decreasing effect on the soil strength of clay and clayey sand but showed increases in the consolidation coefficient using unconfined compression and consolidation tests. Banagan (2010) reported that the shear strength of Ottawa 30 sand estimated using vane shear test was increased by 15.2~87.5% by adding biofilm-forming bacteria *Flavobacterium johnsoniae*.

2.4 APPLICATIONS OF BIOGEOCHEMICAL PROCESSES

The most applicable biogeochemical process is MICP. The potential applications of MICP that has been investigated in the scale model tests include ground improvement and foundation strengthening (Whiffin et al. 2007; Martinez and DeJong 2009; and van Paassen 2009), reducing wind- and water-induced erosion (Bang et al. 2011; and Gomez 2014a), mitigating liquefaction (Montoya et al. 2013), creating impermeable crusts for catchment facilities (Stabnikov et al. 2011; and Chu et al. 2012), healing/stabilizing cracks in concrete (Ramachandran et al. 2001; and Bang et al. 2010), immobilizing heavy metals (Fujita et al. 2004, 2008, 2010), and performing shallow

carbon sequestration (Manning, 2008; Renforth et al. 2009, and 2011), enhancing oil recovery (Ferris et al. 1996; and Yakimov et al. 1997). All these applications cover a wide range of areas, which manifests that MICP is a promising technique and has a sustainable potential.

Several studies on applications using biofilm formation were also reported. Stal (2010) concluded that biofilm plays an important role in stabilizing sediments, and resisting erosion at the surface in riverine and marine environments. Furthermore, several studies have used biofilm to form bioclogging for applications including decreasing hydraulic conductivity in situ beneath and within dams and levees, reducing infiltration from ponds, reducing leakage at landfills, and to control groundwater migration with subsurface barriers (Seki et al. 1998; James et al. 2000; and Lambert et al. 2010).

Bio-mediated gas generation received limited attention for geotechnical application. To date, only one study investigated the application of biogas for mitigation of liquefaction (He et al. 2013). The shaking table tests demonstrated that the biogas is effective in lowering the saturation level and reducing the liquefaction potential of the saturated sand deposit.

In summary, DeJong et al. (2013) summarized application potentials of biogeochemical processes and their approximate ranking considering implementation feasibility, probability of success, cost/viability, and social acceptance in

Table **2.6** shown below.

Table 2.6. Evaluation of application potentials of biogeochemical processes, considering implementation feasibility, probability of success, cost/viability, and social acceptance (DeJong et al. 2013).

Application	Implementation: Easy: 5; Difficult: 1	Probability of success: High: 5; Low: 1	Cost/viability: Economic: 5; Expensive: 1	Societal acceptance: High: 5; Low: 1	Total score out of 20
Structural repair	5	5	3	5	18
Erosion control	4	5	4	5	18
Co-precipitation/immobilisation of contaminants	5	4	4	5	18
Dust mitigation	4	5	4	5	18
Ground improvement for rural roads	5	5	3	4	17
Shallow carbon sequestration	5	3	4	5	17
Leak management	4	3	4	5	16
Rehabilitation of ancient monuments	3	3	5	5	16
Ground improvement for urban road subgrading	5	3	3	4	15
Soil liquefaction mitigation (MICP)	3	5	3	3	14
Ground improvement for ash ponds	1	4	4	5	14
Recycling/reuse of dredging materials	3	2	3	5	13
Soil liquefaction mitigation (biogas)	3	3	3	3	12
Enhanced water/oil/gas recovery	1	3	3	5	12
De-desertification	1	5	1	5	12
Sediment weakening by fluidisation	3	2	3	3	11
Underground creation (pipeline)	3	4	1	3	11
Stabilisation of sinkholes	1	3	2	5	11
Landfills as new energy resource	3	4	1	2	10
Construction products (bricks) using soil-biocementation	2	4	1	3	10
Water storage	3	3	2	2	9
De-swelling of clays	1	1	1	4	7
Deep carbon sequestration	1	1	1	3	6
Underground creation (tunnel)	1	1	2	1	5

3. PARTICLE-SCALE ANALYSIS OF SANDS TREATED BY MICROBIAL INDUCED CARBONATE PRECIPITATION (MICP): $CaCO_3$ DISTRIBUTION AT PORE SPACE AND BOND STRENGTH

3.1 INTRODUCTION

Microbial Induced Carbonate Precipitation (MICP) has been receiving attention for several applications including soil improvement techniques, mineral plugging for enhanced oil recovery, immobilizing contaminants in surface and ground water, and strengthening concrete (Ferris, et al. 1996; Ramakrishnan et al. 2001; Mitchell and Ferris 2005; Whiffin et al. 2007; DeJong et al. 2010a; and Lin et al. 2016a). The investigation on the engineering properties of MICP-treated soil has been focusing on benchtop-scale tests (e.g. consolidation, triaxial, direct shear or unconfined tests with or without shear wave measurement) to assess the feasibility for those applications (e.g. DeJong et al., 2006; van Paassen et al. 2010; Chou et al. 2011; Al Qabany and Soga 2013; Cheng et al. 2013; Montoya and DeJong 2015; and Lin et al. 2016a). However, the engineering properties of MICP-treated soils are controlled by the physical properties of the $CaCO_3$ cementation at the particle-scale (e.g. $CaCO_3$ distribution in pore space and its bond strength); which are not well-understood and not well-documented in the literature (Lin et al. 2014 and 2016a).

The $CaCO_3$ distribution at the pore space may also affect the permeability of MICP-treated sand, which is also not well understood (Whiffin et al. 2007; Al Qabany and Soga 2013; and Cheng et al. 2013). In fact, Evans et al. (2014) and Al Qabany et al. (2012) suggest that there is a lack of fundamental understanding and very limited data of $CaCO_3$ bond strength characteristics and $CaCO_3$ distribution at the pore-scale; a knowledge gap is partially addressed in this paper.

The objective of the research presented in this paper is to investigate the spatial distributions of $CaCO_3$ at the pore-scale and $CaCO_3$ bond strength, and their effects on shear and compression wave (S-and P-wave) velocities, Poisson's ratio, permeability, and shear strength of the sand matrix. To achieve this objective, measurement-based S- and P-wave velocities and Poisson's ratio at variable $CaCO_3$ contents were compared with calculated S-and P-wave velocities and Poisson's ratio using cemented-sand and uncemented-sand models that consider the spatial distribution of $CaCO_3$ at the pore-scale. In addition, measured permeability coefficients reported in the literature were compared with the calculated permeability using Kozeny-Carman and Panda-Lake models (Panda and Lake 1994, 1995) to investigate the effects of $CaCO_3$ distribution at the pore-scale. Furthermore, the $CaCO_3$ bond strength was measured, utilizing a setup that includes glass beads representing soil particles, optical fiber sensors for characterizing bond force, bearing stages, and displacement actuators. Finally, the equation of shear strength of MICP-treated sand matrix with idealized $CaCO_3$

distributions was also derived using the measured tensile and shear strength of the $CaCO_3$ bond.

3.2 BACKGROUND

3.2.1 $CaCO_3$ Nucleation and Bond Physical Characteristics

The bacterium, *Sporosarcina pasteurii*, which is commonly utilized for urea hydrolysis in the MICP process, modify the local geochemical conditions (e.g. increasing the pH and carbonate saturation level) and serve as nucleation sites for $CaCO_3$ precipitation (Stocks-Fischer et al. 1999). During the MICP process, the precipitation of $CaCO_3$ in the pore space starts by nucleation around bacteria cells (Mitchell and Ferris 2005), followed by growth into different crystal morphologies including spherical vaterite and cubic calcite; the type of which is controlled mainly by the hydrolysis rate of urea and $CaCO_3$ precipitation rate (van Paassen, 2009; Cuthbert et al. 2012; Lin et al. 2016a). These two $CaCO_3$ morphologies are shown in the Scanning Electron Microscope (SEM) images for three tested sands (Figure 3.1). It is also observed that the vaterite and calcite crystals grew in clusters containing large amount of micro pores (Figure 3.1, Armstrong and Ajo-Franklin, 2011). And these clusters were not uniform nor symmetric between sand grains. The measured sizes of vaterite and calcite crystals in the SEM images range from 2 to 50 um and from 2 to 40 um, respectively, which is consistent with the results reported in the literature (e.g. van Paassen 2009; Al Qabany 2013). Based on the measurements of crystal sizes utilizing

SEM images from this study and literature (van Paassen 2009; Al Qabany 2013), the average crystal size was calculated as 10 um.

Three different distributions of $CaCO_3$ precipitation were observed from SEM images (Lin et al. 2016a). A schematic of these three distributions is shown in Figure 1d. The effects of these distributions on the mechanical properties and permeability of MICP cemented sand have not been reported in the literature, which will be fully explored in this paper. The pore-scale $CaCO_3$ bond strength between sand grains controls the mechanical behavior of the MICP-treated sand. However, only the compressive strength of $CaCO_3$ was reported in the literature (Ribeiro 2012). Therefore, the tensile and shear strength of the $CaCO_3$ bond was measured and analyzed in this study.

3.2.2 Effects of Pore-Scale $CaCO_3$ Spatial Distributions on Physical Properties of MICP-Treated Sand

Shear Strength and Elastic Modulus

Pore-scale spatial distributions of $CaCO_3$ are affected by the soil mineral type (Rebata-Landa 2007), water saturation level (Cheng et al. 2013) and chemical concentrations (Al Qabany et al. 2012). As shown in Figure 3.1, at micro-scale, $CaCO_3$ can deposit at the particle contact (contact-cementing), coat soil particle (grain-coating), or grow from sand surface into pore space and create cementing-bridge in the sand matrix (matrix-supporting), which were all observed in the SEM images (Figure 3.1).

Different types of $CaCO_3$ distributions may affect sand strength and modulus differently. For example, matrix-supporting distribution (Figure 3.1) may not improve the soil modulus and shear strength until the $CaCO_3$ bridge is formed between soil particles. While, in contact-cementing, all $CaCO_3$ deposits at the particle contacts, which highly increases the modulus and shear strength of the sand matrix (Mavko et al. 1998). However, for grain-coating distribution, only small amount of $CaCO_3$ cement particle contacts, which increases the shear strength and modulus of the MICP-treated sand matrix, but not as abrupt as that of contact-cementing. Similar observations were confirmed by Kleinberg and Dai (2005) who investigated the effects of pore-scale hydrate distributions on S-and P-wave velocities of hydrate bearing sediments.

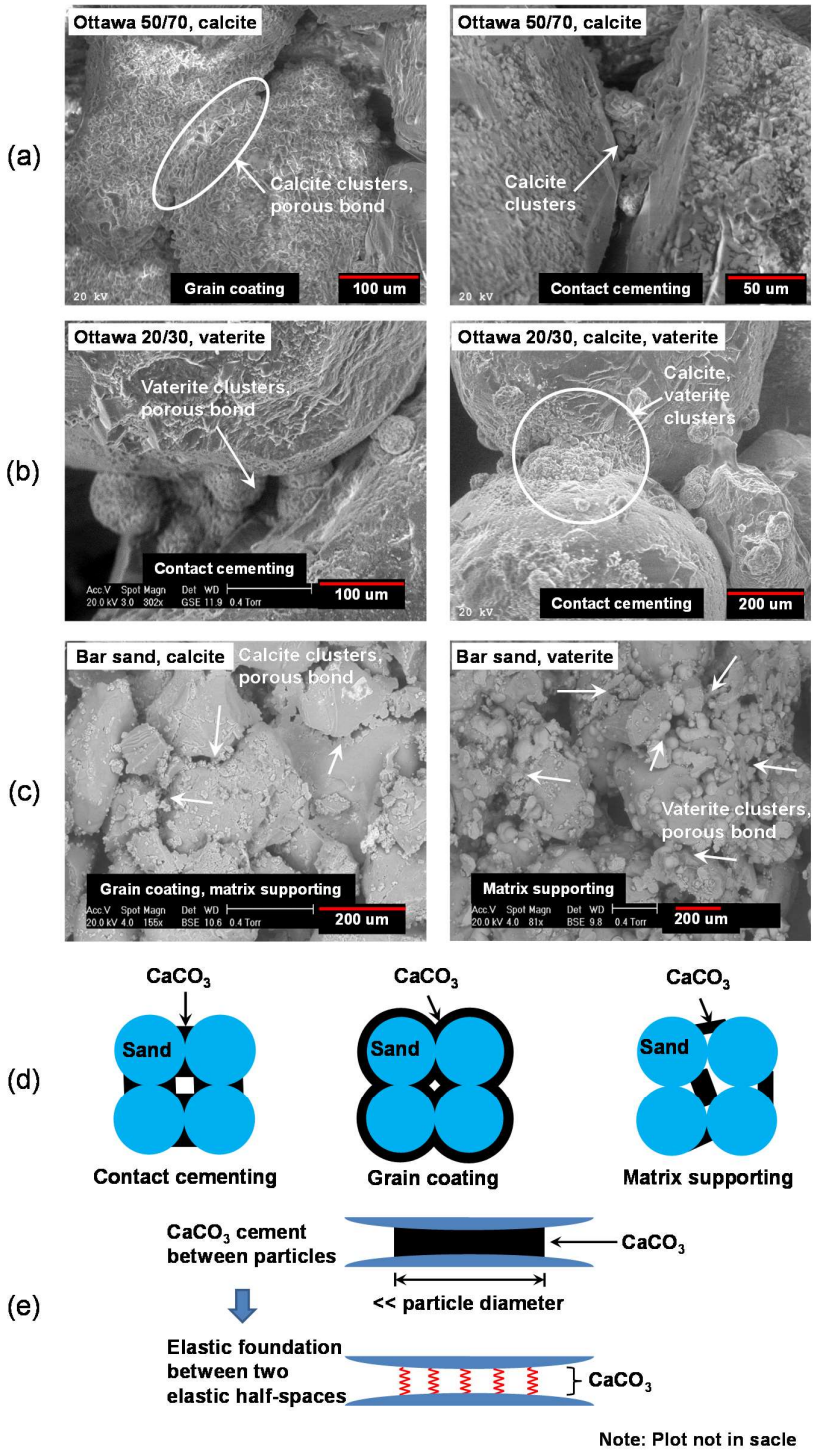

Figure 3.1. SEM images of (a) Ottawa 50/70 sand, (b) Ottawa 20/30 sand, (c) Bar sand; (d) ideal spatial distributions of $CaCO_3$ crystals between particles; (e) approximation of $CaCO_3$ cementation between particles based on cementation theory.

The dependence of the elastic moduli, and hence wave velocities of the MICP-treated sand matrix on different $CaCO_3$ spatial distributions may already caused ambiguity when trying to linearly fit the $CaCO_3$ content versus measured wave velocities (Al Qabany et al. 2011; Weil et al. 2012; Martinez et al. 2013). In addition, analyzing $CaCO_3$ spatial distributions with SEM which showed limited particles in the image may not characterize the distribution of $CaCO_3$ in the whole sand sample (DeJong et al. 2006). To investigate the effects of pore-scale $CaCO_3$ spatial distributions on the mechanical behavior of MICP-treated sand, two models introduced by Mavko et al. (1998) are utilized in this paper. The details of this model will be discussed in the next section. The S-and P-wave velocities and Poisson's ratio as a function of $CaCO_3$ contents are calculated based on these models considering three idealized $CaCO_3$ spatial distributions (e.g. contact cementing, grain coating, and matrix supporting). These calculations were then compared with the measured S-and P-wave velocities and Poisson's ratio.

Permeability

Different pore-scale $CaCO_3$ distributions (e.g. contact cementing, grain coating, matrix supporting) alter the size and the tortuosity of the pore throat between soil particles, affecting the soil permeability (Armstrong and Ajo-Franklin, 2011). For example, contact-cementing, in which $CaCO_3$ deposits only at the particle contacts, may only have minimal effects on the size and the tortuosity of the pore throat and the permeability, especially at low $CaCO_3$ contents. However, grain-coating distribution

may show higher permeability reduction than the contact-cementing as the $CaCO_3$ deposits around the particles and reduce the pore throat size. For matrix-supporting distribution, in which the $CaCO_3$ grows into the pore space, alters the pore size and the tortuosity significantly reducing the permeability. Because contact-cementing and grain-coating may not significantly alter the pore size and tortuosity at low $CaCO_3$ content compared with the matrix-supporting, the Kozeny-Carman model was used to approximately represent these two types of distributions (Carman 1937; Panda and Lake 1994; and Carrier 2003). For matrix-supporting distribution, which significantly alter the pore throat and tortuosity, the Panda-Lake model was utilized to characterize this distribution (Panda and Lake 1995). The details of these two models will be discussed in the next section. It is worth noting that the Panda-Lake model has been used to analyze the effect of pore-scale clay distributions on the change of permeability of sandstone (Panda and Lake 1995).

It is also worth noting that whether permeability is reduced significantly during MICP treatment was questioned by Whiffin et al. 2007; Al Qabany and Soga 2013; and Cheng et al. 2013. To address this controversial conclusions of the literature and the effect of $CaCO_3$ spatial distributions on permeability, the measured permeability reported from the literature were compared with the Kozeny-Carman model by considering the change of the porosity only during MICP treatment (approximately representing contact cementing and grain coating) and Panda-Lake model by

considering the $CaCO_3$ precipitation into pore space (approximately representing matrix supporting).

3.3 MODELLING THE EFFECTS OF $CaCO_3$ SPATIAL DISTRIBUTIONS OF $CaCO_3$ ON PHYSICAL PROPERTIES OF MICP-TREATED SAND

3.3.1 Estimation of S-and P-Wave Velocities for Contact Cementing and Grain Coating

The analytical model named cemented-sand model by Mavko et al. (1998) was utilized to estimate the S-and P-wave velocities based on the cementation theory (Dvorkin and Nur 1996; Mavko et al. 1998). This model has been successfully used to estimate the S-and P-wave velocities of high-porosity sandstone and to determine the distribution of cementation at pore scale (e.g. contact-cementing or grain-coating, Dvorkin and Nur 1996). In this paper, cemented-sand model is being used to investigate the effect of the pore-scale $CaCO_3$ distributions on the S-and P-wave velocities and Poisson's ratio of MICP-treated sand matrix. Furthermore, the predicted S-and P-wave velocities and Poisson's ratio are compared with the measured S-and P-wave velocities and Poisson's ratio from literature to determine the main distribution of $CaCO_3$ cementation at pore-scale.

The cemented-sand model incorporates two types of cement distributions, contact-cementing and grain-coating (Figure 3.1), both of which improve inter-particle contacts. For

contact-cementing, all $CaCO_3$ deposits only at inter-particle contacts. However, for grain-coating, only small amount of $CaCO_3$ deposits at inter-particle contacts (Figure 3.1). The cementation theory describes the effective elastic properties (e.g. deformation and modulus) of elastic spheres (representing soil particles) with elastic cementing material (representing $CaCO_3$ cement in our case) at their contacts. Based on the cementation theory, the modulus of the mixture of cement ($CaCO_3$) and spheres (soil particles) can be calculated by considering the cement-soil particle interaction as an elastic foundation (representing $CaCO_3$ cementing material) cemented to an elastic half-space (representing an elastic sphere (soil particle) assuming the cement-soil particle contact region is much smaller than the soil particle diameter, Figure 1e, Dvorkin et al. 1991, and 1994). The assumptions of the cemented-sand model include: (1) the generated strains in the sand matrix are small; (2) the sand matrix consists identical, homogeneous, isotropic, and elastic spheres; (3) the packing of the sand matrix is random and statistically isotropic; (4) the stiffness of the cemented system does not depend on the confining pressure; (5) the calculated moduli are valid for S-and P-wavelengths that are much longer (more than 10 times) than the particle radius (Mavko et al. 1998).

Based on the cemented-sand model, the effective bulk and shear moduli (K_{eff} and G_{eff}) of the cemented-sand matrix of the contact cementing and grain coating $CaCO_3$ spatial distributions can be calculated using the original porosity of soil without cementation (ϕ_0), coordination number (C), constrained and shear moduli of the cementing material (M_c, and G_c), and normal and tangential stiffness of the cemented particles (S_n and S_τ) as shown in Equation 3-1 and Equation 3-2 (Digby 1982; Dvorkin et al. 1994; and Dvorkin and Nur 1996).

$$K_{eff} = \frac{1}{6} C(1 - \phi_0) M_c S_n \quad \text{Equation 3-1}$$

$$G_{eff} = \frac{3}{5} K_{eff} + \frac{3}{20} C(1 - \phi_0) G_c S_\tau \quad \text{Equation 3-2}$$

Dvorkin et al. (1994) and Dvorkin and Nur (1996) provided statistical approximations to calculate S_n and S_τ, for which the error does not exceed 1%. Parameter α (the ratio of the radius of the cement to the particle radius) was used in the calculation of S_n and S_τ to characterize both the contact-cementing and grain-coating spatial distribution conditions (Equation 3-3 and Equation 3-4).

Contact cementing, $\alpha = 2\left(\frac{S\phi_0}{3C(1-\phi_0)}\right)^{0.25}$ Equation 3-3

Grain coating, $\alpha = \left(\frac{2S\phi_0}{3(1-\phi_0)}\right)^{0.5}$ Equation 3-4

where S is the cement saturation of the pore space. After calculating the effective bulk and shear moduli (Keff and Geff) of the cemented sand matrix, the saturated bulk and shear moduli of the cemented sand matrix are calculated using Gassmann's equations (Gassmann 1951) shown in Table 3.1 (Equation 3-5, Equation 3-6, Equation 3-7, Equation 3-8). The S-and P-wave velocities of the cemented sand matrix are then be calculated using Equation 3-9 and Equation 3-10 in Table 3.1. The input parameters for this model and references for these values are summarized in Table 3.2. It is worth noting that the material bulk and shear modulus, and material density listed in Table 3.2 are standard values of the quartz, calcite, and water (Batzle and Wang 1992; Helgerud et al 1999; Kleinberg and Dai 2005). The original porosity (ϕ0=0.41) of the sand matrix was utilized because it is the average porosity of the prepared sand samples in the literature. The coordination number (C) of the tested soil was calculated

using the original porosity where C=14-16ϕ_0, which was recommended by Santamarina et al. (2001).

Table 3.1. Equations to Calculate Saturated Bulk and Shear Moduli of the Sand Matrix.

Equation	Equation number
$K_{sat} = K_{eff} + \frac{(1 - \frac{K_{eff}}{K_m})^2}{\frac{\phi}{K_f} + \frac{1-\phi}{K_m} - \frac{K_{eff}}{K_m^2}}$	Equation 3-5
$G_{sat} = G_{eff}$	Equation 3-6
$\phi = \phi_0(1 - S)$	Equation 3-7
$K_m = \frac{1}{2}\left[\sum_{i=1}^{m} f_i K_i + (\sum_{i=1}^{m} \frac{f_i}{K_i})^{-1}\right]$	Equation 3-8
$V_p = \left[\frac{K_{sat} + \frac{4}{3}G_{sat}}{\rho}\right]^{1/2}$	Equation 3-9
$V_s = \left[\frac{G_{sat}}{\rho}\right]^{1/2}$	Equation 3-10

K_{sat} and G_{sat}: saturate bulk and shear moduli of the cemented sand matrix, K_f and K_m: bulk moduli for the pore fluid and soil phase, ϕ: fluid filled porosity, m: number of the constituents of the solid phase, f_i and K_i: volumetric fraction and bulk modulus of the i-th constituent in the solid phase, V_p, V_s and ρ: S-and P-wave velocities and bulk density of the cemented sand matrix. Equations are obtained from Gassmann (1951), Hill (1952), Dvorkin et al. (1999), and Kleinberg and Dai (2005).

Table 3.2. Parameters Input for Cemented-Sand and Uncemented-Sand Models.

Consitutent	K (Gpa)	G (Gpa)	σ (kg/m^3)
Quartz	36[a]	44[a]	2650[a]
Calcite	76.8[b]	32[b]	2710[b]
Water	2.2[c]	0[a]	1036[a]

[a] Kleinberg and Dai (2005)
[b] Helgerud et al (1999)
[c] Batzle and Wang (1992)
K and G are material bulk and shrear modulus, respectively, σ is the material density. Two additional parameters were used in the model: original porosity, ϕ_0, =0.41 and coordination number, C=7.4 (C=14-16ϕ_0, Santamarina et al. 2001).

3.3.2 Estimation of S-and P-Wave Velocities for Matrix Supporting Distribution

The analytical model named uncemented sand model by Mavko et al. (1998) is used to analytically estimate the bulk and shear moduli of the sand matrix with matrix-supporting cementing condition. The uncemented-sand model has been successfully used to calculate S-and P-wave velocities of uncemented sand from the North Sea (Dvorkin and Nur 1996) and marine sediments cemented with gas hydrate (Helgerud et al. 1999).

This model is based on the Hashin-Shtrikman lower bound (Hashin and Shtrikman 1963) and the Hertz-Mindlin contact theories (Mindlin 1949). The bulk and shear moduli of the sand matrix without cement (i.e. sand matrix without $CaCO_3$ in this study) was calculated using the Hertz-Mindlin contact theory (Mindlin 1949). The Hashin-Shtrikman lower bound theory was used to calculate the bulk and shear moduli of the cemented sand matrix (i.e. sand matrix with $CaCO_3$ in this study, Hashin and Shtrikman 1963; Mavko et al. 1998; and Dai et al. 2012).

In this study, this uncemented soil model was used to predict the S-and P-wave velocities of the MICP-treated sand for matrix-supporting condition (e.g. cement deposits away from the inter-particle contacts). The equations used to calculate the effective bulk and shear moduli of sand with matrix-supporting $CaCO_3$ spatial distribution are shown in Table 3.3. The elastic moduli of the sand matrix at initial porosity (41%, average porosity of the tested soil samples, Table 3.2) and zero porosity (e.g. all pore space is filled with $CaCO_3$) were calculated based on the Hertz-Mindlin contact theory (Equation 3-11 and Equation 3-12) and Hill's average formula (Equation 3-8 and Equation 3-16). The Hashin-Shtrikman lower bound (Equation 3-13 and Equation 3-14) was used to calculate the elastic moduli at different levels of porosity ranging from 0 and 41%. The saturated bulk and shear moduli, S-and P-wave velocities of the sand matrix under matrix-supporting were calculated using Gassmann's equations as shown in Table 3.1. The input parameters for this model are the same with those for the cemented-sand model (Table 3.2).

Table 3.3. Equations to Calculate Effective Bulk and Shear Moduli under Matrix-Supporting Distribution.

Equation	Equation number
$\mathrm{K_{hm}} = \left[\frac{C^2(1-\phi_0)^2 G_m^2 P}{18\pi^2(1-\upsilon_m)^2}\right]^{1/3}$	Equation 3-11
$\mathrm{G_{hm}} = \frac{5-4\upsilon_m}{5(2-\upsilon_m)}\left[\frac{3C^2(1-\phi_0)^2 G_m^2 P}{2\pi^2(1-\upsilon_m)^2}\right]^{1/3}$	Equation 3-12
$\mathrm{K}_d = \left[\frac{\frac{\phi}{\phi_0}}{K_{hm}+\frac{4G_{hm}}{3}} + \frac{1-\frac{\phi}{\phi_0}}{K_m+\frac{4}{3}G_{hm}}\right]^{-1} - \frac{4G_{hm}}{3}$	Equation 3-13
$\mathrm{G}_d = \left[\frac{\frac{\phi}{\phi_0}}{G_{hm}+Z} + \frac{1-\frac{\phi}{\phi_0}}{G_m+Z}\right]^{-1} - Z$	Equation 3-14
$Z = \frac{G_{hm}}{6}\left[\frac{9K_{hm}+8G_{hm}}{K_{hm}+2G_{hm}}\right]$	Equation 3-15
$\mathrm{G_m} = \frac{1}{2}\left[\sum_{i=1}^{m} \mathrm{f_i G_i} + (\sum_{i=1}^{m} \frac{\mathrm{f_i}}{\mathrm{G_i}})^{-1}\right]$	Equation 3-16

K_{hm} and G_{hm}: effective bulk and shear moduli of sand matrix without cement from the Hertz-Mindlin contact theory, G_m, and υ_m: shear modulus and Poisson's ratio of the solid phase, P: effective confining pressure, K_d and G_d: effective bulk and shear moduli of the sand matrix with matrix supporting from the Hashin-Strikman theory (Hashin and Shtrikman 1963), ϕ: fluid filled porosity, m: number of the constituents of the solid phase, f_i and G_i: volumetric fraction and shear modulus of the i-th constituent in the solid phase. Equations are obtained from Mindlin (1949), Hill (1952), Dvorkin and Nur (1996), and Dvorkin et al. (1999).

3.3.3 Estimation of Permeability

Kozeny-Carman (Carman 1937; Dullien 1992; Panda and Lake 1994; and Carrier 2003) and Panda-Lake (Panda and Lake 1995; Davis et al. 2006) models were used to calculate the change of permeability versus $CaCO_3$ content for MICP treated soil. Kozeny-Carman model considers particle size distribution, particle shape and the

void ratio (Carman 1937; Panda and Lake 1994; and Carrier 2003). The basic equation of the Kozeny-Carman model is shown in Equation 3-17 (Dullien 1992, Panda and Lake 1994).

$$k = \frac{\phi_0^3}{SF\tau_0(1-\phi_0)^2 a_v^2} \qquad \text{Equation 3-17}$$

where k is the permeability of the sand matrix, ϕ_0 is the original porosity without cementation, SF is the shape factor, selected as 3 following the recommendation of Dullien (1992), τ_0 is tortuosity of the uncemented sand matrix (used as 2.5 following Panda and Lake 1995 recommendation), a_v is the specific surface area (surface area of the grain/the volume of the grain) calculated from the statistical parameters of the particle size distribution as illustrated in Panda and Lake (1994). The tortuosity and specific surface area are utilized to characterize the connectivity and pore size of the pore throat in the sand matrix, respectively. When using Kozeny-Carman model to calculate the permeability of cemented soil, only porosity (ϕ_0) is modified based on the increase of the $CaCO_3$ content. The tortuosity and specific surface area are assumed to be constant for different $CaCO_3$ contents because the pore size (represented by specific surface area) and connectivity (represented by tortuosity) of the pore throat will not change significantly for the contact-cementing and grain coating spatial distributions of $CaCO_3$. Therefore, the Kozeny-Carman model will be used to approximately represent the contact-cementing and grain-coating spatial distribution to calculate the permeability versus $CaCO_3$ content.

For matrix-supporting spatial distribution (Figure 3.1), the CaCO3 deposits away from the particle contacts into the pore space, altering the pore size, tortuosity, and porosity of the sand matrix significantly. To consider the effect of matrix-supporting spatial distribution on the permeability of the MICP treated sand, the Panda-Lake model is utilized, which is a modified Kozeny-Carman model as shown in Equation 3-18 in Table 3.4 (Panda and Lake 1995). This model incorporated three correction factors, porosity reduction factor ($\beta\phi$), tortuosity reduction factor ($\beta\tau$), and specific surface area reduction factor (βav), to estimate the permeability reduction of the sand matrix as cementation increases. These correction factors were derived based on the physical principles of cementation into pore space by considering cement saturation of the pore space (S), and specific surface area of the cement crystals (avc) as shown in Equation 3-19 to Equation 3-21 in Table 3.4. Panda and Lake (1995) validated the model by comparing the model calculations with measured permeability of the sandstone, which showed that the maximum error between the modeled and the measured permeability was 10%. Furthermore, the Panda-Lake model was also successfully utilized to estimate the permeability of the cemented porous aquifers (Davis et al. 2006).

Table 3.4. Equations to Calculate Permeability of the Cemented-Sand Matrix.

Equation	Equation number
Panda-Lake equation: $k = \frac{\phi_0^3}{3\tau_0(1-\phi_0)^2 a_v^2} * \beta_\phi * \beta_\tau * \beta_{a_v}$	Equation 3-18
$\beta_\phi = \frac{\phi^3(1-\phi_0)^2}{\phi_0^3(1-\phi)^2}$	Equation 3-19
$\beta_\tau = (1 + \frac{2S}{(1-S)\phi_0^{0.33}})^{-2}$	Equation 3-20
$\beta_{a_v} = (\frac{1-\phi_0}{1-\phi} + \frac{a_{vc}}{a_v} P_c)^{-2}$	Equation 3-21

β_ϕ, β_τ, β_{av}: reduction factor of porosity, tortuosity, and specific surface area, ϕ: fluid filled porosity under cementation, S: cement saturation of the pore space, a_{vc}: specific surface area of the cement crystals, P_c: fraction of cement volume to the total volume of solids.

The parameters used to calculate the permeability using Kozeny-Carman and Panda-Lake models include the density of $CaCO_3$ and quartz, which are summarized in Table 3.2, tortuosity of the uncemented sand matrix (τ_0), which was approximately considered as 2.5 (for packing of single-size spherical particles, Panda and Lake 1995), original porosity without cementation (ϕ_0) (average porosity of prepared sand samples), specific surface area of the cement, which was calculated as 600 mm^{-1} using the average crystal diameter of 10 um (based on the measurements of crystal sizes of SEM images discussed in the background section), unit weight and viscosity of water, 9.8 kN/m^3 and 0.0013 Pa·S, and statistical parameters (i.e. median, standard deviation, and coefficient of variation) of the particle size distribution of the tested sand (calculated using software GRADISTAT developed by Blott and Pye 2001). The detailed procedure of calculating permeability with the statistical parameters of the particle size distribution can be found in Panda and Lake (1994) and (1995). The calculated permeability representing $CaCO_3$

distributions of contact-cementing, grain-coating, and matrix supporting from Kozeny-Carman and Panda-Lake models were compared with the measured permeability of MICP treated sand reported by several researchers to investigate the effects of $CaCO_3$ distributions on the permeability and the main $CaCO_3$ spatial distribution in the pore space.

3.4 PARTICLE-SCALE TESTS

3.4.1 Equipment for Tensile and Shear Tests

In this study, the $CaCO_3$ tensile and shear bond strength was measured. The setup used for the particle-scale tensile test is shown in Figure 3.2. Two glass beads (2 or 3 mm in diameter) were attached on two precision bearing stages with stiff rebar (stainless steel rod, 2.4 mm diameter) and/or optical fiber (Corning SMF-28). High definition microscope (500 Magnification) was used to monitor the beads movement, fiber deformation, and $CaCO_3$ bond size. Two glass beads representing two sand particles were mounted on stiff rebar and optical fiber. The optical fiber was then epoxyed at its two ends onto the stiff rebar. During tension, the displacement actuator (Newport 850G motorized linear actuator, maximum speed: 500 μm/s) was used to accurately move the bearing stage horizontally. The glass bead mounted on the optical fiber was fixed at the middle of the optical fiber. The glass bead-fiber system represent as a fixed-end elastic beam subjected to tensile force at its middle. Based on the theory

of the fixed-end elastic beam subjected to tension at the middle, Equation 3-22 was used to calculate the tension force generated in the $CaCO_3$ bond.

$$F_{tension} = \frac{384EI}{L^3}\Delta \qquad \text{Equation 3-22}$$

where $F_{tension}$ is the bond force, EI is the optical fiber stiffness, in which E is 75 GPa according to Pamukcu and Turel (2005), L is the fiber length, Δ is the measured fiber deflection at the middle.

The test setup described above was modified to measure the shear strength of the $CaCO_3$ bond. Two glass beads were mounted onto the end of the stiff rebar and optical fiber, as shown in Figure 3.2. The displacement actuator was used to move the bearing stage upward to generate shear force between the two glass beads. The bare Fiber Bragg Grating (FBG) sensor (fiber type, SMF-28, length: 2mm, center wavelength 1544 nm, Reflectivity >90%) was fused into the optical fiber to measure the strain generated in the fiber during shear. The force generated in the optical fiber can be calculated using Equation 3-23 as shown below, which equals to the shear force generated in the $CaCO_3$ bond based on the force equilibrium.

$$F_{shear} = E_{FBG}\varepsilon A \qquad \text{Equation 3-23}$$

where F_{shear} is the shear force in the bond, E_{FBG} is the Young's modulus of the FBG, which is 70 GPa according to Cheng et al. (2005), ε is the strain measured by the FBG sensor, A is the cross section area of the FBG.

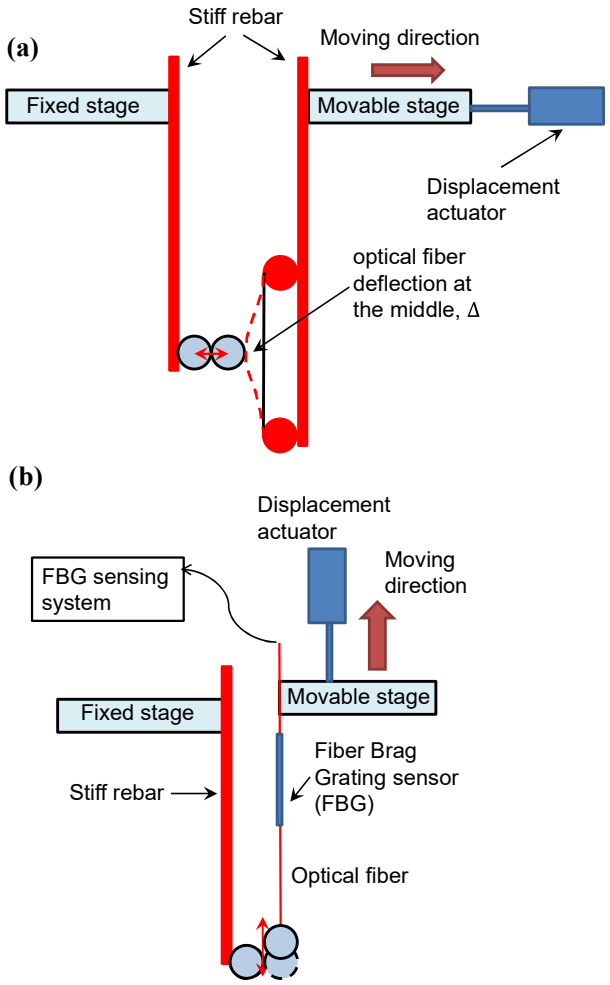

Figure 3.2. Particle-scale test setup for (a) tensile test and (b) shear test.

3.4.2 Materials

The stock culture of *Sporosarcina pasteurii* (ATCC 11859) was cultured in the growth media (10g Yeast Extract, 5g Ammonium Sulfate in 500 mL 0.13M Tris Buffer (pH=9.0) sterilized by filter) in an incubator shaker at 170 rpm, 33°C for approximately 40 hours until OD600=0.8~1. The bacteria were then harvested and centrifuged twice at 4000 g for 30 minutes to target bacteria density 1×10^8 cells/mL. The bacteria were stored in 4°C refrigerator until used. During the test, cementation media for MICP

treatment contains 20 g urea, 2.12 g $NaHCO_3$, 20 g NH_4CL, 3 g Nutrient Broth, and 100 mM $CaCl_2$ in 1 L deionized water (pH=6) sterilized by filter. Two soda-lime glass beads (diameter 3mm from Walter Stern Glass Beads and 2mm from Thermo Scientific Glass Beads) in each test were used to simulate two sand grains. The glass beads were cleaned by soaking into 1M HNO_3 for 24 hours, rinsed thoroughly with deionized water, and then dried at 105°C for 24 hours before being used.

3.4.3 Test Procedures

In both tensile and shear tests, two glass beads were touched each other using displacement actuator and validated by the digital microscope. The beads were then embedded into a small chamber (15 mL) prior to the biological treatment. All influent solutions were injected from the bottom of the small container at flow rate of 1.5 ml/min. The effluent solutions going out of the chamber from the top were collected by a beaker below the syringe. 30 mL of deionized water was pumped into the chamber for cleaning, which was then followed by 25 mL bacteria suspension (bacteria density 1×10^8 cells/mL, 20 g urea, 2.12 g $NaHCO_3$, 20 g NH_4CL, 3 g Nutrient Broth) and waited for 6 hours. After 6 hours incubation, two flushes of cementation media (30 mL of each flush) were then inoculated into the small chamber with time interval of 3 hrs. After finishing two flushes, cementation media without $CaCl_2$ was used to remove the Ca^{2+}. This cycle of injecting bacteria suspension, cementation medium, and cementation medium without $CaCl_2$ was repeated for additional four times. Additional 30 mL

deionized water was inoculated at the end to drain the cementation medium out. The small chamber was removed and the beads were air dried before conducting the tensile and shear tests.

During the tensile and shear tests, the digital microscope was used to monitor the beads movement, fiber deformation, and $CaCO_3$ bond size. The movement rate of the bearing stage was controlled by the linear actuator (0.1 mm/s). The maximum tensile forces were calculated by measuring the maximum deflection at the middle of the optical fiber when the $CaCO_3$ bond broke (Equation 3-22). During the shear test, FBG fiber optic was used to monitor the strain in the fiber with a sampling rate of 10 MSa/s (Mega samples per second) to calculate the shear force generated in the $CaCO_3$ bond (Equation 3-23).

3.5 RESULTS

3.5.1 Effect of $CaCO_3$ Spatial Distributions on S-Wave Velocity

Modeling Results

As discussed before, the cemented-sand model was utilized to calculate the S-wave velocity for contact-cementing and grain-coating spatial distributions, while the uncemented-sand model was used for the matrix-supporting spatial distribution. The S-wave velocities versus $CaCO_3$ contents for the three $CaCO_3$ spatial distribution conditions are shown in Figure 3.3. The results include $CaCO_3$ content ranging from 0 to 41.5%, representing $CaCO_3$ saturation levels from 0 to 100%.

In the contact-cementing model, $CaCO_3$ deposited at the inter-particle contacts only which can significantly improve the moduli and strength of the sand matrix, enabling the highest increasing rate of the S-wave velocity as compared to other distributions (Figure 3.3). As $CaCO_3$ reached higher content, the S-wave velocity increased much slower and reached a plateau due to the already full occupation of $CaCO_3$ at the inter-particle contacts. For the grain-coating model, the $CaCO_3$ deposit uniformly around the sand particles, which also partially cemented particle contacts. The S-wave velocity for the grain-coating condition increase as the $CaCO_3$ content increased, but was not as abrupt as that for the contact-cementing model. As the $CaCO_3$ saturation level approached 100%, the S-wave velocity reached a plateau which was similar to that of the contact-cementing model. However, the contact-cementing curve reached the plateau at much smaller $CaCO_3$ content than the grain-coating curve. For the matrix-supporting model, the cement will not improve the bulk and shear moduli and thus S-wave velocity of the sand matrix significantly at low cement content since the cementing material deposits away from the inter-particle contacts (Figure 3.3). When the $CaCO_3$ saturation exceed 80%, a sudden increase of the S-wave velocity was observed, increasing from 500 to 3800 m/s, which is mainly attributed to the matrix-supporting bridge of the $CaCO_3$ between particles.

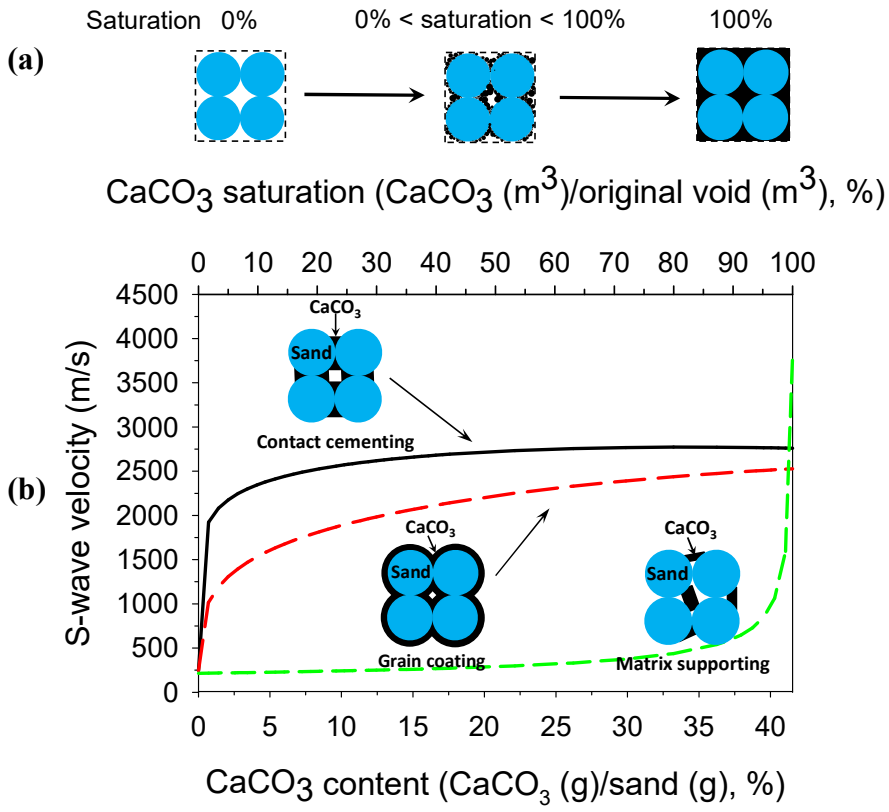

Figure 3.3. Calculated S-wave velocity versus (a) $CaCO_3$ saturation level and (b) $CaCO_3$ content based on ideal spatial distributions of $CaCO_3$: contact-cementing, grain-coating, and matrix-supporting.

Sensitivity Analysis

Model sensitivity were evaluated to investigate the effect of varying input parameters on the change of the S-wave velocities and $CaCO_3$ contents. The comparison of the models using two different $CaCO_3$ densities (2.71 and 1.62 g/cm^3 for polymorph and amorphous precipitated calcite, Helgerud et al. 1999, and Weil et al. 2012) is shown in Figure 3.4. The variation of the S-wave velocity using $CaCO_3$ density of 1.62 g/cm^3 showed a higher increasing rate as compared to that of $CaCO_3$ density of 2.71 g/cm^3 regardless of the types of distributions. At the $CaCO_3$ saturation level of

100%, the ultimate S-wave velocities using $CaCO_3$ density of 1.62 g/cm^3 were 11.5% higher than that using $CaCO_3$ density of 2.71 g/cm^3 for all three $CaCO_3$ distributions. The maximum $CaCO_3$ content also reduced from 41.5 to 29.8% for all three $CaCO_3$ distributions as $CaCO_3$ density decreased from 2.71 g/cm^3 to 1.62 g/cm^3.

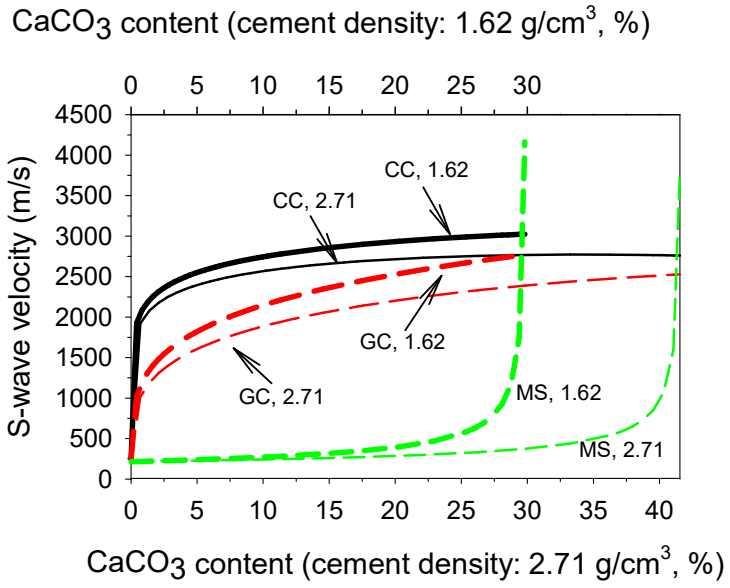

Figure 3.4. Sensitivity analysis of the cemented-sand and uncemented sand models using $CaCO_3$ density of 2.71 and 1.62 g/cm^3, note: CC, contact-cementing, GC, grain-coating, MS, matrix-supporting.

In addition to the cement density, the coordination number (C) and original porosity (ϕ_0) of the sand matrix were also modified to investigate their effects on the change of the S-wave velocities as well as the $CaCO_3$ content (figures not shown). As the coordination number increased from 7.4 to 9 (representing porosity decreased from 41% to 31% of Ottawa 50/70 sand), the S-wave velocities increased by 9.4% without any change of the maximum $CaCO_3$ content. As the porosity decreased from 0.41 to 0.36 (representing relatively density of 51 to 95% of Ottawa 50/70 sand), the maximum

$CaCO_3$ content reduces from 41.5% to 36.5% without any change of the S-wave velocity. For the extreme case by varying all three parameters with cement density of 1.62 g/cm^3, coordination number (C) of 9, and original porosity (ϕ_0) of 0.36, the ultimate S-wave velocity increased by 15.8%, and the maximum $CaCO_3$ content decreased from 41.5% to 25.6%. Thus, based on the range of the variation of the input parameters, the calculated S-wave velocity will have a maximum change of 16%, which will not significantly affect the modeling results. The maximum $CaCO_3$ content could vary 38%. Since the measured $CaCO_3$ content is smaller than 10% as shown next, the change of the maximum $CaCO_3$ content may not pose a significant effect on the calculation results.

3.5.2 Measured vs. Predicted S-Wave Velocities

Measured S-Wave Velocities from Literature

Measured S-wave velocities versus $CaCO_3$ contents reported by several researchers are summarized in Figure 3.5, which includes three types of sand, Ottawa 50/70, 20/30 sands and Bar sand (Table 3.5). The detailed information of the soil sample properties including porosity (used symbol n here instead of ϕ_0), relative density (D_r), coordination number (C=14-16n, Santamarina et al. 2001), concentrations of urea and $CaCl_2$ for MICP treatment, and effective confining pressure are also shown in the legend of Figure 3.5. Initial S-wave velocities with 0% of $CaCO_3$ content ranged from 54 to 207 m/s. As the $CaCO_3$ content increased, the S-wave velocities increased.

However, the increase of the S-wave velocities versus $CaCO_3$ content showed a wide range. Based on all of this data, the upper and lower bound of the S-wave velocities were labelled in Figure 3.5. The upper bound shows an increasing phase and stabilizing phase. For the lower bound, the data showed that the S-wave velocity versus $CaCO_3$ content has a lagging phase, increasing phase, and stabilizing phase. The lagging phase at the beginning of the lower bound ranged from $CaCO_3$ content of 0% to 0.6 % of the $CaCO_3$ content, which is probably attributed to $CaCO_3$ spatial deposition away from the inter-particle contacts (e.g. matrix-supporting). The observed increasing phase of the S-wave velocities indicates that the $CaCO_3$ deposited at the particle contacts (either contact-cementing and/or grain-coating). As the $CaCO_3$ content increased to 3~7 %, the S-wave velocities almost stabilized ranging from 1000 to 1750 m/s (e.g. stable phase).

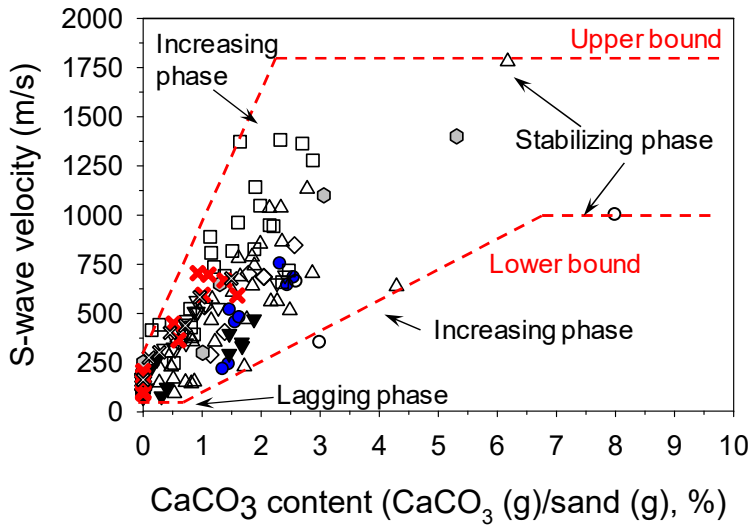

		n(%)/D_r(%)	C=14-16n	Urea/$CaCl_2$ (mM)	Confining pressure during treatment(kPa)
	50/70 sand				
●	(Lin et al. 2016a)	43/40	7.12	333/100, 300	25, 50, 100
⬢	(Montoya and Dejong, 2015)	43/40	7.12	333/50	100
▽	(DeJong et al. 2014)	38/84	7.92	500/250	N/A
△	(Martinez et al. 2013)	35-38/79-100	8.4 to 7.92	333, 50/100, 50	100
○	(Montoya et al. 2013)	43/40	7.12	1000/500	None
□	(Weil et al. 2012)	40-43/40-60	7.6 to 7.12	333/100	100
◇	(Al Qabany et al. 2011)	42/35	7.28	50, 100, 250, 500/same	100
	20/30 sand				
✖	(Lin et al. 2016a)	39/40	7.76	333/100	25, 50, 100
⨯	(Weil et al. 2012)	38-39/40-60	7.92 to 7.76	333/100	100
	Bar sand				
▼	(Lin et al. 2016b and c)	42/29	7.28	333/300	None

Note: N/A, not available
None, no confining pressure
Same, $CaCl_2$ concentration same with urea

Figure 3.5. Measured S-wave velocities versus $CaCO_3$ contents from literature.

Table 3.5. Characteristics of Sands Used in the Tests.

Sand type	D_{10} (mm)	D_{50} (mm)	C_u	G_s	e_{max}	e_{min}	Reference
Ottawa 20-30	0.58	0.71	1.17	2.65	0.74	0.51	Lin et al. (2016a)
Ottawa 50-70	0.26	0.33	1.2	2.65	0.87	0.55	Lin et al. (2016a)
Bar sand	0.18	0.30	2.11	2.65	0.79	0.55	Lin et al. (2016b and c)
Itterbeck sand	0.11	0.17	1.7	2.65	N/A	N/A	Whiffin et al. (2007)
British grade D sand	0.15	0.17	1.23	2.65	0.99	0.59	Al Qabany and Soga (2013)
Toyoura sand	0.16	0.19	1.25	2.65	1	0.60	Yasuhara et al. (2011)
Fine sand	0.16	0.23	1.55	2.62	N/A	N/A	Cheng et al. 2013
Coarse sand	0.53	0.69	1.34	2.62	N/A	N/A	Cheng et al. 2013

Notes: D_{10}=Particle diameter corresponding to 10% finer; D_{50}=Particle diameter corresponding to 50% finer; $Cu = D_{60}/D_{10}$ = coefficient of uniformity; Gs = specific gravity; e_{max} = maximum void ratio; e_{min} = minimum void ratio; N/A=not available.

When focusing on the effect of sand types, for the data reported in Figure 3.5, Ottawa 20/30 sand has the highest increasing rate of the S-wave velocity, which could be attributed to the higher effective $CaCO_3$ content at the inter-particle contacts than other types of sands (Lin et al. 2016a). The variation of the S-wave velocity of 50/70 sand shows a wide increasing range versus $CaCO_3$ content, which may be attributed to the variation of the sample relative densities, coordination numbers, applied confining pressures, urea and $CaCl_2$ concentrations, and $CaCO_3$ spatial distributions in the pore space as shown in the legend of Figure 3.5. The increasing rate of the S-wave velocity of Bar sand is lower than that of 20/30 sand and is in the range of the 50/70 sand. Estimation of the S-wave velocity versus $CaCO_3$ content using the best-fit linear equation has been proposed by several authors (Al Qabany et al. 2011; Weil et al. 2012;

Martinez et al. 2013). However, as shown in Figure 3.5, the best-fit linear equation is difficult to simulate the wide variation of the S-wave velocities versus $CaCO_3$ content. This wide range variation of the S-wave velocity could be attributed to the varying porosity, coordination number, applied confining pressures, urea and $CaCl_2$ concentrations, and $CaCO_3$ spatial distribution in the sand matrix, which was also discussed by Weil et al. (2011). It is also important to note that the $CaCO_3$ content from different sources ranged only from 0 to 10%, covering the $CaCO_3$ saturation of 0 to 24.1 %.

Comparison of Measured and Predicted S-Wave Velocities and Its Implication on $CaCO_3$ Spatial Distribution

To further investigate the real $CaCO_3$ spatial distributions in MICP-treated sands, the measured S-wave velocities shown in Figure 3.5 were compared with the modeling results as shown in Figure 3.6. The initial S-wave velocities with 0% $CaCO_3$ content are 246 m/s for contact-cementing and grain-coating and 214 m/s for matrix-supporting, which are higher than that of the experimental data (e.g. 54 to 207 m/s). This higher S-wave velocities in the models could be attributed to the difference of the confining pressures of the sand matrix between models and experimental data. The comparison of the S-wave velocities from the experimental and modeling results in Figure 3.6 demonstrates that most measured data points locate in the area bounded by the grain-coating and matrix-supporting models, with the upper boundary of the measured S-wave velocities matches the grain coating model curve. The increasing rate

of the measured S-wave velocities is higher than that of the matrix-supporting model but lower than the grain-coating model as shown in Figure 3.6. The maximum S-wave velocities located around the grain coating curve, approximately demonstrating a plateau of S-wave velocity was reached. It is also worth noting that the models predicted the variation of the S-wave velocity versus $CaCO_3$ saturation level ranging from 0 to 100 %.

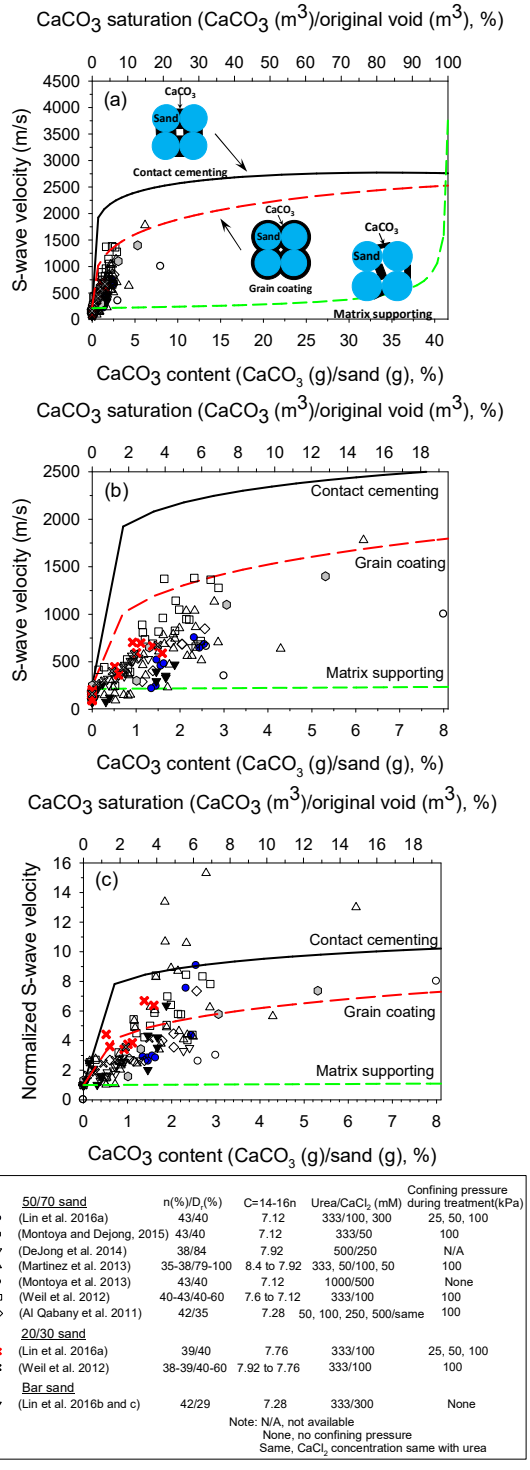

Figure 3.6. Measured S-wave velocities compared with calculated S-wave velocities from models versus (a) full range and (b) small range of $CaCO_3$ content, (c) normalized S-wave velocities versus small range of $CaCO_3$ content.

The measured S-wave velocities were also normalized by their initial values to compare with the normalized S-wave velocities calculated from the models (Figure 3.6). The increasing rate of the measured S-wave velocities is similar to the slope of the grain-coating model. Several data points of the normalized S-wave velocities are higher than that of the contact-cementing model. These measurements had low initial S-wave velocities. The variation of the normalized measured S-wave velocities shows approximately two trends, one with a similar increasing rate as the grain-coating model, the other one with a much lower increasing rate (Figure 3.6). The lower increasing rate is similar to the inefficient line (inefficient $CaCO_3$ precipitation probably due to unbuffered treatment or microbial activity is not properly mediating the reaction network) of the S-wave velocity versus $CaCO_3$ content shown in Weil et al. (2012). Most of the reported data points are located in the range of contact-cementing and matrix-supporting models. Based on the comparison of the S-wave velocities (Figure 3.6), it can be concluded that the $CaCO_3$ spatial distribution of the MICP-treated sand matrix is a combination of grain-coating and matrix supporting, which was also evidenced by the SEM images (Figure 3.1). The best estimation for the variation of the measured S-wave velocities is the grain-coating model, which could serve as a reasonable approximation for discrete element numerical modeling and be used to estimate the $CaCO_3$ content in the field.

3.5.3 Comparison of Measured and Predicted P-wave Velocities and Poisson's Ratios

The variations of the P-wave velocities and Poisson's ratio based on the cemented and uncemented models were also calculated. The variations of the calculated P-wave velocities based on three $CaCO_3$ distributions show similar trend as the modeled S-wave velocities. The initial P-wave velocities at $CaCO_3$ content of 0% between the measurement and models are similar (approximate 1668 m/s). The measured P-wave velocities were also between grain-coating and matrix-supporting models, which is consistent with the S-wave velocities shown in Figure 3.6. The Poisson's ratio calculated from the measured S-and P-wave velocities were also between the contact-cementing and grain-coating models, which confirms that the $CaCO_3$ spatial distribution is a combination of the grain-coating and matrix supporting. It is important to note that this calculated Poisson's ratio is a characterization of a saturated sand at small-strain level.

3.5.4 Comparison of Measured and Predicted Permeability Coefficients

Kozeny-Carman model was used to approximately represent contact-cementing and grain-coating distributions of $CaCO_3$ to calculate the permeability considering the change of the porosity. Panda-Lake model was used to calculate the permeability of the sand matrix with matrix-supporting considering the change of the porosity, tortuosity, and specific surface area. The permeability versus $CaCO_3$ content calculated based on

both models were compared with the measured permeability reported in the literature (Figure 3.7). The basic soil properties of different sands reported in the literature were summarized in Table 3.5.

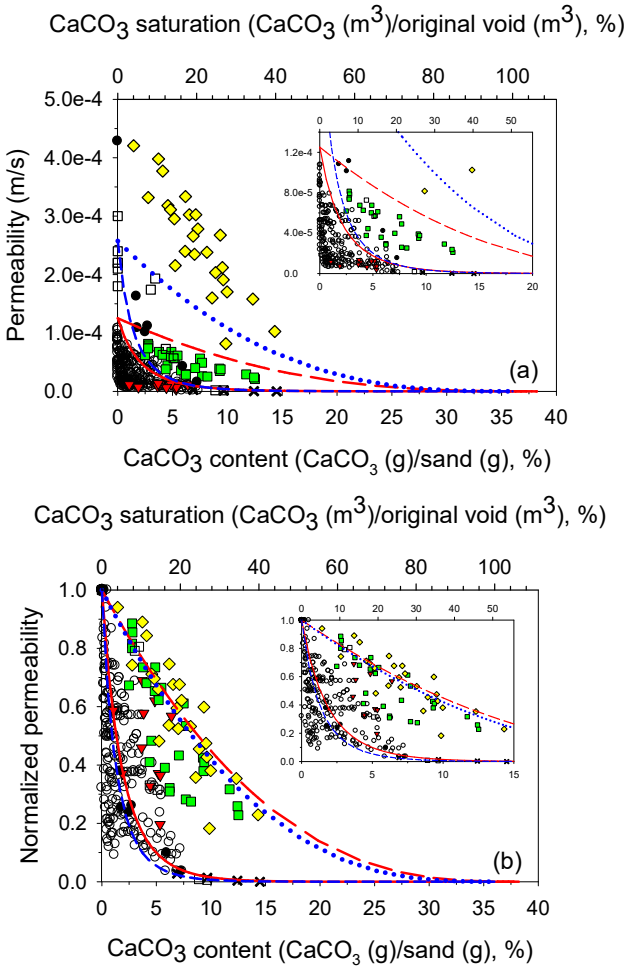

References	Sand type	D_{10}, (mm)	n(%)/D_r(%)	Urea/$CaCl_2$ (mM)	σ_3'(kPa)
○ (Al Qabany and Soga 2013)	British grade D	0.15	37-44/50-100	250, 500,1000/same	20
▽ (Whiffin et al. 2007)	Itterbeck	0.11	38/N/A	1100/1100	None
■ (Cheng et al. 2013)	Fine sand	0.16	39/N/A	1000/1000	None
● (Yasuhara et al. 2011)	Toyoura	0.16	44/49	500,1000/same	50
□ (Martinez et al. 2013)	Ottawa 50/70	0.26	34-37/79-100	333, 50/100, 50	100
◇ (Cheng et al. 2013)	Coarse sand	0.53	39/NA	1000/1000	None
× (Cheng et al. 2013)	Fine sand with Portland cement	0.16	N/A	N/A	None
—— Panda-Lake model	British grade D	PSD	38/93		
— — Kozeny-Carman model	British grade D	PSD	38/93		
– – – Panda-Lake model	Ottawa 50/70	PSD	36/96		
····· Kozeny-Carman model	Ottawa 50/70	PSD	36/96		

Note: σ_3', effective confining pressure during MICP treatment
Same, $CaCl_2$ concentration same with urea
N/A, not available
None, no confining pressure
PSD, statistical parameters of the particle size distribution

Figure 3.7. Comparison of permeability between laboratory (open and solid symbols) and modeling results (solid and dashed lines).

The modeling results using statistical parameters (i.e. median, standard deviation, and coefficient of variation) of the particle size distribution of each sand were calculated. The modeling results using British grade D sand and Ottawa 50/70 sand were shown in Figure 3.7. The results of Panda-Lake model show that the permeability reduced significantly as the $CaCO_3$ content increased to 15%. While, the test results of Kozeny-Carman model show a much slower reduction of permeability as the $CaCO_3$ content increased to 30%. The comparison between the calculated and measured permeability using Panda-Lake model demonstrates a relatively good match, demonstrating that the matrix-supporting largely existed in the MICP-treated sand matrix and controlled the permeability. The permeability of fine and coarse sands reported by Cheng et al. (2013) showed a similar trend with the Kozeny-Carman model (Figure 3.7). This controversial results compared to the rest of the results could be attributed to the dominant $CaCO_3$ distribution as contact-cementing and grain-coating during MICP treatment under unsaturated condition which was observed from the SEM images by Cheng et al. (2013). It is also worth noting that the permeability of the sand matrix treated by Portland cement was also tested by Cheng et al. (2013) and reported in Figure 3.7, which shows a good match with the results of Panda-Lake model. Based on the data reported in Figure 3.7, it can be concluded that the permeability of the MICP-treated sand matrix was controlled by the matrix-supporting distribution of $CaCO_3$ and reduced significantly as $CaCO_3$ content increased.

3.5.5 Tensile and Shear Strength of $CaCO_3$ Bond

Digital images of the tensile test before tension, during tension, and after tension are shown in Figure 3.8. During the tests, the optical fiber deflected as the bearing stage started moving (Figure 3.8). The $CaCO_3$ bond broke when the tension force in its bond equal to its tensile strength (Figure 3.8). When compared to axisymmetric water-bridge between the glass beads (Lu et al. 2008 and Dong 2013), the observed $CaCO_3$ bond shape was not axisymmetric and was not uniformly cemented the glass beads at their contacts as shown in Figure 3.9, which posed a difficulty for measuring bond shape and calculating bond strength. Unlike the water bridge between glass beads, based on the observation of the digital microscope images, the $CaCO_3$ bond size was not affected by the diameter of the glass beads due to the small size of $CaCO_3$ bond and its non-uniform deposition at the particle contacts as shown in Figure 3.9. It was observed that the $CaCO_3$ bond between glass beads responded as a brittle material, and fractured only in the bond, which is consistent with the observation from the SEM images by Martinez and DeJong (2009).

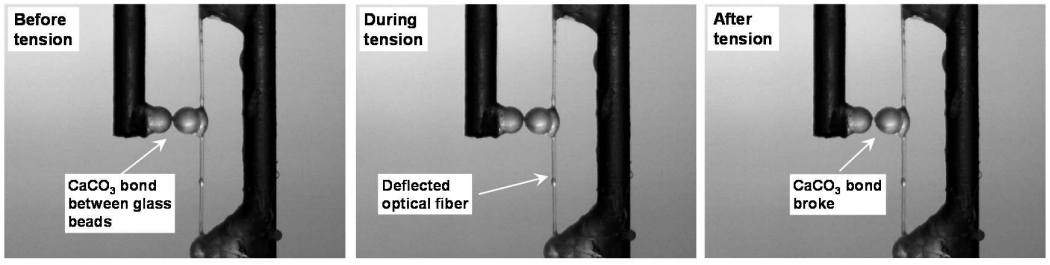

Figure 3.8. Digital microscope images shown (a) before, (b) during, (c) after the tensile test.

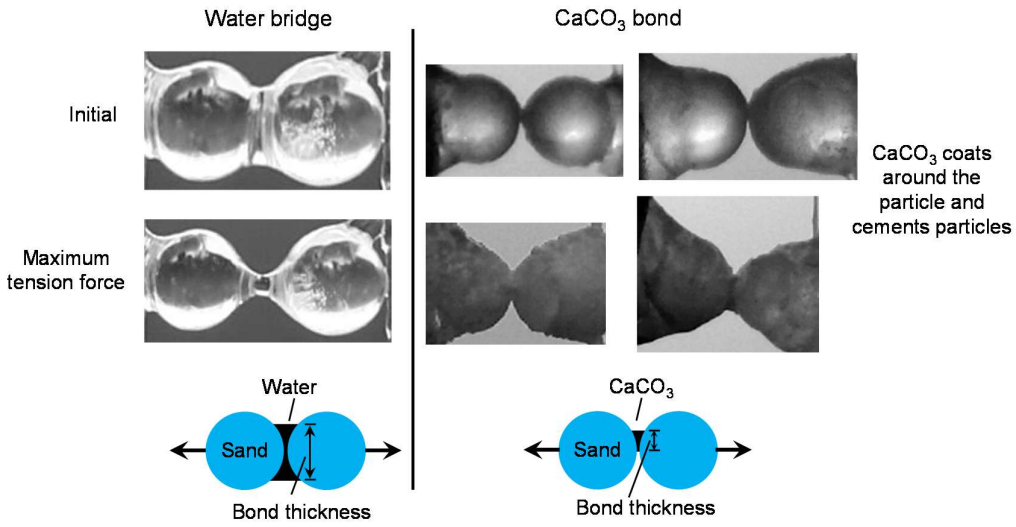

Figure 3.9. Typical water bridge and $CaCO_3$ bond between glass beads

When processing the images versus time, the reference scale was first set up using the diameter of the stiff rebar. The optical-fiber beam length was then measured using the measuring tool in the software. The movement of the stiff rebar on the right hand side was measured versus time, which equals to the deflection of the optical-fiber beam. The tension force versus time was then calculated using the Equation 3-22, which is also shown in Figure 3.10 as an example. Four repeated tension tests were conducted and show that the ultimate tensile force of the $CaCO_3$ bond is 0.026±0.005 N. To calculate the tensile strength of the $CaCO_3$ bond, the bond shape was assumed as a cylindrical bridge between the two glass beads. The thickness of the $CaCO_3$ bond was measured, which was considered as the diameter of the cross section of the cylindrical bridge. The tensile strength was then calculated by dividing the tensile force with the cross section area of the bond. The tensile strength of the $CaCO_3$ bond is 110±60 kPa.

The calculated tensile strength from four tension tests were plotted against the cross section area of $CaCO_3$ bond as shown in Figure 3.11. The data points were fitted with a linear relationship in Figure 3.11. The tensile strength linearly decreases with the cross section area of $CaCO_3$ bond, which could be attributed to the bigger the size of $CaCO_3$ bond, the higher amount of internal micro pores in the $CaCO_3$ bond (discussed in the general background, Figure 3.1), weakening its tensile strength.

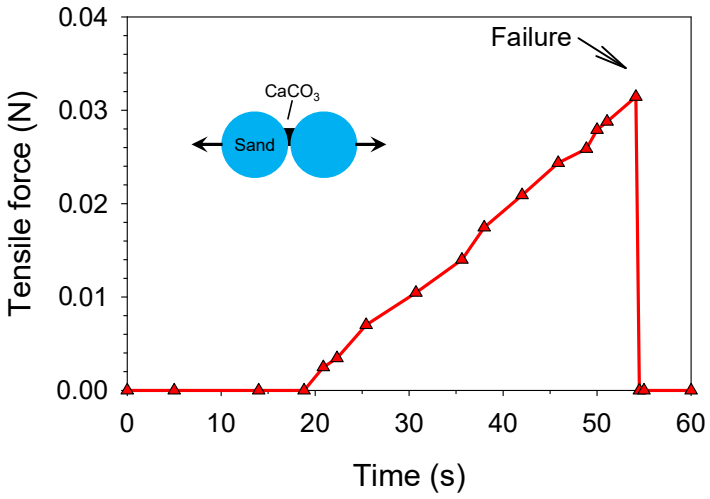

Figure 3.10. Typical measured force-time response during the tensile test.

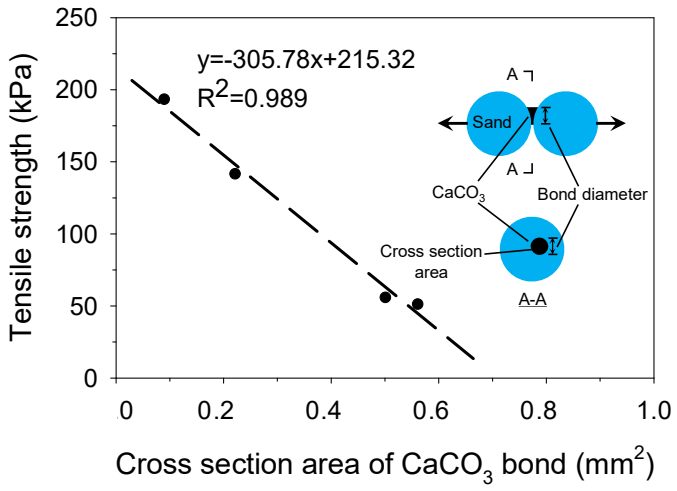

Figure 3.11. Measured tensile strength versus the square of the $CaCO_3$ bond diameter.

The shear strength of the $CaCO_3$ bond was calculated by dividing the maximum shear force (Equation 3-23) with the measured cross section area of the $CaCO_3$ bond. The ultimate shear force was 1.94 N, and the shear stress is 614.4 kPa based on only one test. The research team is currently simplifying the setup of the shear test and will continue to investigate the shear strength of the $CaCO_3$ bond between particles

3.5.6 Implications of $CaCO_3$ Bonding Strength on Shear Strength of the MICP-Treated Sand Matrix

The shear strength of the MICP-treated sand matrix can be calculated using the normal stress (σ_n), the friction angle (φ), the $CaCO_3$ content (e.g. $CaCO_3$ saturation, S_{CaCO3}), and $CaCO_3$ bonding strength (tensile and shear strength, σ_t, and τ_s), and spatial distribution at pore-scale as shown in Figure 3.12, which includes matrix-supporting (Figure 3.12a) and grain-coating (Figure 3.12b). Considering the sand matrix is a simple

cubic packing, the shear force (T) applied at two rows of sand particles under a confinement of N is related to the normal force (N), friction angle (φ), cross section area of the $CaCO_3$ bond (a), $CaCO_3$ spatial distribution and saturation level (S_{CaCO3}), and tensile and shear strength of the $CaCO_3$ bond (σ_τ and τ_s) as shown in the Equations 3-24 and Equations 3-29 shown in Figure 3.12. The shear strength of the MICP-treated sand matrix under matrix-supporting condition was calculated by relating the bond cross section area with the $CaCO_3$ saturation level as shown in Equation 3-24- Equation 3-28 shown in Figure 3.12a. Similar to the shear strength calculation of the matrix-supporting condition, the calculation for shear strength of the grain-coating condition is shown in Equation 3-29-Equations 3-32 shown in Figure 3.12b. The equations shown in Figure 3.12 provide a relationship to calculate the effect of $CaCO_3$ spatial distribution, content, and the particle-scale tensile and shear strength on the shear strength of the MICP-treated sand matrix.

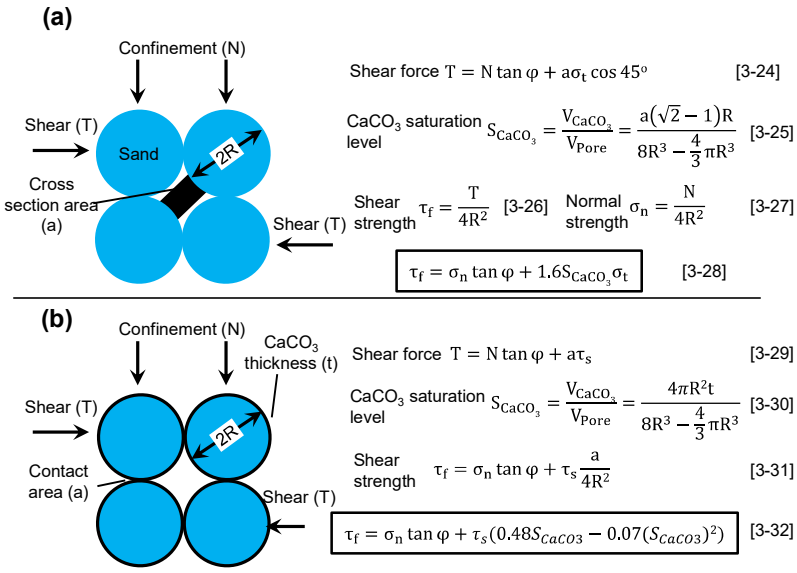

Figure 3.12. The relevance of the (a) tensile and (b) shear strength of the $CaCO_3$ bond on the shear strength of the MICP-treated sand matrix.

3.6 CONCLUSIONS

This study focuses on investigating the $CaCO_3$ distributions and its bond strength in the MICP-treated sand matrix and their effects on the variation of the S-and P-wave velocities, Poisson's ratio, permeability, and shear strength of the sand matrix. The measured S-and P-wave velocities, Poisson's ratio, and permeability were compared with their predicted values based on the cemented-sand, uncemented-sand, Kozeny-Carman, and Panda-Lake models. The particle-scale test setup was used to analyze the bond characteristics and measure the tensile and shear strength of the $CaCO_3$ bond. The implication of the $CaCO_3$ bond strength on mechanical behavior of the MICP-treated sand matrix was analyzed and discussed. The following conclusions were drawn.

1. Three $CaCO_3$ spatial distributions (e.g. contact-cementing, grain-coating, and matrix-supporting) are observed in the real SEM images of MICP-treated sand matrix. Each type showed different effects on the elastic moduli and thus S-and P-wave velocities and Poisson's ratio versus $CaCO_3$ contents using the cemented-sand and uncemented-sand models.
2. The measured S-wave velocities from literature shows a wide range of variation with $CaCO_3$ contents. The main distributions of the $CaCO_3$ at pore-space are grain-coating and matrix supporting. The calculated S-wave velocities combined with the measured S-wave velocities can be used as a tool for future lab and field tests monitoring.
3. Based on the comparison of the permeability between the measurement and modeling predictions, the matrix-supporting mainly controlled the permeability of the MICP-treated sand matrix. The measured permeability combined with the modeling results could serve as a monitoring tool for future lab or field tests.
4. The permeability of the MICP-treated sand matrix reduced significantly as the $CaCO_3$ content increased to approximate 15%. Thus, it may not be applicable for large-are soil improvement by reducing the number of injection wells.
5. The cemented-sand and uncmented-sand models can be used to estimate the S-and P-wave velocities, Poisson's ratio of the sand matrix cemented by other agents. The Panda-Lake model could also be served as a potential tool to calculate permeability of the sand matrix cemented by many other agents.

6. The observed $CaCO_3$ bond shape was not axisymmetric and was not uniformly cemented at the contacts. The $CaCO_3$ bond was fractured only in the $CaCO_3$ phase under tension or shear force.

7. The ultimate tensile force of the $CaCO_3$ bond is 0.026±0.005 N. The tensile strength of the $CaCO_3$ bond is 110±60 kPa. The tensile strength linearly decreases with the square of the diameter, which may be attributed to micro pores existing in the bond as the $CaCO_3$ bond size increases.

8. The equations used to calculate the Mohr-Coulomb failure envelope of the sand matrix under matrix-supporting and grain-coating were derived using the measured tensile and shear strength of the $CaCO_3$ bond, which could be used for future modeling of lab and field tests.

4. MECHANICAL BEHAVIOR OF SANDS TREATED BY MICROBIALLY INDUCED CARBONATE PRECIPITATION (MICP)

4.1 BACKGROUND

Bio-mediated soil improvement is an innovative ground improvement solution that could be suitable for many geotechnical problems (Mitchell and Santamarina 2005; Ivanov and Chu 2008; Kavazanjian and Karatas 2008; DeJong, et al. 2010a; DeJong et al. 2013). One promising bio-mediated technique that has attracted a lot of attention recently is Microbially Induced Carbonate Precipitation (MICP) (DeJong et al. 2006; Whiffin et al. 2007; Karatas et al. 2008; van Paassen 2009; Hamdan et al. 2011; Al Qabany et al. 2012; Burbank et al. 2013).

The most common MICP process described in the technical literature is hydrolysis of urea by the enzyme urease (ureolysis). The microorganism most commonly employed for MICP via ureolysis is *Sporosarcina pasteurrii* (ATCC 11859 and DSM-33). *Sporosarcina pasteurrii* is an alkalophilic soil bacterium with a highly active urease enzyme (Ferris et al. 1996). The bacteria produce urease to hydrolyze urea into ammonium and carbonic acid, which is accompanied by an increase of alkalinity (the logarithmic of acid dissociation constant, pKa of ammonia/ammonium is 9.3 and pH of ~9). This alkaline environment shifts the equilibrium of calcium carbonate

($CaCO_3$) precipitation/dissolution toward precipitation by increasing the availability of the carbonate ion (Stocks-Fischer et al. 1999; Ebigbo et al. 2012).

The precipitated calcium carbonate can coat soil particles, cement the soil matrix, and fill the soil void space, increasing its strength, stiffness, and dilatancy. MICP has been investigated for several geotechnical applications including soil improvement, liquefaction mitigation, stabilizing costal sand dunes, radionuclide sequestration, and fugitive dust stabilization (Whiffin et al. 2007; Bang et al. 2009; Kavazanjian, et al. 2009; van der Ruyt and van der Zon 2009; Fujita et al. 2010; Burbank et al. 2013; Montoya et al. 2013). In spite of the considerable interest in MICP, available information on the mechanical behavior of MICP-treated sands on both the macro-scale and the micro-scale is still limited.

Recently, Lin et al. (2015, 2016b and c) investigated the use of MICP to improve the static axial capacity of permeable piles focusing on pervious concrete piles. Lin et al. (2015, 2016b and c) reported that the $CaCO_3$ content of the soil surrounding the tested pervious concrete piles ranged from 0% to 3%. Therefore, the triaxial tests reported in this paper focus on the drained response of MICP-mediated sands with $CaCO_3$ contents in the range reported by Lin et al. (2015, 2016b and c).

4.1.1 Macro-Scale Behavior of MICP-Treated Sand

At the macro-scale, the mechanical behavior of MICP-treated sands is controlled by the $CaCO_3$ content, sand gradation, relative density, and confining stress

(Rebata-Landa 2007; Chou et al. 2011; van Paassen 2012; Al Qabany and Soga 2013; Cheng et al. 2013a). However, most researchers have been focusing on investigating the behavior of one type of MICP-treated sand under undrained condition, providing limited information on the variations of volume change, modulus, friction angle, and cohesion. In addition, very limited drained triaxial stress-strain responses have been reported in the literature for MICP-treated specimens at different $CaCO_3$ contents. Furthermore, tests performed on MICP-treated sands under confined compression condition (one-dimensional compression loading) are limited in the literature. Therefore, the focus of the tests reported in this paper is to investigate the evolution of strength, stiffness, volumetric strain as a function of confinement, axial strain, and $CaCO_3$ cementation level for different sand types under consolidated drained (CD) and one-dimensional (K_o) loading conditions.

4.1.2 Micro-Scale of MICP-Treated Sand

At the micro-scale, the precipitated calcium carbonate has been observed to nucleate around bacteria cells attached to the sand particle surface, forming calcite and vaterite $CaCO_3$ crystals or amorphous $CaCO_3$ (Burbank et al. 2013). The types of $CaCO_3$ isomorphs formed in the precipitation process are mainly determined by the urea hydrolysis rate (van Paassen 2009). For example, spherical vaterite and amorphous $CaCO_3$ are dominant under higher urea hydrolysis rates, while rhomboidal calcite formation is dominant under low hydrolysis rates (van Paassen 2009).

$CaCO_3$ may deposit at or near particle contact points (contact cementing), coat the soil particles (grain coating), fill the void space without contacting a soil particle, or grow from the particle surface into the pore space and eventually create a $CaCO_3$ bridge between sand particles (matrix supporting). Figure 4.1 shows a schematic illustration of the contact cementing, grain coating, and matrix supporting mechanisms. Contact cementing and grain coating were observed in Scanning Electron Microscopy (SEM) and/or Energy Dispersive X-ray Spectroscopy (EDS) images by several researchers (Martinez and DeJong 2009; van Paassen 2009; DeJong et al. 2010b; and Al Qabany et al. 2012). However, observation of the matrix supporting mechanism has not been reported in the literature for MICP-treated sands.

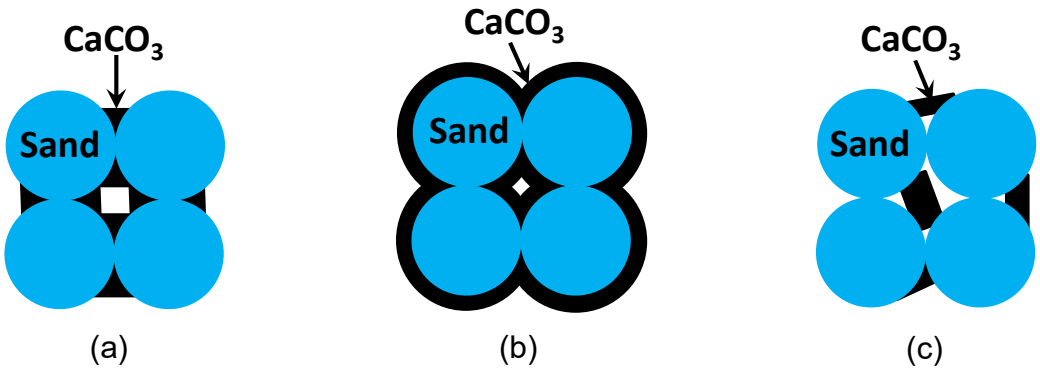

Figure 4.1. Ideal spatial distributions of $CaCO_3$ during MICP: (a) contact cementing, (b) grain coating, and (c) matrix supporting. Note: figures not to scale (modified after Kleinberg and Dai 2005; Dai et al. 2012; Waite et al. 2009).

The goal of this paper is to investigate the macro-scale mechanical behavior of MICP-treated sands under drained triaxial compression and under zero lateral strain (i.e. one dimensional confined compression) conditions and to investigate the spatial

distribution of $CaCO_3$ at the micro-scale. Triaxial and confined compression tests with embedded shear and compression wave (S-wave and P-wave) sensors were conducted on two MICP-treated sands, Ottawa 50/70 and 20/30 silica sands. The triaxial compression tests were conducted at three different confining pressures (25, 50, and 100 kPa). Tests were also performed at different $CaCO_3$ cementation contents targeting the range reported by Lin et al. (2015, 2016b and c) surrounding pervious concrete piles. After the tests, samples at different locations within the specimens were saved for $CaCO_3$ content measurement and SEM and EDS imaging. The morphology and spatial distribution of $CaCO_3$ at the micro-scale were analyzed using the SEM and EDS results.

4.2 EQUIPMENT

Triaxial and confined compression (i.e. one-dimensional compression) tests were used to investigate the mechanical behavior of the two MICP-treated sands. Figure 4.2 presents schematic diagrams of the test equipment. For the triaxial cell, S-and P-wave sensors were sealed inside two fabricated acrylic plates fixed to the top and bottom caps (Figure 4.2a). The confined compression test device was constructed of a stainless steel cell with two embedded pairs of S-wave sensors to measure the S-wave velocity in the vertical and horizontal directions (Figure 4.2b and c). The S- and P-wave sensors were fabricated in-house using piezo elements (4×8 mm parallel type-PSI-5H4E T226-H4-303Y from Piezo Systems, Inc.) and unimorph bender discs (8.9 mm diameter, 0.11 mm thickness FT-8.9T-9.0A1 from APC International, Ltd). A 2 V

square wave with 100 HZ frequency provided by a function generator (Agilent 33220A) was used as an input signal for the S-wave sensors. The received signal was filtered by a band-pass filter (Krohn-Hite 3944) of 100 Hz to 30 kHz, and a digital oscilloscope (Agilent DSO5014A) was used to stack 128 signals to reduce non-coherent noise (Yun and Santamarina 2005). The S-wave velocity (V_s) was determined by dividing the tip to tip distance (L in Figure 4.2) between two sensors by the travel time (t) using the first arrival point of the signal (Lee and Santamarina 2005). To generate a P-wave through the specimen, a 3 V square wave with a frequency of 50 HZ from the function generator was used as the input signal. The received signal is filtered by a band-pass filter of 600 Hz to 300 kHz. The P-wave velocity (V_p) was calculated in a similar manner to the S-wave velocity measurement described above.

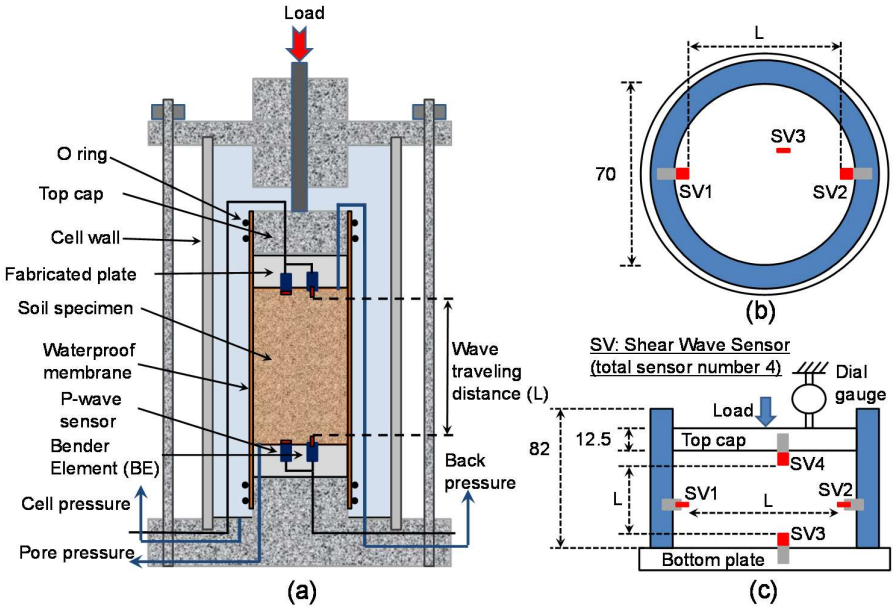

Figure 4.2. Test setup and instrumentation: (a) triaxial cell, (b) top view of the confined compression cell, and (c) side view of confined compression cell. All dimensions in mm.

4.3 MATERIALS

4.3.1 Bacteria Cultivation and MICP Recipe

The gram-positive bacteria strain *Sporosarcina pasteurii* (ATCC 11859) was used in this study. Bacterial cultures were grown in an ATCC specified medium (Table 4.1), harvested in the late exponential growth phase, and then stored in 15% glycerol at -86°C using the glass bead method to maintain a uniform bacterial stock (Jones et al. 1991). Before each experiment, bacteria from the frozen stock were grown in the growth medium inside an incubator shaker at 170 rpm and 33°C. The bacteria were harvested at OD_{600} of 0.8~1.2 (OD_{600}: optical density of a sample measured at a wavelength of 600 nm), centrifuged twice at 4000xg for 30 minutes to a target bacteria density of $1x10^8$ cells/mL, and stored at 4°C until used. Tris buffer and growth medium were used to grow the bacteria cells. Table 4.1 presents the chemical recipe that was used for growing the bacteria cells.

Table 4.1. Summary of Microbially Induced Carbonate Precipitation (MICP) Recipe.

Solution	Constituents
Tris Buffer	7.6 g Tris hydrochloric acid 54.7 g Tris base in 500 mL distilled water
Growth Medium	10 g Yeast extract 5 g Ammonium sulfate in 500 mL of 0.13 M Tris buffer (pH 9.0) sterilized by filter
Urea Medium	20 g/L Urea 2.12 g/L $NaHCO_3$ 20 g/L NH_4CL 3 g/L Bacto nutrient broth Adjust pH of the medium to 6.0 with 5 M HCL sterile filtration
Cementation Medium	Urea medium constituent 0.1 M $CaCl_2$ or 0.3 M $CaCl_2$

4.3.2 Sand Types

Two types of silica sands, Ottawa 50/70 and Ottawa 20/30, were used in the experiments. Ottawa 50/70 sand has a particle diameter at 10% finer by mass (D_{10}) of 0.26 mm, a particle diameter at 50% finer by mass (D_{50}) of 0.33 mm, a coefficient of uniformity (C_u) of 1.43, a coefficient of curvature (C_c) of 1.01, and maximum and minimum void ratio (e_{max} and e_{min}) of 0.87 and 0.55. Ottawa 20/30 sand has a D_{10} of 0.58 mm, a D_{50} of 0.71 mm, a C_u of 1.17, a C_c of 1.02, and e_{max} and e_{min} of 0.74 and 0.51, respectively. Both sands have greater than 98.7% silica (SiO_2). To keep the sand surface clean and deplete any soluble chemicals that may interfere with the $CaCO_3$ content measurement, the sands were initially soaked in 1M nitric acid solution for 24

hours followed by cleaning with deionized water and drying in an oven at 105°C for 24 hours before being used.

4.4 EXPERIMENTAL PROCEDURES

4.4.1 Sample Preparation

Triaxial test specimens 72 mm in diameter and 145 mm in height were prepared using the wet-raining method (Chaney and Mulilis 1978). Then, a vacuum pressure similar to the target confining pressure during the test (e.g. 25, 50, and 100 kPa) was applied to the specimens. The average measured void ratio (e) after vacuum consolidation was 0.74 and 0.65 for the 50/70 and 20/30 sand specimens, respectively, corresponding to relative densities of 41% and 39%, respectively. After filling the triaxial cell with water, the vacuum pressure was decreased by 10 kPa and the cell pressure increased simultaneously by 10 kPa until the cell pressure increased to the target confining pressure (25, 50, and 100 kPa) and the vacuum pressure returned to 0 kPa. In the confined compression tests, specimens 70 mm in diameter and 60 mm in height were also prepared by wet-raining into the cell to approximately the same relative densities as the triaxial samples (approximately 40%). Then, a 10 kPa normal (compression) pressure was applied on the top cap. It is important to note that all tests were successfully duplicated to verify repeatability and validate the results.

4.4.2 MICP Treatment

A peristaltic pump (Cole-Parmer, C/L tubing pump) was used to introduce chemical and bacteria solutions from the bottom port of the triaxial and confined compression cells. The flow rate was set at 10 mL/min. Each specimen was initially flushed by two pore volumes of deionized water (500 mL for triaxial test, 200 mL for confined compression test). Stored bacteria were suspended in two pore volumes of urea media prepared in accordance with the proportions provided in Table 4.1, stirred, and introduced into the triaxial and confined compression specimens from the bottom port. The bacteria-urea solution was kept within the specimen for seven hours to allow the bacteria to attach to the sand surface and for hydrolysis to occur. After seven hours, two pore volumes of cementation medium prepared in accordance with the proportions provided in Table 4.1 was introduced through the bottom port 5 times at three hours intervals. During treatment, the S-and P-wave velocities of the specimens were monitored with a sampling rate of 1 sample/30 minutes. After three hours of finishing the fifth cementation medium, five pore volumes of deionized water were flushed through each specimen from the bottom port to remove residual chemicals.

4.4.3 Saturation and Loading

After MICP treatment, consolidated drained triaxial tests were performed. Triaxial specimens were back pressure saturated until the B value (pore water pressure ratio) exceeded 0.95. The S-wave velocity was monitored during saturation and the

changes were less than 50 m/s for all tests, which indicates that the saturation process did not significantly change either the S-wave velocity or other mechanical properties of the sands. Following saturation, the specimens were loaded by displacement control with a loading rate of 0.5 mm/min (0.34% axial strain/min) until the axial strain was approximately equal to 10%. During loading, the S-wave velocity was measured with a sampling rate of 1 sample/0.1% axial strain up to an axial strain of 1% and 1 sample/0.35% axial strain afterwards.

In the confined compression tests, after MICP treatment under 10 kPa vertical stress, the vertical (normal) stress was increased to 50, 100, 200, 400, 600, 800, 1000, 1200, 1400, 1600 kPa and then decreased targeting the same values. Each loading and unloading increment lasted for 15 min as recommended by Yun and Santamarina (2005). S-wave velocity and displacement measurements were recorded at the end of each loading stage.

4.4.4 SEM and EDS Imaging

After loading, samples were saved for SEM imaging and EDS analysis. The EDS system was integral to the SEM device (FEI XL30). The SEM images of the samples were produced first. Then, EDS was used to scan the sample for Si and Ca elements mapping.

4.4.5 $CaCO_3$ Content Measurement

After each triaxial and confined compression test, samples of approximately 15 g in mass were collected at a frequency of 1 sample every 10 mm of specimen height for $CaCO_3$ content analysis. The samples were placed in glass tubes and oven-dried at 105°C for at least 48 hours. After oven drying, 15 mL of 5 M Hydrochloric acid was added to the glass tube. The tubes were capped and shaken gently to facilitate dissolution of the $CaCO_3$ in the sample. The liquid samples were extracted and diluted by 1000 times. The Ca^{2+} concentration (C_{Ca}, g/mL) of the diluted samples were measured using an Atomic Absorption Spectrometer (AAnalyst 200, PerkinElmer). Then, the $CaCO_3$ content was calculated using Equation 4-1 and Equation 4-2 below.

$$W_{CaCO_3}=C_{ca}\times 1000/40\text{g/mol}\times 100\text{g/mol}\times 15\text{mL} \quad \text{Equation 4-1}$$

$$CaCO_3 \text{ content } (\%)=\frac{W_{CaCO_3}}{W_{tube+sand}-W_{tube}-W_{CaCO_3}}\times 100\% \quad \text{Equation 4-2}$$

where W_{CaCO_3} is the total weight of $CaCO_3$ in the specimen, $W_{tube+sand}$ is the weight of treated sand and glass tube, W_{tube} is the weight of the glass tube, the factor of 1000 in equation [1] is to account for the 1000 times dilution, 40 g/mol is the calcium atomic weight, 100 g/mol is the $CaCO_3$ molecular weight, and 15 mL is the volume of Hydrochloric acid solution added into the glass tube. The detailed information on sand and treatment types, effective confining pressures, $CaCl_2$ concentrations in cementation media, and average $CaCO_3$ contents ($CaCO_3$ (g)/sand (g)) after the tests are summarized in Table 4.2 and Table 4.3 for the triaxial and confined compression tests, respectively.

Table 4.2. Characteristics of Triaxial Test Specimens

Sand types	Untreated or MICP	Effective confining stress, σ_3', (kPa)	$CaCl_2$ in cementation medium[a], (mM)	Measured $CaCO_3$ content[b], (%)
Ottawa 50/70	Untreated	25	0	0
	Untreated	50	0	0
	Untreated	100	0	0
	MICP	25	100	1.6
	MICP	50	100	1.6
	MICP	100	100	1.5
	MICP	25	300	2.5
Ottawa 20/30	Untreated	25	0	0
	Untreated	50	0	0
	Untreated	100	0	0
	MICP	25	100	1.1
	MICP	50	100	1.0
	MICP	100	100	0.9

[a] From Table 4.1.

[b] Calculated from $W_{CaCO_3}=C_{ca}\times 1000/40 g/mol\times 100 g/mol\times 15mL$ Equation 4-1 and CaCO3 content (%)$=\frac{W_{CaCO_3}}{W_{tube+sand}-W_{tube}-W_{CaCO_3}}\times 100\%$ Equation 4-2.

Table 4.3. Characteristics of Confined Compression Test Specimens

Sand types	Untreated or MICP	Initial effective confining stress, σ_0', (kPa)	$CaCl_2$ in cementation medium[a], (mM)	Measured $CaCO_3$ content[b], (%)
Ottawa 50/70	Untreated	10	0	0
	MICP	10	100	1.4
	MICP	10	300	2.6
Ottawa 20/30	Untreated	10	0	0
	MICP	10	100	0.6
	MICP	10	300	1.6

[a] from Table 4.1.

[b] Calculated using $W_{CaCO_3}=C_{ca}\times 1000/40 g/mol\times 100 g/mol\times 15mL$ Equation 4-1 and $CaCO_3$ content (%)$=\frac{W_{CaCO_3}}{W_{tube+sand}-W_{tube}-W_{CaCO_3}}\times 100\%$ Equation 4-2.

4.5 TRIAXIAL TESTS

4.5.1 Sands Treated with 0.1 M $CaCl_2$

S-and P-Wave Velocities During MICP Treatment

Figure 4.3a and b show the variation of S-and P-wave velocities versus time during MICP treatment for the 50/70 and 20/30 sands treated with 0.1 M $CaCl_2$ cementation medium. S-wave velocities for both sands show an increase following each injection of the cementation medium. By the end of the MICP treatments, the S-wave velocities increased by an average of 1.8 times for the 50/70 sand and 2.6 times for the 20/30 sand. After the end of treatment, the P-wave velocities increased by an average of 8.7% for the 50/70 sand and 10.5% for the 20/30 sand. The smaller increase of P-wave velocity compared to the S-wave velocity may be attributed to the dominant influence of the pore water on the bulk modulus of saturated specimens. The variation of the S-wave velocity during treatment shown in Figure 4.3 agrees well with the trend shown in DeJong et al. (2010b).

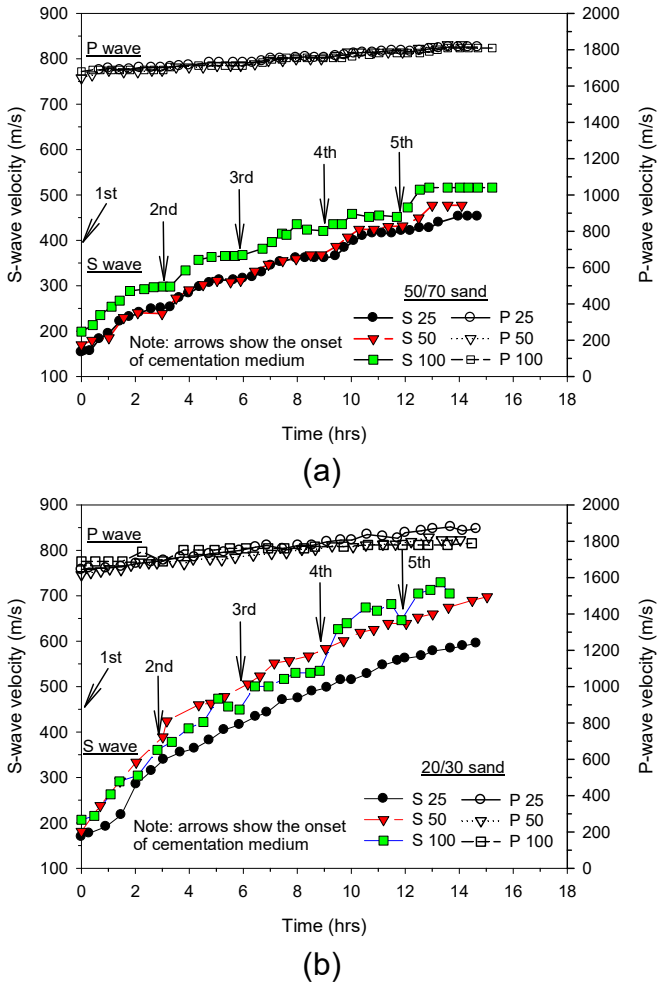

Figure 4.3. S-and P-wave velocities versus time during MICP treatment: (a) for 50/70, and (b) 20/30 sands. Numbers in the legend are effective confining pressures in kPa.

Consolidated Drained Sand Behavior

The deviator stress versus axial strain for untreated specimens under 25, 50, and 100 kPa effective confining pressures reveal strain hardening behavior for both sands (Figure 4.4a and b). However, the deviator stress versus axial strain curves of the 0.1 M $CaCl_2$ / MICP-treated specimen show strain softening behavior, with a post-peak strength decrease. A comparison of untreated and 0.1 M $CaCl_2$ / MICP-treated

specimen indicates that the peak strength of MICP-treated specimen increased by an average of 93% for the 50/70 sand and 171% for the 20/30 sand compared to the peak strength of the untreated specimen. The ultimate strength (defined as the deviator stress at strains ≥ 10%) for both untreated and 0.1 M $CaCl_2$ / MICP-treated specimens are approximately the same for the 50/70 sand. However, the ultimate strength of 0.1 M $CaCl_2$ / MICP-treated 20/30 sand for the three confining pressures ranges from 14% to 41% higher than that of the untreated specimens. This increase in ultimate strength could be attributed to residual cohesion in the MICP-treated 20/30 sand, as discussed later in this section, similar to the observation reported by Clough et al. (1981) for sands modified by Portland cement.

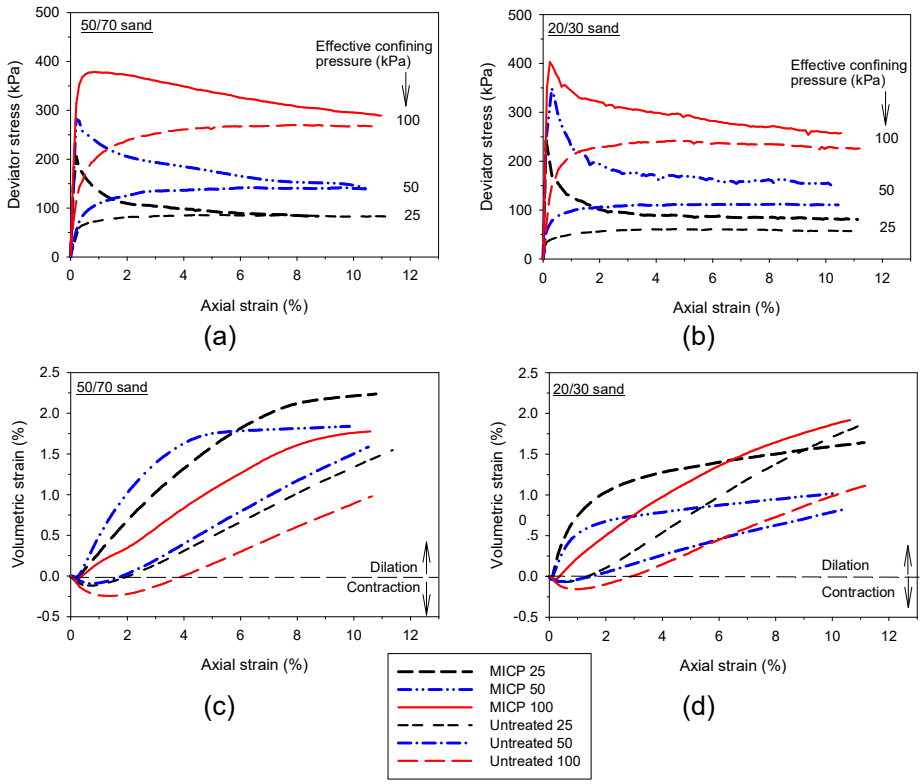

Figure 4.4. Consolidated drained triaxial test results: (a) stress-strain for 50/70 sand, (b) stress-strain for 20/30 sand, (c) volumetric strain for 50/70 sand, and (d) volumetric strain for 20/30 sand.

Figure 4.4c and d present the volumetric strain versus axial strain behavior for 50/70 and 20/30 sands. MICP treatment with 0.1 M $CaCl_2$ significantly increase the dilatancy of both sands. The 0.1 M $CaCl_2$ / MICP-treated specimen experienced less contraction at small strains (in some cases almost no contraction is observed) followed by more dilation at large strains than the untreated specimens. Observation of the specimens failure mode revealed bulging failures for the untreated specimens and localized shear-band failures for the 0.1 M $CaCl_2$ / MICP-treated specimens.

The Mohr-Coulomb friction angle and cohesion were calculated from the triaxial tests results. The peak (equal to ultimate) friction angles are 35° and 32° for untreated 50/70 and 20/30 sands, respectively. For samples treated with 0.1 M $CaCl_2$, the peak friction angles are 32° for the 50/70 sand and 31° for the 20/30 sand with associated cohesions of 41 and 58 kPa for 50/70 and 20/30 sands, respectively. In addition, the ultimate friction angles are 36° for the 50/70 sand and 33° for the 20/30 sand. The cohesions at the ultimate strength were 1 and 7 kPa for MICP-treated 50/70 and 20/30 sands, respectively. These friction angles of MICP-treated sands are similar to those of untreated sands. However, the cohesion increased after MICP treatment, showing residual cohesion at ultimate state. A similar residual cohesion was reported by Clough et al. (1981) for sands treated by Portland cement as discussed before.

The initial tangent Young's moduli (E_i) were calculated from stress-strain curves. These E_i values are presented in Figure 4.5a. E_i as a function of confining pressure was evaluated using the power function suggested by Janbu (1963) (Equation 4-3), where P_a is the atmospheric pressure, k is the modulus number and n is the modulus exponent.

$$E_i = kP_a\left(\sigma_3/P_a\right)^n \qquad \text{Equation 4-3}$$

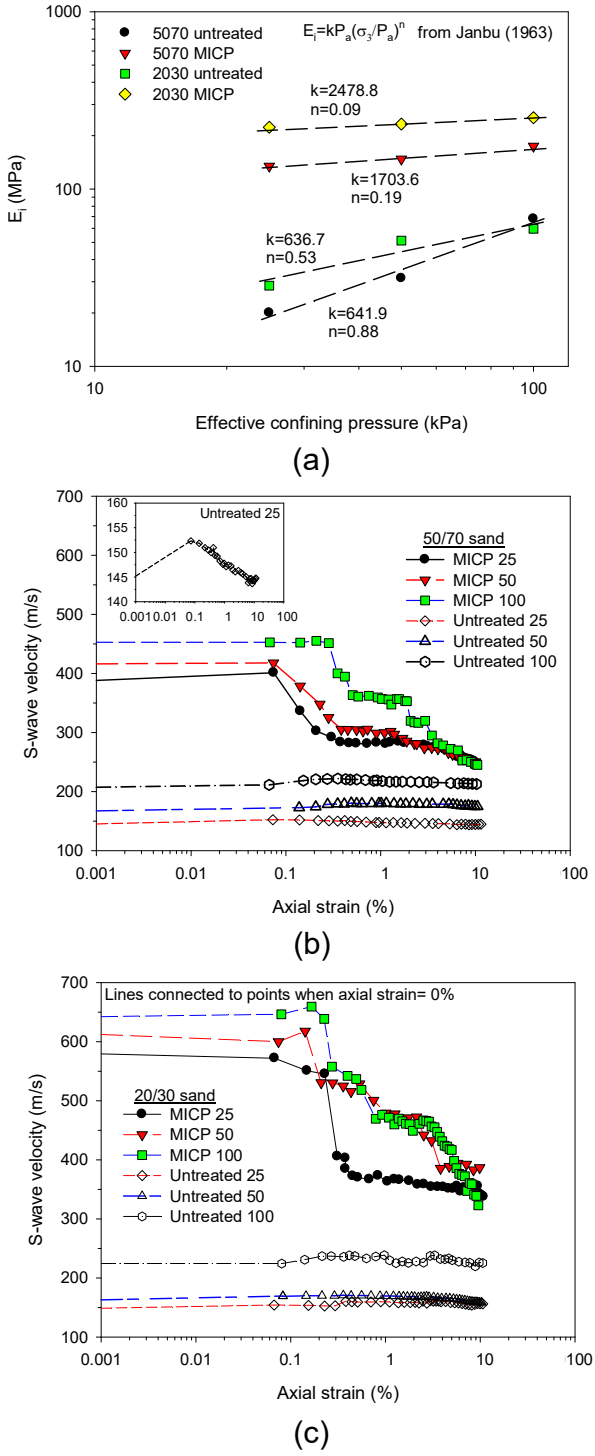

Figure 4.5. Stiffness during shear loading for specimens treated with 0.1 M $CaCl_2$ cementation medium: (a) initial tangent modulus, (b) S-wave velocity of 50/70 sand, and (c) S-wave velocity of 20/30 sand. Numbers in the legend are effective confining pressures in kPa.

Figure 4.5a shows that the modulus exponent (n) of the untreated sand was 0.53 for the 20/30 sand and 0.88 for the 50/70 sand. For the 0.1 M $CaCl_2$ / MICP-treated sands, n decreased to 0.09 for the 20/30 sand and to 0.19 for the 50/70 sand. These values of n indicate that E_i of MICP-treated sands are less sensitive to the change of confining pressure (within the tested range) than untreated sands and may be largely controlled by the level of $CaCO_3$ cementation. The results of initial modulus trend as a function of effective confining pressure presented in Figure 4.5a are consistent with information provided by Clough et al. (1981) on naturally-cemented soils and sands cemented by Portland cement and those reported by Yun et al. (2007) on hydrate bearing sediments.

S-Wave Velocity During Shear Loading

Figure 4.5b and c present the S-wave velocities of the untreated and 0.1 M $CaCl_2$ / MICP-treated 50/70 and 20/30 sands during triaxial compression loading. The S-wave velocities at axial strains of 0% and 0.07% were connected with straight lines in these figures based on the assumption of constant small-strain stiffness (Clayton 2011). The S-wave velocities were essentially constant for the untreated specimens. A reduction of S-wave velocities in the 0.1 M $CaCl_2$ / MICP-treated specimens was observed starting at an axial strain between 0.1% and 0.2% in both sands. At an axial strain of approximately 10%, the S-wave velocities decreased by an average of 170 m/s and 265 m/s for 50/70 and 20/30 sands, respectively, which is an average decrease by 41% and 43%, respectively. The small figure included in Figure 4.5b shows the change of S-

wave velocities for untreated 50/70 sand at a confining pressure of 25 kPa (a change of less than 10 m/s). While the S-wave velocities of the 0.1 M $CaCl_2$ / MICP-treated specimens decreased towards the values for the untreated specimens, the S-wave velocities in the treated specimens at an axial strain of 10% were still higher than that of untreated samples. This could be attributed to $CaCO_3$ cementation away from the localized shear-band failure zones observed in the treated specimens. This response is similar to the S-wave degradation behavior reported by Tatsuoka and Shibuya (1991) on cement-treated sands.

$CaCO_3$ Content of Triaxial Specimens

Figure 4.6 presents the measured $CaCO_3$ content along the height of specimens treated with 0.1 M $CaCl_2$ for both sands. The average $CaCO_3$ contents of the 50/70 and 20/30 sands were 1.6% and 1%, respectively (Table 4.2). The finer grained 50/70 sand under 25 and 50 kPa confinement shows a gradient of $CaCO_3$ content along the height of the specimens. However, the 50/70 sand under 100 kPa confinement shows a parabolic shape with higher $CaCO_3$ content at the middle section. It should be noted that the void ratios of 50/70 sand specimens are similar under 25, 50, and 100 kPa confinement. The two types of $CaCO_3$ content profiles (linear and parabolic) are similar to those reported by Martinez et al. (2013). Martinez et al. (2013) reported that the $CaCO_3$ content profiles are generally determined by the microbe distribution along the specimen. Furthermore, the distribution of $CaCO_3$ along the 50/70 sand specimens may be affected by bio-clogging (i.e. a decrease in void ratio and hydraulic conductivity near

the solution injection and effluent points due to $CaCO_3$ precipitation). In contrast, the $CaCO_3$ content of the coarser, more permeable 20/30 sand has a uniform distribution along the height of the specimens.

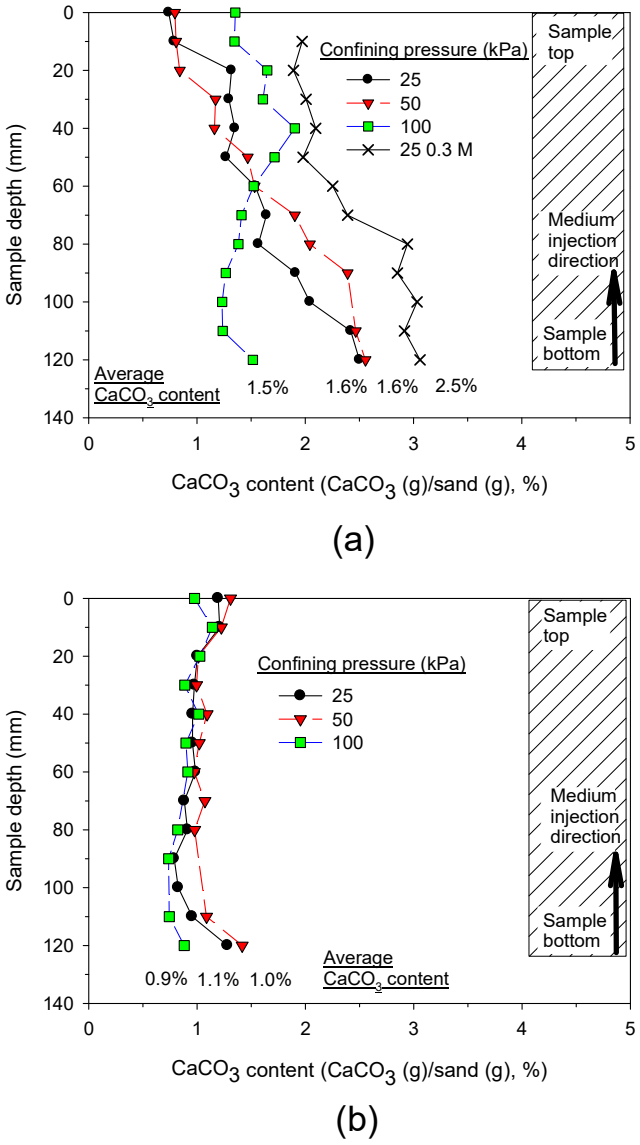

Figure 4.6. $CaCO_3$ content distribution of (a) 50/70 sand, and (b) 20/30 sand for specimens treated with 0.1 M concentration of $CaCl_2$ except where noted in the legend.

It is also worth noting that the 0.1 M $CaCl_2$ / MICP-treated 20/30 sand specimens have lower average $CaCO_3$ content (1%) compared to the 50/70 sand specimens (1.6%), which were treated using the same procedure and solution. The average increase in S-wave velocity, peak deviator stress and cohesion for the 0.1 M $CaCl_2$ / MICP-treated 20/30 sand (2.6 times, 171%, and 58 kPa, respectively) are higher than that of the 50/70 sand (1.8 times, 93% and 41 kPa, respectively). This demonstrates that the mechanical properties of MICP-treated sands are not only controlled by the average or bulk $CaCO_3$ content. The spatial distribution of $CaCO_3$ in the pore space (e.g. the effective $CaCO_3$ content at particle contacts), which is affected by factors such as particles size, pore size, particle surface area, and bacteria distribution, is an important factor controlling the properties of MICP-treated sands (Rebata Landa 2007; Cheng et al. 2013a; Martinez et al. 2013). It is also worth noting that unlike Whiffin et al. (2007) who reported a threshold calcium carbonate content of approximately 3.6% by weight before the unconfined compressive strength of MICP-treated sand started to increase, the results of triaxial tests presented in this paper show an increase of the soil strength in the 20/30 sand at 1% calcium carbonate content.

4.5.2 Sands Treated with 0.3 M $CaCl_2$

Effect of $CaCl_2$ Concentration

As discussed in the background section, Lin et al. (2015, 2016b and c) who investigated the effects of MICP treatment on the static axial capacity and soil-pile

interaction of pervious concrete piles reported that the $CaCO_3$ content surrounding the tested piles ranged from 0% to 3%. Therefore, the effects of $CaCO_3$ cementation levels on the 50/70 sand were investigated using cementation medium with 0.3 M $CaCl_2$ to target a $CaCO_3$ closer to 3%. Figure 4.6a shows the average $CaCO_3$ content of the triaxial specimens treated using 0.3 M $CaCl_2$ cementation medium. Using the same treatment procedure (5 flushes of the cementation medium), the average $CaCO_3$ contents of the specimens treated using the 0.3 M $CaCl_2$ concentration was 2.5%, which is higher than the 1.6% for the specimens treated with the 0.1 M $CaCl_2$ solution. The calculated yield of $CaCO_3$ (weight of precipitated $CaCO_3$ in the specimen / equivalent weight of $CaCO_3$ from the input cementation media) were 57% and 29% for the 50/70 sand specimens treated by 0.1 and 0.3 M $CaCl_2$, respectively, and 37% for 20/30 sand specimen treated by 0.1 M $CaCl_2$. To acquire a high yield efficiency (>80%), Al Qabany et al. (2012) reported that the threshold input rate of urea and $CaCl_2$ should be slow (lower than 0.042 mol/L/h). However, the urea and $CaCl_2$ input rates in our tests were 0.27 and 0.8 mol/L/h for specimens treated with 0.1 and 0.3 M $CaCl_2$, respectively, which were controlled by injecting 2 pore volumes of solution over an interval of 3 hours.

During treatment, the S-wave velocity of the specimens treated with 0.3 M $CaCl_2$ show an average increase by a factor of 5.5 compared to the untreated specimens, which is compared to a factor of 1.8 for specimens treated with 0.1 M $CaCl_2$ solution. It is worth mentioning, however, that there is no direct relationship between the S-wave

velocities and $CaCO_3$ contents (Al Qabany et al. 2011; Weil et al. 2011). The S-wave velocities versus $CaCO_3$ contents reported herein are in a good agreement with the results reported in the literature (Al Qabany et al. 2011; Weil et al. 2011). P-wave velocities of the specimens treated with 0.3 M $CaCl_2$ increased by an average of 10.1% relative to untreated specimens, which is compared to 8.7% increase for specimens treated with 0.1 M $CaCl_2$ solution.

Figure 4.7a compares the stress-strain responses of the 50/70 sand at a confining pressure of 25 kPa for specimens treated with 0.1 M and 0.3 M $CaCl_2$ solutions. At this confining pressure, the peak deviator stress of the specimens treated with 0.3 M $CaCl_2$ increased by an average factor of 4.8 relative to the untreated specimens, while the peak deviator stress of the specimens treated with 0.1 M $CaCl_2$ solution increased by a factor of 1.4. Furthermore, the specimens treated with the 0.3 M $CaCl_2$ solution showed a 45% increase in the deviator stress at an axial strain of 10% compared to the untreated specimens while the specimens treated with the 0.1 M $CaCl_2$ solution had essentially the same deviator stress at a strain of 10% compared to the untreated specimens. The higher ultimate deviator stress of the specimens treated with 0.3 M $CaCl_2$ could be attributed to the increased particle roughness due to the precipitated $CaCO_3$ (Montoya and DeJong 2015) and residual cohesion in the specimens (Clough et al. 1981).

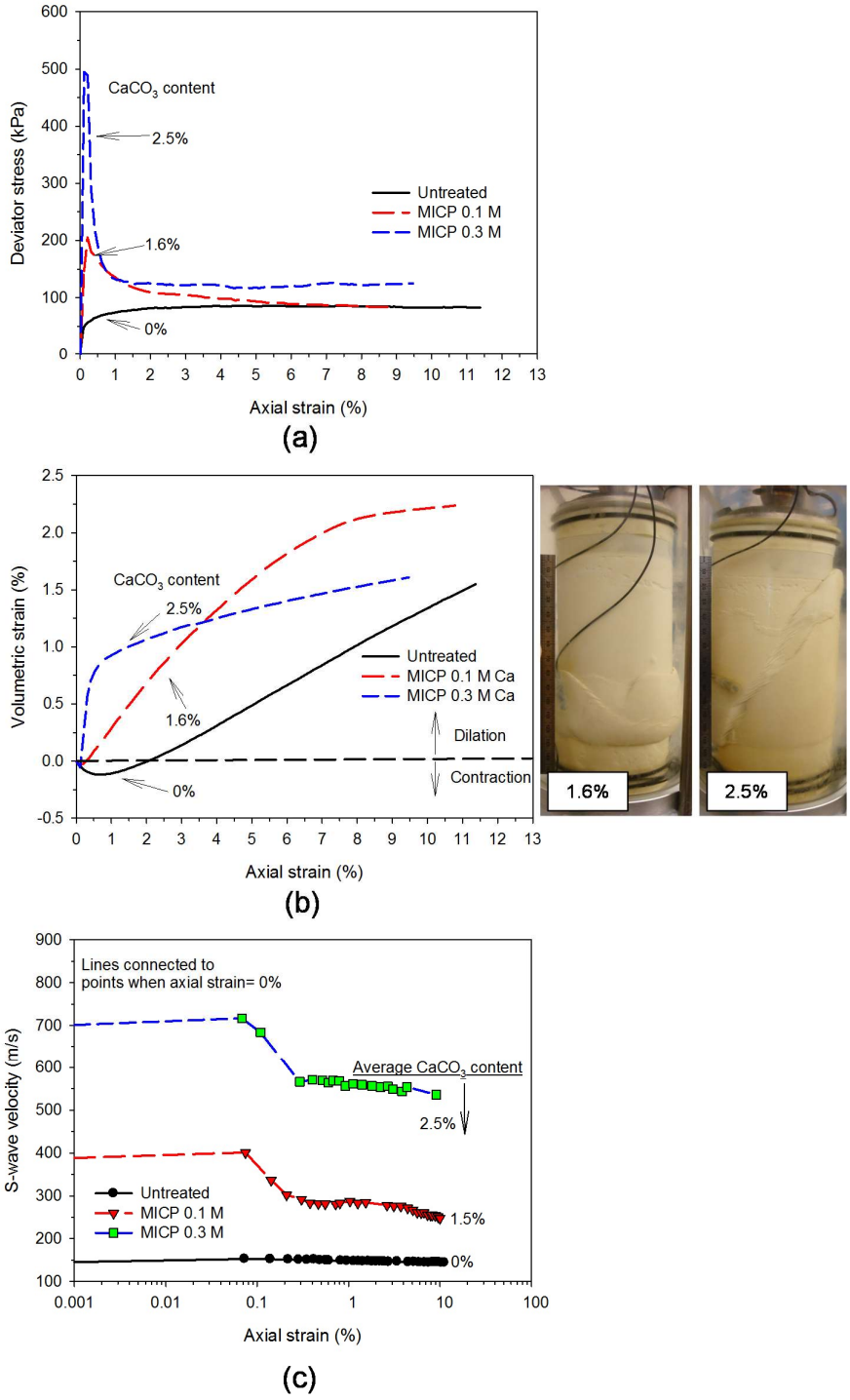

Figure 4.7. Effect of $CaCl_2$ concentration of cementation medium on consolidated drained triaxial test behavior of 50/70 sand at 25 kPa effective confining pressure: (a) stress-strain behavior, (b) volumetric strain, and (c) S-wave velocity during shear loading. The numbers in the legend are $CaCl_2$ concentrations.

The volumetric strain versus axial strain data presented in Figure 4.7b shows that the 50/70 specimens treated with MICP were more dilatant than the untreated specimens. It is worth noting that untreated specimens showed bulging failure, while, as $CaCO_3$ content increases, the specimens treated by MICP manifest more concentrated shear band failure, as shown in Figure 4.7b. The change of volumetric strain behavior may be controlled by the formation of the shear band. The shear band was more concentrated in the specimens with $CaCO_3$ content of 2.5% (0.3 M $CaCl_2$) than that with $CaCO_3$ content of 1.6% (0.1 M $CaCl_2$). At small strain, more dilation was experienced by the specimens with $CaCO_3$ content of 2.5% (0.3 M $CaCl_2$) than by the specimens with $CaCO_3$ content of 1.6% (0.1 M $CaCl_2$). As the strain increased, the soil particles movement is localized to the shear band, resulting in smaller volume change than that of the specimens with 0.1 M $CaCl_2$. Similar shear band formation at high $CaCO_3$ cementation level was also recently reported by Montoya and DeJong (2015).

Using the measured S-wave and P-wave velocities, the Poisson's ratio of the specimens can be calculated using Equation 4-4.

$$\frac{V_p}{V_s} = \sqrt{\frac{M}{G}} = \sqrt{\frac{2(1-\upsilon)}{1-2\upsilon}} \qquad \text{Equation 4-4}$$

where V_p and V_s are the P-wave and S-wave velocities, G, M are shear and constrained moduli, and υ is the Poisson's ratio. The initial (before treatment) Poisson's ratio was 0.496. After MICP treatment, the Poisson's ratio decreased to 0.467 and 0.435 for the 50/70 sand treated by 0.1 M and 0.3 M $CaCl_2$, respectively. The Poisson's ratios at the end of the testing (axial strain ~10%) were 0.486 and 0.440 for the 50/70 sand

treated by 0.1 M and 0.3 M $CaCl_2$, respectively. These results suggest that the specimens treated with 0.3 M $CaCl_2$ experienced less lateral deformation (e.g. less volume change at the same axial strain) than that of the specimens treated with 0.1 M $CaCl_2$.

During triaxial compression loading, a similar degradation of S-wave velocity was observed in the specimens treated with 0.3 M $CaCl_2$, compared to the specimen treated with 0.1 M $CaCl_2$, as shown in Figure 4.7c. However, the S-wave velocity at an axial strain of 10% was still substantially higher in the specimens treated with 0.3 M $CaCl_2$ solution compared to either the specimens treated with 0.1 M $CaCl_2$ solution or the untreated specimens. Higher S-wave velocity at 10% axial strain in the specimens treated with 0.3 M $CaCl_2$ could be mainly attributed to the non-fractured bonding between soil particles away from the concentrated shear band shown by the pictures in Figure 4.7b.

4.6 CONFINED COMPRESSION TESTS

Confined compression tests were also performed on untreated and MICP-treated sands. S-wave velocities in both the vertical direction (V_v) and the horizontal direction (V_{vh}) were measured. The $CaCO_3$ content of the MICP-treated confined compression specimens was measured in a similar manner as for the triaxial test specimens. The $CaCO_3$ content of the 50/70 sand was 1.4% when treated with 0.1 M $CaCl_2$ solution and 2.6% when treated with 0.3 M $CaCl_2$ solution. The $CaCO_3$ content

of the 20/30 sand was 0.6% when treated with 0.1 M $CaCl_2$ solution and 1.6% when treated with 0.3 M $CaCl_2$ solution (Table 4.3). The comparison between Table 4.2 and Table **4.3** shows that the $CaCO_3$ contents measured from confined compression tests were lower (with a difference ranging from 0.2% to 0.4%) than that measured from triaxial tests using the same treatment procedure. This difference could be attributed to the pore size distribution, bacteria distribution and urease activity along the sample, and their influence on $CaCO_3$ distribution (Rebata Landa 2007; Cheng and Cord-Ruwisch 2013b; Martinez et al. 2013). In addition, the observed higher cementation levels around the inlets or outlets of the triaxial specimens could be another reason for this difference.

Figure 4.8a and b show the variation of void ratio as a function of vertical effective stresses for treated and untreated specimens of both sands. The MICP-treated specimens are less compressible compared to the untreated specimens and the specimens with higher $CaCO_3$ content are less compressible than the specimens of the same grain size with lower $CaCO_3$ content. The results of void ratio versus vertical effective stresses are in good agreement with the results reported by Feng and Montoya (2014). The calculated compression index (C_c) of 50/70 sand decreased from 0.024 (0% $CaCO_3$ content) to 0.009 (2.6% $CaCO_3$ content). The calculated compression indexes (C_c) of 20/30 sand decreased from 0.019 (0% $CaCO_3$ content) to 0.009 (1.6% $CaCO_3$ content). This decrease of compression index is similar to that of residual soils treated by MICP before the fracture of $CaCO_3$ bonds presented by Lee et al. (2013).

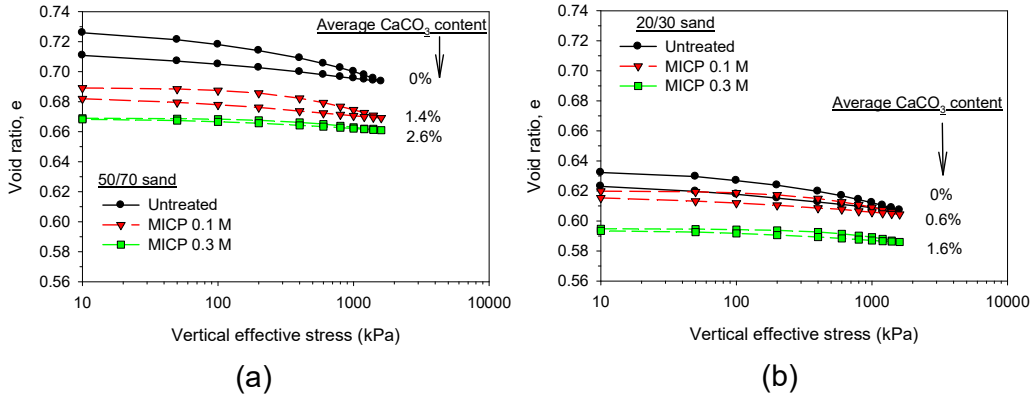

Figure 4.8. Confined compression test results for 50/70 and 20/30 sands: (a) compressibility for 50/70 sand, and (b) compressibility for 20/30 sand.

Figure 4.9a, b, c, and d present the variation of normalized S-wave velocities (S-wave velocity divided by initial S-wave velocity) for the horizontal and vertical directions as a function of vertical effective stress (σ'_v). The untreated specimens show confined compression behavior characteristic of sand, with the normalized S-wave velocities increasing as the vertical effective stress increases and then decreasing during unloading, though with some hysteresis (i.e. normalized S-wave velocities are higher after unloading than during initial (virgin) loading for the same vertical effective stress). The MICP-treated specimens have higher initial normalized S-wave velocities than that of untreated specimens and show a different pattern. For the specimens treated with 0.1 M $CaCl_2$ and thus with the smaller amounts of $CaCO_3$ content (the 50/70 sand with 1.4% and the 20/30 sand with 0.6%), there was initially no hysteresis and then a lower shear wave velocity at the same effective stress during unloading as in the loading phase

(trending towards the same value as for the untreated specimen after unloading). For the specimens treated with 0.3 M $CaCl_2$ and thus with greater amounts of $CaCO_3$ (the 50/70 sand with 2.6% and the 20/30 sand with 1.6%), there was no hysteresis for the shear wave velocity in the horizontal direction and less hysteresis for the vertical direction shear wave velocity during unloading compared to the shear wave velocity of specimens treated with 0.1 M $CaCl_2$ solution.

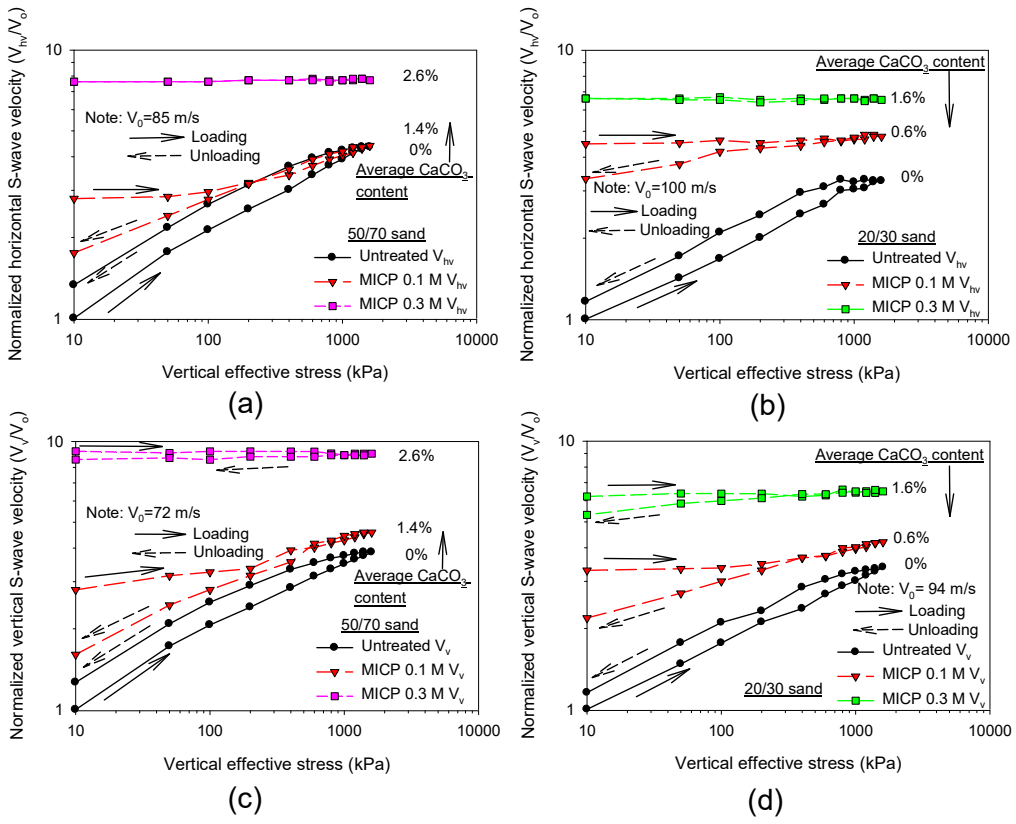

Figure 4.9. Confined compression test results for 50/70 and 20/30 sands: (a) V_{hv} for 50/70 sand, (b) V_{hv} for 20/30 sand, (c) V_v for 50/70 sand, and (d) V_v for 20/30 sand. V_{hv} is the S-wave velocity transmitted in horizontal direction with vertical polarization and V_v is the S-wave velocity transmitted in vertical direction as show in Figure 2c.

The measured S-wave velocity as a function of vertical effective stress for both MICP-treated sands were compared to the loose Nevada sand modified using Portland cemented (Yun and Santamarina 2005). The comparison shows similar trends of S-wave velocities as the effective stress increases. However, the sudden change of S-wave velocity as the stress increases in samples treated with Portland cement was not observed in MICP-treated sand specimens. This could be attributed to the higher void ratio (e_o= 1.1) of the loose Nevada sand, which may induce collapse during loading as

discussed by Feng and Montoya (2014). Furthermore, small-strain shear modulus can be calculated using the measured S-wave velocity (Equation 4-5).

$$G = \rho_{sat} \times v_s^2 \qquad \text{Equation 4-5}$$

where ρ_{sat} is the saturated density of sand. The calculated small-strain shear modulus versus vertical effective stress on log-scale for 50/70 sands is similar to that reported by Montoya et al. (2013) for untreated, and MICP moderately-treated specimens with $CaCO_3$ content of ~2.6%.

4.7 MICRO-SCALE PROPERTIES OF MICP-TREATED SANDS

The SEM and EDS images from the triaxial test specimens are shown in Figure 4.10. To investigate a similar range of $CaCO_3$ contents (0 to ~3%) reported by Lin et al. (2015, 2016b and c), the specimens treated by 0.3 M $CaCL_2$ was also investigated by SEM and EDS images. The images of MICP-treated 50/70 and 20/30 samples subjected to 0.1 M $CaCl_2$ treatment (1.6% $CaCO_3$ content for 50/70 sand and 1% $CaCO_3$ content for 20/30 sand) show $CaCO_3$ precipitated at particle contacts and coating particle surfaces. As the $CaCl_2$ treatment concentration increases from 0.1 M and 0.3 M, the images of the MICP-treated 50/70 sands show an increase in the $CaCO_3$ content (area increased shown in EDS Ca element mapping) consistent with the $CaCO_3$ content measurement ($CaCO_3$ content increased from 1.6% to 2.5%).

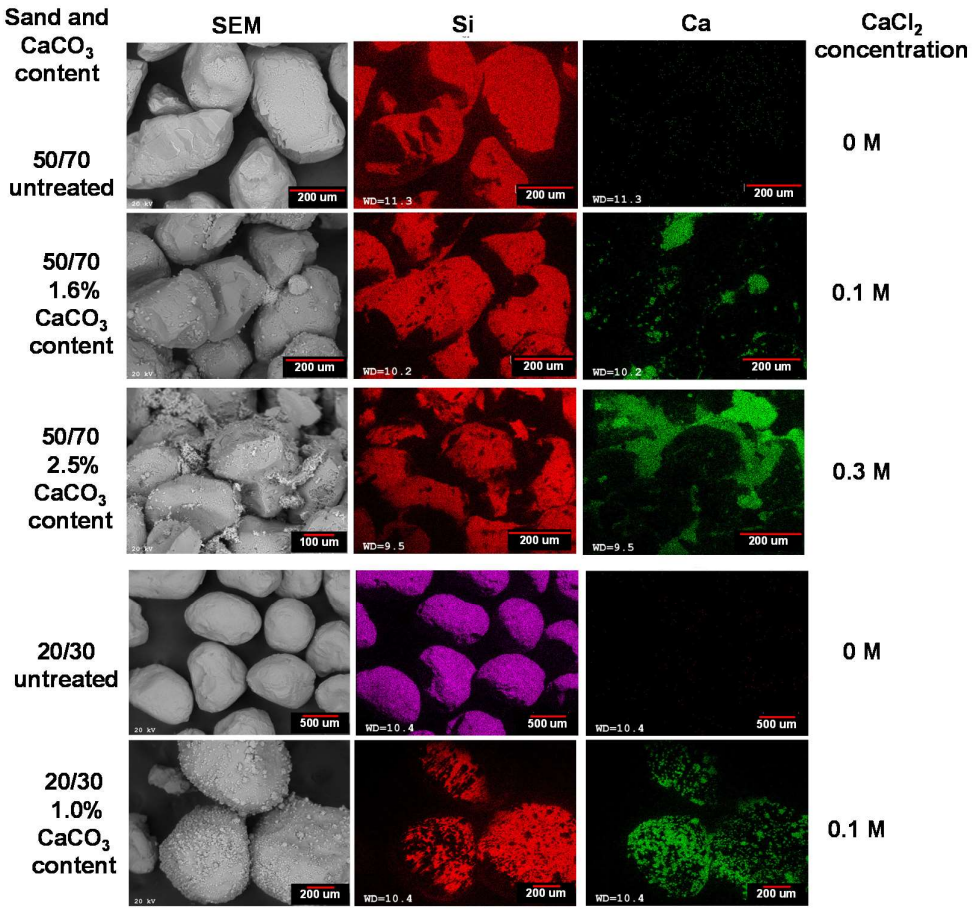

Figure 4.10. Scanning Electron Microscopy (SEM) and Energy-Dispersive X-ray Spectroscopy (EDS) images of untreated and MICP-treated samples for 50/70 and 20/30 sands.

Based on the shape of the $CaCO_3$ crystals in Figure 4.11a, b, and c, two types of $CaCO_3$ morphologies, calcite and vaterite crystals, are present in both the 50/70 and 20/30 sands. In the 20/30 sand, smaller sand particles (~400 μm) can be seen in Figure 4.11b and c filling the pore space created by larger particles. Figure 4.11d, e, and f show that all three of the idealized $CaCO_3$ distributions shown in Figure 4.1 have occurred in the treated specimens, i.e. $CaCO_3$ can be seen to be deposited at particle contacts (contact cementing, Figure 4.1a), coating particles (grain coating, Figure 4.1b), and

growing into the pore space to create cement bridges in the sand matrix (matrix supporting, Figure 4.1c).

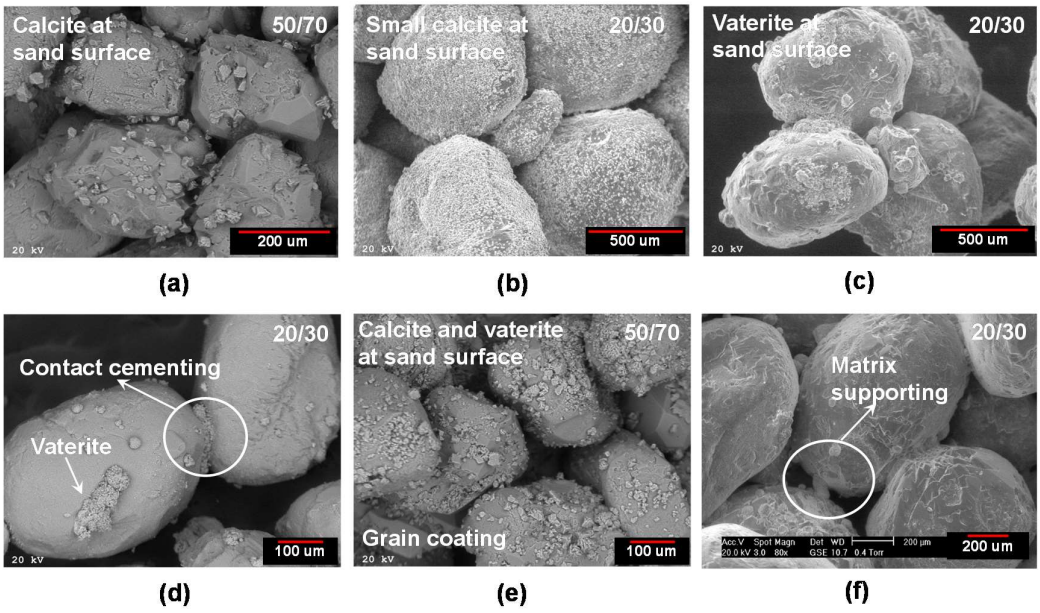

Figure 4.11. SEM images showing $CaCO_3$ morphologies and spatial distributions of $CaCO_3$ around sand surface.

4.8 CONCLUSIONS

This paper describes an investigation into the mechanical behavior of MICP-treated Ottawa 20/30 and 50/70 silica sands using drained triaxial and confined compression tests with P-wave and S-wave velocity measurements. Data on the micro-scale $CaCO_3$ distribution from SEM and EDS images are also presented herein. The tests results reported in this paper will be employed to further investigate the use of MICP modification and the effects of $CaCO_3$ content on improving the static axial capacity and soil-pile interaction of permeable piles. Based on the data presented in this paper, the following observations were made and conclusions were drawn:

1. The S-wave velocity was used to monitor MICP cementation during treatment and loading phases. Although no direct relationship was established between the S-wave velocity and $CaCO_3$ content, the S-wave velocity increases as the $CaCO_3$ content increases. During loading in triaxial tests, S-wave velocity shows degradation as the axial strain increases. Combining measured S-wave and P-wave velocities, the Poisson's ratio was calculated and shows a decrease as $CaCO_3$ content increases.
2. During triaxial tests, the peak deviator stress of the Ottawa 20/30 sand with $CaCO_3$ content of 1.6% and the Ottawa 50/70 sand with $CaCO_3$ content of 1% increased by an average of 93% and 171%, respectively, compared to their corresponding untreated specimens. MICP treatment can be seen to significantly increase the dilatancy of both sands. Observation of the failure mode reveals bulging failures for the untreated specimens. As $CaCO_3$ content increases, the peak strength increases and more concentrated shear band has formed, resulting in higher dilation at small strain and lower dilation at large strains.
3. Triaxial results show that initial tangent Young's moduli (E_i) of MICP-treated sands are controlled by the $CaCO_3$ content and are less sensitive to the increase of the effective confining pressure than untreated specimens. In confined compression tests, as the $CaCO_3$ content increases, the stiffness of the specimens increase and becomes less sensitive to the increase in normal stress.

4. Although the 20/30 sand had a lower $CaCO_3$ content compared to 50/70 sand when treated using a 0.1 M $CaCl_2$ solution, the increase of S-wave velocity, peak shear strength and cohesion for the MICP-treated 20/30 sand were higher than that of the MICP-treated 50/70 sand. This indicates that the strength and stiffness of MICP-treated sands are controlled by factors other than the average or bulk $CaCO_3$ content of the specimens, e.g. by the effective $CaCO_3$ content at particle-contacts.
5. The MICP-treated specimens are less compressible than untreated specimens. As the $CaCO_3$ content increases, the compressibility of the treated soil specimens decreases. As $CaCO_3$ content increases, the S-wave velocity shows less decrease or no change as the normal stress increase, and there is less hysteresis for the S-wave velocity upon unloading.
6. SEM and EDS images show that the three idealized $CaCO_3$ distributions can occur in the treated specimens, i.e. $CaCO_3$ can deposit at particle contacts (contact cementing), coat particles (grain coating), and grow into the pore space (matrix supporting).

5. ENANCING THE AXIAL PULL-OUT RESPONSE OF PERVIOUS CONCRETE GROUND IMPROVEMENT PILES USING BIO-GROUTING

5.1 INTRODUCTION

Post-grouting methods have been utilized successfully to increase shaft and/or tip resistances of ground improvement and foundation systems (Gouvenot and Gabiax 1975; Bruce 1986a and b; Plumbridge and Hill 2001). Constructing grouted foundations involves injecting pressurized grout through a proprietary system consisting of pipes that are attached to the steel cage and/or a base grouting plate at the tip, creating a grouted zone along the shaft or below the tip (Plumbridge and Hill 2001; Ruiz and Pando 2009; Fattahpour at al. 2015). For drilled shafts, post-grouting has successfully utilized to improve the tip resistance for foundations. However, the application of grouting along the shaft of deep foundations in the U. S. is not commonly used due to the complex injection technique and difficult quality control (Joer et al. 1998; Thiyyakkandi et al. 2013; Fattahpour et al. 2015). To explore the possibility of bio-grouting, Lin et al. (2016b and c) presented an innovative grouted ground improvement pile alternative, bio-grouted permeable piles (pervious concrete piles), focusing on their response when subjected to axial compression. This paper focuses on investigating the responses of bio-grouted pervious concrete piles under axial pull-out loading.

The bio-grouting process relies on microbially induced carbonate precipitation (MICP) process to induce calcium carbonate ($CaCO_3$) precipitation (Stocks-Fischer et al. 1999; Ivanov and Chu 2008; van Paassen 2009; Mortensen et al. 2011; Burbank et al. 2013; DeJong et al. 2013; Lin et al. 2016b). MICP grouting process could realize similar outcome to the cement-based grouting along the shaft and at the tip of permeable piles using a simple percolation process (Lin et al. 2015 and 2016a). The bio-grouting process show a potential of offering a cost-effective and lower environmental-impact solution to enhance the response of ground improvement and foundation systems (Ivanov and Chu 2008; Suer et al. 2009). In addition, enhancing the mechanical response of permeable piles using MICP bio-grouting requires only a limited zone of soil improvement around the pile, mitigating the practical difficulty of bio-clogging encountered in mass soil stabilization using MICP (van Paassen et al. 2010b; Cheng and Cord-Ruwisch 2013).

This paper describes the instrumentation and results of two axial pull-out pervious concrete pile tests with and without bio-grouting.

5.2 BACKGROUND

Pull-out loading is experienced in many practical cases including transmission towers, jetties, and mooring system for ocean surface or submerged platforms, etc. (Gouvenot and Gabiax 1975; Vanitha et al. 2007). Post-grouting has been utilized to improve the performance of foundations subjected to axial pull-out loading and their

safety and economy (Gouvenot and Gabiax 1975; Joer et al. 1998). However, post-grouting is mainly used to enhance tip resistance with very limited cases to improve shaft resistance due to the complex injection technique, difficult quality control, and proprietary systems (Joer et al. 1998; Thiyyakkandi et al. 2013; Fattahpour et al. 2015). This paper focuses on bio-grouting of permeable piles to improve the shaft resistance utilizing simple percolation injection.

5.2.1 Bio-Grouted Pervious Concrete Pile Alternative

Pervious concrete is a special single-size aggregate concrete with high porosity and permeability (Suleiman et al. 2014). Recently, pervious concrete pile has been successfully investigated to serve as an innovative ground improvement alternative (Suleiman et al. 2014). Based on the experimental results, the axial-compression behavior of pervious concrete piles showed higher strength and stiffness than that of an identical granular column, while having similar permeability coefficient (Suleiman et al. 2014; Ni et al. 2016). This high permeability of pervious concrete piles allows for easy grouting along the pile shaft and at the tip of the pile without the need of using complex proprietary injection systems by percolation of a low viscosity bio-grout (i.e., without applying pressure).

MICP bio-grouting involves a microbially-regulated process of $CaCO_3$ precipitation to cement soil particles and clog pore space, improving strength, stiffness, volume-dilatancy, and reducing permeability of the soil matrix (Ferris, et al. 1996;

Stocks-Fischer et al. 1999; DeJong et al. 2006; Whiffin et al. 2007; Al Qabany and Soga 2013; Soon et al. 2014; Montoya and DeJong 2015; and Lin et al. 2016b). The bio-grouted pervious concrete pile alternative avoids the limitation of bio-clogging by focusing on improving a limited zone (or $CaCO_3$ cemented zone) along the pile, which will enhance the response of the bio-grouted pile system when subjected to axial pull-out loading.

5.2.2 Financial and Environmental Impact of MICP Bio-Grouting

Studies comparing MICP bio-grouting with jet or chemical grouting showed that bio-grouting is more cost-effective and have a lower environmental impact than jet grouting (Ivanov and Chu 2008; and Suer et al. 2009). Suer et al. (2009), who also carried out a life cycle assessment on a real project to analyze the environmental and economic impacts of MICP and jet grouting, concluded that the total energy used for MICP (3 GJ per m^3 of soil) was half of that used for jet grouting (6 GJ per m^3 of soil), with MICP costing 55% of jet grouting. This difference is mainly attributed to the use of heavier equipment, large amount of spoil waste and related transportation of jet grouting. It was also noted that the byproducts of MICP bio-grouting (e.g. ammonium cation and chloride ion with high pH of approximately 9) may affect groundwater and soil ecosystem, which still lacks a thorough investigation.

5.2.3 Objectives and Methodology

The objective of this paper is to evaluate the use of bio-grouting for enhancing the response of permeable foundations subjected to axial pull-out loading. To achieve this goal, two instrumented pervious concrete pile tests were performed at the Soil-Structure Interaction (SSI) testing facility at Lehigh University. Tests No. 1 was performed without MICP bio-grouting and Tests No. 2 with MICP bio-grouting. The pile and surrounding soil were instrumented using strain gauges and bender elements. The responses of the pile and surrounding soil without MICP bio-grouting and with MICP bio-grouting were analyzed and compared. Soil samples after the tests were analyzed for moisture and $CaCO_3$ contents, and the crystal formation at particle-scale using Scanning Electron Microscope (SEM) were also characterized.

5.3 MATERIALS AND PREPARATION METHODS

5.3.1 Soil Properties

The bar sand was used for the tests. Its particle size distribution curve is shown in Figure 5.1a, which is classified as poorly graded sand (SP) using the Unified Soil Classification System. The minimum and maximum unit weights of sand at oven-dry condition are 14.54 kN/m^3 and 16.75 kN/m^3, respectively (maximum void ratio of 0.79 and a minimum void ratio of 0.55) (ASTM D4253 2009a and ASTM D4254 2009b). The sand placed in the soil box (introduced next in the section of testing facility) had

an average unit weight of 15.1 kN/m^3, relative density of 29% and water content of 0.4%, which were measured by a nuclear density gauge (Humboldt HS-13 5001EZ). A series of consolidated drained (CD) triaxial tests with different confining pressures (25, 50, and 100 kPa) were performed to characterize the soil mechanical properties. The triaxial samples (70-mm-diameter, length-diameter ratio: 2:1) were prepared at the smae relative density of the sand in the soil box (i.e., 29% relative density, or unit weight of 15.1 kN/m^3). The measured deviator stress-axial strain and volume change during the CD triaxial tests are presented in Figure 5.1b. The initial soil modulus (E_i) was evaluated as a function of confining pressure (σ_3) as $E_i=kP_a(\sigma_3/P_a)^n$ (Janbu, 1963), where P_a is the atmospheric pressure of 101 kPa and k and n are calculated as 401.6 and 0.48, respectively (Figure 5.1b). The K_f line presented in Figure 5.1c indicates that the peak friction angle of the soil equals to 38°.

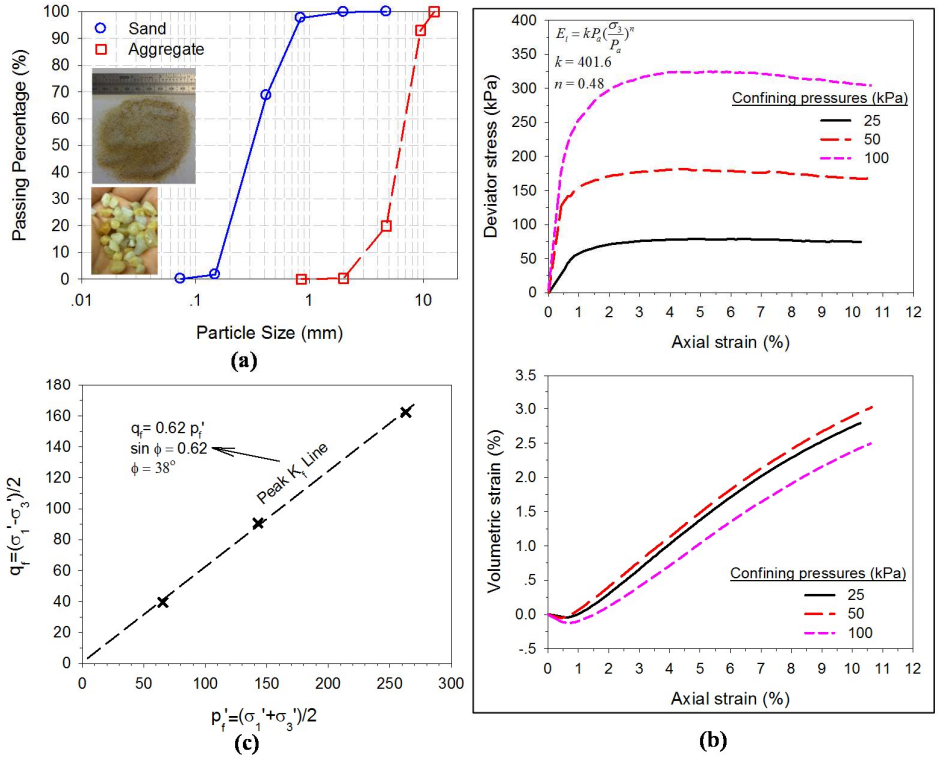

Figure 5.1. Material properties: (a) gradation of aggregate used for casting test piles and of soil used in the soil box; (b) stress-strain and volumetric strain of sand samples without bio-grouting under CD triaxial tests; (c) p_f'-q_f diagram at peak stresses of soil samples.

5.3.2 Pervious Concrete Properties

A series of pervious concrete mixtures were tested by Suleiman et al. (2014) to acquire adequate compressive strength and permeability for ground improvement and foundation applications. A pervious concrete mixing recipe based on the previous results was selected to cast the pile for the bio-grouting tests. The mixture used a 0.275 water/cement ratio, a 7% sand/aggregate ratio, 377 kg/m^3 cement, and 1,497 kg/m^3 coarse aggregate. Aggregate (pea river gravel) was washed and sieved, and the portion passing through a 9.5 mm sieve and retained on a No. 4 (4.75-mm) sieve was used

(Figure 5.1a). Five seconds of vibration compaction per layer was used to compact the pervious concrete samples. For this research, one pervious concrete pile and several cylindrical samples were prepared. The cylindrical samples were used to measure the porosity, permeability, compressive strength, and split tensile strength. The compressive strength was determined using ASTM C39 (ASTM 2009c), the permeability was measured using an in-house designed falling-head permeameter, the porosity was measured using ASTM C1688 (ASTM 2009d), and the split tensile strength was measured using ASTM C496 (ASTM 2009e). The pervious concrete samples have an average porosity of 19%, a permeability coefficient of 0.3 cm/s, a 28-day compressive strength of 18.5 MPa, and a split tensile strength of 1764 kPa. These properties are similar to those reported by Lin et al. (2016), Suleiman et al. (2014) and Ni et al. (2015) for pervious concrete piles with and without MICP bio-grouting.

5.3.3 Bacteria Preparation and MICP Recipes

The bacterial strain *Sporosarcina pasteurii* (*S. pasteurii*, ATCC 11859) was used for the tests. A stock culture of *S. pasteurii* was innoculated into a growth media (10 g yeast extract and 5 g ammonium sulfate in 500 mL 0.13 M Tris Buffer (pH=9.0) sterilized by filtration) until optical density (OD_{600}) reached 0.8~1, corresponding to a bacteria density of 1.5×10^7cells/mL. The bacteria were then harvested and centrifuged. The bacteria were stored at 4^{o}C until used. The detailed information of bacteria preparation can be found from Lin et al. (2016a).

During the test, the MICP recipes include urea medium (20 g urea, 2.12 g $NaHCO_3$, 20 g NH_4CL and 3 g Nutrient Broth in 1 L deionized water at pH=6) and cementation medium (urea medium with 300 mM $CaCl_2$) to induce $CaCO_3$ precipitation. Before MICP bio-grouting treatment, bacteria were suspended into urea medium to a bacteria density of 5×10^7 cells/mL. The treatment procedure is discussed in further details later in the paper.

5.4 TESTING FACILITY AND INSTRUMENTATION

A test soil box with dimensions of 1.1×1.1×1.2 m at the Soil-Structure Interaction (SSI) facility of Lehigh University was utilized for the two axial pull-out load tests.

The setup of the tests and detailed instrumentation are shown in Figure 5.2 and Figure 5.3. For both tests, one pervious concrete pile with a diameter of 76 mm and a length of 1.08 m was casted and utilized. Pile length of 927 mm was embedded in sand (Figure 5.2). A threaded rebar (9.5 mm in diameter) was placed along the center of the pile during concrete casting for strain gauge measurement and pile attachment to the load cell. During the test preparation, the pile was attached to the load cell first as shown in Figure 5.3a. The bar sand was then rained into the soil box using the soil raining system (Lin et al. 2015; and Ni et al. 2016). As shown in Figure 5.2a, five strain gauges were installed along the threaded rebar at depths of 0, 203, 406, 609, and 812 mm below

the soil surface. Bender elements which were fabricated in-house, were installed in the soil box to monitor S-wave velocities during MICP bio-grouting treatment. As shown in Figure 5.3b, bender elements sensors No. 2, 6, and 8 were placed at soil depth of 458 mm and at distances of 25, 102, 305 mm from the pile surface. Bender element sensors No. 1 and 5 were installed at soil depth of 229 mm and distance of 25 and 102 mm from the pile. Bender element sensors No. 3 was installed at soil depth of 687 mm and distance of 25 mm to the pile. Bender element sensors No. 4 and 7 were installed at 76 and 203 mm below the tip of the pile.

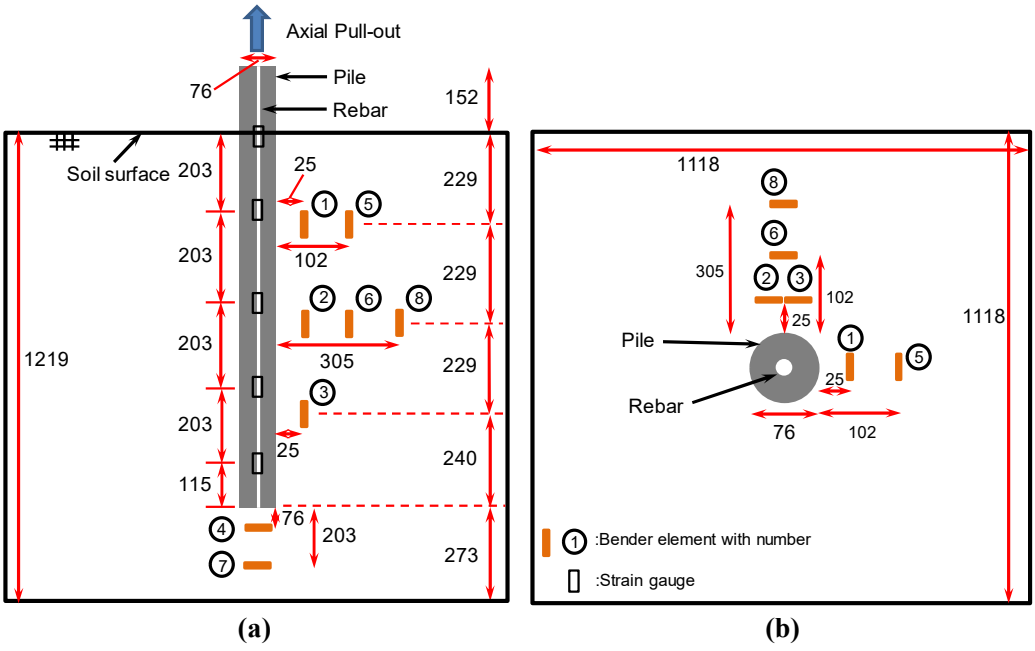

Figure 5.2. Instrumentation for two pull-out loading tests: (a) side view; (b) top view.

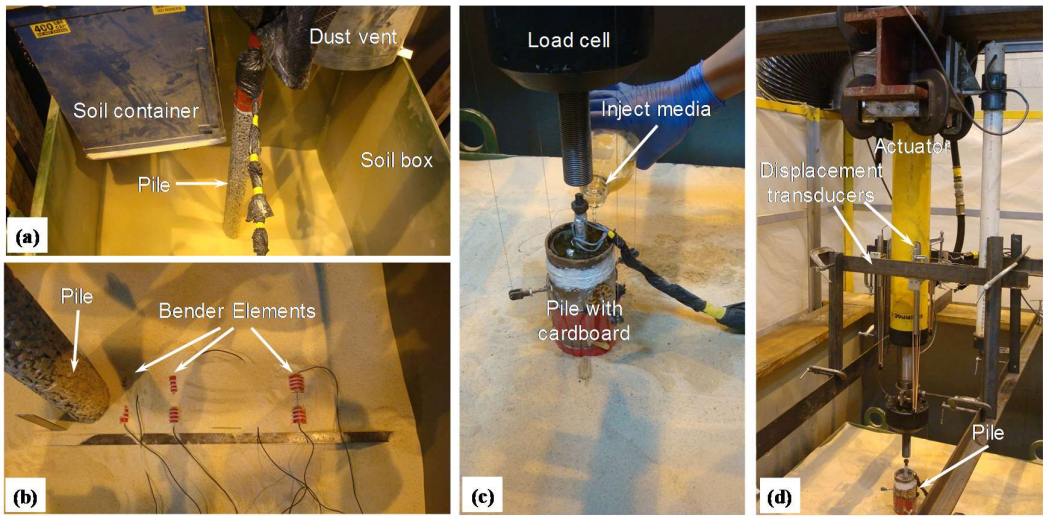

Figure 5.3. Instrumentation, MICP bio-grouting and pull-out loading setup: (a) soil raining; (b) bender element installation; (c) media injected form the top of the pile; (d) pull-out loading setup.

5.5 EXPERIMENTAL PROCEDURES

5.5.1 MICP Bio-grouting

After sensor instrumentation, the pile was detached from the load cell. The top of the pile was wrapped with a cardboard (Figure 5.2c). For Test No. 1 (without MICP bio-grouting), 16 L deionized water was percolated from the top of the pile to achieve similar soil moisture content around the pile in both tests. For Test No. 2 with MICP bio-grouting, urea medium (UM) with bacteria and cementation medium (CM) were percolated into the pile by following the detailed procedure summarized in Table 5.1. During the media injection, the infiltration rates were monitored following ASTM C1701 (2009f). S-wave velocities were also monitored during the whole MICP bio-grouting process as shown in Table 5.1.

Table 5.1. Summary of MICP bio-grouting procedure and S-wave velocity monitoring schedule.

Injection No.	Time (hrs)	Urea medium with bacteria (L)	Cementation medium (L)
		Measure Initial V_s	
	0.25	1.5	
			1.5
		Measure V_s	
1	0.6	1.5	
			1.5
		Measure V_s	
	0.98	1.5	
			1.5
		Measure V_s every hour	
2	12		8
		Measure V_s every hour	
3	24		8
		Measure V_s every 2 hours	
	50	1.5	
4			1.5
		Measure V_s every 6 hours	
Total		6	22

5.5.2 Loading Procedure

After the deionized water injection or MICP bio-grouting treatment, the cardboard was removed and the actuator was connected to the pile. Four displacement transducers were installed to measure the pull-out displacement at the top of the pile (Figure 5.2d). The two axial pull-out tests were conducted in accordance with the fast procedure outlined in ASTM D3689 (2009g). During the test, loading at each increment was held constant for at least 4 minutes or until the pile head displacement stabilized. The tests were stopped when the displacement at the pile head continued increasing

without an increase of the applied load. For Test No. 1 (without bio-grouting), a load increment of 22.2 N was used for loads until 150 N and a load increment of 44.5 N was used for larger loads. For Test No. 2 (with MICP bio-grouting), load increments of 44.5, and 89 N were used for loads until 932, and 3879 N, respectively.

5.5.3 Moisture and Calcium Carbonate Contents Measurement

After the pull-out loading tests, soil samples were collected across the soil box. A total of 40 and 270 soil samples (each sample weight: ~30 g) from Test No. 1 and No. 2, respectively, were collected. Samples from Test No. 1 and 2 were dried, which were used to measure the moisture content. The samples from Test No. 2 were then mixed with 20 mL of 5 M Hydrochloric acid to measure the Ca^{2+} concentration (C_{Ca}, g/mL) using Atomic Absoprtion Spectrometer (AAnalyst 200, PerkinElmer). The measured Ca^{2+} concentration was used to calculate the $CaCO_3$ content. The detailed procedure of calcium carbonate content calculation can be found in Lin et al. (2016a and b). In addition, soil samples were also used for SEM and EDS imaging (Environmental SEM FEI XL30) to characterize crystal formation.

5.6 RESULTS

5.6.1 S-Wave Velocities during MICP Bio-grouting

Measuring S-wave velocity of soils has been considered as a feasible method for monitoring MICP bio-grouting process, which could be used to further analyze soil

shear modulus and $CaCO_3$ content (van Paassen 2009; Al Qabany et al. 2011; Weil et al. 2011; and Lin et al. 2016b). The results of the S-wave velocities measurement during MICP bio-grouting is shown in Figure 5.3. Bender element No. 1 to 3 were installed 25 mm from the pile surface and at soil depths of 229, 458, and 687 mm, respectively. Bender element No. 4 and 7 were installed at 76 and 203 mm below the pile tip. Sensor 6 was located at soil depth of 458 mm and 102 mm distance from the pile surface. The original S-wave velocities before MICP bio-grouting treatment were measured and shown at time 0 hour, ranging from 78 to 126 m/s along the soil depth. After the first injection between 0.25 to 0.98 hours, the S-wave velocities measured by sensor No. 2, 4, and 7 show immediate increases with time, indicating $CaCO_3$ cementation at the sensors' locations. While the S-wave velocities of sensor No. 1, 3, and 6 showed small or no increases, indicating less $CaCO_3$ cementation at their locations. The S-wave velocity measured by sensor No. 2 continued to increase after the media injections of 12 and 24 hours (Table 5.1), and then reached a plateau at 430 m/s after media injection of 50 hrs. The comparisons of the S-wave velocities measured from sensors No. 4 and 7 show that the S-wave velocity of sensor No. 4 increased faster between 12 and 38 hours, however, after 38 hours, S-wave velocity of sensor No. 7 increased faster. This could be attributed to the bacteria, urea, $CaCl_2$ media flow path from the pile tip to the soil below, which induced $CaCO_3$ cementation first at the position of sensor No. 4 and then No. 7. At the end of the MICP bio-grouting treatment (72 hours), the S-wave velocities measured by sensor No. 4 and 7 reached similar S-wave velocities of 260 m/s.

S-wave velocities of sensor No. 1 and 3 showed similar variation before 35 hours. After 35 hours, the S-wave velocity of sensor No. 3 showed a much higher increase rate than that of sensor No. 1, and then followed by reaching a plateau at the end of the bio-grouting treatment. The S-wave velocity of sensor 1 after 35 hours showed a slower increase rate than that of sensor No. 3, but, continued increasing until the end of the bio-grouting treatment without showing a plateau. The S-wave velocity of sensor 6, located 102 mm away from the pile, showed almost no change before 50 hours and then followed by an increase by only 30% till the end of the treatment. Sensors No. 5, and 8 did not show clear changes of S-wave velocities during the MICP bio-grouting, indicating that bio-grouting extended to a distance of approximately 102 mm (distance of bender element No. 5 and 6 to the pile) around the pile. The S-wave velocities of sensors at the end of the MICP bio-grouting treatment showed plateau except sensor No. 1, 6, and 7 (Figure 5.4), which could be attributed to bio-clogging along most of the test pile surface that greatly reduced the flow of media solution out of the pile and produced less $CaCO_3$ cementation at the sensors locations. The observed bio-clogging was also confirmed by the low infiltration rates after 50 hours as will be discussed in the next paragraph. At the end of the MICP bio-grouting (72 hours), the S-wave velocities of sensors No. 1, 2, 3, 4, 6, and 7 had increased by an average of 1.5 times. It is important to note that the S-wave velocities of Test No. 1 (without MICP bio-grouting) during deionized water injection were constant, which are similar to the

measured S-wave velocities of Test No. 2 before MICP bio-grouting treatment with maximum difference of 22 m/s between the two tests.

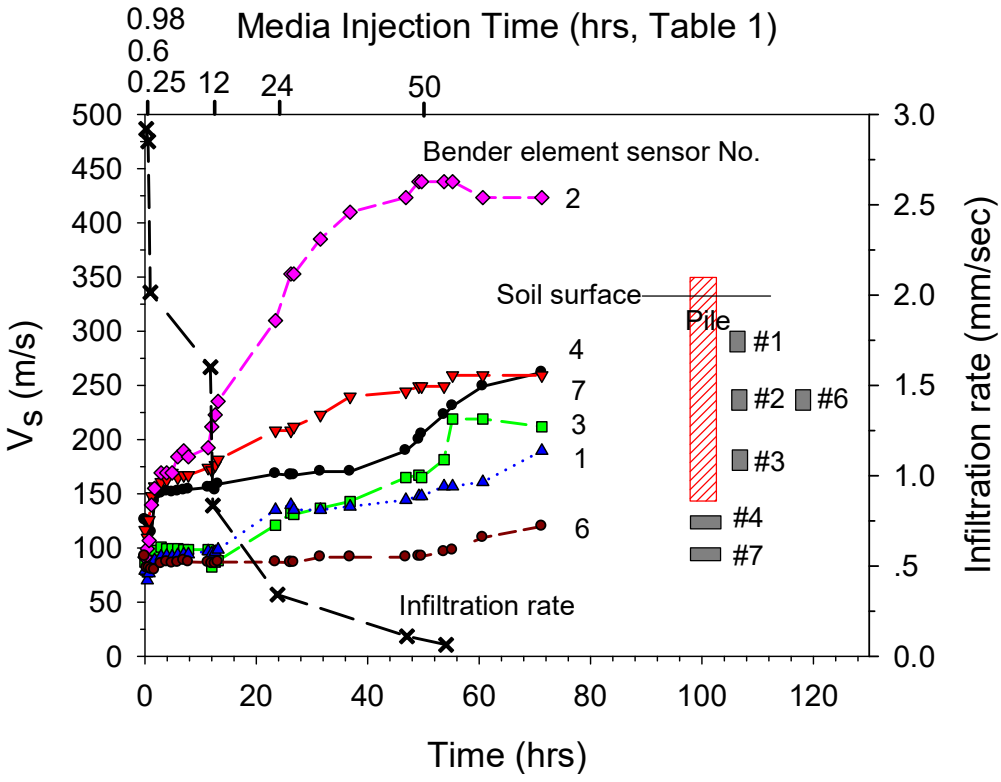

Figure 5.4. S-wave velocities and infiltration rate versus time during MICP bio-grouting of Test No. 2.

ASTM (2009f) provides Equation 5-1 to calculate the infiltration rate.

$$I = \frac{KM}{(D^2 \times t)} \qquad \text{Equation 5-1}$$

where I is the infiltration rate, (mm/sec), M is the mass of the infiltrated solution (kg), D is the diameter of infiltration cylinder (i.e. the pile in our case, mm), t is the time required for measured amount of solution to infiltrate the concrete pile (sec), K is a constant parameter [4,583,666,000 ($(mm^3 \times s)/(kg \times h)$) according to ASTM (2009f)]. Figure 5.4 shows that the infiltration rate kept decreasing from 2.9 mm/sec

before the MICP bio-grouting to 0.06 mm/sec at the end of bio-grouting (i.e., 98% reduction), indicating the formation of bio-clogging in the sand matrix around the pile. In addition, the observed bio-clogging was also confirmed by the plateau of most measured S-wave velocities at the end of the MICP bio-grouting.

This low infiltration rate was also confirmed by the measured permeability of the pervious concrete samples cut from the pile after the pull-out tests. The average porosity and permeability coefficient of the pile after MICP bio-grouting were 13% and 0.12 cm/s, respectively. When compared to the porosity and permeability coefficient of the cylindrical pervious concrete samples (discussed previously in the materials section), the porosity and permeability coefficient of the pervious concrete samples after MICP bio-grouting decreased by 32% and 60%, respectively. The decreased porosity and permeability coefficient could be due to the differences in preparation between the pile and samples and/or due to the bio-clogging formed at the soil-pile interface.

Figure 5.5a shows the variation of the S-wave velocities along the pile length during MICP bio-grouting. At 0 hour (before MICP bio-grouting), the S-wave velocities linearly increased as the soil depth increased. This linearly increased S-wave velocity with soil depth is similar to the results of measuring S-wave velocity of sand in centrifuge test by Fu et al. (2004). During the MICP bio-grouting, S-wave velocities of sensors No. 2 and 4 started increasing immediately. While the S-wave velocities measured by sensors No. 7, 1, and 3 showed a delayed increase. At the end of the MICP

bio-grouting, the S-wave velocities of sensors No.1, 2, 3, 4, and 7 increased by 1.4, 3.6, 1.4, 1.2, and 1.1 times as compared to their initial S-wave velocities. The variation of the S-wave velocities along the pile length indicates the level of $CaCO_3$ cementation content in the sand matrix along the pile length and at the pile tip. For example, higher S-wave velocity indicates a higher $CaCO_3$ cementation content (Al Qabany et al. 2011; Weil et al. 2011; Lin et al. 2016b). Figure 5.5a indicates that $CaCO_3$ contents are highest at the location of sensor No. 2, followed by sensors No. 1, 3, 4, and 7.

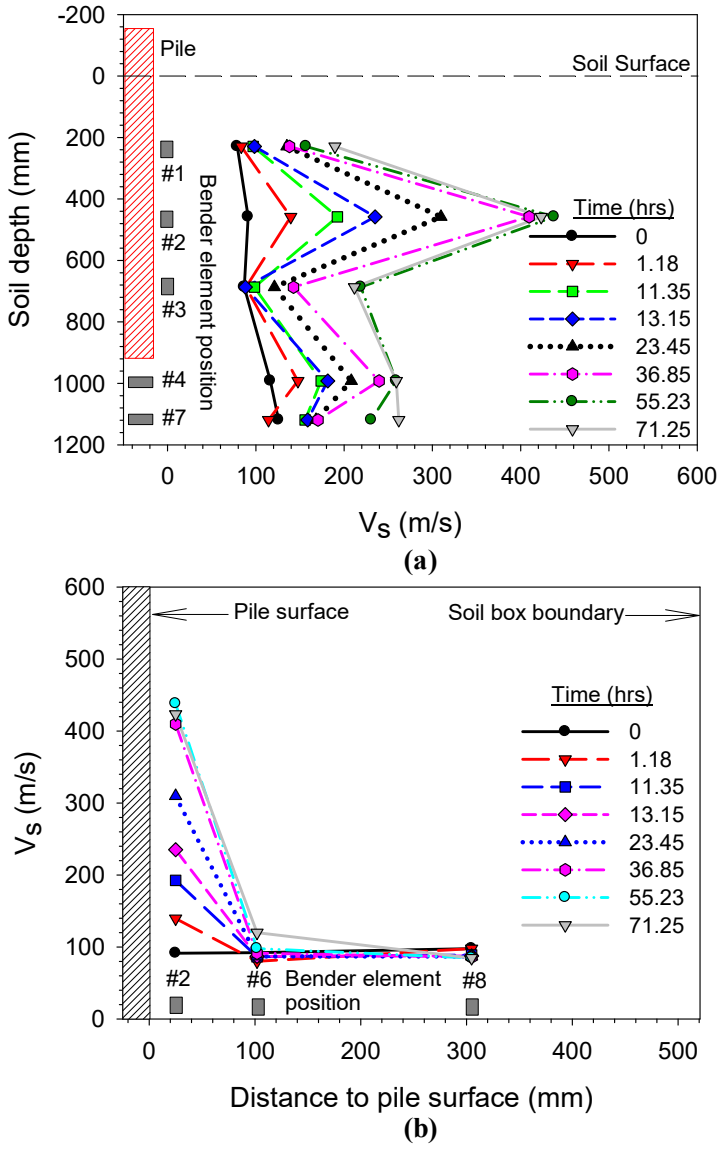

Figure 5.5. S-wave velocities profile versus time during MICP bio-grouting in Test No. 2, (a) at different soil depths; b) at soil depth of 458 mm, but at different distances from the pile.

The S-wave velocities measured by sensors No. 2, 6, and 8 which were located at the soil depth of 458 mm are shown in Figure 5.5b. Sensors No. 2, 6, and 8 are located at 25, 102, and 305 mm from the pile surface. During the MICP bio-grouting, the S-wave velocity at sensors No. 2 and 6 increased by 3.6 times and 30%, respectively. The

S-wave velocities at sensor No. 8 showed almost no change. The variation of the S-wave velocities at soil depth of 458 mm indicates that the $CaCO_3$ precipitated in a limited zone along the pile extending to approximately 100 mm radial distance (location of sensor No. 6) from the pile surface, which is mainly attributed to bio-clogging as discussed before.

5.6.2 Load-Displacement Response

For test No.1 (without bio-grouting) after deionized water injection and Test No.2 (with bio-grouting) after MICP bio-grouting treatment, pull-out loading tests were conducted. The deformation of the soil surface of Test No.2 during the pull-out loading is shown in Figure 5.6a. As the axial pull-out load increases, the cemented soil-pile system was pulled out of the surrounding soil, showing a clear cemented zone around the pile. The deformation of the soil surface of Test No.1 (without bio-grouting) was negligible since no cemented soil was formed around the pile, which will be discussed in details in the next paragraph. The measured vertical load-displacement responses at the top of the pile for Test No. 1 (without bio-grouting) and Test No. 2 (with bio-grouting) are shown in Figure 5.6b. The load-displacement responses from both tests showed a linear relationship at the beginning. The initial stiffness (initial slope of load-displacement response) of Test No. 2 was 1.1 times higher than that of Test No. 1, showing the ratio of initial stiffness between two tests was 2.2. As the load increased, nonlinear plastic responses were observed followed by large displacement under almost

constant load. The ultimate loads for Tests No. 1 and 2 were 919 and 3,879 N, respectively, with a ratio of the ultimate loads between MICP-grouted and non-grouted piles of 4.2. This ultimate capacity ratio is similar to the capacity improvements (ratio: 3 to 4 times) under shaft grouting from literature presented by Gouvenot and Gabiax (1975) who investigated shaft-grouted steel piles under variable soil layers containing sand and clay and Plumbridge and Hill (2001) who investigated bored concrete piles with shaft post-grouting in several types of soils including completely decomposed granites, weathered volcanics to sands and alluvial deposits.

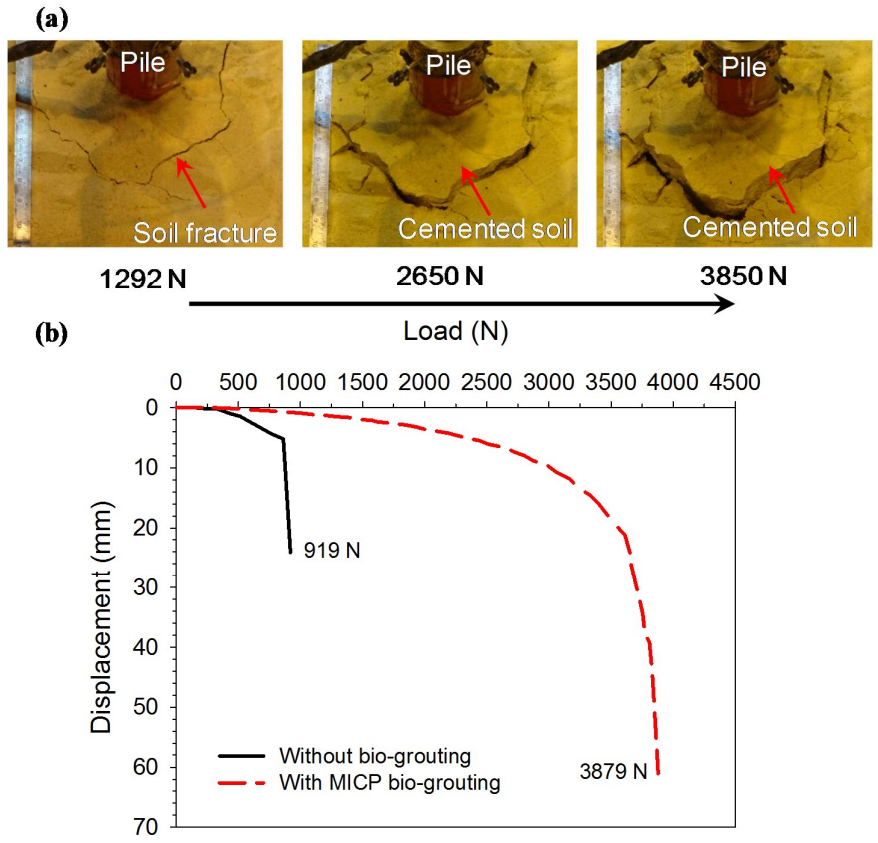

Figure 5.6. (a) Characteristics of the soil surface in Test No. 2 during pull-out loading; (b) vertical load vs. displacement at the top of the pile.

After the pull-out loading tests, the deformation of the soil surface surrounding the pile is shown in Figure 5.7a and b. For Test No. 2 with MICP bio-grouting, the cemented sand surrounding the pile was pulled out of the soil with the pile, showing an effective pile diameter increased from 76 to 229 mm, which was not observed in Test No. 1 (without bio-grouting). The pile after the pull-out tests was also excavated and inspected as shown in Figure 5.7c and d. The pile recovered from Test No.1 (without bio-grouting) showed a pervious concrete surface with small amount of soil filling in the void of the concrete. For pile of Test No. 2 (with bio-grouting), the approximate zone of cemented sand surrounding the top part of the pile is shown in dashed line in Figure 5.7d (because it was unfortunately damaged dueing handling the pile after the test), increase its effective diameter. The cemented sand matrix at the bottom part of the pile extended the pile effective diameter from 76 mm to approximately 148 mm, and increased the pile length by 76 mm. Based on these results, this limited zone of cemented sand matrix surrounding the pile was successfully achieved, improving the pile response when subjected to axial pull-out loading (Figure 5.6b). Thus, it can be concluded that during pull-out loading, the cemented soil-pervious concrete pile system treated with MICP bio-grouting experienced shear failure within the cemented soil along most of the pile length, not along the soil-pile interface.

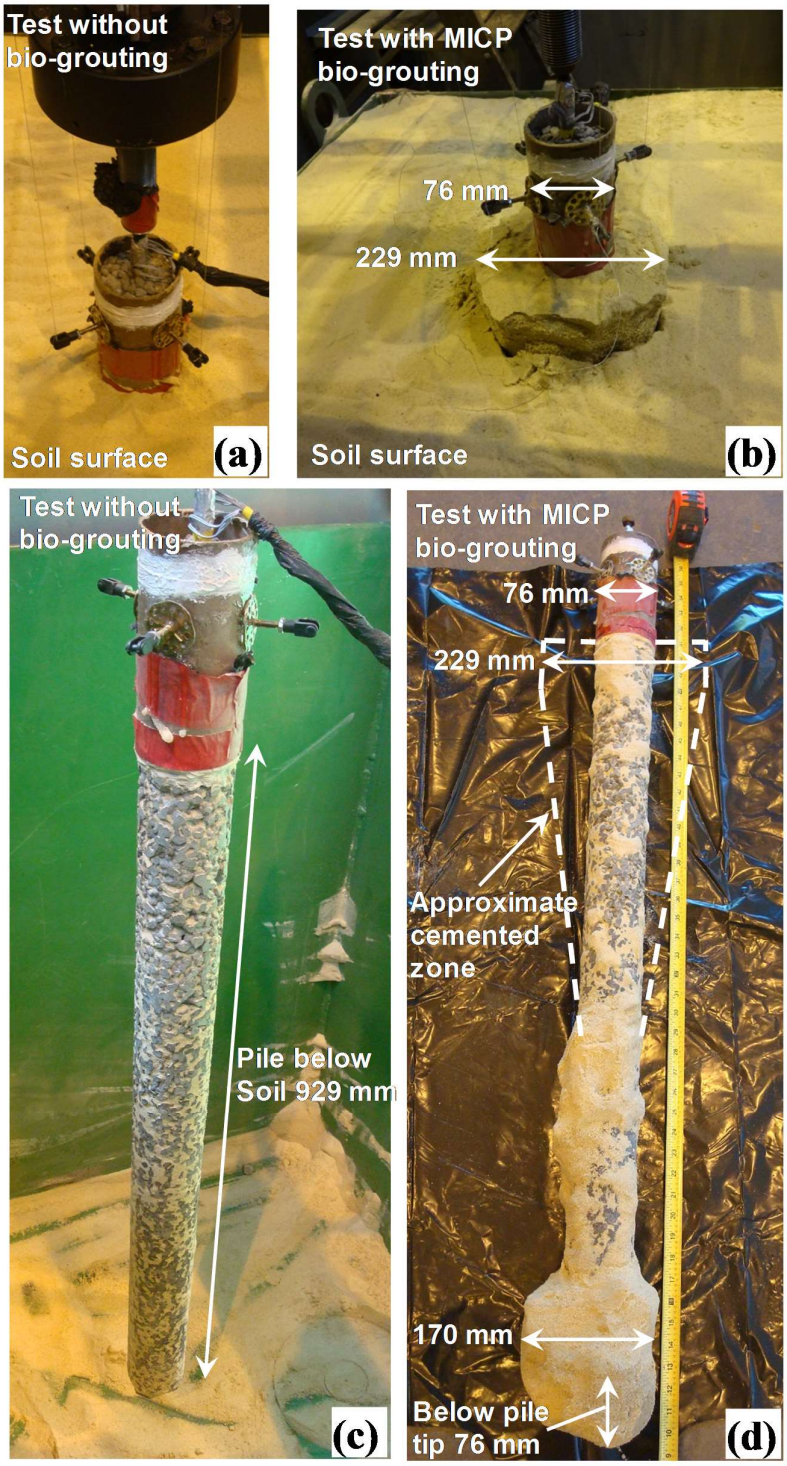

Figure 5.7. Characteristics of the piles and soil surrounding it of two pull-out tests: piles and soil surface in (a) Test No. 1 and (b) Test No. 2 after pull-out loading; excavated piles of (a) Test No. 1 and (b) Test No. 2 after pull-out test.

5.6.3 Load Transfer along Pile Length

Figure 5.8a shows the load transfer along the pile length for both tests. The load transfer was calculated using the strain gauge measurements and the initial elastic modulus of the pervious concrete composite including the steel threaded rebar. Loads of 145, 502, 643, and 855 N were selected to compare the load transfer along the pile length in both tests, which represents loading from the initial (linear) stage, through the transition stage, to the ultimate load for Test No. 1. The load transfer rates (e.g. slope of the curve or unit friction) for both tests located at soil depth from 0 to 406 mm are highest compared to the deeper soil depth. At soil depth from 0 to 406 mm, the load transfer rate of Test No. 2 (with MICP bio-grouting) is higher than that of Test No. 1 (without bio-grouting) with maximum difference of 34%. This highest load transfer rate of Test No.2 (0 to 406 mm depth) is approximately attributed to the higher $CaCO_3$ content and/or largest cemented zone surrounding the pile, which is confirmed by the achieved maximum S-wave velocities (e.g. bender element No. 2) (Figure 5.4) and $CaCO_3$ content measurement (discussed later in the paper) at soil depth of 0 to 406 mm. The skin friction along the pile were calculated by dividing the differences of the transferred forces by the surface area of the corresponding pile section. The averaged skin friction along the pile versus displacement measured from the top of the pile is shown in Figure 5.8b. The averaged skin friction of Test No. 2 (with MICP bio-grouting) is up to 7.8 times higher than that of Test No. 1 (without bio-grouting). Similar to bio-grouting, the shaft grouting reported from the literature increased the skin friction of

bored piles (diameter of 570 to 900 mm, length of 6 m) in loose to dense sand by up to 73 % (Stocker 1983; Plumbridge and Hill 2001), indicating a lower improvement rate using shaft grouting as compared with MICP bio-grouting. This difference could be attributed to the encountered sand conditions and physical characteristics of the used piles.

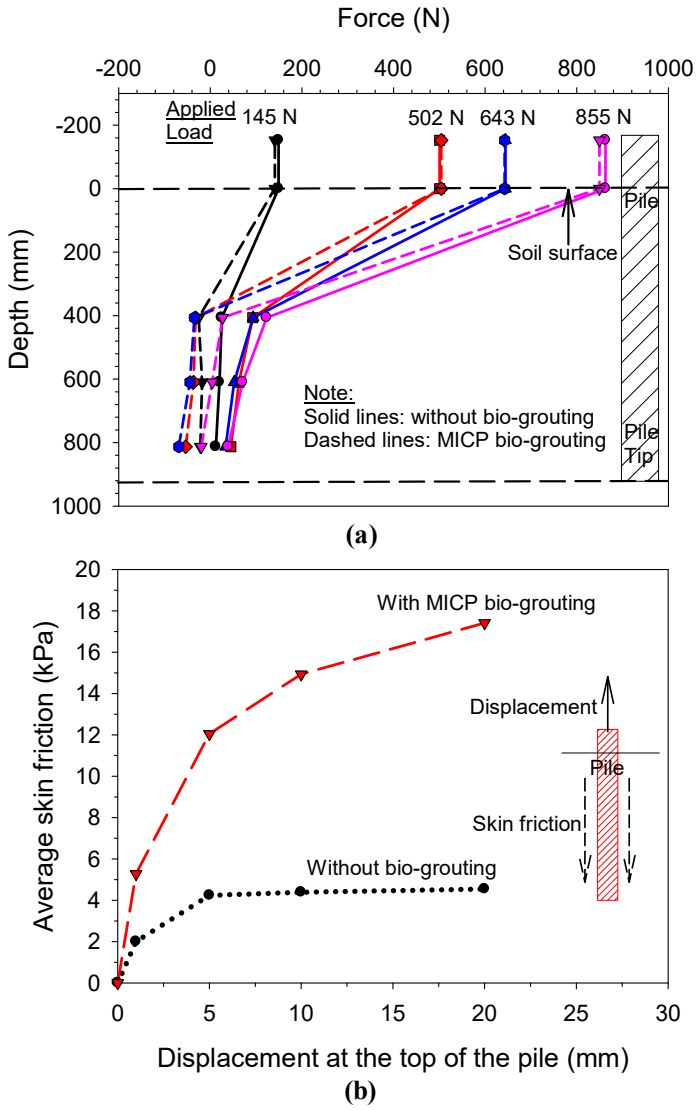

Figure 5.8. Comparison of (a) transferred forces along pile length of both tests at different loading stages and (b) averaged interface friction stress versus displacement at the top of the pile.

5.6.4 Moisture and Calcium Carbonate Contents in Sand Box

Soil samples were collected across the soil box in both Test No. 1 without bio-grouting (40 samples) and Test No. 2 with MICP bio-grouting (270 samples). The measured moisture contents of samples from Test No.2 were plotted in a contour as shown in Figure 5.9a, which also includes the profile of the cemented zone around the pile. Most of the moisture contents were found around the pile and at the bottom of the soil box. The measured moisture contents ranged from 0% to 13.9%, with an average of 4.9% near the soil-pile interface, which is similar to the moisture content measured from Test No. 1. The highest moisture content was observed at the tip of the pile and confined in the cemented sand zone due to bio-clogging.

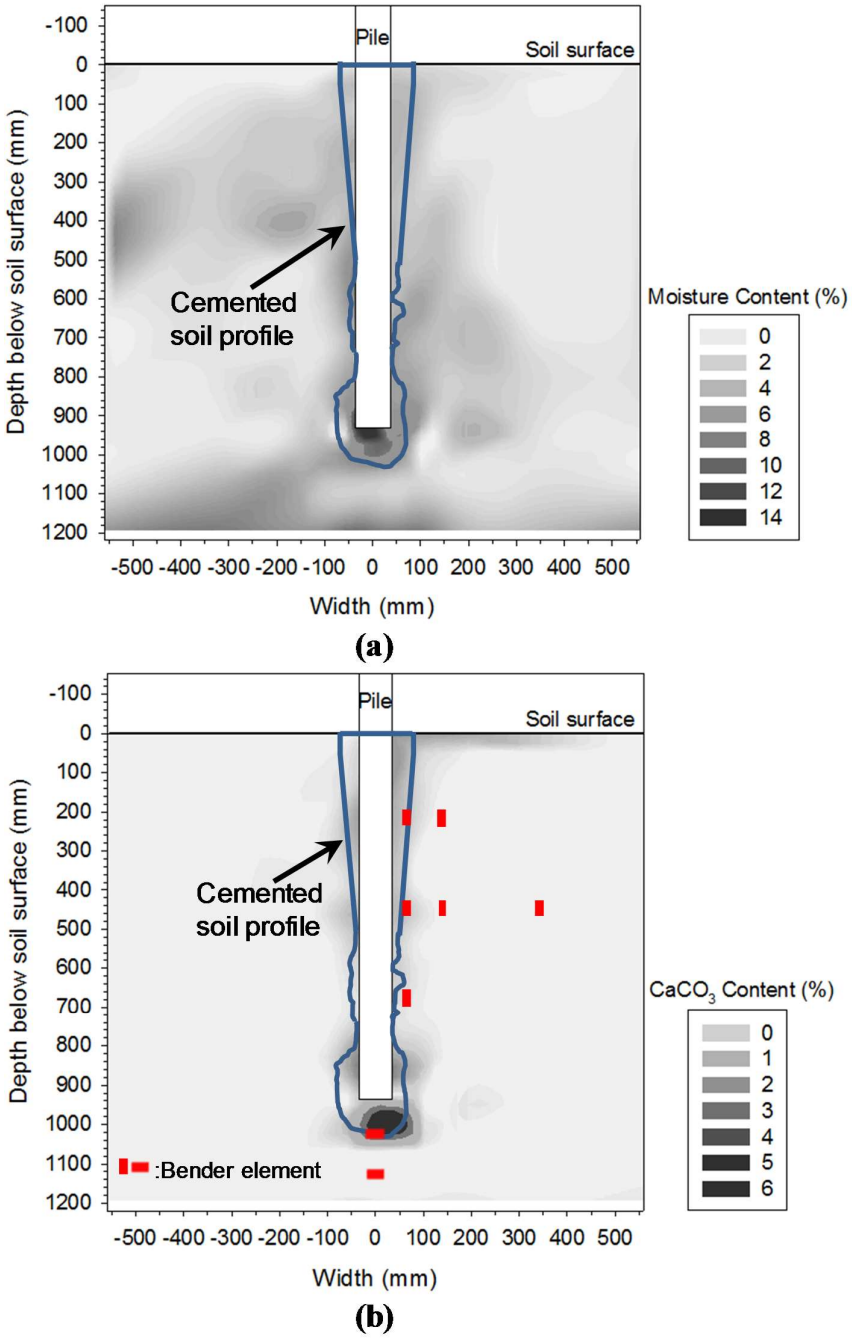

Figure 5.9. Color contour of (a) moisture content and (b) $CaCO_3$ content and retrieved pile profile in Test No. 2.

After the moisture content measurements, the 270 samples were utilized to determine the $CaCO_3$ content. A cross-section of the measured $CaCO_3$ content contour

in the soil box from Test No. 2 is shown in Figure 5.9b. The $CaCO_3$ precipitated only around the pile, extending the cemented zone from pile surface to approximate 87 mm. It is important to note that the $CaCO_3$ content at shallow soil depth (0 to 406 mm) and below the pile tip was higher than the remaining part along the pile, which results in highest load transfer rate and higher S-wave velocities. The observed higher $CaCO_3$ content at both locations could be attributed to the media flow pattern (either flow to the tip of the pile or the interface of the pile) which is controlled by the flow channel distribution in the casted pervious concrete pile. The pile profile after soil removal (i.e., showing the pile and soil cemented to it after the test) is also shown in Figure 5.9b. Based on the pile profile after soil removal and the $CaCO_3$ content contour, the shear failure along the pile occured in the cemented sand zone. The locations of the bender elements are also shown in Figure 5.9b. The bender element sensors located within the $CaCO_3$ cemented zone indicated significant measurement changes as shown in Figure 5.4 and Figure 5.5.

Figure 5.10 demonstrates the $CaCO_3$ content at different distance from the pile surface at four soil depths along the pile length. The distribution of $CaCO_3$ content was not uniform along the soil-pile interface. The $CaCO_3$ content at soil depth of 203 mm were highest and then started decreasing along the pile length, which causes the higher load transfer rate at shallow soil depth shown in Figure 5.8a. The average $CaCO_3$ content along the soil-pile interface (i.e., pile surface) at different depths was 1.8%. However, the $CaCO_3$ content (6.2%) at the pile tip (soil depth 940 mm) was 2.4 times

higher than the average $CaCO_3$ content at the soil-pile interface. In addition, it is worth noting that the distribution of $CaCO_3$ as a function of distance from the pile (Figure 5.10) matched the S-wave velocity profile shown in Figure 5.5b. The measured $CaCO_3$ contents indicates that the small $CaCO_3$-cemented zone around the pile was successfully achieved in Test No. 2. The approximate average location of shear failure surface of Test No. 2 was approximately at 36 mm distance to the pile surface (Figure 5.7), which was labelled in Figure 5.10, demonstrating that the $CaCO_3$ content at the failure interface ranged from 0.6% to 1.2%.

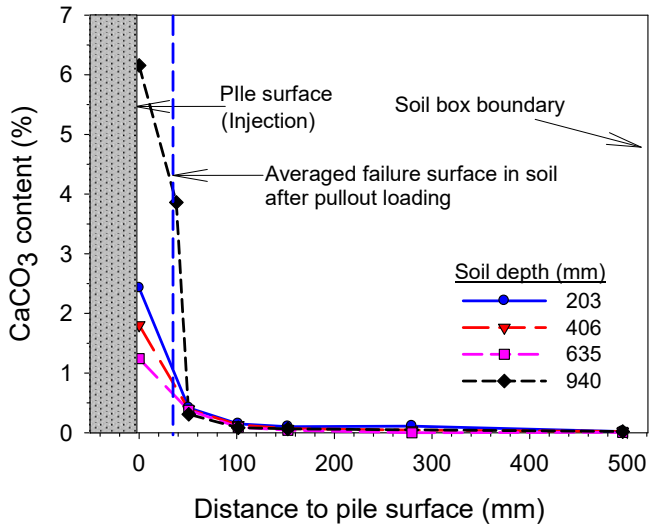

Figure 5.10. $CaCO_3$ content as a function of distances to pile at several soil depths.

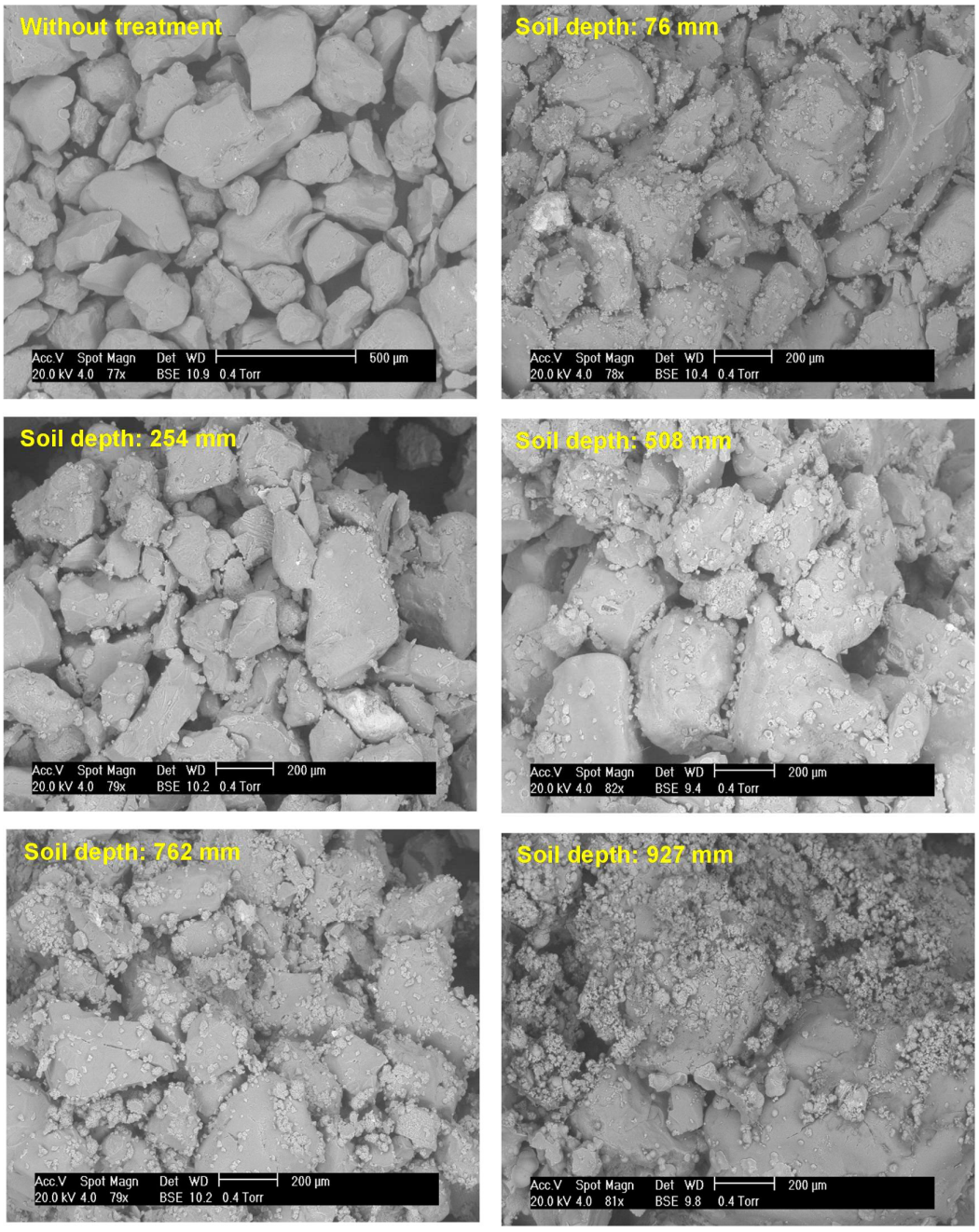

Figure 5.11. SEM images of sand matrix without MICP treatment and with MICP bio-grouting at different soil depths at the soil-pile interface.

5.6.5 Crystal Characteristics of $CaCO_3$ in Sand Matrix

Figure 5.11 shows SEM images of sand samples collected around the pile surface. The image of sand sample without MICP treatment shows the angular shape and particle size distribution of the sand matrix. The remaining images for sand matrix with MICP bio-grouting treatment. Two main types of $CaCO_3$ morphologies, rhomboidal calcite and spherical vaterite crystals, were observed in these images. It is important to note that the formations of $CaCO_3$ crystals are determined mainly by the urea hydrolysis rate (van Paassen 2009; Lin et al. 2016 a and b). However, it is still unexplored if the type of $CaCO_3$ crystals can affect the shaft and tip resistance of the pervious concrete piles. In addition, based on Figure 5.11, it is observed that the main $CaCO_3$ distributions in the bar sand were grain-coating (coating sand particles) and matrix supporting (grow from particle surface into pore space creating a cementation bridge between soil grains), which are the main distribution types of $CaCO_3$ crystals at pore space of the sand matrix (Lin et al. 2016b).

5.7 SUMMARY AND CONCLUSIONS

This paper focuses on investigating the feasibility of enhancing the axial pull-out response of permeable ground improvement piles using MICP bio-grouting. Two instrumented pervious concrete pile tests without and with MICP bio-grouting (Test No. 1 and 2, respectively) were performed at the SSI facility at Lehigh University. The measured pile responses, S-wave velocities, moisture and $CaCO_3$ contents, and crystal

characteristics of $CaCO_3$ were analyzed. Based on the results presented in this paper, the following conclusions are drawn:

1. The S-wave velocities of sensors close to the pile increased by an average of 1.5 times compared to the measurements before bio-grouting due to the formation of $CaCO_3$ cemented-soil zone around the pile. The infiltration rate of the soil-pile system decreased by up to 98% due to the same reason, confirming the clogging of the soil surrounding MICP injection points. The S-wave velocity and infiltration rate can be used to monitor future field tests of permeable piles with bio-grouting.
2. The S-wave velocity at sensor No. 2, 6, and 8 increased by 3.6 times, 30%, and 0%, respectively, indicating that the cemented soil zone surrounding the pile is limited to radial distance approximately 100 mm to the pile surface.
3. The ratios of the stiffness (initial slope) of the load-displacement response and the ultimate load between Test No. 1 (without bio-grouting) and Test No. 2 (with MICP bio-grouting) was 2.2 and 4.2 times, respectively. This stiffness and load capacity improvement confirmed the significant effects of limited zone bio-grouting on enhancing the pull-out response of permeable piles.
4. The load transfer rate of Test No. 2 (with MICP bio-grouting) is up to 34% higher than that of Test No. 1 (without bio-grouting). The averaged skin friction of Test No. 2 is up to 7.8 times higher than that of Test No. 1 without bio-grouting. The observed improvement of the load transfer and skin friction confirmed the pile capacity improvement using MICP bio-grouting.

5. The contour of $CaCO_3$ contents showed a limited cemented soil zone surrounding the pile. The precipitation of $CaCO_3$ is not uniform around the pile. The maximum $CaCO_3$ content (6 %) was at the tip of the pile.
6. Based on the pile profile after soil removal (the pile and soil cemented to it after the test), the $CaCO_3$ content at the failure surface in the cemented soil-pile system ranged from 0.6% to 1.2%.
7. Both calcite and vaterite crystals were observed around the pile with the main types of $CaCO_3$ distributions in the bar sand were grain-coating and matrix supporting.

6. ENANCING THE AXIAL COMPRESSION RESPONSE OF PERVIOUS CONCRETE GROUND IMPROVEMENT PILES USING BIO-GROUTING

6.1 INTRODUCTION

Post-grouting of deep foundations and ground improvement systems has been utilized to improve their performance by increasing shaft and/or tip resistances of the foundation systems. These grouting methods utilize complex construction techniques, high pressures, cement-based grout, and/or proprietary systems (Gouvenot and Gabiax 1975; Bruce 1986a and b; Plumbridge and Hill 2001). This paper presents an innovative grouted ground improvement pile alternative using bio-grouting for permeable piles (pervious concrete piles).

The proposed system allows for grouting along the shaft and at the tip of the permeable piles using a simple percolation process that does not require applying high pressures or using a proprietary system. In addition, this grouting process utilizes grout that relies on natural soil bacteria to induce calcium carbonate ($CaCO_3$) precipitation; a process commonly known as microbially induced carbonate precipitation (MICP) (DeJong et al. 2006; Ivanov and Chu 2008; van Paassen 2009; Burbank et al. 2013; DeJong et al. 2013; Lin et al. 2015). MICP has been extensively investigated at the laboratory sample-scale; however, field-scale and/or large-scale laboratory experiments have been facing practical difficulties related to bio-clogging around injection points,

limiting its use in stabilizing large soil volumes (Ivanov and Chu 2008; van Paassen et al. 2010a; Cheng and Cord-Ruwisch 2013). The proposed bio-grouting to improve the axial compression response of permeable piles avoids this limitation because it only requires improving a limited zone around the pile. To achieve the goal of this research, two instrumented pervious concrete pile tests were performed under axial compression loading. Test No. 1 was performed without MICP bio-grouting and Test No. 2 with MICP bio-grouting. This paper describes the used instrumentation and testing procedure, and summarizes the measurements of instrumentation and the analysis performed on soil samples collected after the tests.

6.2 BACKGROUND

6.2.1 Post-grouting of Foundation Systems

Post-grouting has been utilized to provide improved performance of deep foundations and ground improvement systems (i.e., higher load capacity and lower settlement). Post-grouting methods include post-tip-grouted and/or shaft-grouted foundation systems (Bruce 1986a and b). These grouting methods are mainly used to increase the tip and shaft resistances of foundations, which could increase their capacity or allow for utilizing foundations with reduced dimensions that provide the same capacity as non-grouted foundations (Gouvenot and Gabiax 1975; Bruce 1986 a and b). Constructing grouted foundations involves injecting pressurized grout through a proprietary system consisting of pipes that are attached to the steel cage and/or a base

grouting plate at the tip, creating a grouted zone along the shaft or below the tip (Plumbridge and Hill 2001; Ruiz and Pando 2009; Fattahpour at al. 2015). Although drilled shafts with post-grouted tip have been successfully utilized, the application of grouting along the shaft of deep foundations in U. S. has been limited mainly due to the complex injection technique and difficult quality control (Joer et al. 1998; Thiyyakkandi et al. 2013; Fattahpour et al. 2015). This paper presents an innovative grouted ground improvement pile alternative using bio-grouting to improve the response of axially-loaded pervious concrete piles.

6.2.2 Pervious Concrete Ground Improvement Piles

A pervious concrete pile is an innovative ground improvement alternative that has been developed by Suleiman et al. (2014). When compared with permeable granular columns (e.g. aggregate piers), the strength and stiffness of pervious concrete pile are higher than that of an identical granular column, while having similar permeability coefficient. In addition, unlike granular columns which fail by bulging into the surrounding soil, pervious concrete piles fail by punching into the soil (Suleiman et al. 2014; Ni et al. 2015). The permeability of pervious concrete piles allows for easy grouting (without applying pressure) that is expected to improve the shaft and tip resistances of the pile without the need of using complex proprietary systems. Furthermore, the investigated system uses bio-grouting method.

6.2.3 Bio-grouting

Bio-grouting utilizes soil bacteria to induce calcium carbonate ($CaCO_3$) precipitation to cement soil particles, improving its strength, stiffness, and dilantancy (van Paassen 2009; Burbank et al. 2013; Lin et al. 2016a). The most commonly investigated bio-grouting process is the microbially induced carbonate precipitation (MICP) (DeJong et al. 2006; Ivanov and Chu 2008; DeJong et al. 2013). MICP involves a microbially-regulated process of $CaCO_3$ precipitation, which can be induced by different metabolic activities including microbial-catalyzed hydrolysis of urea and microbial-denitrification of calcium nitrate (Stocks-Fischer et al. 1999; DeJong et al. 2006; Ivanov and Chu 2008; van Paassen et al. 2010b; Hamdan et al. 2011). The precipitated $CaCO_3$ cements the sand matrix and fills the soil void space, increasing its strength, stiffness, and dilatancy (e.g., Lin et al. 2016a). Most research related to MICP technique have been focusing on laboratory sample-scale characterization of soil mechanical properties and treatment process control and optimization (DeJong et al. 2006; Chou et al. 2011; Mortensen et al. 2011; Al Qabany et al. 2012; van Paassen et al. 2012; Al Qabany and Soga 2013; Burbank et al. 2013; Martinez et al. 2013; Lin et al. 2016a). The limited MICP field-scale and/or large-scale laboratory tests have been facing practical difficulties related to the heterogeneous distribution of $CaCO_3$ due to bio-clogging around injection points (Ivanov and Chu 2008; van Paassen et al. 2010a; Cheng and Cord-Ruwisch 2013). Therefore, stabilization of large soil volume (or mass stabilization) using MICP remains limited. The proposed bio-grouting of pervious

concrete piles avoid these limitations by focusing on improving a limited zone (or $CaCO_3$ cemented zone) surrounding permeable piles to enhance their soil-pile interaction and mechanical response when subjected to axial loading.

6.2.4 Objectives and Methodology

The research presented in this paper focuses on evaluating the feasibility of bio-grouting pervious concrete piles, where the pile is used as an injection point, to enhance the soil-pile interaction and pile capacity under axial compression loading. The extent of the cemented zone required to enhance the response of pervious concrete piles subjected to axial loading is relatively small compared to stabilization of large soil areas, thereby mitigating problems associated with bio-clogging. To achieve the goal of this research, two instrumented pervious concrete pile tests were performed under axial compression loading at the Soil-Structure Interaction (SSI) testing facility at Lehigh University. In both tests, the pile was initially placed vertically in the soil box. Then, the sand was rained around it. Test No. 1 was performed without MICP bio-grouting and Test No. 2 with MICP bio-grouting. To investigate the soil-pile interaction of vertically loaded piles, the pile and surrounding soil were instrumented using strain gauges, bender elements, in-soil null pressure sensors, and a tactile pressure sheet. The change of shear wave (S-wave) velocities measured by bender elements during MICP bio-grouting and vertical loading were compared and analyzed. The responses of the pile and surrounding soil without MICP bio-grouting and with MICP bio-grouting were

compared. Soil samples across the soil box were collected and analyzed for soil moisture, $CaCO_3$ and ammonium (NH_4^+) contents, and the crystal morphology of $CaCO_3$ was characterized using Scanning Electron Microscope (SEM).

6.3 MATERIALS AND PREPARATION METHODS

6.3.1 Soil Properties

The soil used in the tests was classified as poorly graded sand (SP) using the Unified Soil Classification System (Ni et al. 2015). In order to provide homogeneous soil condition, the sand was rained from a height of approximately 0.5 m through a bottom-dump container fitted with a sieve. The sand placed in the soil box (introduced in the section of test units and instrumentation) had an average unit weight of 15.1 kN/m^3, relative density of 29% and water content of 0.4%, which were measured by a nuclear density gauge (Humboldt HS-13 5001EZ). The standard deviation of the unit weight measurements was 0.315 kN/m^3, which confirmed the uniformity of the placed soil. To characterize the soil properties, a series of consolidated drained (CD) triaxial tests with different confining pressures (25, 50, and 100 kPa) were performed. The 70-mm-diameter samples were prepared at the similar relative density of the sand in the soil box (i.e., 29% relative density, or unit weight of 15.1 kN/m^3). The measured initial soil modulus (E_i) was evaluated as a function of confining pressure (σ_3) as $E_i=kP_a(\sigma_3/P_a)^n$ (Janbu, 1963), where P_a is the atmospheric pressure of 101 kPa and k

and n are calculated as 401.6 and 0.48, respectively. The measured peak friction angle of the soil equals to 38°.

6.3.2 Pervious Concrete Properties

Suleiman et al. (2014) has developed a series of pervious concrete mixtures that provided adequate compressive strength and permeability for ground improvement and foundation applications. Based on these results, a pervious concrete mixing recipe was selected to cast the pile for the tests. The mixture used a 0.275 water/cement ratio, a 7% sand/aggregate ratio, 377 kg/m^3 cement, and 1,497 kg/m^3 coarse aggregate. Pea river gravel (commercially available at home-improvement stores) was used as the aggregate material. Aggregate was washed and sieved, and the portion passing through a 9.5 mm sieve and retained on a No. 4 (4.75-mm) sieve was used. To compact the pervious concrete samples, five seconds of vibration compaction per layer was used. For this research, one pervious concrete pile and several cylindrical samples were prepared. The cylindrical samples were used to measure the porosity, permeability, compressive strength, and split tensile strength using ASTM C39, C1688, and C496 (ASTM 2009a, b, and c). The permeability was measured using an in-house designed falling-head permeameter. The pervious concrete samples have an average porosity of 20%, a permeability coefficient of 1.0 cm/s, a 28-day compressive strength of 18.0 MPa, and a split tensile strength of 1.9 MPa. These properties are similar to those reported by Suleiman et al. (2014) and Ni et al. (2015) for pervious concrete piles. It is also worth

noting that the reported 28-day compressive strength of pervious concrete samples is similar to the compressive strength of grouted gravel samples (16.4 MPa) taken from a grouted granular foundation system reported by Liu et al. (2015).

Pervious concrete samples cut from the pile were used to measure the porosity and permeability of the pile. The average porosity and permeability coefficient of the pile after MICP bio-grouting were 12% and 0.16 cm/s, respectively. When compared to the measured sample properties, the porosity and permeability coefficient of the pervious concrete samples after MICP bio-grouting decreased by 40% and 84%, respectively. The decreased porosity and permeability coefficient could be due to differences in preparation between the pile and samples and/or due to bio-clogging which will be discussed later.

6.3.3 Bacteria Preparation and MICP Recipes

Bio-grouting used the bacterial strain *Sporosarcina pasteurii* (*S. pasteurii*, ATCC 11859) for the tests. A stock culture of *S. pasteurii* was innoculated into a growth media (10g yeast extract and 5g ammonium sulfate in 500 mL 0.13M Tris Buffer (pH=9.0) sterilized by vacuum filtration at 0.2 μm) and grown in an incubator shaker at 170 rpm and 33°C for approximately 40 hours until optical density (OD_{600}) reached 0.8~1, which corresponded to a bacteria density of 1.5×10^7cells/mL. The bacteria were then harvested and centrifuged twice at 4000×g for 30 minutes. The bacteria were stored at 4°C (for less than two weeks) until used.

Before the test, the bacteria were suspended into filter-sterilized urea media (20 g urea, 2.12 g $NaHCO_3$, 20 g NH_4CL and 3 g Nutrient Broth in 1 L deionized water at pH=6) to a bacteria density of 5×10^7 cells/mL. During the MICP bio-grouting pile test, this suspension was percolated from the top of the pile, and then followed by the cementation media (urea medium with 300 mM $CaCl_2$) to induce $CaCO_3$ precipitation. The detailed treatment procedure is discussed in further details later in the paper.

6.4 TEST UNITS AND INSTRUMENTATION

The Soil-Structure Interaction (SSI) facility at Lehigh University was used to perform the two axial compression pile load tests. A pervious concrete pile with a diameter of 76 mm and a length of 1.07 m was casted and utilized for both tests. Pile length of 916 mm was embedded in a sand box with dimensions of 1.1×1.1×1.55 m (Figure 6.1). During the casting of the pervious concrete pile, a threaded rebar (9.5 mm in diameter) was placed along the center of the pile, which was used for strain gauge monitoring and attaching the pile to the load cell (Figure 6.2a and b). The pile was first attached to the load cell and hung vertically under its own weight. Then, the soil raining system, which consists of a bottom dump soil container with an attached sieve, was used to rain the sand into the soil box from a height of approximately 0.5 m (Figure 6.2a).

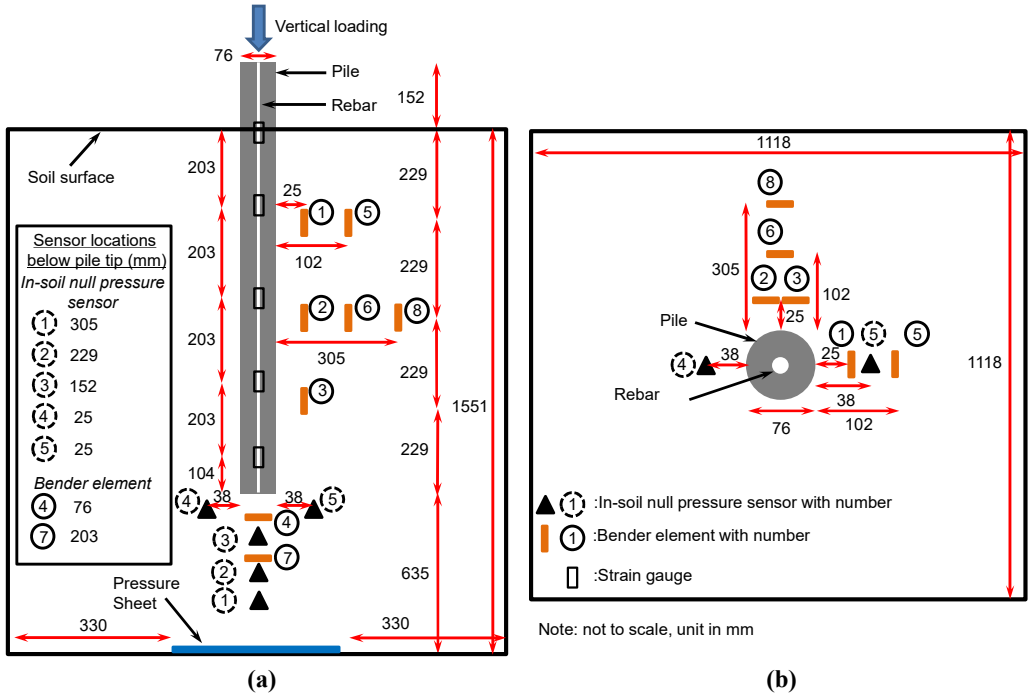

Figure 6.1. Instrumentation for the two vertical loading tests: (a) side view; (b) top view.

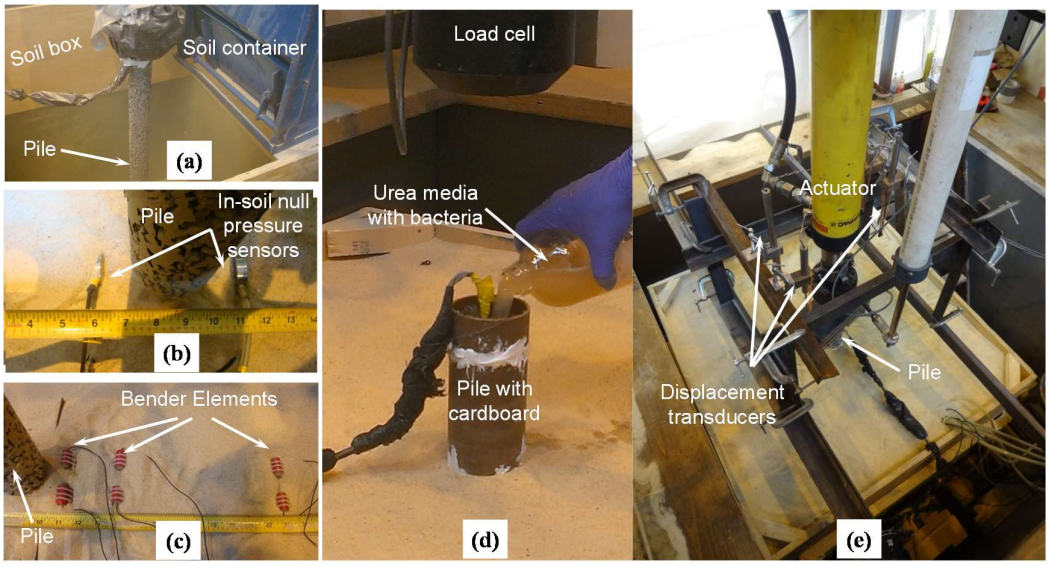

Figure 6.2. Instrumentation, MICP bio-grouting and compression loading setup: (a) soil raining; (b) in-soil null pressure sensor installation; (c) bender element installation; (d) urea media with bacteria injected form the top of the pile; (e) compression tests setup.

The sensors, including strain gauges, in-soil null pressure sensors, bender elements, and tactile pressure sheet, were used to instrument the pile and surrounding soil as shown in Figure 6.1 and Figure 6.2b and c. Bender elements were fabricated in-house using piezo elements (Yun and Santamarina 2005; Lee and Santamarina 2005; Lin et al. 2016a). The in-soil null pressure sensors are 42 mm in diameter and 7 mm thick and each sensor has an air pressure chamber with a diaphragm strain gauge embedded inside. A tactile pressure sheet, which is 0.7 mm thick, consists of a matrix of small sensing cells that provides discrete pressure measurements. The accuracy of the in-soil null pressure sensor and tactile pressure sheet measurement was discussed by Palmer et al. (2009), Talesnick (2013), and Lin et al. (2014). It is important to note that -n-soil null pressure sensors No. 4 and 5 were used to monitor the horizontal soil pressure change around the pile tip (Figure 6.1b and Figure 6.2b). One tactile pressure sheet was placed at the bottom of the soil box to monitor the boundary effect of the soil box during the load tests (Figure 6.1a). During both tests, the maximum change of pressure measured by the tactile pressure sheet was 1.0 and 2.4 kPa from Test No. 1 (without bio-grouting) and Test No. 2 (with MICP bio-grouting), respectively. These measurements validate a minimal or no effect of soil box boundary on the measured responses.

6.5 EXPERIMENTAL PROCEDURES

6.5.1 MICP Bio-grouting

After soil placement, the top of the pile was wrapped with a cardboard (Figure 6.2d). Before conducting Test No. 1 (without MICP bio-grouting), 16 L of deionized water was percolated from the top of the pile in order to achieve similar water content conditions in the sand around the pile for both tests. For MICP bio-grouting in Test No. 2, the percolation method was used to inject urea medium (UM) with bacteria and cementation medium (CM). The detailed procedure of MICP treatment was summarized in Table 6.1. During the MICP bio-grouting, the infiltration rates during each injection of both tests were monitored following ASTM C1701 (2009d). Furthermore, S-wave velocities were also monitored during the MICP bio-grouting process as shown in Table 6.1.

Table 6.1. Summary of MICP bio-grouting procedure and S-wave velocity monitoring schedule.

Injection No.	Time (hrs)	Urea medium with bacteria (L)	Cementation medium (L)
		Measure Initial V_s	
	0.13	1.5	
			1.5
		Measure V_s	
1	0.38	1.5	
			1.5
		Measure V_s	
	0.68	1.5	
			1.5
		Measure V_s every hour	
2	12		8
		Measure V_s every hour	
3	24		8
		Measure V_s every 2 hours	
	48	1.5	
4			1.5
		Measure V_s every 6 hours	
Total		6	22

6.5.2 Loading Sequence

After the deionized water injection of Test No. 1 and MICP bio-grouting in Test No. 2, the actuator was connected to the pile, and 4 displacement transducers were utilized to measure the vertical displacement of the pile top (Figure 6.2e). The two axial compression pile load tests were conducted in accordance with the quick procedure outlined in ASTM D1143 (2009e). The tests were stopped when the displacement at the pile head continued increasing without an increase of the applied load.

6.5.3 Moisture, Calcium Carbonate and Ammonium Contents Measurement

After the tests, soil samples were collected at different locations across the soil box. 40 and 150 soil samples (each sample weight: ~100 g) from Test No. 1 and No. 2, respectively, were collected. Samples from Test No. 1 were used to measure moisture content only. A portion of each sample (~25 g) from Test No. 2 was first used to measure the moisture content. Then, this same portion of each sample was added into 15 mL of 5 M Hydrochloric acid, from which the liquid samples were extracted and diluted by 1000 times. The diluted samples were used to measure the Ca^{2+} concentration (C_{Ca}, g/mL) using Atomic Absoprtion Spectrometer (AAnalyst 200, PerkinElmer, Lin et al. 2016a).

To measure the ammonium content of samples collected from Test No. 2 (with MICP bio-grouting), 30 samples (each with a weight of 17 g) were extracted from the original soil samples into new tubes. The samples were added with 40 ml deionized water and then shaken by vortex mixer for 10 sec to dissolve ammonium and ammonia into the deionized water. The liquid samples were extracted and diluted by 200 times. The diluted samples were used to measure the ammonium nitrogen concentration ($C_{NH4^+\text{-}N}$, mg/L) using Nessler Method (APHA et al. 1992). Then, the ammonium content (C_{NH4^+}, ammonium molar concentration in the soil volume, mM) was calculated based on the measured ammonium nitrogen concentration and Equation 6-1 and Equation 6-2 shown below.

$$W_{NH_4^+}=C_{NH_4^+-N} \times 200 \times \frac{18\text{g/mol}}{14\text{g/mol}} \times 0.04\text{L} \quad \text{Equation 6-1}$$

$$C_{NH_4^+} = \left(W_{NH_4^+} \times 1000/(\frac{18\text{g}}{\text{mole}})\right) \Big/ (\frac{W_{\text{dry soil}}}{\gamma_{\text{dry soil}}}) \quad \text{Equation 6-2}$$

where $W_{NH_4^+}$ is the total mass of NH_4^+ in the sample, the factor of 200 in Equation 6-1 is to account for 200 times dilution, 18 g/mol is the ammonium molecular weight, 14 g/mol is the nitrogen molecular weight, 0.04 L is the total deionized water added into the sample tube, $W_{\text{dry soil}}$ is the weight of the soil in one sample, $\gamma_{\text{dry soil}}$ is the dry unit weight of soil in the testing box.

6.6 RESULTS

6.6.1 S-Wave Velocities during MICP Bio-grouting

The variation of S-wave velocities during MICP bio-grouting of Test No. 2 is shown in Figure 6.3. The S-wave velocities measured by sensors No. 1, 2, and 3, which are located at the distance of 25 mm from the pile surface and depths of 229, 458, and 687 mm, respectively, show an immediate increase following the first and second injections of the medium at 0 and 12 hrs (Table 6.1). The S-wave velocity of sensor No. 4, which is located at 76 mm below the pile tip, showed a small increase after the first injection followed by larger increase after the second injection (12 hrs). The S-wave velocity of sensor 7, which is located at 203 mm below the pile tip, started increasing after the third injection (24 hrs). This delayed increase of S-wave velocities of sensors No. 4 and 7 below the pile tip demonstrated that $CaCO_3$ mainly started to be produced

near sensors No. 4 and 7 after 12 hours. This delay could be attributed to the longer flow path to the pile tip for bacteria, urea, and cementation media, which could induce large amount of $CaCO_3$ precipitation along the flow path and then decrease the amount of $CaCO_3$ precipitation at the locations of sensor No. 4 and 7 (76 and 203 mm below the pile tip). After 40 hrs, the S-wave velocities of all sensors indicate almost constant values. It is worth noting that there was no increase of S-wave velocity after media injection No. 4 at 48 hrs. This could be attributed to bio-clogging around the test pile that greatly reduced the flow of media solution out of the pile, which is evident by the low infiltration rates as will be discussed in the next paragraph. At the end of the MICP bio-grouting (72 hrs), the S-wave velocities of sensors No. 1, 2, 3, 4 and 7 had increased by an average of 2.5 times. However, S-wave sensors No. 5, 6, and 8 did not show clear changes during the MICP bio-grouting indicating that bio-grouting extended to a maximum distance of approximately 102 mm around the pile (distance of bender elements No. 5 and 6 to the pile). It is worth noting that the measured S-wave velocities of Test No. 1 (without MICP bio-grouting) during the injection of deionized water showed negligible variation, which were similar to the S-wave velocities of Test No. 2 before the start of the MICP treatment (t=0 hrs in Figure 6.3) with maximum difference of 20m/s between the two tests. This comparison confirms the similarity of the S-wave velocity measurement of both tests.

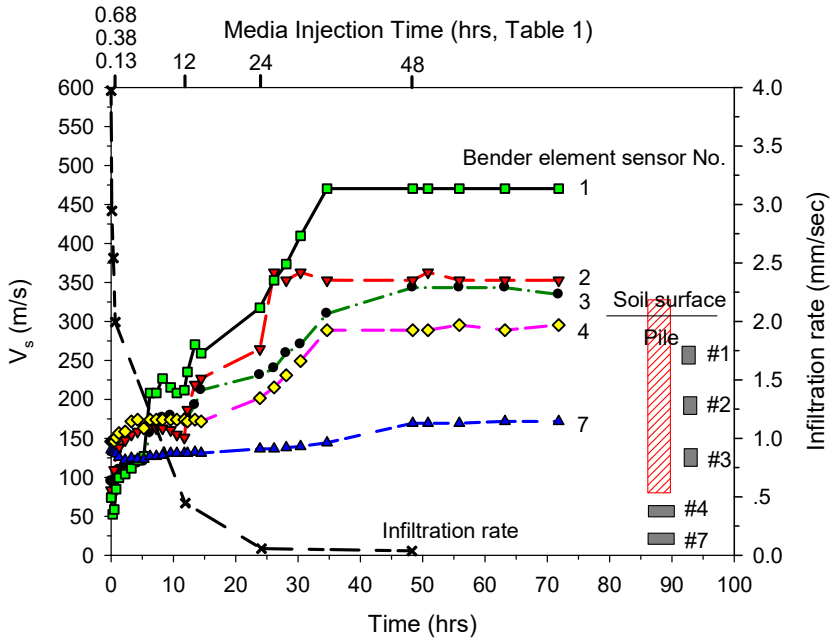

Figure 6.3. Measured S-wave velocities and infiltration rate versus time during MICP bio-grouting of Test No. 2.

The infiltration rate was calculated using Equation 6-3 according to ASTM (2009d).

$$I = \frac{KM}{(D^2 \times t)} \qquad \text{Equation 6-3}$$

where I is the infiltration rate, (mm/sec), M is the mass of the infiltrated solution (kg), D is the diameter of infiltration cylinder (i.e. the pile in this case, mm), t is the time required for measured amount of solution to infiltrate the concrete pile (sec), K is a constant parameter [4,583,666,000 ($(mm^3 \times s)/(kg \times h)$) according to ASTM (2009d)]. As shown in Figure 6.3, the infiltration rate continuously decreased during MICP bio-grouting. The initial value of the infiltration rate was 3.97 mm/sec that decreased to 0.04 mm/sec at the end of bio-grouting (i.e., 99% reduction). This decrease of infiltration rate confirms the formation of $CaCO_3$-clogged sand matrix around the

pile, which was also manifested by the constant S-wave velocities during MICP bio-grouting after the 4th injection (t = 48 hrs). The infiltration rate for Test No. 1 (without MICP bio-grouting) was similar to the initial infiltration rate of Test No. 2 (with MICP bio-grouting) shown in Figure 6.3.

The S-wave velocity profile along the pile length during MICP bio-grouting is shown in Figure 6.4a. Before the beginning of the MICP bio-grouting (t=0 hrs), the S-wave velocity increased approximately linearly with depth, which agrees with Fu et al. (2004) who reported similar S-wave velocity increase for sand in centrifuge tests. During bio-grouting, the S-wave velocities of sensors No. 1, 2, and 3, located at 25 mm from the pile surface and at soil depths of 229, 458, and 687 mm along the pile, showed a clear increase while the S-wave velocities of sensors No. 4 and 7, located at 76 and 203 mm below the pile tip, showed much slower increase. At the end of the MICP bio-grouting (72 hrs), the S-wave velocities had a maximum increase of 5.3 times at sensor No. 1 (25 mm from the pile and 229 mm below soil surface). This increase of S-wave velocity decreased along the soil depth to a minimum increase of 27% at sensor No. 7 (203 mm below the pile tip). Although there is no direct relationship between the S-wave velocities and $CaCO_3$ contents (Al Qabany et al. 2011; Weil et al. 2011; Lin et al. 2016a), this trend indicates that the amount of $CaCO_3$ cementation at the sensors' locations decreased along the pile length. As discussed before, the longer flow path to the pile tip for bacteria, urea, and cementation media resulted in large amount of $CaCO_3$ precipitation (i.e. $CaCO_3$ clogging) along the path, which reduced the increase of the S-

wave velocity at sensors No. 4 and 7 located at 76 and 203 mm below the pile tip. Figure 6.4b shows the S-wave velocity profile at the same depth (458 mm below the soil surface) but with different radial distances from the pile surface. The S-wave velocity at sensor No. 2 (25 mm from the pile) increased by 3.2 times when compared to the measurement before bio-grouting. However, the S-wave velocities at sensors No. 6 and 8 (102, and 305 mm from the pile) showed almost no change. Based on these observations, Figure 6.4b indicates that the $CaCO_3$ precipitated only within a limited zone (less than 102 mm radial distance from the pile surface) along the soil-pile interface.

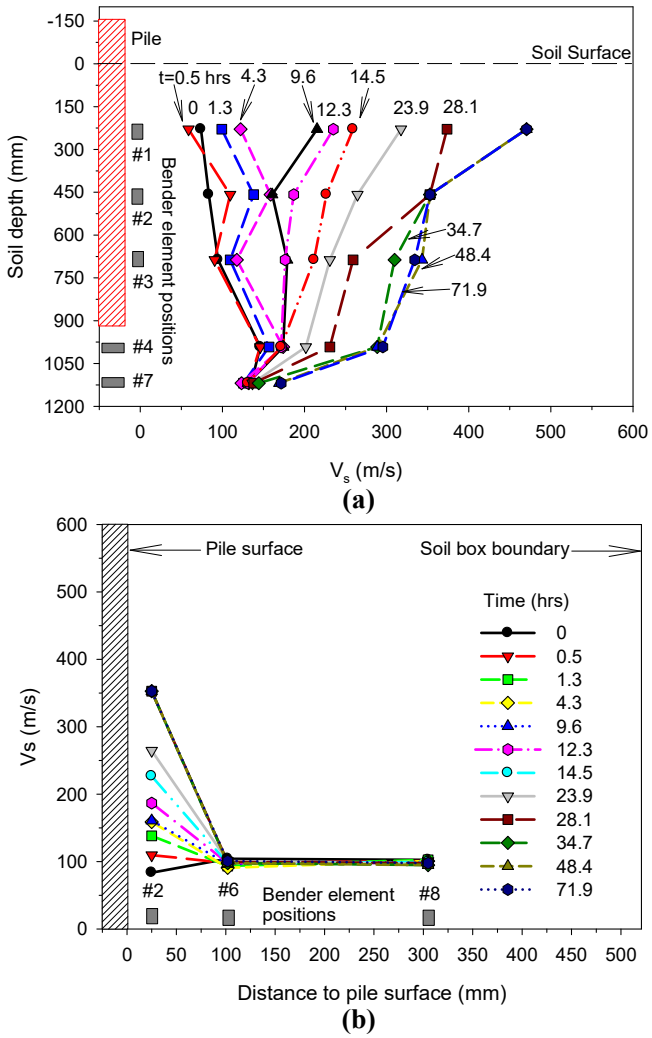

Figure 6.4. Measured S-wave velocities profile versus time during MICP bio-grouting in Test No. 2, (a) at different soil depths; and (b) at soil depth of 458 mm with different distances from the pile.

6.6.2 Load-Displacement Response

The measured vertical load versus displacement at the top of the pile for Test No. 1 (without bio-grouting) and Test No. 2 (with bio-grouting) are shown in Figure 6.5. The load-displacement responses from both tests showed a linear response at the beginning. The stiffness (initial slope of load-displacement response at small

displacements) of Test No. 2 was 2.8 times that of Test No. 1. As the load increased, nonlinear plastic responses were observed followed by large displacement under almost constant load. The ultimate loads for Tests No. 1 and 2 were 5,117 and 12,648 N, respectively, with a ratio of the ultimate loads between MICP-grouted and non-grouted piles of 2.5. It is worth noting that Suleiman et al. (2014) reported that the capacity of tested granular column with similar diameter to the tested pile and length of 864 mm embedded in sand was 2200 N, indicating a ratio of the ultimate loads of the MICP-grouted pervious concrete pile to a granular column of approximately 5.7.

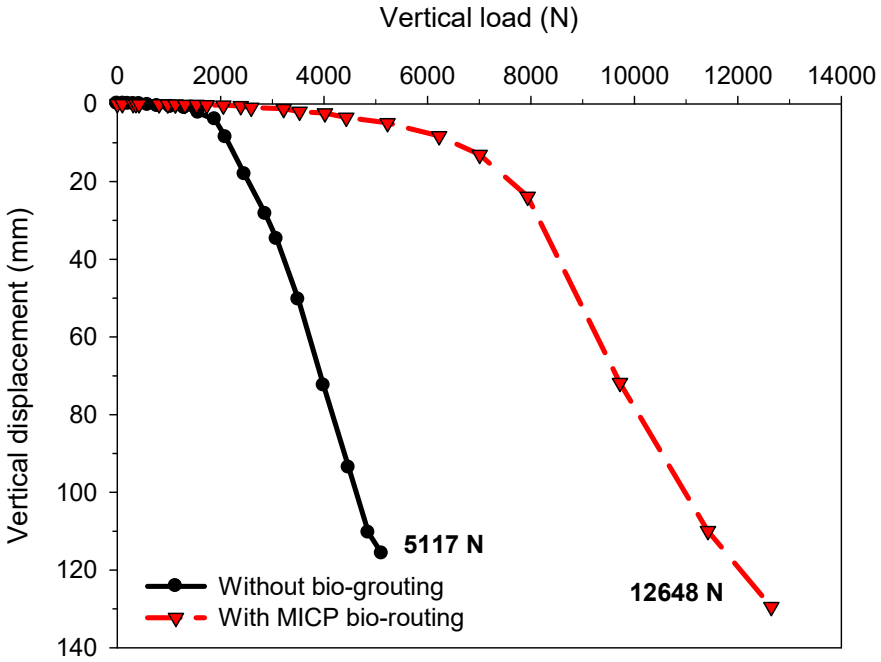

Figure 6.5. Measured vertical load vs. displacement at the top of the pile.

After the tests, soil samples were collected and the pile was inspected. Figure 6.6 illustrates the piles of Test No. 1 and Test No. 2 after soil removal. Comparison of the pile surfaces in Figure 6.6 confirms that a $CaCO_3$-cemented sand zone around the

pile was created during the MICP bio-grouting process, which extended the effective diameter of the pile from 76 to approximately 165 mm, increased the pile length by ~25 mm, and improved its response when subjected to axial compression loading (Figure 6.5). In addition, as shown in Figure 6.6b, soil clumps were also observed surrounding the pile tip, which indicated breaking and failure of the cemented soil around the pile tip under applied loads. Thus, it can be concluded that the soil-pervious concrete pile system treated with MICP bio-grouting experienced shear failure in the cemented soil along most of the pile length and failure of the cemented soil near the pile tip.

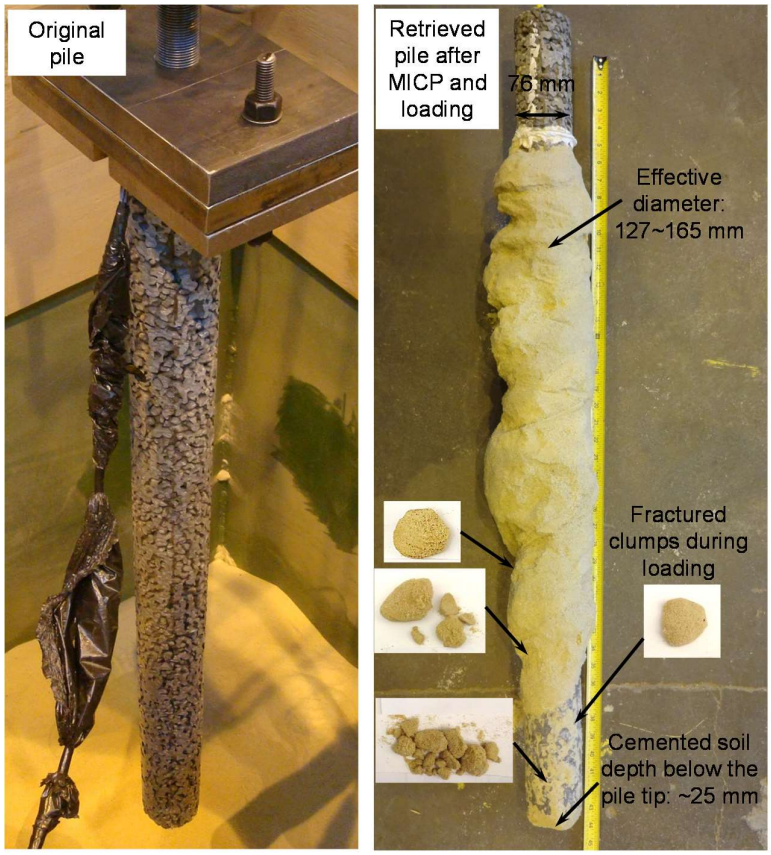

Figure 6.6. Test No. 2 pile (a) original pile before soil placement; and (b) retrieved pile after MICP bio-grouting and loading.

6.6.3 Load Transfer along Pile Length

The load transfer along the pile length for both tests was calculated using measured strains and the initial elastic modulus of the pervious concrete composite section including the steel threaded rebar. Four loading stages, 1306, 2426, 4004, 5117 N were selected to compare the load transfer along the pile length in both tests (Figure 6.7). These four loading stages represent loading from the initial (linear) stage, through the transition stage, to the ultimate load for Test No. 1. As shown in Figure 6.7, the load transfer rate (e.g. slope of the curve or unit friction) of Test No. 2 (with MICP bio-grouting) is up to 3.5 times higher than that of Test No. 1 (without bio-grouting). The maximum unit friction, which was located between depths of 0 mm and 406 mm at applied load of 5117 N, was 6.5 N/mm for Test No. 1 and 10.2 N/mm for Test No. 2, indicating that the MICP bio-grouted pile (Test No. 2) had a 57% higher load-transfer rate through shaft resistance than the pile without bio-grouting (Test No. 1). It is worth noting that the location of the maximum load transfer rate of Test No.2 (0 to 203 mm depth) approximately correspond with the location of maximum S-wave velocities (e.g. bender element No. 1) achieved during the MICP treatment (Figure 6.4) and higher $CaCO_3$ content along the pile (discussed later in the paper). To estimate the tip resistance, the load transfer curves were extended to the pile tip as shown in Figure 6.7 (i.e. lines extended to the horizontal dashed line at the pile tip). At applied load of 5,117 N, the tip resistances were 2,300 N for Test No. 1 (i.e. shaft friction resisted 56% of the applied load) and 200 N for Test No. 2 (i.e. shaft friction resisted 96% of the applied

load). At the ultimate load of Test No. 2 (12,648 N), the tip resistance was 1,200 N, which was approximately 9% of the applied load (i.e. shaft friction resisted 91% of the applied load), indicating that the improved capacity and load transfer rate of Test No. 2 are mainly attributed to the increase of the shaft resistance. It is worth noting that McVay et al. (2009) reported that the capacity of a jetted precast concrete pile treated by compaction grouting along the pile and at the pile tip in loose silty sand increased by two to three times when compared to the same size driven pile. However, McVay et al. (2009) attributed this capacity improvement to tip resistance because the shaft resistance showed negligible improvement, which was attributed to the poor bonding between the grout and the pile as a result of high grouting pressure. When compared to the jetted precast concrete pile using compaction grouting reported by McVay et al. (2009), the pervious concrete pile treated with MICP bio-grouting showed a significant improvement of shaft resistance as a result of the cemented soil-pile system, which could be attributed to the permeability of pervious concrete pile and the use of percolation bio-grouting (no pressure was applied).

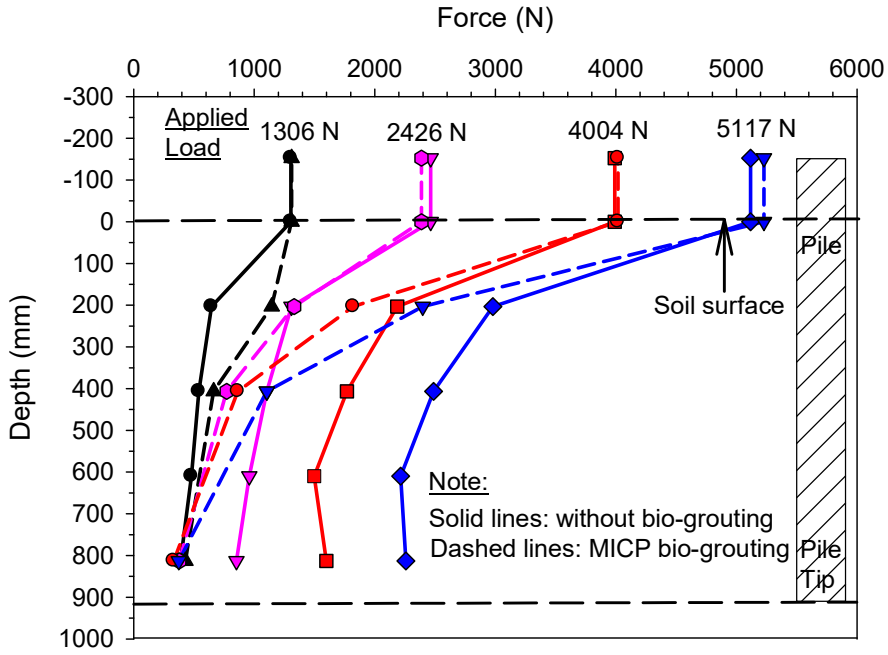

Figure 6.7. Comparison of force transferred along pile length for Test No. 1 without bio-grouting (solid lines) and Test No. 2 with MICP bio-grouting (dashed lines) at different loading stages.

6.6.4 S-Wave Velocities during Loading

Figure 6.8 compares the measured S-wave velocities during loading from Test No. 1 (without bio-grouting) and Test No. 2 (with MICP bio-grouting). The S-wave velocities of sensors No. 1, 2, and 3 from Test No. 1 showed almost constant or small increases with increasing load. The S-wave velocities of Test No. 2 showed decrease at small loads followed by approximately constant S-wave velocities, which indicates disturbance or breakage of the $CaCO_3$ bond in the sand matrix. After applied load of 4,448 N, the curves showed a decrease with higher rate, which could be attributed to the massive breakage of the $CaCO_3$ bond. At the end of the test, the S-wave velocities along the pile length of Test No. 2 decreased to values similar to the S-wave velocities

measured during Test No. 1. Below the pile tip, S-wave velocity of sensor No. 4 (76 mm below the tip of the pile) in Test No. 1 increased with the increasing load and reached a constant value, which could be attributed to the increase of soil density and load transferred to the sensor location. While, S-wave velocity of sensor No. 4 in Test No. 2 decreased with the increasing load to reach values similar to that in Test No. 1. S-wave velocities of sensor No. 7 (203 mm below the tip of the pile) of Test No. 2 showed only very small decrease under loading (data not shown in Figure 6.8).

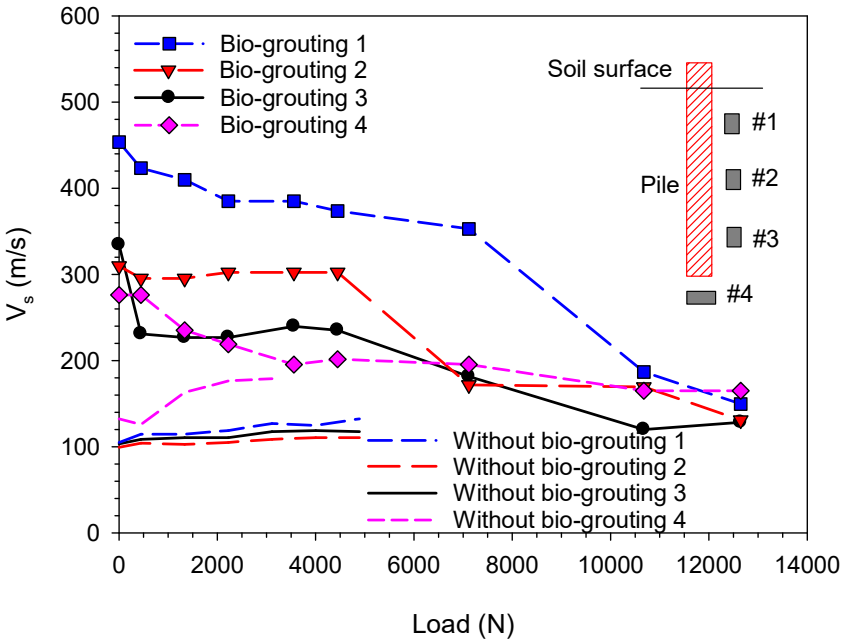

Figure 6.8. Measured S-wave velocities versus applied load during vertical loading from both tests.

6.6.5 Vertical and Horizontal Soil Pressures

Figure 6.9 illustrates the variation of the measured change of soil pressures during compression loading. As shown from Figure 6.9, the measured change of

vertical pressures from sensors No. 1, 2 and 3 in both tests showed a nonlinear increase. Under the same vertical load of both tests, the change of soil pressure of sensor No. 3 (152 mm below the pile tip) showed the highest increase rate. Furthermore, sensor No. 2, located at 229 mm below the pile tip, recorded a lower increase rate compared to that of sensor No. 3, but a higher increase rate compared to sensor No. 1 (305 mm below the pile tip). For applied loads smaller than 2,000 N in Test No. 2, sensors No. 1, 2, and 3 experienced negative soil pressure changes, which was not observed in Test No. 1. This negative soil pressure changes could be attributed to the dilatancy of MICP-treated soils (Lin et al. 2016a). Comparison of the pressure changes of sensors No. 1, 2, and 3 between Test No. 1 and 2 showed that the increase rate of the pressures from Test No. 2 was lower than that of the pressure change from Test No. 1, which is consistent with the conclusion that bio-grouted pile resisted applied loads mainly by shaft resistance. The transferred loads at the location of in-soil null pressure sensor No. 3 calculated from its pressure change measurement was close to that interpolated value using strain measurement near the pile tip (average difference of 10%), confirming the accuracy of the pressure change measured by in-soil null pressure sensors.

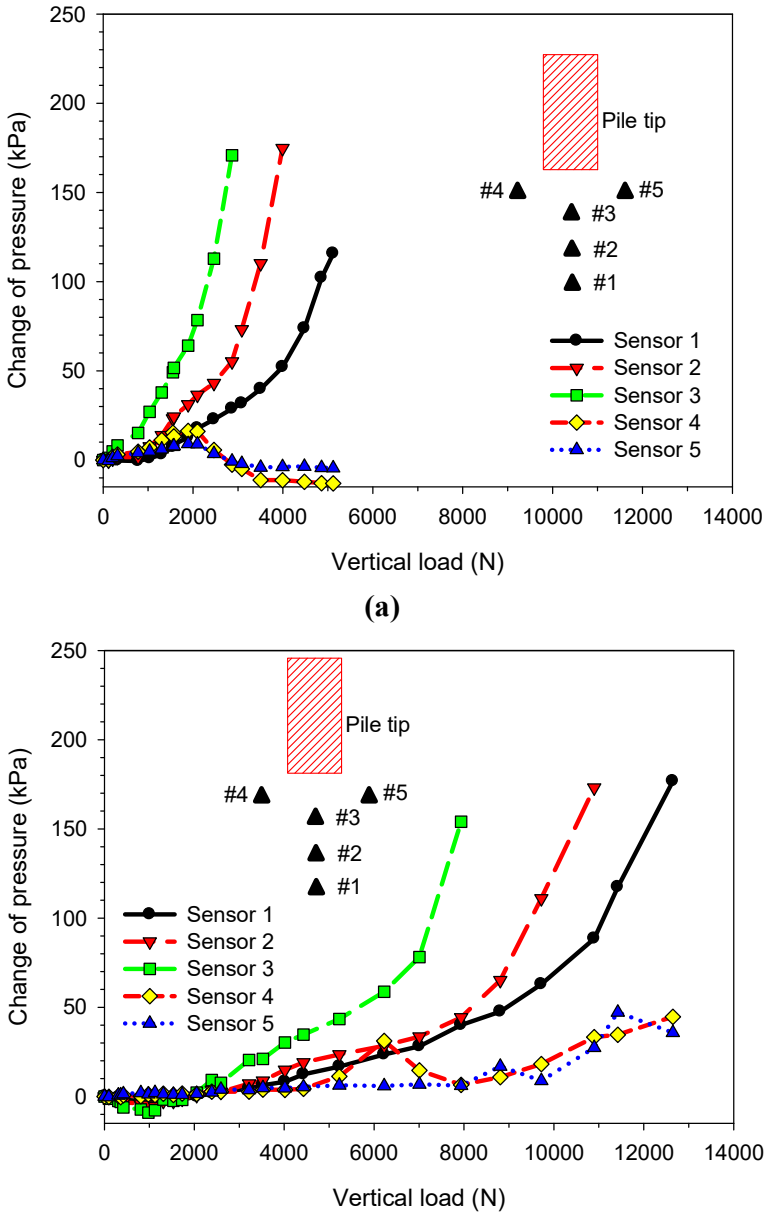

Figure 6.9. Change of soil pressure during vertical loading for: (a) Test No. 1; (b) Test No. 2.

The soil horizontal pressure change was also monitored during the tests using sensors No. 4 and 5 (located at a depth of 25 mm below the tip of the pile at a horizontal distance of 38 mm from the pile surface). During the compression loading of Test No.

1, the change in horizontal pressures increased until the pile passed the location of the sensors (Figure 6.9. Then, the horizontal pressure change started to decrease as the pile advanced deeper. This pressure trend could be attributed to cavity expansion followed by shearing along soil-pile interface, which is similar to the results reported by Basu et al. (2011), who conducted one-dimensional (1D) finite-element analysis, and measurements reported by Suleiman et al. (2014 and 2015). The negative changes of soil pressures were also observed from sensors No. 4 and 5 in Test No. 2 when the applied load was smaller than 2,000 N. For loads larger than 2,000 N, the change of the horizontal soil pressure from sensors No. 4 and 5 increased until the pile passed the location of the sensors. However, the horizontal pressure change started to increase again as the pile advanced deeper. This could be attributed to an enlarged cavity created by the extended diameter of pile-cemented soil system during pile advancement as confirmed by inspecting the pile after soil removal (Figure 6.6b). It is worth noting that in-soil null pressure sensors No. 4 and 5 present very similar pressure change shown in Figure 6.9a and b, validating the repeatability of the sensor measurements.

6.6.6 Moisture, Calcium Carbonate and Ammonium Contents in Sand

As mentioned previously, 16 L of water was injected into the pile of Test No. 1 in order to maintain similar moisture content at the soil-pile interface for both tests. The measured moisture contents were between 0% and 6%, with an average of 2.9% at soil-pile interface. The moisture contents in Test No. 2 were also between 0% and 6%, with

an average of 2.3% at soil-pile interface, which validates similar moisture content conditions between both tests.

Figure 6.10a shows a cross-section of the measured $CaCO_3$ content contour in the soil box from Test No. 2. The contour was calculated using the results of 150 sand samples taken cross the soil box. The dashed line shown in Figure 6.10a is the pile profile after soil removal (i.e., showing the pile and soil cemented to it after the test), which approximately matches the $CaCO_3$ contour. This contour shows that the precipitated $CaCO_3$ extended to small distance from the pile (~100 mm). As shown in Figure 6.10a, bender elements located within the $CaCO_3$ cemented zone indicated significant measurement changes (see Figure 6.3 and Figure 6.4). Figure 6.10b illustrates the $CaCO_3$ content at different distance from the pile surface at four different soil depths along the pile length. The distribution of $CaCO_3$ was not uniform. The $CaCO_3$ content at soil depth of 229 mm were highest and then started decreasing along the pile depth, which could cause the higher load transfer rate at shallow soil depth shown in Figure 6.7. The average $CaCO_3$ content along the soil-pile interface at different depths was 2.7%. The $CaCO_3$ content (6.5%) at the pile tip (soil depth 916 mm) was 2.4 times higher than the average $CaCO_3$ content at the soil-pile interface (Figure 6.10a and b). In addition, it is worth noting that the distribution of $CaCO_3$ as a function of distance from the pile (Figure 6.10b) matched the S-wave velocity profile shown in Figure 6.4b. The measured $CaCO_3$ content clearly illustrates that the small $CaCO_3$-cemented zone around the pile was successfully realized in Test No. 2. Based

on the pile profile after soil removal (the pile and soil cemented to it after the test), the approximate average location of failure surface in the cemented soil-pile system after compression loading is shown in Figure 6.10b, demonstrating that the average $CaCO_3$ content at the failure surface ranged from 0.5% to 1.5%.

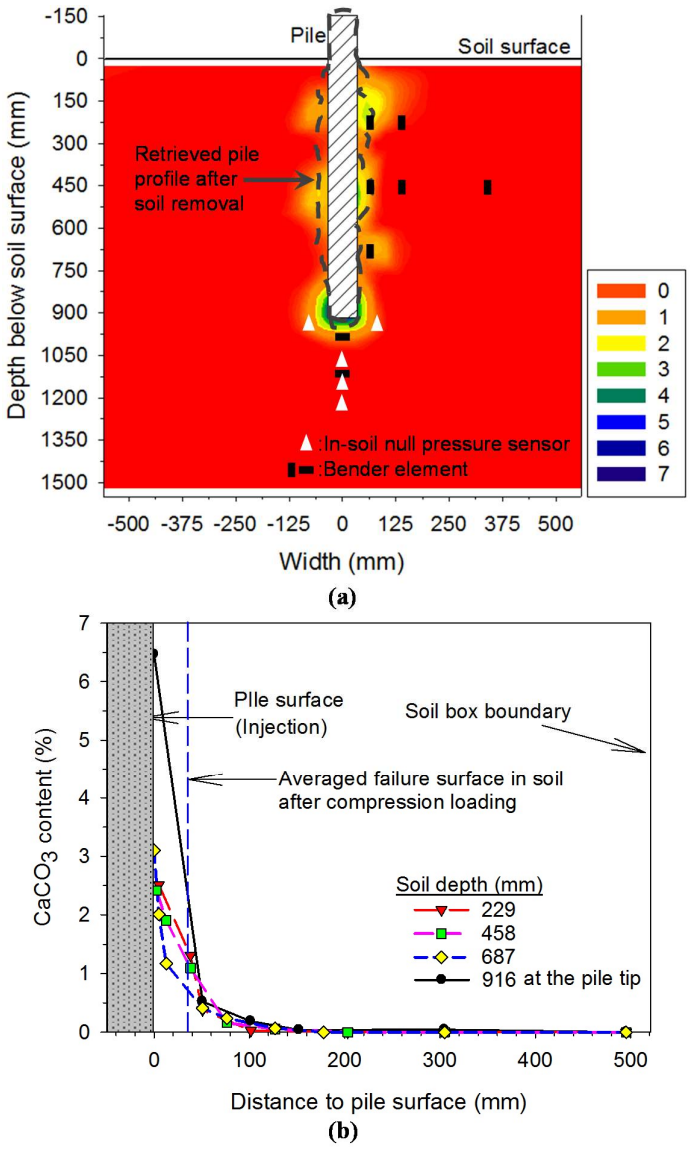

Figure 6.10. $CaCO_3$ content: (a) color contour and retrieved pile profile in soil box; and (b) content as a function of distances to pile at several soil depths.

The ammonium contents of 30 samples from Test No. 2 were measured. The ammonium concentration from the collected sand samples was between 0 mM to 100 mM. The average ammonium content around the pile was 45.2 mM. This high ammonium content was mainly attributed to the addition of 20g/L NH_4Cl in the recipes of urea and cementation media. It is worth noting, however, that no after-grouting flushes were made to try to reduce the concentration of ammonium.

6.6.7 Crystal Characteristics of $CaCO_3$ in Sand

SEM images of soil samples collected at different locations close to the pile surface and tip are shown in Figure 6.11. Based on the shape of $CaCO_3$ crystals shown in Figure 6.11, two types of $CaCO_3$ morphologies, calcite and vaterite crystals, were present in the sand samples (Lin et al. 2016a). Van Paassen (2009) concluded that the type of $CaCO_3$ crystals were determined by the urea hydrolysis rate. Calcite and vaterite are produced under low and high hydrolysis rate, respectively. Figure 6.11a, b, and c show three soil samples collected at the same soil depth of 152 mm but at different distances from the pile. The soil samples at distances of 13 and 51 mm indicate massive rhomboidal calcite crystals and small amount of spherical vaterite crystals around soil particles. Energy Dispersive X-ray analysis (EDS) of soil sample at a distance of 200 mm shows no $CaCO_3$ (figure not shown). Figure 6.11d, e, and f show three soil samples collected at the same distance (13 mm from the pile surface) but at different depths. Soil samples at depths of 152 and 635 mm show massive rhomboidal calcite crystals

and small amount of spherical vaterite crystals around soil particles. In contrast, soil sample at a depth of 916 mm (0 mm below the pile tip) shows large amount of spherical vaterite crystals covering soil particles and clogging the pore space, which could be attributed to a higher urea hydrolysis rate at the tip of the pile (van Paassen 2009). This high urea hydrolysis rate at the pile tip may be achieved by the accumulated bacteria which induced large amount of $CaCO_3$ precipitation around the pile tip as shown in Figure 6.10a and b. It is not clear, however, if the type of crystal formation affect the observed significant increase in shaft resistance along the pile.

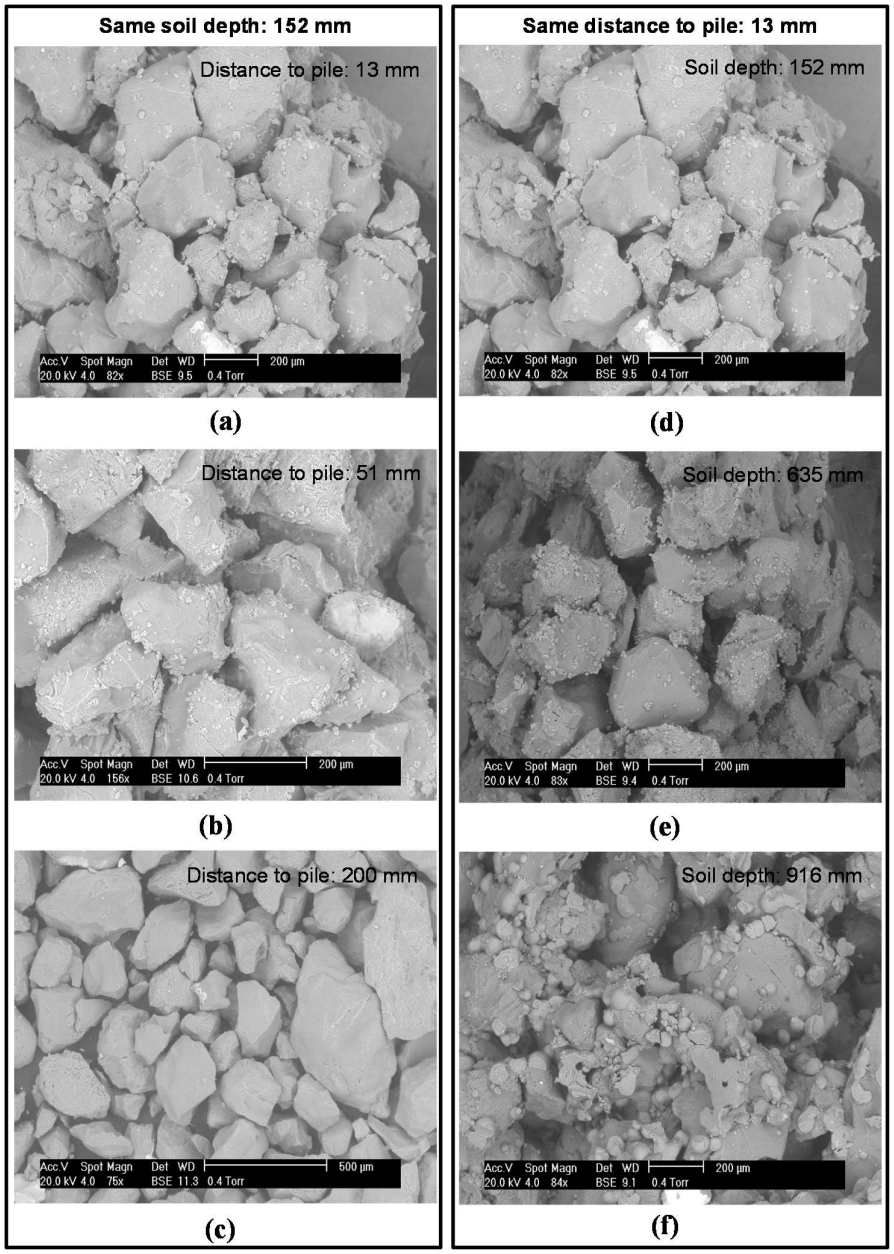

Figure 6.11. SEM pictures of samples obtained at different distances from the pile (a, b, and c) and different depths (d, e, and f).

6.7 SUMMARY AND CONCLUSIONS

This paper focuses on investigating the feasibility of enhancing the axial compression response of pervious concrete ground improvement piles using MICP bio-

grouting. This technique avoid the practical problems of bio-clogging associated with large soil volumes. Two instrumented pile tests without and with MICP bio-grouting (Test No. 1 and 2, respectively) were performed at the SSI facility at Lehigh University. The measured pile response, S-wave velocities, moisture content, $CaCO_3$ and ammonium contents, and crystal characteristics of $CaCO_3$ were analyzed. Based on the results presented in this paper, the following conclusions are drawn:

1. At the end of the MICP bio-grouting, the S-wave velocity measurements close to the pile (25 mm distance along the pile and 203 mm below the pile tip) showed an average increase of 2.5 times compared to the measurements before bio-grouting due to the formation of $CaCO_3$ cemented-soil zone around the pile. In addition, the infiltration rate of the soil-pile system decreased by up to 99% due to the same reason. The S-wave velocity and infiltration rate can be used to monitor future field tests of permeable piles with bio-grouting.
2. During bio-grouting, the increase of S-wave velocity decreased along the pile length to a minimum increase below the pile tip. Based on the S-wave measurements at same soil depth of 458 mm, the cemented soil zone surrounding the pile is limited to approximately 100 mm.
3. The stiffness (initial slope) of the load-displacement response and the ultimate load increased to 2.8 and 2.5 times of that of non-grouted pile, respectively, validating the significant effects of limited-zone bio-grouting on enhancing the response of axially loaded permeable piles.

4. The load transfer rate (slope of the curve or unit friction) of Test No. 2 was up to 3.5 times higher than that of Test No. 1 as a result of a limited $CaCO_3$ cemented-soil zone around the pile. The maximum load transfer rate occurred at shallow soil depth of 0 to 203 mm, which corresponds to the maximum S-wave velocity increase and highest $CaCO_3$ content along the shaft.
5. Bio-grouting significantly increased the shaft resistance along the length of the pile (from 56% of the applied load for non-grouted pile to more than 90% of the applied load for bio-grouted pile). The longer flow path to the pile tip for bacteria, urea, and cementation media and corresponding $CaCO_3$ clogging along the path may have minimized the effects of bio-grouting on tip resistance. Unlike previous attempts using jetted precast concrete pile treated by compaction grouting where shaft resistance showed negligible improvement, the pervious concrete pile treated with MICP bio-grouting showed a significant improvement of shaft resistance, which could be attributed to the permeability of pervious concrete pile and the use of percolation bio-grouting (no pressure was applied).
6. The dilatancy of MICP-treated soils may be responsible for the negative pressure changes measured below the bio-grouted pile tip at small applied loads, which was not observed for the non-grouted pile.
7. The measured $CaCO_3$ contents at several locations surrounding the pile show that the precipitation of $CaCO_3$ is not uniform and extended to approximately 100 mm surrounding the pile, which is consistent with indications from the S-wave measurements.

8. The pile profile after soil removal (the pile and soil cemented to it after the test) indicate that the average $CaCO_3$ content at the failure surface in the cemented soil-pile system ranged from 0.5% to 1.5%.
9. Calcite crystals were observed along the shaft, while spherical vaterite crystals were observed at the pile tip. It is not clear if the type of crystal formation affect the observed significant increase in shaft resistance along the bio-grouted pervious concrete pile.

7. EBEHAVIOR OF BIOFIM CEMENTED SAND

7.1 INTRODUCTION

The world population is expected to increase by ~33% by the year of 2050 (Lee, 2012). Therefore, the demand of sustainable civil infrastructures will continue to increase. Biomediated soil modification offers the potential for sustainable solutions to geotechnical problems (DeJong et al. 2011 and 2013). It involves subsurface microbiology-regulated geochemical process, including bio-mineralization, biofilm formation, and bio-gas generation (Ivanov and Chu 2008; DeJong et al. 2010). The research on bio-mineralization and bio-gas generation and their application potentials on geotechnical engineering has been well-documented (DeJong et al. 2006; Whiffin et al. 2007; Kavazanjian et al. 2009; Van Paassen 2009; Chou et al. 2011; Rebata-Landa and Santamarina 2012; Al Qabany and Soga 2013; Burbank et al. 2013; He et al. 2013; Montoya et al. 2013; Cheng et al. 2014; He and Chu 2014; Lin et al. 2016a). However, the application potentials of biofilms still require further investigation.

The biofilm is a combination of microbial cells and associated exopolysacharide (EPS). The common view of the biofilm formation starts with adhesion of individual cells to a solid surface, and then followed by cell replication and EPS secretion which binds the cells to a surface, eventually forming a complex three-dimensional biofilm structure (Bryers and Characklis 1981; Alavi and Belas 2001; Dunne 2002; Gilbert et al. 2013). Biofilms can grow in many locations, such as water distribution and

collection systems, landfill leachate drainage systems, etc., which may sometimes clog those pipeline systems (Fleming, et al. 1999; Flemming 2002; Yan et al. 2009). Biofilm accumulation in soil will also cause a reduction of permeability by decreasing the available pore volume and changing the shape of pore spaces (Taylor and Jaffe 1990; Stewart and Fogler 2000; Rockhold et al. 2002). These phenomenon are usually referred to as bioclogging. For example, hydraulic conductivity of compacted silty sand was reduced by 2 to 3 orders of magnitude by adding exopolysacharide (EPS)-producing bacteria (*Beijerinckia indica*), which can be used as a low cost soil stabilization additive for containment barriers and landfills (Dennis and Turner, 1998).

Biofilm accumulation in porous media depends on microbial adsorption and metabolic activities on surfaces, which involve many short-range forces such as dipole-dipole interactions, dipole-induced dipole interactions, ion-dipole interactions, hydrogen bonding, hydrophobic interactions, or polymeric bridging, etc. (Robb 1984; O'Toole et al. 2000; Donlan 2002; Palmer 2007). These forces may provide additional cohesion for shear resistance of the sand matrix. On the other hand, the lubricating properties of the biofilm resulting from its viscous property may lead to a decrease of the inter-particle friction leading to a reduction of soil shear resistance (Perkins et al. 2000). These short-range bonding forces along with the viscous nature of the biofilm will affect the mechanical behavior of soil interactively. The research on mechanical behavior of biofilm-cemented soils is very limited and shows contradictory conclusions. For example, Perkins et al. (2000) showed that *Klebsiella oxytoca*-produced biofilm

has negligible influence on the strength and stiffness of the sand using triaxial and oedometer tests. Daniels et al. (2009) concluded that *Beijerinckia indica*-produced biofilm has a decreasing effect on the soil strength of clay and clayey sand using unconfined compression tests. Banagan (2010) reported that the shear strength of Ottawa 30 sand estimated using vane shear test was increased by 15.2~87.5% by adding biofilm-forming bacteria *Flavobacterium johnsoniae*.

To further investigate the mechanical behavior of biofilm-cemented sand, three types of tests at variable conditions were conducted. Because the environment in the saturated sand matrix is usually anaerobic (Mitchell and Santamarina, 2005), an anaerobic test was designed to determine whether the selected bacteria *Staphylococcus epidermidis* (*S. Epidermidis*, ATCC 35984) can grow under anaerobic condition using nitrate as electron acceptor. Then, a syringe test was designed to investigate the biofilm growth and morphology in the sand matrix under anaerobic condition. Finally, triaxial test was utilized to investigate the mechanical behavior of sand treated by *S. Epidermidis* biofilm. This paper presents the equipment, material properties, experimental procedures, and results of each test.

7.2 EQUIPMENT

Three types of tests (anaerobic test, syringe test, and triaxial test) were used to investigate the bacteria metabolic activity under anaerobic condition, the biofilm

growth and morphology in the sand matrix, and the mechanical behavior of sand treated by biofilm (Figure 7.1).

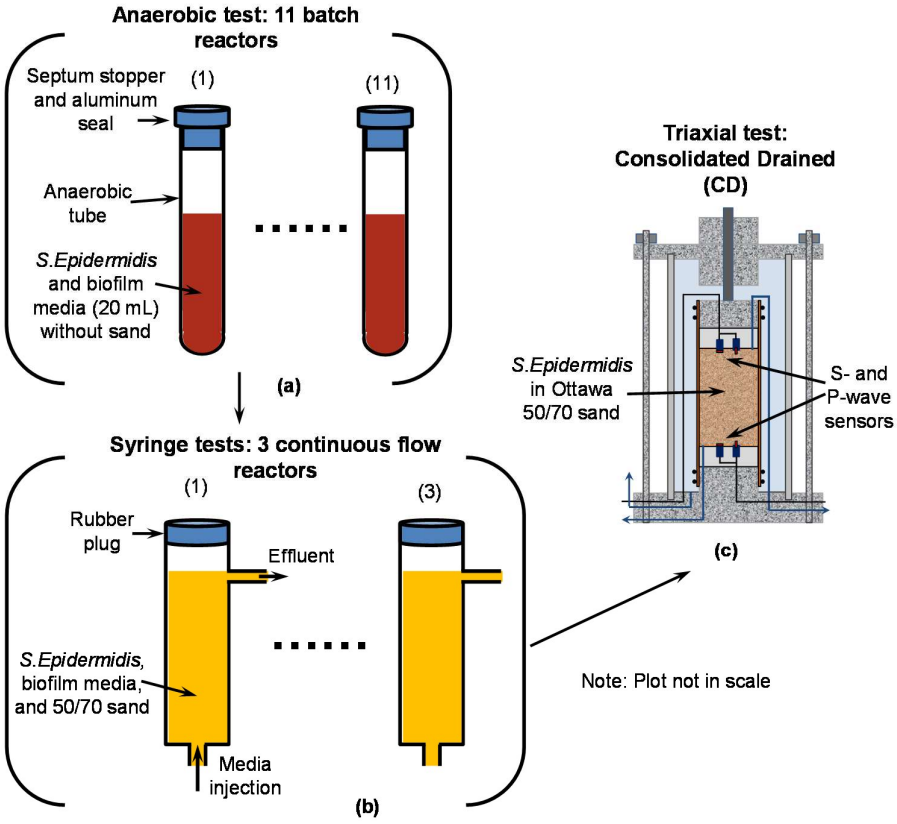

Figure 7.1. Test plan and setup: (a) anaerobic batch reactor; (b) continuous flow reactor; (c) triaxial test.

The anaerobic test was mainly used to understand the growth activity of *S. Epidermidis* under anaerobic condition. The anaerobic test consists of 11 anaerobic batch reactors in which each reactor consists of an anaerobic tube, septum stopper, and aluminum seal with bacteria and biofilm medium but without sand (Bellco Glass, Inc. Figure 7.1a and Figure 7.2a). The syringe test was used to investigate the biofilm growth and morphology in the sand matrix under anaerobic condition. The syringe test

consists of three 60 mL syringes which were used as continuous flow reactors filled with sand. The bottom port of the syringe was connected with a peristaltic pump (Cole-Parmer, L/S tubing pump). Above the 60 mL mark, an effluent tube was inserted into the syringe serving as an effluent port (Figure 7.1b and Figure 7.2b). Triaxial test was utilized to evaluate the mechanical behavior of *S. Epidermidis* biofilm-cemented sand. In addition, shear and compression wave (S-and P-wave) sensors were fabricated at two ends of the sample caps to monitor the sand modulus variation during biofilm growth and compression loading (Figure 7.1c and Figure 7.2c). The detailed fabrication and equipment setup of S-and P-wave sensors can be found in Lin et al. (2016a).

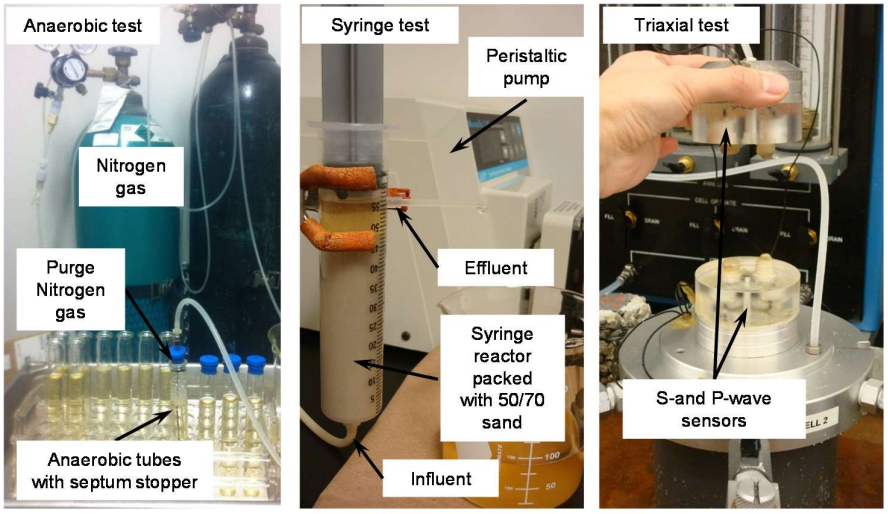

Figure 7.2. Test equipment and sensors: (a) anaerobic batch reactor and the process of purging nitrogen gas; (b) syringe continuous flow reactor and peristaltic pump; and (c) triaxial test equipment with S-and P-wave sensors.

7.3 MATERIALS AND BACTERIA PREPARATION

7.3.1 Soil Properties

The soil used in the test was Ottawa 50/70, which is classified as poorly graded sand (SP) using the Unified Soil Classification System. Ottawa 50/70 sand has a particle diameter at 10% finer by mass (D_{10}) of 0.26 mm, a particle diameter at 50% finer by mass (D_{50}) of 0.33 mm, a coefficient of uniformity (C_u) of 1.43, a coefficient of curvature (C_c) of 1.01, and maximum and minimum void ratio (e_{max} and e_{min}) of 0.87 and 0.55. The sand has greater than 98.7% silica (SiO_2). The sand was dried in an oven at 105 ^oC for 24 hours before being used. The target relative density in the test was 40%.

7.3.2 Bacteria Preparation and Media Recipes

Staphylococcus epidermidis (ATCC 35984), facultative anaerobic and gram-positive bacteria, was used for this research to induce biofilm formation in sand matrix. Although *S. epidermidis* was not a soil native bacterium, it was chosen for this study because of its produced extracellular polysaccharide adhesion, which could help biofilm better cement sand particles (O'Gara and Humphreys 2001). *S. epidermidis* has spherical shape, 0.5-1.5 μm in diameter, and can produce a type of EPS that acts as glue, which helps it grow in sticky clumps and biofilms (O'Toole et al. 2000). The stock culture of *S. epidermidis* was innoculated into sterilized Tryptic Soy Broth (TSB) growth media and grown in an incubator shaker at 120 rpm and 33^oC for approximately

24 hours until OD_{600}=1.1~1.6. Then, the bacteria solution was immediately injected into the sand matrix.

During the tests, the TSB was amended with NO_3^- as the electron acceptor (biofilm medium: TSB, and 3 mM KNO_3 for anaerobic and syringe tests, 6 mM KNO_3 for triaxial test because of its higher pore volume compared to that of the previous two test) were injected continuously from the bottom port of the sample. The detailed treatment procedure will be introduced next.

7.4 EXPERIMENTAL PROCEDURES

For the anaerobic test, the eleven batch reactor tubes were filled with 20 mL of biofilm medium (Figure 7.1a). To create an anaerobic environment in each tube, a pipetting needles (Cadence Inc., 152.4 mm long) was inserted into the septum stopper and lowered down into the biofilm medium to purge nitrogen gas for 6 minutes (Figure 7.2a). The needle was then moved above the biofilm medium surface to purge with nitrogen gas in the headspace for 1 minute. After purging, each tube was sealed with a septum stopper and aluminum seal. The tubes were then autoclaved for sterilization. Once the tubes cooled down to room temperature, 0.5 mL of *S. Epidermidis* suspension with the target optical density (1.1~1.6) was added into each tube. The experiment started immediately after the bacteria injection (e.g. time is 0). During the test, anaerobic tubes No. 1-11 were sequentially stopped at 14, 19, 28, 31, 36, 40, 46, 59, 70,

79, and 97 hours, and the bacteria density (OD_{600}), pH, and nitrate concentration were then measured.

For the syringe test, sand was wet-rained into the syringe to have a target relative density of 40% (Chaney and Mulilis 1978). A rubber plug was then placed above the effluent tube for air sealing. During the test, all flow rates were set at 0.33 mL/min. First, 40 mL 75% ethanol (2 pore volumes of the sand matrix) was injected to sterilize the sand matrix and this was then followed by 200 mL (10 pore volumes) of sterilized deionized water to wash ethanol out of the sand matrix. Next, 40 mL of *S. Epidermidis* suspension (2 pore volumes) with target optical density (1.1~1.6) was pumped into the syringe through the bottom port. The bacteria suspension was kept in the sand matrix for approximately 8 hours to allow the bacteria to attach to the sand surface. After 8 hours, biofilm medium was introduced through the bottom port. The effluent solution was monitored continuously to measure the bacteria density (OD_{600}), pH, and nitrate concentration. The biofilm medium injection was stopped after 3 days for syringe No. 1, 6 days for syringe No. 2, and 10 days for syringe No. 3. After the test, samples (~40 g) were saved from all three syringes to measure the biomass content in the sand matrix. The samples were first dried in the oven and weighed at 105 ^{o}C. Samples were then dried and weighed in the muffle furnace at 550 ^{o}C. The difference of these two weights is the weight of the biomass, and the biomass content can be calculated by dividing the biomass weight by the weight of the sand only. Additional samples were also saved for

Scanning Electron Microscope (SEM) imaging (FEI XL30) to investigate the biofilm morphology at the micro-/particle-scale.

Triaxial test specimens 72 mm in diameter and 145 mm in height were prepared using the wet-raining method (Chaney and Mulilis 1978). a vacuum pressure similar to the target confining pressure during the test (100 kPa) was applied to the specimens. The average measured void ratio (e) after vacuum consolidation was 0.74 for the 50/70 sand specimen, corresponding to relative density of 41%. After filling the triaxial cell with water, the vacuum pressure was decreased by 10 kPa and the cell pressure increased simultaneously by 10 kPa until the cell pressure increased to the target confining pressure of 100 kPa and the vacuum pressure returned to 0 kPa. The same peristaltic pump used for the syringe tests was utilized to introduce bacteria and biofilm medium through the bottom port of the triaxial cell. The flow rate was set at 1.5 mL/min throughout the test. The solution injection scheme was similar to the procedure used for the syringe test, including 2 pore volumes of 75 % ethanol, 10 pore volumes sterilized deionized water, 2 pore volumes of *S. Epidermidis*, and biofilm medium injected continuously for 10 days (one pore volume equals 250 mL). During biofilm medium injection, the bacteria density (OD_{600}), pH and nitrate concentration of the effluent solution was monitored at an average interval of 8 hours. In addition, the S-and P-wave velocities were measured during biofilm medium injection. The biofilm medium injection was stopped after 10 days. Then, sample saturation and loading was conducted. Triaxial specimens were back pressure saturated until the B value (pore water pressure

ratio) exceeded 0.95. Following saturation, the specimens were loaded by displacement control with a loading rate of 0.5 mm/min (0.34% axial strain/min) until the axial strain was approximately equal to 10%. During loading, the S-wave velocity was measured with a sampling rate of 1 sample/0.1% axial strain up to an axial strain of 1% and 1 sample/0.35% axial strain afterwards. After loading, samples (~30 g) were collected along the height of the specimen to measure the biomass content in the specimen. It is important to note that all tests were successfully duplicated to verify repeatability and validate the results.

7.5 EXPERIMENTAL RESULTS

7.5.1 Anaerobic Test

The variation of OD_{600}, pH, and nitrate concentration versus time during anaerobic batch reactor test are presented in Figure 7.3. The OD_{600} increased with time up to 60 hours followed by a stationary stage until 80 hours. At the end of the test, OD_{600} decreased due to the depletion of growth substrate in the batch reactor (Figure 7.3a). The pH decreased with time from 6.9 at the beginning of the test to 5.9 at 45 hours. Then the pH reached a stationary phase. The curve of the nitrate concentration (Figure 7.3b) showed a similar trend as the pH. The variation of the OD_{600}, pH and nitrate concentration showed that the anaerobic batch reactors reached the steady state after 60 hours. The increase of OD_{600} combined with the reduction of the nitrate

concentration indicated that *S. Epidermidis* could utilize nitrate as electron acceptor to grow under anaerobic conditions (e.g. denitrification).

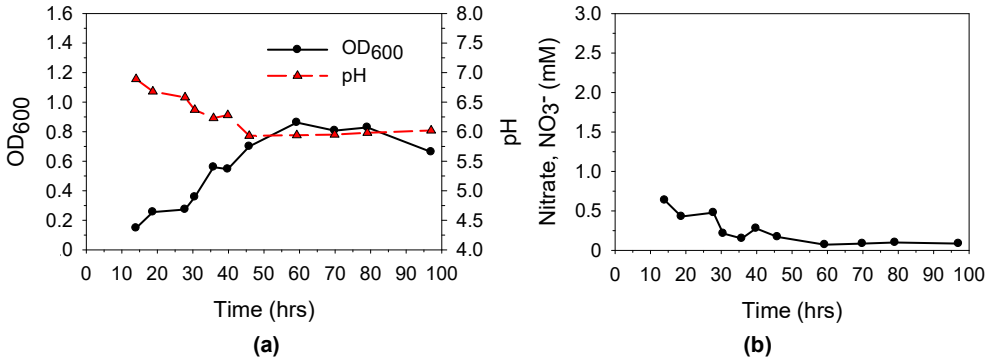

Figure 7.3. Anaerobic test results: (a) OD_{600} and pH versus time; (b) nitrate concentration versus time.

7.5.2 Syringe Test

The variation of OD_{600} versus time for syringes 1, 2, and 3, which were treated with biofilm for three different time (3, 6, and 10 days, respectively) are presented in Figure 7.4. The OD_{600} measured from all three syringes show a similar trend. The OD_{600} initially decreased and then increased, combined with fluctuations afterwards. The variation of the pH from all three syringes also showed a similar trend (Figure 7.4b). The pH initially increased showing a small peak and then decreased reaching a steady state. All these syringes had a similar nitrate concentration variation (Figure 7.4c). The curve of the nitrate concentration shows a similar trend as that of the pH. The results of OD_{600}, pH, and nitrate concentration include that the bacteria grew well in the sand matrix and the syringe reactors No. 2 and 3 researched steady state. In order to analyze the biomass content versus time, the biomass content of three syringes was measured

(Figure 7.4d). The biomass content increased with time at the beginning and then reached a stationary stage. This stationary stage indicates that the syringe reactor system reached a steady state, which was also confirmed by the pH and nitrate concentration results.

To confirm the biofilm was formed in the sand matrix, samples were used for SEM imaging to analyze its morphology. SEM images of clean sand (without biofilm treatment), sand samples with different biofilm treatment (3 and 10 days), and a magnified biofilm image are provided in Figure 7.5. The untreated sand shows uncemented angular shape typical of sand particles. The images of sand samples containing biofilm show that the biofilm (marked by arrows) cemented and grew around the sand particles. The biofilm content filling the pore space and cementing the sand particles (marked by the red arrows in Figure 7.5b and c) increased over time. This increase is consistent with the biofilm content measurement (Figure 7.4d, biofilm content increased from 2.6 to 9 mg/g). As seen in Figure 7.5d, the biofilm consisted of many spherical bacterial cells.

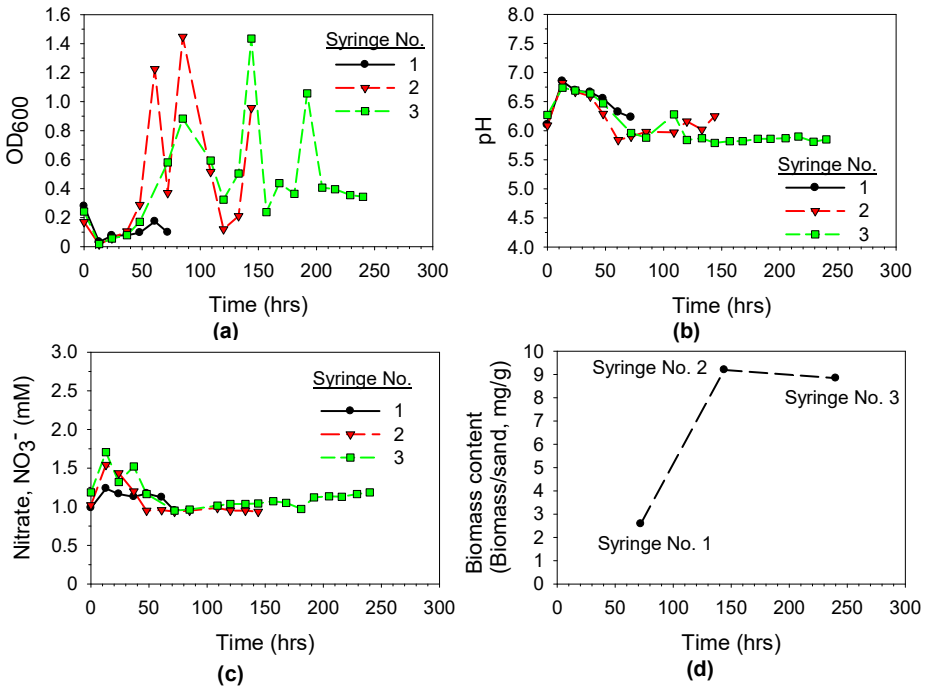

Figure 7.4. Syringe test results of (a) OD_{600} versus time; (b) pH versus time; (c) nitrate concentration versus time; and (d) biomass content versus time.

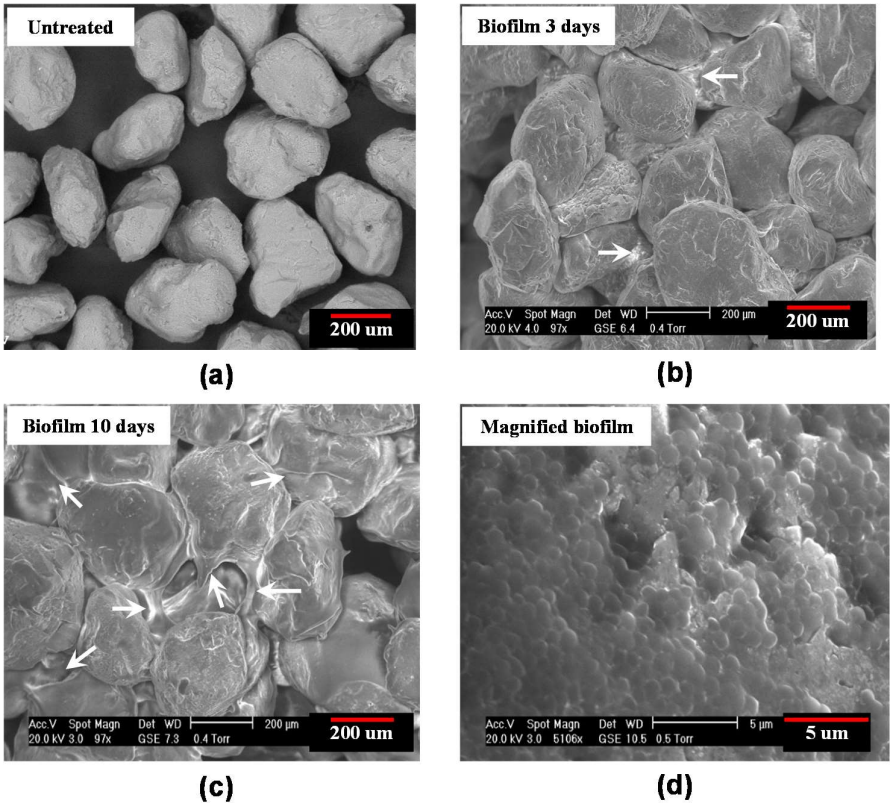

Figure 7.5. Scanning Electron Microscopy (SEM) images of (a) untreated sand (without biofilm treatment), sand treated with biofilm for (b) 3 and (c) 10 days, and (d) a magnified biofilm image.

7.5.3 Triaxial Test

The measured OD_{600}, pH, and nitrate concentration versus time during biofilm treatment of triaxial samples are shown in Figure 7.6. The OD_{600} initially decreased and then increased a steady state with some fluctuations. The pH and nitrate concentration versus time show a small peak at the beginning and then a steady state (Figure 7.6a and b). The variation of OD_{600}, pH, and nitrate concentration showed similar trends as those observed in the syringe test, confirming the repeatability of the tests. In addition, the water pressure in the column kept increasing and decreasing contiguously, showing

many peaks (maximum pressure, 90 kPa, data not shown). This could be attributed to biofilm plug development in porous media reducing the hydraulic conductivity of the porous media (Stewart and Fogler 2001).

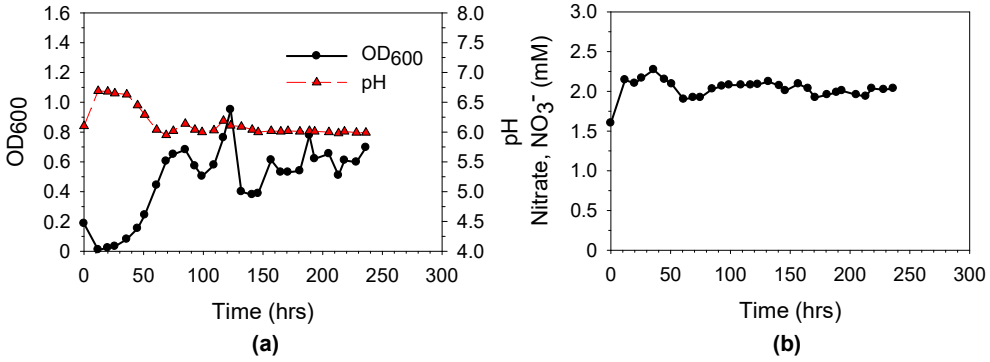

Figure 7.6. Triaxial test results during biofilm treatment: (a) OD_{600} and pH versus time; (b) nitrate concentration versus time.

The mechanical behavior of the untreated and biofilm-treated sand specimens is presented in Figure 7.7. The deviator stress versus axial strain of untreated and biofilm-treated specimens reveal strain hardening behavior with similar initial modulus (Figure 7.7a). A comparison of the untreated and biofilm-treated specimens indicates that the ultimate strength of biofilm-treated specimen is lower than the untreated soil by 9.3%. During the shear loading, the volumetric strain versus axial strain of biofilm-treated sand experienced more contraction after axial strain of 1% and less dilation after axial strain of 7% compared to that of untreated specimen. Similar results were reported by Perkins et al. (2000), who performed consolidated drained tests on biofilm-cemented Ottawa F-110 sand utilizing *Klebsiella oxytoca* for biofilm treatment. This decrease in sand strength was also observed by Daniels et al. (2009), who used biofilm producing

bacterium *Beijerinckia indica* to improve clay and clayey sand with unconfined compression test. The reduced strength and increased contraction of the biofilm-cemented sand indicates that the viscous property of the biofilm may control its mechanical behavior instead of the EPS bridging between sand grains.

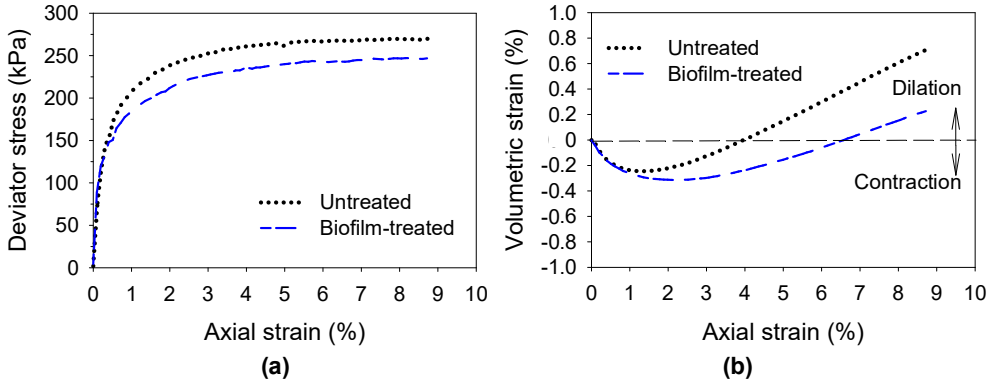

Figure 7.7. Triaxial test results during compression loading: (a) stress-strain and (b) volumetric strain.

The variation of the S-and P-wave velocities during biofilm treatment and shear loading is shown in Figure 7.8. The S-wave velocity was essentially constant (Figure 7.8a) indicating a constant shear modulus. However, P-wave velocity showed a sudden decrease from 1700 m/s to 740 m/s at 72 hours. During the biofilm treatment, continuous gas bubbles from the effluent port were observed, which could be nitrogen gas resulting from the denitrification process. The decrease of the P-wave velocity is attributed to the desaturation of the specimen with the generation of the nitrogen gas (Rebata-Landa and Santamarina, 2012). However, it is worth noting that this biogenic gas generation could mitigate liquefaction of saturated sands (He et al. 2013). As shown in Figure 7.8b, the S-wave velocities of the untreated specimens during the triaxial

compression loading were essentially constant (a change of less than 10 m/s, 4% increase). However, a 14% increase of S-wave velocity (a change of 30 m/s) was observed in the biofilm-treated specimen during loading. This increase of S-wave velocity indicates that the soil shear modulus increased during shear loading, which could be contributed to the bonding and short-range forces resulting from the denser packing of the sand matrix under shear loading.

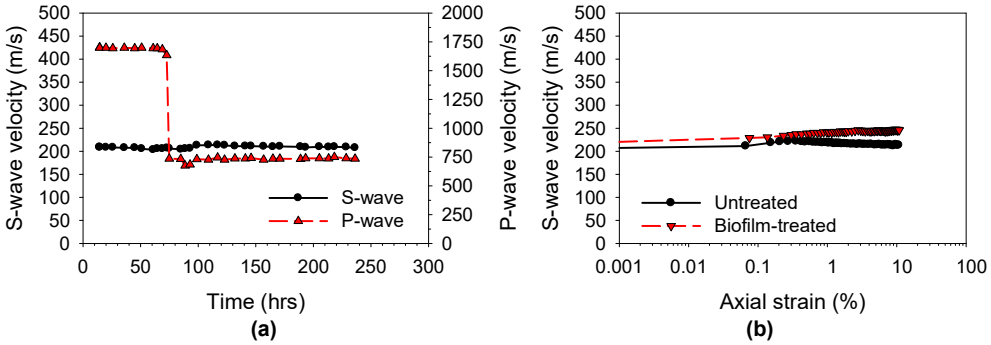

Figure 7.8. S-and P-wave velocities during (a) biofilm treatment and (b) compression loading.

The measured biomass content along the height of the specimen treated with biofilm is shown in Figure 7.9. The average biomass content in the sand matrix along the sample length was 9 mg/g. The distribution of the biomass content shows a gradient along the height of the specimen. The biomass content close to the effluent port at the top was 1.6 mg/g, 9.5 times lower than the highest biomass content (16.8 mg/g at 78 mm depth of the specimen). After the test, the real sample shows the bulging failure between 40 and 90 mm depth of the specimen.

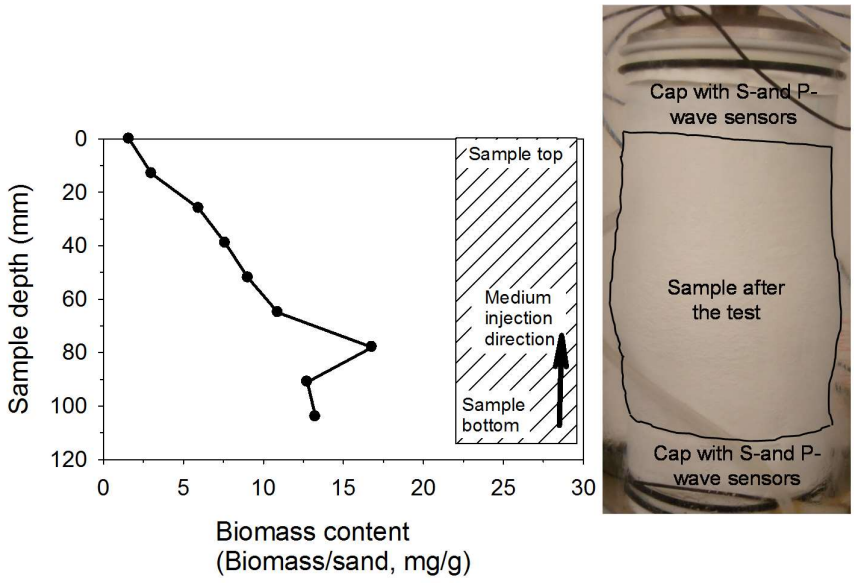

Figure 7.9. Biomass content along the height of the biofilm treated specimen.

7.6 CONCLUSIONS AND DISCUSSION

This paper describes three types of tests conducted to investigate the behavior of biofilm cemented sand. This research focused on using *Staphylococcus epidermidis* bacteria (ATCC 35984) to induce biofilm formation in the sand matrix. The bacteria density (OD_{600}), pH, and nitrate concentration were monitored throughout the biofilm treatment. S-and P-wave velocities were also monitored during biofilm treatment and loading of the triaxial test. After the tests, biomass content and Scanning Electron Microscope (SEM) images were analyzed to understand biofilm growth and morphology. Based on the test results, it was concluded that the selected bacteria (*S. Epidermidis*) can grow and form biofilm in the sand matrix under anaerobic conditions. However, the biofilm cemented sand showed decreasing effect on specimen strength and more contraction than that of sand without biofilm treatment.

Compared with literature, the research on mechanical behavior of biofilm-cemented soil shows contradictory conclusions. However, most related research reported that the biofilm cemented sand showed less or similar ultimate strength to sand without treatment (e.g. Perkins et al. 2000; Daniels et al. 2009; and this study) except Banagan (2010) who reported a 15.2~87.5% increase of strength under biofilm treatment. The differences between the results of different studies could be attributed to the bacterium used for the study. However, it is important to note that although the biofilm may not contribute a strength increase to the soil, some type of slime (poly-s-hydroxybutyrate (PHB), xanthan gum, and sodium alginates) produced by bacteria (e.g. *Alcaligenes faecalis* or *Alcaligenes viscolactis*) could be used for strength increasing (Yang et al. 1993). Although *S. Epidermidis* used in our study is a bacterium than could produce slime, the lower soil strength of biofilm cemented sand could be attributed to the viscous property of the biofilm which exceeded the bonding effects and short-range forces. It is important to note that the cohesive strength of *S. epidermidis* biofilms ranged from 61 to 5,840 Pa (Aggarwal et al. 2010). In addition, porous media clogging under biofilm treatment (e.g. reducing the hydraulic conductivity) can be used for many applications such as oil recovery enhancement, bio-barriers used for reducing seepage and remediation of contaminated groundwater.

8. SUMMARY AND CONCLUSIONS

8.1 SUMMARY AND CONCLUSIONS

This PhD dissertation research centered on investigating physical properties of MICP-treated sand and MICP bio-grouted permeable pile system ranging from particle- to large lab-scale (e.g. micrometer to meter scale). In addition, the potential of biofilm modification on the physical properties of sand was conducted. This research will advance the research on bio-mediated geochemical processes towards field-scale applications based on the conclusions shown below.

1. The experimental characterization and analytical modelling of the $CaCO_3$ cementation at particle-scale (e.g. $CaCO_3$ distribution in pore space and its bond strength) showed that the main distributions of the MICP $CaCO_3$ at pore-space are grain-coating and matrix supporting. The equations to calculate shear strength of MICP-treated sand matrix were derived by considering $CaCO_3$ spatial distribution, $CaCO_3$ content, measured strength of the $CaCO_3$ bond. These work provided references (S-and P-wave velocities and coefficient of permeability versus $CaCO_3$ content, derived soil shear strength equations) for future planning and monitoring of the field test and fundamental input parameters for particle-based discrete element modelling method.
2. The results of triaxial and confined compression tests on sands treated by MICP demonstrated that the measured S-wave velocity increased as the $CaCO_3$ content

increased. Soil peak strength increased by an average of 132% after the MICP treatment. Initial moduli of MICP-treated sands are controlled by the $CaCO_3$ content. As the $CaCO_3$ content increased, the compressibility of the treated soil specimens decreased (less settlement). These test results will provide basic soil parameters (e.g. friction angle, cohesion, shear strength, and modulus) for future field test design.

3. For the tests of pervious concrete pile enhancement using MICP bio-grouting, the stiffness (initial slope) and ultimate load of the load-displacement responses under MICP bio-grouting has increased by an average of 1.5 and 2.4 times. Investigating the improved capacity of MICP bio-grouted pervious concrete pile subject to axial tension and compression conditions is an advance of MICP technology toward real field applications.
4. The sand treated with biofilm showed limited (sometimes decreasing) effect on the strength of the sand specimen. Investigating the mechanical behavior of biofilm-cemented sand help clarify the contradictory conclusions in the literature.

REFERENCES

Aggarwal, S., Poppele, E. H., and Hozalski, R. M. (2009). "Development and testing of a novel microcantilever technique for measuring the cohesive strength of intact biofilms." *Biotechnology and Bioengineering*, 105 (5), 924-934.

Aggarwal. S., and Hozalski, R. M. (2010). "Determination of biofilm mechanical properties from tensile tests performed using a micro-cantilever method." *Biofouling: The Journal of Bioadhesion and Biofilm Research*, 26 (4), 479-486.

Ahimou F, Semmens MJ, Novak PJ, Haugstad G. (2007). "Biofilm cohesiveness measurement using a novel atomic force microscopy methodology." *Appl Environ Microbiol*, 73, 2897-2904.

Alavi, M., and Belas., R. (2001). "Surface sensing, swarmer cell differentiation, and biofilm development." *Methods in Enzymology*, 336, 29-40.

Al Qabany, A. (2011a). "Microbial carbonate precipitation in soils". *Doctoral dissertation*, University of Cambridge, UK.

Al Qabany, A., Mortensen, B., Martinez, B., Soga, K., and DeJong, J. (2011b). "Microbial carbonate precipitation: correlation of S-wave velocity with calcite precipitation." *Proceedings of ASCE Geo-Frontiers 2011 Conference*, ASCE, Reston, VA.

Al Qabany, A., Soga, K., and Santamarina, C. (2012). "Factors affecting efficiency of microbially induced calcite precipitation." *Journal of Geotechnical and Geoenvironmental Engineering*, 138(8), 992-1001.

Al Qabany, A., and Soga, K. (2013). "Effect of chemical treatment used in MICP on engineering properties of cemented soils." *Géotechnique*, 63(4), 331-339.

Alavi, M., and Belas., R. (2001). "Surface sensing, swarmer cell differentiation, and biofilm development." *Methods in Enzymology*, 336, 29-40.

APHA, AWWA, and WEF. (1992). "Standard methods for the examination of water and wastewater." *American Public Health Association*, 18th Edition, Washington, DC."

Armstrong, R., and Ajo-Franklin, J. (2011). "Investigating biomineralization using synchrotron based X-ray computed microtomography." *Geophysical Research Letters*, 38, 10.1029/2011GL046916.

ASCE, American Society of Civil Engineers (2006). "Report card for america's infrastructure." downloaded from www.asce.orgjreportcard, 195 pp.

ASTM. (2009a). “Standard test method for maximum index density and unit weight of soils using a vibratory table.” *D4253*, West Conshohocken, PA.

ASTM. (2009b). “Standard test method for minimum index density and unit weight of soils and calculation of relative density.” *D4254*, West Conshohocken, PA.

ASTM. (2009c). “Standard test method for compressive strength of cylindrical concrete specimens.” *C39*, West Conshohocken, PA.

ASTM. (2009d). “Standard test method for density and void content of freshly mixed pervious concrete.” *C1688*, West Conshohocken, PA.

ASTM. (2009e). “Standard test method for splitting tensile strength of cylindrical concrete specimens.” *C496*, West Conshohocken, PA.

ASTM. (2009f). “Standard test method for infiltration rate of in place pervious concrete.” *C1701*, West Conshohocken, PA.

ASTM. (2009g). “Standard test method for deep foundations under static axial tensile load.” *D3689*, West Conshohocken, PA.

ASTM. (2009h). “Standard test method for deep foundations under static axial compressive load.” *D1143*, West Conshohocken, PA.

Baig, S., Picornell, M., and Nazarian, S. (1997). “Low strain shear moduli of cemented sands.” *Journal of Geotechnical and Geoenvironmental Engineering*, 123(6), 540-545.

Banagan, B. L., Wertheim, B. M., Roth, M. J. S., and Caslake, L. F. (2010). “Microbial strengthening of loose sand.” *Letters in Applied Microbiology*, 51, 138-142.

Bang, S. S., Frutiger, S., Nehl, L. M., and Comes, B. L. (2009). “Application of novel biological technique in dust suppression.” *Transportation Research Board 88th Annual Meeting*, 11–15 January 2009, Washington, DC.

Bang, S. S., Lippert, J. J., Yerra, U., Mulukutla, S. and Ramakrishnan, V. (2010). “Microbial calcite, a bio-based smart nanomaterial in concrete remediation.” *Int. J. Smart Nano Mater.*, 1(1), 28–39.

Bang, S., Min, S. H., and Bang, S. S. (2011). “Application of microbiologically induced soil stabilization technique for dust suppression.” *Int. J. Geo-Engng 3*, No. 2, 27–37.

Barnes, J. M., Apel, W. A., and Barrett, K. B. (1995). “Removal of nitrogen oxides from gas streams using biofiltration.” *J. Hazard. Mater.*, 41(2–3), 315–326.

Basu, P., Loukidis, D., Prezzi, M., and Salgado, R. (2011). “Analysis of shaft resistance of jacked piles in sands.” *International Journal for Numerical and Analytical Methods in Geomechanics*, 35(15), 1605-1635.

Batzle, M., and Wang, Z. (1992). “Seismic properties of pore fluids.” *Geophysics*, 57(11), 1396-1408.

Beeldens, A., Gemert, D. V., and Caestecker, C. (2003). “Porous concrete: laboratory versus field experience.” *Proceedings of 9th International Symposium on Concrete Roads*, European Concrete Paving Association (EUPAVE), Brussels, Belgium.

Behlulgil, K., and Mehmetoglu, M. T. (2002). “Bacteria for improvement of oil recovery: A laboratory study.” *Energy Sources*, 24(5), 413–421.

Blott, S.J. and Pye, K. (2001). “GRADISTAT: a grain size distribution and statistics package for the analysis of unconsolidated sediments.” *Earth Surface Processes and Landforms* 26, 1237-1248.

Bryers, J., and Characklis, W. (1981). “Early fouling biofilm formation in a turbulent flow system: overall kinetics.” *Water Resources*, 15, 483-491.

Bruce, D. A. (1986a). “Enhancing the performance of large diameter piles by grouting: Part 1.” *Ground Engineering*, 19(4), 9–15.

Bruce, D. A. (1986b). “Enhancing the performance of large diameter piles by grouting: Part 2.” *Ground Engineering*, 19(5), 1121–1126.

Burbank, M., Weaver, T., Green, T. L., Williams, B. C., and Crawford, R. L. (2013a). “Precipitation of calcite by indigenous microorganisms to strengthen liquefiable soils.” *Geomicrobiology Journal*, 28(4), 301–312.

Burbank, M., Weaver, T., Lewis, R., Williams, T., Williams, B., and Crawford, R. (2013b). “Geotechnical tests of sands following bioinduced calcite precipitation catalyzed by indigenous bacteria.” *J. Geotech. Geoenviron. Eng.*, 139(6), 928–936.

Cannavo, P., Richaume, A., and Lafolie, F. (2004). “Fate of nitrogen and carbon in the vadose zone: In situ and laboratory measurements of seasonal variations in aerobic respiratory and denitrifying activities.” *Soil Biol. Biochem.*, 36(3), 463–478.

Cardenas, L. M., Hawkins, J. M. B., Chadwick, D., and Scholefield, D. (2003). “Biogenic gas emissions from soils measured using a new automated laboratory incubation system.” *Soil Biol. Biochem.*, 35(6), 867–870.

Carman, P. C. (1937). “Fluid flow through a granular bed.” *Transactions of the Institution of Chemical Engineers*, London, 15, 150-167.

Carrier, W., III (2003). “Goodbye, hazen; hello, kozeny-carman.” *Journal of Geotechnical and Geoenvironmental Engineering*, 129(11), 1054–1056.

Chaney, R. C., and Mulilis, J. P. (1978) "Suggested method for soil specimen remolding by wet-raining," *Geotechnical Testing Journal*, 1(2), 107-10.

Chen M, Zhang Z, Bott T. (1998). “Direct measurement of the adhesive strength of biofilms in pipes by micromanipulation.” *Biotechnol Tech*, 12, 875-880.

Chen MJ, Zhang Z, Bo11 TR. (2005). “Effects of operating conditions on the adhesive strength of Pseudomonas fluorescens biofilms in tubes.” *Colloids Surf B Biointerfaces*, 43, 61-7 1.

Cheng, C., Lo, Y., Pun, B. S., Chang, Y. M., and Li, W. Y. (2005). “An Investigation of bonding-layer characteristics of substrate-bonded fiber bragg grating.” *Journal of Lightwave Technology*, 23(11): 3907-3915.

Cheng, L. and Cord-Ruwisch, R. (2012). “In situ soil cementation with ureolytic bacteria by surface percolation.” *Ecological Engineering*, 42, 64-72.

Cheng, L., Cord-Ruwisch, R., and Shahin, M. A. (2013a). “Cementation of sand soil by microbially induced calcite precipitation at various degrees of saturation.” *Canadian Geotechnical Journal*, 50(1), 81-90.

Cheng, L., and Cord-Ruwisch, R. (2013b). “Upscaling effects of soil improvement by microbially induced calcite precipitation by surface percolation.” *Geomicrobiology Journal*, 31(5).

Chou, C., Seagren, E. A., Aydilek, A. H., and Lai, M. (2011). “Biocalcification of sand through ureolysis.” *Journal of Geotechnical and Geoenvironmental Engineering*, 137(12), 1179-1189.

Chu, J., Stabnikov, V. and Ivanov, V. (2012). “Microbially induced calcium carbonate precipitation on surface or in the bulk of soil.” *Geomicrobiol. J*. 29(6), 544–549.

Chung, Y. C., and Chung, M. S. (2000). “BNP test to evaluate the influence of C/N ratio on N_2O production in biological denitrification.” *Water Sci. Technol.*, 42(3–4), 23–27.

Clayton, C. R. I. (2011). “Stiffness at small strain: research and practice.” *Géotechnique*, 61(1), 5-37.

Clough, G. W., Sitar, N., and Bachus, R. C. (1981). “Cemented sands under static loading.” *Journal of the Geotechnical Engineering Division*, 107(6), 799-817.

Coufort C, Derlon N, Ochoa-Chaves J, Line A, Paul E. (2007). "Cohesion and detachment in biofilm systems for different electron acceptor and donors." *Water Sci Techno*, 155, 421 428.

Cuthbert, M. O., Riley, M. S., Handley-Sidhu, S., Renshaw, J. C., Tobler, D. J., Phoenix, V. R., and Mackay, R. (2012). "Controls on the rate of ureolysis and the morphology of carbonate precipitated by S. Pastrurii biofilms and limits due to bacterial encapsulation." *Ecological Engineering*, 41, 32-40.

Dai, S., Santamarina, J. C., Waite, W. F., and Kneafsey, T. J. (2012). "Hydrate morphology: physical properties of sands with patchy hydrate saturation." *Journal of Geophysical Research*, 117, B11205, doi:10.1029/2012JB009667.

Daniels, L., Fulton, G., Spencer, R. W., and Orme-Johnson, W. H. (1980). "Origin of hydrogen in methane produced by Methanobacterium thermoautotrophicum." *J. Bacteriol.*, 141(2), 694–698.

Daniels, J. L., Cherukuri, R., and Ogunro, V. O. (2009). "Consolidation and strength characteristics of biofilm amended barrier soils." *Appropriate Technologies for Environmental Protection in the Developing World,* 257-270.

Davis, J. M., Roy, N. D., Mozley, P. S., Hall, J. S. (2006). "The effect of carbonate cementation on permeability heterogeneity in fluvial aquifers: an outcrop analog study." *Sedimentary Geology*, 184(3-4), 267-280.

DeJong, J., Fritzges, M., and Nüsslein, K. (2006). "Microbially induced cementation to control sand response to undrained shear." *Journal of Geotechnical and Geoenvironmental Engineering*, 132(11), 1381–1392.

DeJong, J. T., Soga, K., Banwart, S. A., Whalley, W. R., Ginn, T. R., Nelson, D. C., Mortensen, B. M., Martinez, B. C., and Barkouki, T. (2011). "Soil engineering in vivo: harnessing natural biogeochemical systems for sustainable, multi-functioning engineering solutions." *Journal of the Royal Society Interface*, 8(1), 1–15.

DeJong, J. T., Mortensen, B. M., Martinez, B. C., and Nelson, D. C. (2010b). "Bio-mediated soil improvement." *Ecology Engineering*, 36(2), 197-210.

DeJong, J. T., Soga, K., Banwart, S. A., Whalley, W. R., Ginn, T. R., Nelson, D. C., Mortensen, B. M., Martinez, B. C., and Barkouki, T. (2011). "Soil engineering in vivo: harnessing natural biogeochemical systems for sustainable, multi-functioning engineering solutions." *Journal of the Royal Society Interface*, 8(1), 1–15.

DeJong, J. T., Soga, K., Kavazanjian, E., Burns, S., van Paassen L. A., Al Qabany, A., Aydilek, A., Bang, S. S., Burbank, M., Caslake, L. F., Chen, C. Y., Cheng, X., Chu, J., Ciurli, S., Esnault-Filet, A., Fauriel, S., Hamdan, N., Hata, T., Inagaki,

Y., Jefferis, S., Kuo, M., Laloui, L., Larrahondo, J., Manning, D. A. C., Martinez, B., Montoya, B. M., Nelson, D. C., Palomino, A., Renforth, P., Santamarina, J. C., Seagren, E. A., Tanyu, B., Tsesarsky, M., and Weaver, T. (2013). "Biogeochemical processes and geotechnical applications: progress, opportunities and challenges." *Géotechnique*, 63(4), 287 –301.

DeJong, J. T., Martinez, B. C., Ginn, T. R., Hunt, C., Major, D., and Tanyu, B. (2014). "Development of a scaled repeated five-spot treatment model for examining microbial induced calcite precipitation feasibility in field applications." *Geotechnical Testing Journal*, 37(3), 10.1520/GTJ20130089

Dennis, M. L., and Turner, J. P. (1998). "Hydraulic conductivity of compacted soil treated with biofilm." *Journal of Geotechnical and Geoenvironmental Engineering*, 124(2), 120-127.

Digby, P. J. (1981). "The stiffness elastic moduli of porous granular rocks." *Journal of Applied Mechanics*, 48, 803-808.

Dong, Y. (2013). "Engineered Soil with Thermally Controlled Wettability." *Ph. D. dissertation*, Lehigh University, Bethlehem, PA.

Donlan, R. M. (2002). "Biofilms: microbial life on surfaces." *Emerging Infectious Diseases,* 8 (9), 881-890.

Dullien, F. A. L. (1992). "Porous media fluid transport and pore structure, 2nd ed." *Academic Press*, New York, 396P.

Dunne, W. M., Jr. (2002). "Bacterial adhesion: seen any good biofilms lately?" *clinical microbiology review*, 15(2), 155-166.

Dvorkin, J., Prasad, M., Sakai, A., and Lavoie, D. (1999). "Elasticity of marine sediments: rock physics modeling." *Geophysical Research Letters*, 26(12), 1781-1784.

Dvorkin, J., and Nur, A. (1996). "Elasticity of high-porosity sandstones: theory for two north sea data sets." *Geophysics*, 61(5), 1363-1370.

Dvorkin, J., Nur, A., Yin, H. (1994). "Effective properties of cemented granular materials." *Mechanics of Materials*, 18(4), 351-366.

Dvorkin, J., Mavko, G., Nur, A. (1991). "The effect of cementation on the elastic properties of granular material." *Mechanics of Materials*, 12(3-4), 207-217.

Ebigbo, A., Phillips, A., Gerlach, R., Helmig, R., Cunningham, A. B., Class, H., and Spangler, L. H. (2012). "Darcy-scale modeling of microbially induced carbonate mineral precipitation in sand columns." *Water Resources Research*, 48(7), 1-17.

Evans, T. M., Khoubani, A. and Montoya, B. M. (2014). "Stimulating mechanical response in bio-cemented sands." *Computer Methods and Recent Advances in Geomechanics*, Taylor & Francis Group, 1569–1574.

Fattahpour, V., Baudet, B. A., and Sze, J. W. (2014). "Laboratory investigation of shaft grouting." *Proceedings of the ICE-Geotechnical Engineering*, 168(1), 65-74.

Feng K., and Montoya, B. M. (2014). "Behavior of bio-mediated soil in k_0 loading." *New Frontiers in Geotechnical Engineering Geo-Shanghai Proceedings*, 1-10.

Feng, K., and Montoya, B. M. (2015). "Influence of confinement and cementation level on the behavior of microbial-induced calcite precipitated sands under monotonic drained loading." *J. Geotech. Geoenviron. Eng.*, 10.1061/(ASCE)GT.1943-5606.0001379 , 04015057.

Ferris, F. G., Stehmeier, L. G., Kantzas, A., and Mourits, F. M. (1996). "Bacteriogenic mineral plugging." *Journal Canadian Petroleum Technology*, 35(8), 56–61.

Firestone, M. K., Firestone, R. B., and Tiedje, J. M. (1980). "Nitrous oxide from soil denitrification: Factors controlling its biological production." *Science*, 208(4445), 749–751.

Fleming, I. R., Rowe, R. K., Cullimore, D. R. (1999). "Field observations of clogging in a landfill leachate collection system." *Canadian Geotechnical Journal*, 36(4), 685-707.

Flemming, H. C. (2002). "Biofouling in water systems-cases, causes and countermeasures." *Applied Microbiology and Biotechnology*, 59(6), 629-640.

Fu, L., Zeng, X., and Figueroa, J. L. (2004). "Shear wave velocity measurement in centrifuge using bender elements." *International Journal of Physical Modelling in Geotechnics*, 2, 01-11.

Fujita, Y., Redden, G. D., Ingram, J. S., Cortez, M. M. and Smith, R. W. (2004). "Strontium incorporation into calcite generated by bacterial ureolysis." *Geochim. Cosmochim. Acta*, 68(15), 3261–3270.

Fujita, Y., Taylor, J. L., Gresham, T. L. T., Delwiche, M. E., Colwell, F. S., McLing, T. L., Petzke, L. M. and Smith, R. W. (2008). "Stimulation of microbial urea hydrolysis in groundwater to enhance calcite precipitation." *Environ. Sci. Technol.,* 42(8), 3025–3032.

Fujita, Y., Taylor, J. L., Wendt, L. M., Reed, D. W. and Smith, R. W. (2010). "Evaluating the potential of native ureolytic microbes to remediate a 90Sr contaminated environment." *Environ. Sci. Technol.,* 44(19), 7652–7658.

Gassmann, F. (1951). “Elasticity of porous media: Uber die elastizitat poroser medien: Vierteljahrsschrift der Naturforschenden Gesselschaft, 96, 1-23.

Gibert, O., Lefevre, B., Fernandez, M., Bernat, X., Paraira, M., Calderer, M., and Martinez-Llado, X. (2013). “Characterising biofilm development on granular activated carbon used for drinking water production.” *Water Resources*, 47(3), 1101-10.

Gollapudi, U. K., Knutson, C. L., Bang, S. S., Islam, M. R. (1995). “A new method for controlling leaching through permeable channels.” *Chemosphere*, 30, 695-705.

Gomez, M. G., Martinez, B. C., DeJong, J. T., Hunt, C. E., deVlaming L. A., Major, D. W., Dworatzek, S. M. (2014a). “Field-scale bio-cementation tests to improve sands.” *Proceedings of the ICE - Ground Improvement*, 168(3), 206-216.

Gomez, M., Anderson, C., DeJong, J., Nelson, D., and Lau, X. (2014b). “Stimulating in situ soil bacteria for bio-cementation of sands.” *Geo-Congress 2014 Technical Papers*, pp. 1674-1682. doi: 10.1061/9780784413272.164.

Gouvenot, D., and Gabiax, F. D. (1975). “A new foundation technique using piles sealed by concrete under high pressure.” *Proc., 7th Annual Offshore Technology Conf.*, Houston, 641–656.

Hamdan, N., Kavazanjian, E., Jr., Rittmann, B.E., and Karatas, I. (2011) “Carbonate mineral precipitation for soil improvement through microbial denitrification,” *Proceedings of GeoFrontiers 2011: Advances in Geotechnical Engineering, American Society of Civil Engineers Geotechnical Special Publication 211*, pp. 3925 – 3934.

Hamdan, N. M. (2014). “Applications of enzyme induced carbonate precipitation (EICP) for soil improvement.” *PhD Thesis*, Arizona State University.

Hashin, Z., and Shtrikman S. (1963). “A variational approach to the theory of the elastic behavior of multiphase materials.” *Journal of the Mechanics and Physics of Solids*, 11, 127–140, doi:10.1016/0022-5096(63)90060-7.

Harkes, M. P., van Paassen, L. A., Booster, J. L., Whiffin, V. S., van Loosdrecht, M. C. M. (2010). “Fixation and distribution of bacterial activity in sand to induce carbonate precipitation for ground reinforcement.” *Ecological Engineering*, 36, 112-117.

He, J., Chu, J., and Ivanov, V. (2013). “Mitigation of liquefaction of saturated sand using biogas.” *Geotechnique*, 63(4), 267–275.

He, J., and Chu, J. (2014). "Undrained responses of microbially desaturated sand under monotonic loading." *J. Geotech. Geoenviron. Eng.*, 140(5), 04014003.

Helgerud, M. B., Dvorkin, J., Nur, A., Sakai, A., and Collett, T. (1999). "Elastic-wave velocity in marine sediments with gas hydrates: effective medium modeling." *Geophysical Research Letters*, 26(13), 2021-2024.

Hermansson, M. (1999). "The DLVO theroy in microbial adhesion." *Colloids and Surfaces B: Biointerfaces*, 14, 105–119.

Hill, R. (1952). "The elastic behavior of crystalline aggregate." *Proceedings of the Physics Society*, London, 65(5), 349-354.

Ip, Y. K., Chew, S. F., and Randall, D. J. (2001). "Ammonia toxicity, tolerance and excretion, nitrogen excretion." *Fish Physiology*, 20, 109-148.

Ishihara, K., Huang, Y., and Tsuchiya, H. (1998). "Liquefaction resistance of nearly saturated sand as correlated with longitudinal velocity." *Poromechanics—A tribute to Maurice*, A. Biot, J. F. Thimus, Y. Abousleiman, A. H. D. Cheng, O. Coussy, and E. Detournay, eds., Balkema, Rotterdam, Netherlands, 583–586.

Ismail, M. A., Joer, H. A., Sim, W. H. & Randolph, M. F. (2002). "Effect of cement type on shear behavior of cemented calcareous soil." *J. Geotech. Geoenviron. Engng,* 128(6), 520–529.

Ivanov, V., and Chu J. (2008). "Applications of microorganisms to geotechnical engineering for bioclogging and biocementation of soil in situ." *Reviews in Environmental Science and BioTechnology*, 7(2), 139-153.

Ivanov, V., Chu, J., Stabnikov, V., He, J. & Naeimi, M. (2010). "Iron-based bio-grout for soil improvement and land reclamation." *Proc. 2nd Int. Conf. Sustainable Construction Mater. Technol, Ancona Special,* 415–420.

Janbu, N. (1963). "Soil compressibility as determined by oedometer and triaxial tests." *In Proceedings of European Conference on Soil Mechanics and Foundation Engineering*, Wiesbaden, Germany, Vol. 1, 19-25.

James, G. A., Warwood, B. K., Hiebert, R., and Cunningham, A. B. (2000). "Microbial barriers to the spread of pollution." In *Bioremediation* (ed. J. J. Valdes), pp. 1–14. Amsterdam, the Netherlands: Kluwer Academic.

Joer, H. A., Randolph, M. F., and Gunasena, U. (1998). "Experimental modeling of the shaft capacity of grouted driven piles." *Geotechnical Testing Journal*, 21(3), 159–168.

Johns, D., Williams, H., Farrish, K., and Wagner, S. (2004). "Denitrification and soil characteristics of wetlands created on two mine soils in east Texas, USA." *Wetlands*, 24(1), 57–67.

Jones, D., Pell, P. A., and Sneath, P. H. A. (1991). "Maintenance of bacteria on glass beads at -60°C to -76°C." p. 45–50. In B. E. Kirsop and A. Doyle (ed.), Maintenance of microorganisms and cultured cells: a manual of laboratory methods. *Academic Press*, San Diego, CA.

Kajio, S., Tanaka, S., Tomita, R., Noda, E., and Hashimoto, S. (1998). "Properties of porous concrete with high strength." *Proceedings of 8th International Symposium on Concrete Roads*, 171-177.

Karatas, I., Kavazanjian, E. Jr., and Rittmann, B. E. (2008) "Microbially Induced Precipitation of Calcite Using Pseudomonas Denitrificans." *Proceedings of the First International Conference on Biogeotechnical Engineering*, Technical University of Delft, Delft, The Netherlands (on CD ROM

Kavazanjian, E., Jr. and Karatas, I. (2008) "Microbiological improvement of the physical properties of soil." *Symposium to Honor James K. Mitchell, Proc. 6th International Conference on Case Histories in Geotechnical Engineering*, Missouri University of Science and Technology, Rolla, MO (on CD ROM).

Kavazanjian, E. Jr, Iglesias, E., and Karatas, I. (2009). "Biopolymer soil stabilization for wind erosion control." *Proceedings of the 17th International Conference on Soil Mechanics and Geotechnical Engineering*, Alexandria , Egypt, 881–884.

Kleinberg, R. L., and Dai, J. (2005). "Estimation of the mechanical properties of natural gas hydrate deposits from petrophysical measurements." *paper OTC 17205 presented at the Offshore Technology Conference*, Houston, Texas.

Lambert, J. W. M., Novakowski, K., Blauw, M., Latil, M. N., Knight, L., and Bayona, L. (2010). "Pamper bacteria, they will help us: application of biochemical mechanisms in geo-environmental engineering." *In GeoFlorida 2010: Advances in Analysis, Modeling & Design* (eds D. O. Fratta, A. J. Puppala and B. Muhunthan), ASCE Geotechnical Special Publication 199, pp. 618–627. Reston, VA, USA: ASCE.

Lee, R. (2011). "The outlook for population growth." *Science*, 333, 569–573.

Körstgens V, Flemming HC, Wingender J, Borchard W. (2001). "Infiuence of ca1cium ions on the mechanical properties of a model biofilm of mucoid Pseudomonas aerugznosa." *Water Sci Technol*, 43, 49-57.

Lee, M. L., Ng W. S., and Tanaka, Y. (2013). "Stress-deformation and compressibility responses of bio-mediated residual soils." *Ecological Engineering*, 60, 142-149.

Lee, J., and Santamarina, J. C. (2005). "Bender elements: performance and signal interpretation." *Journal of Geotechnical and Geoenvironmental Engineering*, 131(9), 1063–1070.

Lee, M. L., Ng W. S., and Tanaka, Y. (2013). "Stress-deformation and compressibility responses of bio-mediated residual soils." *Ecological Engineering*, 60, 142-149.

Li, W., Liu, L. P., Zhou, P. P., Cao, L., Yu L. J. and Jiang, S. Y. (2011). "Calcite precipitation induced by bacteria and bacterially produced carbonic anhydrase." *Current Science*, 100(4), 502-508.

Lin, H., Suleiman, M. T., Helm, J., and Brown, D. G. (2014). "Measurement of bonding strength between glass beads treated by microbial-induced calcite precipitation (MICP)." *ASCE Geo-Congress 2014*, Atlanta, GA, 1625-1634.

Lin, H., Suleiman, M., Jabbour, H., and Brown, D. (2015). "Enhancement of pervious concrete pile subjected to uplift load using microbial induced carbonate precipitation." *IFCEE 2015*, 775-783, San Antonio, Texas.

Lin, H., Suleiman, M. T., Brown, D. G., and Kavazanjian, E. (2016a). "Mechanical behaviors of sands treated by microbial induced carbonate precipitation." *Journal of Geotechnical and Geoenvironmental Engineering*, 10.1061/(ASCE)GT.1943-5606.0001383, 04015066.

Lin, H., Suleiman, M. T., Jabbour, H. M., Brown, D. G., and Kavazanjian, E. (2016b). "Enhancing the axial compression response of pervious concrete ground improvement piles using bio-grouting." *Journal of Geotechnical and Geoenvironmental Engineering*, In Publication.

Lin, H., Suleiman, M. T., Jabbour, H. M., Brown, D. G. (2016c). "Bio-grouting to enhance axial pull-out response of pervious concrete ground improvement piles." *Journal of Geotechnical and Geoenvironmental Engineering,* In Preparation.

Liu, Y., and Tay, J. H. (2002). "The Essential role of hydrodynamic shear force in the formation of biofilm and granular sludge." *Water Research*, 36, 1653-1665.

Liu, H., Kong, G., Chu, J., Ding, X. (2015). "Grouted gravel column supported highway embankment over soft clay: case study." *Canadian Geotechnical Journal*, 10.

Logan, B. E., Jewett, D. G., Arnold, R. G., Bouwer, E. J., and O'Melia, C. R. (1995). "Clarification of clean-bed filtration models." *Journal of Environmental Engineering*, 121(12), 869–873.

Logan, B. E., Oh, S. E., Kim, I. S., and van Ginkel, S. (2002). "Biological hydrogen production measured in batch anaerobic respirometers." *Environ. Sci. Technol.*, 36(11), 2530–2535.

Lu, N., Lechman, J., and Miller, K. T. (2008). "Experimental Verification of Capillary Force and Water Retention between Uneven-Sized Spheres." *Journal of Engineering Mechanics*, 134(5): 385-395.

Manning, D. A. C. (2008). "Biological enhancement of soil carbonate precipitation: passive removal of atmospheric CO_2." *Mineral. Mag.,* 72(2), 639–649.

Martens, C. S., and Berner, R. A. (1974). "Methane production in interstitial waters of sulfate-depleted marine sediments." *Science*, 185(4157), 1167–1169.

Martinez, B. C., and DeJong, J. T. (2009). "Bio-mediated soil improvement: load transfer mechanisms at the micro- and macro-scales." *US-China Workshop on Ground Improvement Technologies*, ASCE, Reston, VA, 242–251.

Martinez, B. C., DeJong, J., Ginn, T., Montoya, B., Barkouki, T., Hunt, C., Tanyu, B., and Major, D. (2013). "Experimental optimization of microbial-induced carbonate precipitation for soil improvement." *Journal of Geotechnical and Geoenvironmental Engineering*, 139(4), 587–598.

Mavko, G., Mukerji, T., and Dvorkin, J. (1998). "The rock physics handbook: tools for seismic analysis in porous media." *Cambridge University Press*, Cambridge, U. K.

McVay, M., Bloomquist, D., Forbes, H., and Johnson, J. (2009). "Precasted concrete pile installation: utilized jetting and pressure grouting." *Rep., BD545-031*, Florida DOT, Tallahassee, FL.

Mindlin, R. D. (1949). "Compliance of elastic bodies in contact." *Trans. ASME*, 71, A-259.

Mitchell, J. K. and Santamarina, J. C. (2005). "Biological considerations in geotechnical engineering." *ASCE J. Geotech. Geoenviron. Engng*, 131(10), 1222–1233.

Mitchell, A. C., and Ferris, F. G. (2005). "The co-precipitation of Sr into calcite precipitates induced by bacterial ureolysis in artificial groundwater-temperature and kinetic dependence." *Geochim Cosmochim Acta*, 69, 4199-4210.

Mitchell, A. C., and Ferris, F. G. (2006). "The Influence of Bacillus pasteurii on the Nucleation and Growth of Calcium Carbonate." *Geomicrobiology Journal*, 23 (3-4), 213-226.

Möhle RB, Langemann T, Haesner M, Augustin W., Scholl S, Neu TR, Hempel DC, Horn H. (2007). "Structure and shear strength of microbial biofilms as determined with confocal laser scanning microscopy and fiuid dynamic gauging using a novel rotating disc biofilm reactor." *Biotechnol Bioeng*, 98, 747-755.

Montoya, B. M., DeJong, J. T., Boulanger, R. W. (2013). "Dynamic response of liquefiable sand improved by microbial-induced calcite precipitation." *Géotechnique*, 63(4), 302 –312.

Montoya, B. M., and DeJong, J. T. (2015). "Stress-strain behavior of sands cemented by microbially induced calcite precipitation." *Journal of Geotechnical and Geoenvironmental Engineering,* 141(6), 04015019.

Mortensen, B. M., Haber, M. J., DeJong, J. T., Caslake, L. F., and Nelson, D. C. (2011). "Effects of environmental factors on microbial induced calcium carbonate precipitation." *Journal of Applied Microbiology*, 111(2), 338-349.

Muhunthan, B., and Sariosseiri, F. (2008). "Interpretation of geotechnical properties of cement treated soils." *Report WA-RD 715.1.,* Olympia, WA, USA: Washington State Department of Transportation.

Nakamura, M., Kanbe, H., and Matsumoto, J. I. (1993). "Fundamental studies on hydrogen production in the acid-forming phase and its bacteria in anaerobic treatment processes—The effects of solids retention time." *Water Sci. Technol.*, 28(7), 81–88.

Neupane, D., Yasuhara, H., Kinoshita, N., and Unno, T. (2013). "Applicability of enzymatic calcium carbonate precipitation as a soil-strengthening technique." *Journal of Geotechnical and Geoenvironmental Engineering*, 139(12), 2201–2211.

Ni, L., Suleiman, M. T., and Raich, A. (2015). "Behavior and soil-structure interaction of pervious concrete ground improvement piles under lateral loading." *Journal of Geotechnical and Geoenvironmental Engineering*, Accepted.

NRC (2006). "Geological and geotechnical engineering in the new millennium: opportunities for research and technological innovation." *National Research Council*, Washington, DC, USA.

O'Gara J. P. and Humphreys, H. (2001). "Staphylococcus epidermidis biofilms: importance and implications." *Journal of Medical Microbiology*, 50, 582-587.

Ohashi A, Harada H. (1994). "Adhesion strength of biofilm developed in an attached-growth reactor." *Water Sci Technol*, 29, 281-288.

Ohashi A, Harada H. (1996). “A novel concept for evaluation of biofilm adhesion strength by applying tensile force and shear force.” *Water Sci Technol*, 34, 201-211.

Ohashi A, Koyama T, Syutsubo K, Harada H. (1999). “A novel method for evaluation of biofilm tensile strength resisting erosion.” *Water Sci Technol*, 39, 261-268.

O’Toole, G., Kaplan, H. B., and Kolter, R. (2000). “Biofilm formation as microbial development.” 54, 49-79.

Palmer, J., Flint, S., and Brooks, J. (2007). “Bacterial cell attachment, the beginning of a biofilm.” *Journal of international Microbiology Biotechnology,* 34, 577-588.

Palmer, M. C., O'Rourke, T. D., Olson, N. A., Abdoun, T., Ha, D., and O'Rourke, M. J. (2009). “Tactile pressure sensors for soil-structure interaction assessment.” *Journal of Geotechnical and Geoenvironmental Engineering*, 135(11), 1638-1645.

Pamukcu, S and Turel, M. (2007). "Use of BOTDR to measure distributed strains of geosynthetics.” *GRI-20 Conference Proceedings couched with the Geosynthetics 2007*, Washington, D.C.

Panda, M.N., Lake, L.W. (1994). “Estimation of single-phase permeability from parameters of particle-size distribution.” *American Association of Petroleum Geologists Bulletin 78*, 1028–1039.

Panda, M.N., Lake, L.W. (1995). “A physical model of cementation and its effects on single-phase permeability.” *American Association of Petroleum Geologists Bulletin 79*, 431–443.

Park, S., and Tia, M. (2004). “An experimental study on the water-purification properties of porous concrete.” *Cement and Concrete Research*, 34(2), 177–184.

Pasten, C., and Santamarina, J. C. (2012). “Energy and quality of life.” *Energy Policy*, 49, 468-476.

Perkins, S. W., Gyr, P., and James, G. (2000). “The influence of biofilm on the mechanical behavior of sand.” *Geotechnical Testing Journal,* 23(3), 300-312.

Phillips, A. J., Lauchnor, E., Eldring, J., Esposito, R., Mitchell, A. C., Gerlach, R., Cunningham, A. B., and Spangler, L. H. (2013). “Potential CO_2 leakage reduction through biofilm-induced calcium carbonate precipitation.” *Environmental Science Technology*, 47(1), 142-149.

Plumbridge, G. D., and Hill, S. J. (2001). “Performance of shaft grouted piles and barrettes.” *Proc., 14th Southeast Asian Geotechnical Conf.: Geotechnical*

Engineering: Meeting Society's Needs, A. A. Balkema, Lisse, Netherlands, 407–412.

Poppele, E. H., and Hozalski, R. M. (2003). "Micro-cantilever method for measuring the tensile strength of biofilms and microbial flocs." *Journal of Microbiological Methods*, 55, 607-615.

Ramachandran, S. K., Ramakrishnan, V. and Bang, S. S. (2001). "Remediation of concrete using micro-organisms." *ACI Mater. J.,* 98(1), 3–9.

Ramakrishnan, V., Ramesh, K. P. and Bang, S. S. (2001). "Bacterial concrete." *Proceedings of SPIE, Smart Materials 4234*, 168–176. (doi:10.1117/12.424404).

Rasband, W. (2010). "ImageJ" software, National Institutes of Health.

Rebata-Landa, V. (2007). "Microbial activity in sediments: effects on soil behavior." *Ph.D. dissertation*, Georgia Institute of Technology, Atlanta, GA.

Rebata-Landa, V., and Santamarina, J. (2012). "Mechanical effects of biogenic nitrogen gas bubbles in soils." *J. Geotech. Geoenviron. Eng.*, 138(2), 128–137.

Renforth, P., Manning, D. A. C., and Lopez-Capel, E. (2009). "Carbonate precipitation in artificial soils as a sink for atmospheric carbon dioxide." *Appl. Geochem.,* 24(9), 1757–1764.

Renforth, P., Edmondson, J., Leake, J. R., Gaston, K. J., and Manning, D. A. C. (2011). "Designing a carbon capture function into urban soils." *Proc. ICE – Urban Design and Planning*, 164(2), 121–128.

Ribeiro, L. (2012) "Mechanics of Calcite-Polymer Microcomposites Using Nanoindentation and Micro-Compression." *Doctor of Philosophy Dissertation*, the University of Manchester, School of Materials, Manchester, United Kingdom.

Robb, T. D. (1984). "Stereo-biochemistry and function of polymers." Microbial Adhesion and Aggregation (Dahlem Konferenzen). K. C. Marshall, Ed., Springer-Verlag, Berlin, p. 39.

Rockhold, M. L., Yarwood, R. R., Niemet, M. R., Bottomley, P. J., Selker, J. S. (2002). "Considerations for modeling bacterial-induced changes in hydraulic properties of variably saturated porous media." *Advances in Water Resources,* 25(5), 477-495.

Ruiz, M. and Pando, M. (2009). "Load transfer mechanisms of tip post-grouted drilled shafts in sand." *Contemporary Topics in Deep Foundations*, 23-30.

Santamarina, J. C., Klein, K. A., and Fam, M. A. (2001). “Soils and Waves.” *John Wiley & Sons*, New York.

Schaefer, V. R., Wang, K., Suleiman, M. T., and Kevern, J. T. (2006). “Mix design development for pervious concrete in cold weather climates.” *National Concrete Pavement Technology Center*, Report No. 2006-01, Iowa State University, Ames, IA.

Sills, G. C., and Gonzalez, R. (2001). “Consolidation of naturally gassy soft soil.” *Geotechnique*, 51(7), 629–639.

Seki, K., Miyazaki, T., and Nakano, M. (1998). “Effects of microorganisms on hydraulic conductivity decrease in infiltration.” *Eur. J. Soil Sci.* 49(2), 231–236.

Soon, N., Lee, L., Khun, T., and Ling, H. (2014). “Factors affecting improvement in engineering properties of residual soil through microbial-induced calcite precipitation.” *J. Geotech. Geoenviron. Eng.*, 140(5), 04014006.

Stabnikov, V., Naeimi, M., Ivanov, V. and Chu, J. (2011). “Formation of water-impermeable crust on sand surface using biocement.” *Cement Concrete Res.* 41(11), 1143–1149.

Stal, L. J. (2010). “Microphytobenthos as a biogeomorphological force in intertidal sediment stabilization.” *Ecol. Engng*, 36(2), 236–245.

Stewart, T. L., and Fogler, H. S. (2001). “Biomass plug development and propagation in porous media.” *Biotechnology and Bioengineering,* 72(3), 353-63.

Stocker, M.F. (1983). "The influence of post grouting on the load bearing capacity of bored piles." *Proc. 8th European Conference on Soil Mechanics and Foundation Engineering*, Helsinki, Paper 2.12.

Stocks-Fischer, S., Galinat, J. K., and Bang, S. S. (1999). “Microbiological precipitation of $CaCO_3$.” *Soil Biology and Biochemistry*, 31(11), 1563-1571.

Stoodley P, Lewandowski Z, Boyle JD, Lappin-Scott HM. (1999). “Structural deformation of bacterial biofilms caused by short-term fiuctuations in fiuid shear: an in situ investigation of biofilm rheology.” *Biotechnol Bioeng*, 65, 83-92.

Suer, P., Hallberg, N., Carlsson, C., Bendz, D., Holm, G. (2009). “Biogrouting compared to jet grouting: environmental (LCA) and economical assessment.” *Journal of Environmental Science and Health Part A*, 44(4):346-53.

Suleiman, M. T., and White, D. J. (2006). “Load transfer in rammed aggregate piers.” *International Journal of Geomechanics*, 6(6), 389–398.

Suleiman, M. T., Ni, L., and Raich, A. (2014). "Development of pervious concrete pile ground-improvement alternative and behavior under vertical loading." *Journal of Geotechnical and Geoenvironmental Engineering*, 140(7), 04014035.

Suleiman, M. T., Ni, L., Davis, C., Lin, H., and Xiao S. (2015). "Installation effects of controlled modulus column ground improvement piles on surrounding soil." *Journal of Geotechnical and Geoenvironmental Engineering*, Accepted.

Taylor, S. W., and Jaffe, P. R. (1990). "Biofilm growth and the related changes in physical properties of a porous medium: 1. experimental investigation." *Water Resources Research*, 26(9), 2153-2159.

Talesnick, M. (2005). "Measuring soil contact pressure on a solid boundary and quantifying soil arching." *Geotechnical Testing Journal*, 28(2), 171–179.

Talesnick, M. (2013). "Measuring soil pressure within a soil mass." *Canadian Geotechnical Journal*, 50, 716-722.

Tatsuoka, F., and Shibuya, S. (1991) "Deformation characteristics of soils and rocks from field and laboratory tests." *Ninth Asian Regional Conference on Soil Mechanics and Foundation Engineering*, 2, Bangkok, Thailand.

Tennis, P. D., Leming, M. L., and Akers, D. J. (2004). "Pervious concrete pavements." *EB302*, Portland Cement Association, Skokie, IL

Thiyyakkandi, S., McVay, M., Bloomquist, D., and Lai, P. (2013). "Measured and predicted response of a new jetted and grouted precast pile with membranes in cohesionless soils." *Journal of Geotechnical and Geoenvironmental Engineering*, 139(8), 1334–1345.

Towler B. W., Rupp C. J., Cunningham A. B., Stoodley P. (2003). "Viscoelastic properties of a mixed culture biofilm from rheometer creep analysis." *Biofouling*, 19, 279-285.

Tsukamoto, Y., Ishihara, K., Nakazawa, H., Kamada, K., and Huang, Y. N. (2002). "Resistance of partly saturated sand to liquefaction with reference to longitudinal and shear wave velocities." *Soils Found.*, 42(6), 93–104.

U.S. Environmental Protection Agency. (1998). "Addendum to Ambient water quality criteria for ammonia-1984." *National Technical Information Service*, Springfield,VA.

van der Ruyt, M. and van der Zon, W. (2009). "Biological in situ reinforcement of sand in near-shore areas." *Proceedings of the ICE - Geotechnical Engineering*, 162(1), 81 –83.

van Paassen L. A. (2009). “Biogrout ground improvement by microbially induced carbonate precipitation.” *PhD Thesis*, Delft University of Technology.

van Paassen, L., Daza, C., Staal, M., Sorokin, D. Y., van der Zon, W., and van Loosdrecht, M. (2010a). “Potential soil reinforcement by biological denitrification.” *Ecological Engineering*, 36(2), 168–175.

van Paassen, L., Ghose, R., van der Linden, T., van der Star, W., and van Loosdrecht, M. (2010b). “Quantifying biomediated ground improvement by ureolysis: large-scale biogrout experiment.” *Journal of Geotechnical and Geoenvironmental Engineering*, 136(12), 1721–1728.

van Paassen, L. A., van Loosdrecht, M.C.M., Pieron, M., Mulder, A., Ngan-Tillard, D. J. M., van der Linden, T. J. M. (2012). “Strength and deformation of biologically cemented sandstone.” *Proceedings of the Regional Symposium of the International Society for Rock Mechanics*, EUROCK 2009, 405-410

Vanitha, L., Patra, N. R., Chandra, S. (2007). “Uplift capacity of pile group anchors.” *Geotechnical and Geological Engineering*, 25(3), 339-347.

Waite, W. F., Santamarina, J. C., Cortes, D. D., Dugan, B., Espinoza, D. N., Germaine, J., Jang, J., Jung, J. W., Kneafsey, T. J., Shin, H., Soga, K., Winters, W. J., and Yun, T.-S. (2009). “Physical properties of hydrate-bearing sediments.” *Reviews of Geophysics*, 47(4).

Weil, M. H., DeJong, J. T., Martinez, B. C., and Mortensen, B. M. (2012). “Seismic and resistivity measurements for real-time monitoring of microbially induced calcite precipitation in sand.” *Geotechnical Testing Journal*, 35(2), 1-11.

Whiffin, V. S., van Paassen, L. A., and Harkes, M. P. (2007). “Microbial carbonate precipitation as a soil improvement technique.” *Geomicrobiology Journal*, 24(5), 417–423.

Yakimov, M. M., Amro, M. M., Bock, M., Boseker, K., Fredrickson, H. L., Kessel, D. G., et al. (1997). “The potential of Bacillus licheniformis strains for in situ enhanced soil recovery.” *Journal of Petroleum Science and Engineering*, 18(1-2), 147-160.

Yan, D., Bai, Z., Rowan, M., Gu, L., Shumei R. , Yang, P. (2009). “Biofilm structure and its influence on clogging in drip irrigation emitters distributing reclaimed wastewater.” *Journal of Environmental Sciences*, 21(6), 834-841.

Yang, I.C-Y., Li, Y., Park, J. K., and Yen, T. F. (1993). "The use of slime-forming bacteria to enhance the strength of the soil matrix." *Microbial enhanced oil recovery – Recent advances, Elsevier Scientific Publishers*, Amsterdam, 89-96.

Yasuhara, H., Hayashi, K., and Okamura, M. (2011). “Evolution in mechanical and hydraulic properties of calcite-cemented sand mediated by biocatalyst.” *Geo-Frontiers 2011*, 3984-3992.

Yun, T. S., and Santamarina, J. C. (2005). “Decementation, softening, and collapse: changes in small-strain shear stiffness in K_0 loading.” *Journal of Geotechnical and Geoenvironmental Engineering*, 131(3), 350-358.

Yun, T. S., Santamarina, J. C., and Ruppel, C. (2007). “Mechanical properties of sand, silt, and clay containing tetrahydrofuran hydrate.” *Journal of Geophysical Research*, 112(B4), 1-13.

Zhong, L., and Islam, M. R. (1995). “A new microbial plugging process and its impact on fracture remediation (SPE 30519).” *Proceedings of the 70th Annual Technical Conference and Exhibition of the Society of Petroleum Engineers*, Dallas, TX, 703-715.

VITA

Hai (Thomas) Lin was born on December 18, 1986 at Panjin, Liaoning Province of China. He received his Bachelor Degree of Civil Engineering at Dalian University of Technology in 2010. He started research on this doctoral dissertation at Lehigh University in August 2010.